UNIVERSITÄT
PADERBORN

Iron Oxide Catalysts for CO Oxidation - From Basic Structure-Activity-Correlation to an Advanced Preparation Strategy for Highly Active Catalysts

---

DISSERTATION

vorgelegt von

STEFFEN SCHLICHER

zur Erlangung des akademischen Grades

DOKTOR DER NATURWISSENSCHAFTEN
(DR. RER. NAT.)

des Fachbereichs Naturwissenschaften
der Universität Paderborn

Paderborn 2020

Promotionskommission

Prof. Dr. Thomas Kühne	Vorsitz
Prof. Dr. Matthias Bauer	Erstgutachter
Jun. Prof. Dr. Hans-Georg Steinrück	Zweitgutachter
Prof. Dr.-Ing. Hans-Joachim Warnecke	Drittprüfer

Tag der Einreichung: 15.12.2020
Tag der Disputation: 29.01.2021

UNIVERSITÄT
PADERBORN

Eidesstattliche Erklärung

Hiermit versichere ich, die vorliegende Arbeit selbstständig angefertigt und keine anderen als die von mir angegebenen Hilfsmittel verwendet zu haben. Wörtliche und sinngemäße Zitate wurden als solche gekennzeichnet und die Genehmigungen zur Veröffentlichung der urheberrechtlich geschützten Publikationen wurden eingeholt.

Paderborn, den 15.12.2020

…………………………….
Steffen Schlicher

Science is the key to our future,
and if you don´t believe in science,
then you´re holding everybody back.
Bill Nye

Abstract

Iron oxides present potent candidates for replacement of unecological and uneconomical noble metal catalysts for CO oxidation in automotive applications. In the herein described work a structure-activity-correlation of basic iron oxide catalysts supported on γ-Al_2O_3 was established, in which high turnover frequencies could be correlated to a high amount of isolated and finely dispersed iron oxide species in tetrahedral oxygen coordination. A new multistep-impregnation-calcination procedure was deduced, in which the catalysts were impregnated and calcined in 1 wt% steps of iron successively to hinder the formation of inactive agglomerates. The as-prepared catalysts showed outstanding structural properties with a high amount of isolated iron oxide species in tetrahedral coordination geometry up to 8 wt%. A second route for enhanced catalytic activity was tested by addition of Co and Mn to the alumina supported Fe_2O_3 catalysts, resulting in outstanding catalytic activity even at ambient temperature. Their high activity was linked to Co while Mn containing catalysts featured a higher long-term stability. From catalytic activity the optimum Co-Mn ratio was extrapolated, resulting in a catalyst with superior catalytic properties that could possibly enter the race against noble metal catalysts. Additionally, diffusion limitation experiments were carried out with which effects of diffusion onto the measured catalytic activity were minimized and which emphasized the importance of experimental parameters.

Kurzzusammenfassung

Eisenoxide stellen eine Alternative zu teuren, unökologischen Edelmetall-Katalysatoren für die CO-Oxidation in Autoabgasen dar. In der vorliegenden Arbeit wurde eine Struktur-Aktivitäts-Korrelation geträgerter Fe_2O_3-Katalysatoren auf γ-Al_2O_3 erzielt. Höhere Wechselzahlen konnten einer höheren Anzahl isolierter, fein dispergierter Fe_2O_3-Spezies in tetraedrischer Koordinationsgeometrie zugeschrieben werden. Hieraus wurde eine neue Präparationsmethode entwickelt, in der die Eisen(III)-Vorstufe in Schritten von 1 Gew% sukzessive auf den Träger imprägniert und kalziniert wird, um Agglomeration vorzubeugen. Die so hergestellten Katalysatoren zeigten einzigartige strukturelle Eigenschaften mit einer hohen Zahl isolierter Eisenoxid-Spezies in tetraedrischer Koordinationsgeometrie bis zu 8 Gew%. Zusätzlich wurde diese Präparationsmethode mit der Addition von Co und Mn kombiniert. Hierbei konnten Katalysatoren mit herausragender katalytischer Aktivität erhalten werden. Co führte zu einer deutlichen Steigerung der Aktivität, während Mn die Langzeitstabilität erhöhte. Durch Extrapolation der Aktivität konnte zudem ein ideales Co-Mn Verhältnis ermittelt werden. Der entsprechende Katalysator zeigte eine erhöhte katalytische Aktivität und Stabilität und könnte einen potenziellen Ersatz für Edelmetall-Katalysatoren darstellen. Zusätzlich wurden Experimente zur Untersuchung von Diffusionseffekten durchgeführt, um deren Einfluss auf die gemessene katalytische Aktivität zu minimieren und durch welche die immense Bedeutung der Reaktionsparameter gezeigt werden konnte.

Danksagung

Hier möchte ich die Gelegenheit ergreifen und mich bei allen Personen bedanken, die maßgeblich Anteil an dieser Arbeit haben, sei es durch die direkte Mitarbeit oder durch mentale Unterstützung im Laufe der letzten Jahre.

Zunächst möchte ich mich bei Herrn Prof. Dr. Matthias Bauer für die Aufnahme in seine Forschungsgruppe und die Bereitstellung des sehr interessanten und vor allem aktuell relevanten Themas bedanken. Er ermöglichte mir nicht nur die Chance zur Promotion, sondern auch die Teilnahme an fordernden, aber auch sehr spannenden Messzeiten an diversen Forschungseinrichtungen, sowie meine fachliche und persönliche Weiterbildung auf zahlreichen Konferenzen. Auch hatte er stets ein offenes Ohr, stand für fachlichen Rat immer zur Verfügung und hat die auf Gegenseitigkeit beruhenden Sticheleien stets humorvoll gekontert.

Herrn Prof. Dr. Thomas Kühne danke ich für die Übernahme des Vorsitzes bei meiner Disputation, sowie Herrn Jun. Prof. Dr. Hans-Georg Steinrück und Herrn Prof. Dr. Hans-Joachim Warnecke für die Übernahme der Stelle des Zweitgutachters und Drittprüfers.

Außerdem möchte ich Herrn Dr. Jürgen Gieshoff (Umicore AG), Herrn Christian Singer (TU BA Freiberg) und Herrn Prof. Dr. Sven Kureti (TU BA Freiberg) danken, die im Rahmen des DFG-Forschungsprojektes, innerhalb dessen der Großteil der hier beschriebenen Arbeiten stattgefunden hat, mitgearbeitet haben und durch fachliche Diskussionen und parallele Arbeiten an dem Themengebiet maßgeblich an den gezeigten Ergebnissen beteiligt sind.

Des Weiteren möchte ich mich bei den Personen bedanken, die die Durchführung von Analysemethoden vorgenommen haben, die nicht in unserem Arbeitskreis möglich waren: Andrej Paul, Markus Schmitz, Dr. Christian Weinberger und Christiane Gloger für die XRD- und N_2-Physisorptions-Messungen, Annelies DeCuyper (TU Kaiserslautern) für die Durchführung der DRUVS Messungen, Andreas Omlor (TU Kaiserslautern) für die Mößbauer Messungen, Julius Bürger (AK Lindner) für die Aufnahme der HAADF und STEM-EDX Messungen, Herrn Prof. Dr. Wolfgang Kleist und seiner Arbeitsgruppe (Ruhr-Universität Bochum) für die Aufnahme der hochauflösenden XRD-Messungen und Christian Singer (TU BA Freiberg) für die Aufnahme von Mößbauer-Spektren und DRUVS Messungen. Herrn Prof. Dr. Sven Kureti und seinem Arbeitskreis und insbesondere Christian Singer möchte ich außerdem für die freundliche Aufnahme während meines kurzen Forschungsaufenthalts in ihrem Labor danken.

Außerdem möchte ich mich bei Jennifer Klaucke bedanken, die ich bei den Arbeiten im Rahmen ihres Vertiefungspraktikums und ihrer Bachelorarbeit betreuen durfte und die mich durch die Literaturrecherche und anschließende Synthese und Arbeiten zur Charakterisierung der bi- und trimetallischen Übergangsmetallkatalysatoren maßgeblich unterstützt hat.

Nun möchte ich mich natürlich noch bei den aktuellen, sowie auch den ehemaligen Mitgliedern des Arbeitskreises für die freundliche Aufnahme, die angenehme Arbeitsatmosphäre, die zahlreichen fachlichen Diskussionen aber auch Gespräche fernab von Forschung und auch die außeruniversitären Unternehmungen bedanken. Mein ganz besonderer Dank gilt hier Dr. Roland Schoch, der mir bereits in Kaiserslautern in einem Vertiefungspraktikum das Themengebiet *Heterogene Katalyse an Eisen-basierten Katalysatoren* schmackhaft gemacht hat und von dem ich das hier beschriebene Thema letztlich übernommen habe. Er stand stets mit Rat und Tat zur Seite, wobei die fachlichen Diskussionen oft auch eine sehr lustige Komponente hatten. Gemeinsam wurden in diesem Rahmen auch viele zusätzliche Projekte, wie zum Beispiel die Entwicklung von *in situ* Zellen für verschiedenste röntgenspektroskopische Anforderungen, durchgeführt. Insbesondere möchte ich den Personen danken, die es immer wieder geschafft haben, meine Laune zu steigern (v. A. in zahlreichen Kaffeepausen) und mit denen auch tolle Freundschaften entstanden sind: Dr. Maike Tünnermann, Dr. Regina Meinhardt, Dr. Hatice Söyler, Voicu Muntean, Dr. Patrick Müller, Lorena Fritsch, Pia Rehsies, Tanja Hirschhausen und Dr. Yannik Vukadinovic.

Mein größter Dank gilt aber meiner Familie sowie meinen langjährigen Freunden, die mir sowohl während des Studiums als auch in der Zeit der Dissertation trotz der großen Entfernung immer Rückhalt geboten und mich stets in meinen Vorhaben unterstützt haben.

List of Beamtimes

Deutsches Elektronensynchrotron (DESY)

- P64
  - July 02-09 2018
  - October 24 - November 01 2018
  - April 11-17 2019
  - November 07-13 2019

- P65
  - July 29 - August 02 2016
  - October 22 - November 02 2016
  - April 20-25 2017
  - June 02-07 2017
  - August 31 - September 05 2017
  - December 10-12 2017
  - May 29 - June 03 2020
  - June 11-17 2020
  - October 01-06 2020

Diamond Light Source

- B18
  - August 07-11 2017
  - October 04-06 2019

European Synchrotron Radiation Facility (ESRF)

- ID26
  - November 15-22 2016
- BM26a
  - July 08-12 2018

Spring-8 Angstrom Compact free electron Laser (SACLA)

- July 05-08 2018

List of Publications

Publications in Journals

1. S. Schlicher, Nils Prinz, Julius Bürger, Andreas Omlor, Christian Singer, Mirijam Zobel, Jörg Lindner, Volker Schünemann, Sven Kureti, Matthias Bauer, „Quality or Quantity? How Structural Parameters Affect Catalytic Activity of Iron Oxides for CO Oxidation", *manuscript in preparation.*

2. S. Schlicher, Christian Singer, Sven Kureti, Matthias Bauer, „Keep it Simple! A New Preparation Technique for Iron Oxide Catalysts with Outstanding Structural Properties for CO Oxidation", *manuscript in preparation.*

3. S. Schlicher, Jennifer Klaucke, Matthias Bauer, „Bi- and Trimetallic 3d-Metal Catalysts for Low Temperature CO Oxidation", *manuscript in preparation.*

Talks

1. S. Schlicher, M. Bauer: „Can Iron Oxides Keep Up with Noble Metals in Carbon Monoxide Oxidation?", 52. Jahrestreffen Deutscher Katalytiker, Weimar (Germany), March 14, 2019.

2. S. Schlicher, M. Bauer: „Can Iron Oxides Keep Up with Noble Metals in Carbon Monoxide Oxidation?", Oral Poster Presentation, Webinar, 53. Jahrestreffen Deutscher Katalytiker, May 20, 2020. *

   **Honored with a poster award.*

Poster Presentations

1. S. Schlicher, M. Bauer: „New Iron Catalysts for CO Oxidation", 26th ATC (Industrial Inorganic Chemistry), Frankfurt (Germany), February 23-24, 2017.

2. S. Schlicher, M. Bauer: „New Iron Catalysts for CO Oxidation", 50. Jahrestreffen Deutscher Katalytiker, Weimar (Germany), March 15-17, 2017.

3. S. Schlicher, M. Bauer: „Novel Iron Catalysts for CO Oxidation", 27th ATC (Industrial Inorganic Chemistry), Frankfurt (Germany), February 22-23, 2018.

4. S. Schlicher, M. Bauer: „Can Iron Oxides Keep Up with Noble Metals in Carbon Monoxide Oxidation?”, NAM26, Chicago (USA), June 23-28, 2019.

5. S. Schlicher, M. Bauer: „Can Iron Oxides Keep Up with Noble Metals in Carbon Monoxide Oxidation?”, EuropaCat, Aachen (Germany), August 18-23, 2019.

Table of Contents

Page

Abstract iii

Kurzzusammenfassung v

Danksagung vii

List of Beamtimes xi

List of Publications xiii

1 Introduction 1

- 1.1 Environmental Pollution 1
- 1.2 Catalytic Emission Reduction 3
  - 1.2.1 Catalysis 3
  - 1.2.2 Applications 4
  - 1.2.3 Carbon Monoxide Oxidation 8
    - 1.2.3.1 CO Oxidation Catalysts 11
    - 1.2.3.2 Preparation Method 12
    - 1.2.3.3 Support Material 13
    - 1.2.3.4 Promoters 14
    - 1.2.3.5 Catalytically Active Species 14
    - 1.2.3.6 Iron in CO Oxidation 16

2 Aim of this Work 23

3 Quality or Quantity? 25

- 3.1 Results 25
- 3.2 Summary and Discussion 37

4 Keep it Simple! 39

- 4.1 Results 39
- 4.2 Summary and Discussion 51

5 Bi- and Trimetallic 3d-Metal Catalysts for CO Oxidation 55

5.1 Results 55
5.2 Summary and Discussion 68

6 Reaction Parameter Optimization 71

7 Conclusion & Outlook 75

8 Experimental 79

8.1 Preparation of the γ-Al_2O_3 support 79
8.2 Preparation of Fe01 to Fe20 79
8.3 Preparation of MI01 to MI10 and SI10 79
8.4 Preparation of MM01 to MM06 80
8.5 Catalytic experiments 80
8.6 Analytics 81
8.6.1 N_2 Physisorotion 81
8.6.2 PXRD 82
8.6.3 HRPXRD 82
8.6.4 Mößbauer 82
8.6.5 DRUVS 83
8.6.6 HAADF/STEM-EDX 83
8.6.7 XAS 84

References 87

Abbreviations 103

Figures 105

9 Appendix 111

9.1 Phase Purity of the γ-Al_2O_3 Support 111
9.2 Low Temperature Mößbauer Spectroscopy 112
9.3 UV/Vis-Spectroscopy 116
9.3.1 Peak Deconvolution: Fe01 - Fe20 116
9.3.2 Peak Deconvolution: MI01 - MI10 and SI10 121
9.4 X-Ray Absorption Spectroscopy 132
9.4.1 Pre-Peak Analysis: Fe01 - Fe20 132
9.4.2 Pre-Peak Analysis: MI01 - MI10, SI10 142
9.4.3 Pre-peak Analysis: Mn K-edge, MM01 - MM04 164
9.4.4 Pre-peak Analysis: Fe K-edge, MM01 - MM05 172

9.4.5 Pre-peak Analysis: Co K-edge, MM02 - MM05 182
9.4.6 Pre-peak Analysis: References 190
9.4.7 EXAFS Analysis 198
9.4.7.1 Fe01 - Fe20 198
9.4.7.2 MI01 - MI10 & SI10 199
9.4.7.3 MM01 - MM04: Mn K-edge 201
9.4.7.4 MM01 - MM05: Fe K-edge 202
9.4.7.5 MM02 - MM05: Co K-edge 203
9.5 Optimization MM06 204

1 INTRODUCTION

1.1 Environmental Pollution

As one lets the eyes wander around over the aquascape of a well operating aquarium, the nicely growing plants and the delightful inhabitants, the thing that comes to one´s mind besides the beauty is the fact, that it is basically a self-preserving ecosystem, that just needs minor help from outside. This ecosystem is so fragile, that, by the slightest change of one parameter, the well-being of all organisms in it can be endangered. When maltreated, eutrophication with pollutants such as nitrates or phosphates can take place, lowering the amount of oxygen that can be stored in the water, threatening life in it. The earth is a similar ecosystem, just bigger and by far much more complex, but just as sensitive to mistreatment. The lives of humankind and of all organisms such as plants and other animals depend on the well-being of this single ecosystem.

Since mankind is steadily evolving and continuously trying to improve its situation while outgrowing the capacities of earth, such as raw materials or food supply, there is an ever-growing demand for industrial applications and the generation of energy. These lead to an increase in emission of pollutants into the above-mentioned ecosystem[1]. Growth of agricultural industry leads to contamination of soils and groundwater with fertilizers, pesticides or other harmful substances[2-7], clearing of woodlands leads to less conversion of carbon dioxide to oxygen by plants and trees, hence contributing to climate change[8,9]. Expansion of industry, especially automotive, causes vast amounts of gaseous and volatile organic compounds as well as particulate matter to be emitted into the air. A major effect of this, that can be observed, is climate change[10-12]. Normally, high amounts of energy-rich radiation from the sun are either absorbed by the ozone layer in the stratosphere or backscattered from the surface of the earth, while air is almost totally transparent for them. Vast amounts of so-called greenhouse gases, including carbon dioxide, nitrous oxide and methane, lead to a high absorption of this radiation and thus to an increase in temperature of the earth and its atmosphere[13-15]. Besides primary effects on organisms sensitive to temperature fluctuation or for example lowered amounts of oxygen that can be stored in a body of water, this can also lead to cascading consequences, like melting of glaciers and polar ice, resulting in an elevated sea level, threatening coastal ecosystems all over the world. These are just minor examples, while the overall number of consequences seems to be endless.

In 2015, emission of greenhouse gases was as high as 4.3 gigatons (CO_2 equivalent) just for fuel combustion in the European Union and even higher for the USA and China[16]. In the EU actual carbon dioxide took in roughly 80 percent of this, methane about 10 and nitrous oxide followed by hydrofluorocarbons the remaining part. The effects of these numbers on climate change are tremendous, as there has already been a global warming of approximately 1 °C since the industrial revolution, and it is expected to lead to further global warming of 0.5 °C within the next 30 years[17]. The, without any doubt, needed countermeasures have already been defined in arrangements like the Kyoto Protocol[18] or the Paris Agreement[19] and already show positive trends in decreasing greenhouse gas emissions, but due their slow depletion in the atmosphere, positive effects on climate change will take their time.

Environmental pollution also has direct impacts on living organisms, such as allergic effects, chronic diseases or even death, depending on the kind and amount of pollutants the organisms are exposed and over which period of time. Especially in highly populated areas emissions by industries or traffic are tremendous. In Germany 55.6 million vehicles were registered in the year 2017 (see Figure 1.1)[20], a number that increased by almost 2 million until 2019[21]. Although strict regulations for automotive industry and the biannual inspections led to a decline in the resulting emission of pollutants, the quantities were still tremendous. In 2017 besides 160 million tons of carbon dioxide, 704 thousand tons of carbon monoxide were set free by street traffic, as well as 402 thousand tons of nitrous gases (NO_x) and 94 thousand tons of non-methane volatile organic compounds (VOC), just to mention some. Needless to say that most of them, in some way, are known to have adverse impacts on human health. These include effects on the cardiovascular[22,23] and pulmonary system[24] while some pollutants can even be linked to pregnancy loss[25] and a higher risk of malignant tumors, especially in brain[26] and lung[27].

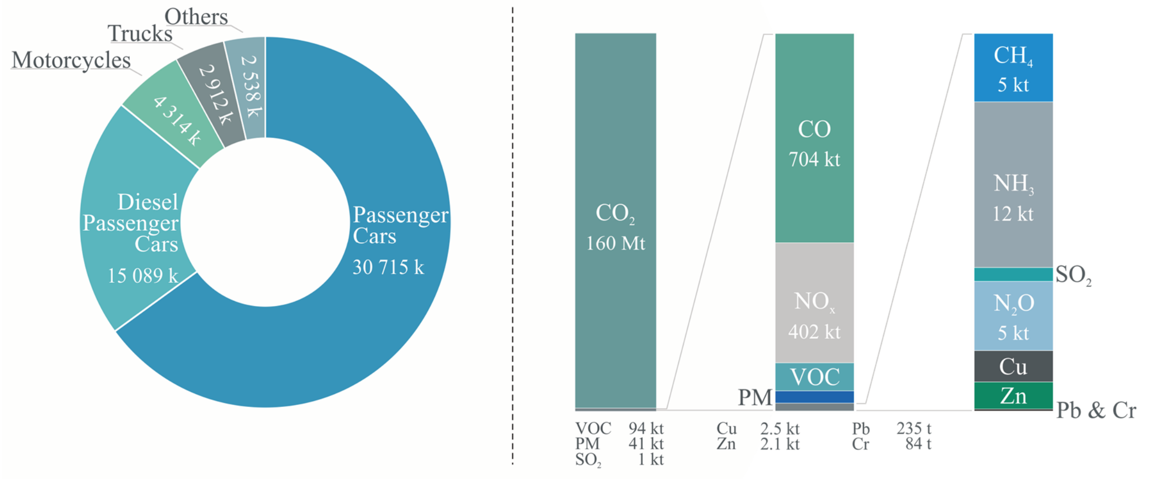

Figure 1.1: German road traffic 2017; numbers of registered vehicles by categories (left) and emissions resulting from road traffic (right) per year[21].

To regulate these emissions in order to protect people and the environment, especially in highly populated and thus highly polluted urban areas, restrictions were put in place for automotive industry. First in the USA in the sixties, including the establishment of the California Air Resources Board (CARB) and then in 1970 by the European Community (EC). The initial thresholds for automotive exhaust gases were only set for hydrocarbons and carbon monoxide. In the EC a strictly predefined test protocol had to be passed by every new car, enduring 13 minutes with several intervals of acceleration, change of gears, constant speed and deceleration. For passenger cars the amount of pollutants emitted during this test was not allowed to exceed 100 to 265 g for CO, respectively 8 to 16.6 g for hydrocarbons (HC), depending on the vehicle weight[28]. In 1977 the EC included nitrogen oxides in their directives with a maximum of 10 to 19.2 g[29] and from 1988 also particulate matter (PM), which were regulated to a maximum of 1.4 g per measurement[30].

Throughout the next decades these limits as well as the test protocol were successively adjusted to the steadily increasing number of vehicles on the streets and the consequential raised levels of air pollution. Regarding the newest European norm “Euro 6d” emissions within the *worldwide harmonized light vehicles test procedure* (WLTP) protocol have to be kept below 1 g/km of CO, 100 mg/km of hydrocarbons of which a maximum of 68 mg/km can be non-methane hydrocarbons (NMHC), 60 mg/km NO_x and for vehicles with direct fuel injection 4.5 mg/km of PM with a total particle number (PN) below $6 \cdot 10^{11}$. For diesel engines the CO emission is limited by 500 mg/km, NO_x by 80 mg/km while HC and NO_x together must not exceed a total of 170 mg/km. Here again PM are limited by 4.5 mg/km and the total particle number by $6 \cdot 10^{11}$[31]. To stay within these limits, tremendous amounts of optimization had to be conducted and are still going on. In this regard, approaches include alteration[32-34] or even exchange of the fuels[35,36] commonly used for combustion as well as an efficiency improvement of the combustion engines themselves[37].

1.2 Catalytic Emission Reduction

Removal of pollutants out of the exhaust gas is an approach contrary to the above mentioned. This commonly used principle utilizes derivatization of unwanted substances to less harmful or non-toxic alternatives. As such a reaction usually does not proceed on its own, a catalyst is required.

1.2.1 Catalysis

The term *catalysis* was first used by Berzelius in 1835 in a progress report for the Royal Swedish Academy of Science based on his own findings and of scientists like Thénard, Humphry and Edmund Davy, Döbereiner, Dulong and especially Mitscherlich[38]. It was at this time, the 19th century, when scientists started to realize what the mysterious force was, although it had already been utilized in many ways without knowing. For example fermentation is a concept that can be dated back to as early as 7000 b. c. and has been used in countless variations over time[39]. The modern definition of catalysis was coined by Ostwald, who said:

> *“Katalyse ist die Beschleunigung eines langsam verlaufenden chemischen Vorganges durch die Gegenwart eines fremden Stoffes”*[40]

This can be translated to “catalysis is the acceleration of a slow proceeding chemical process by the presence of another substance” with which he commented on a definition by Strohmann who said, catalysis was a process of motion of the atoms in molecules of labile bodies, that occurs by transmission of force from another body and that, under loss of energy, leads to the formation of more stable bodies.

From then on, catalysis was not just an obscure phenomenon, it evolved into a powerful tool in the toolbox of natural scientists. It became a whole field of research on its own and within the next decades processes such as the Haber-Bosch process for ammonia synthesis[41] and its further processing into nitric acid by Wilhelm Ostwald[42], which both revolutionized agricultural industry by means of a new and efficient way for the production of fertilizers. Without these achievements it would be almost impossible to feed over 7.7 billion people on earth.

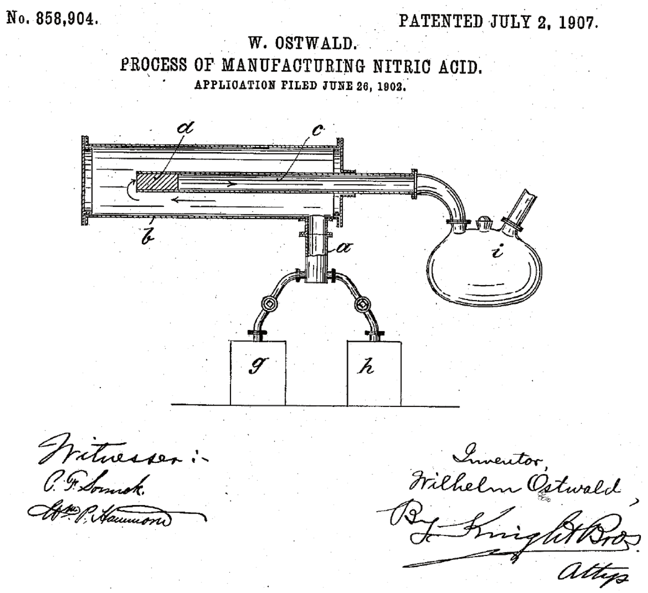

No. 858,904. PATENTED JULY 2, 1907.

W. OSTWALD.

PROCESS OF MANUFACTURING NITRIC ACID.

APPLICATION FILED JUNE 26, 1902.

Witnesses:-
C. F. Sonnek.
Wm. P. Hammond

Inventor,
Wilhelm Ostwald
By Knight Bros.
Attys

Figure 1.2: Extract of the patent W. Ostwald obtained for his process of nitric acid synthesis in 1907[42].

There are many other catalytic applications that changed the world we live in substantially and are now indispensable. May it be the production of bulk chemicals via catalytic cracking[43,44], Fischer-Tropsch[45-47] or Bergius-Pier[48,49], or the processing of these to even more valuable materials such as fine chemicals respectively pharmaceuticals (e. g. Wacker[50-53] or the hydroformylation discovered by Roelen[54,55]), the catalytic reforming to fuels[56-58] or the Ziegler-Natta polymerization[59,60]. Latter leads to polymers, also known as plastics, which nowadays are a huge part of our lives. Over 90 % of products from chemical industry are estimated to undergo at least one catalytic transformation[61]. However, the mentioned processes are just a few of the most noticeable to outline the impact of catalysis on humankind.

1.2.2 Applications

The steady growth of the human population is accompanied with an ongoing increase in pollution of water, soil and air due to increasing numbers of traffic and industrial processes. To minimize the risk of adverse health effects, as mentioned before, pollutants have to be removed from exhaust gases or at least kept below certain thresholds. To do so, the catalytic conversion of harmful substances to less or non-harmful derivatives is a well-established method, for example in the treatment of wastewater.

Water is essential for life but despite the tremendous amounts of water on earth, only a few percent of it can be considered clean enough to be consumable. Especially in developing countries, clean water is often distributed insufficiently. This is due to the low standards for wastewater treatment of industry and agriculture and the resulting expenses that must be put into water purification. Pollutants like heavy metals and toxic organic compounds are removed by adsorption on substrates or coagulation, which is inefficient. Catalysis, again, offers a promising alternative for removal of contaminants, namely photocatalytic degradation of such[62,63]. After absorption of sunlight, transition metal oxides, mostly variations of titanium dioxide, can generate hydroxyl radicals which are able to degrade any organic compound by oxidation and mineralization, the so-called advanced oxidation processes (AOP)[62].

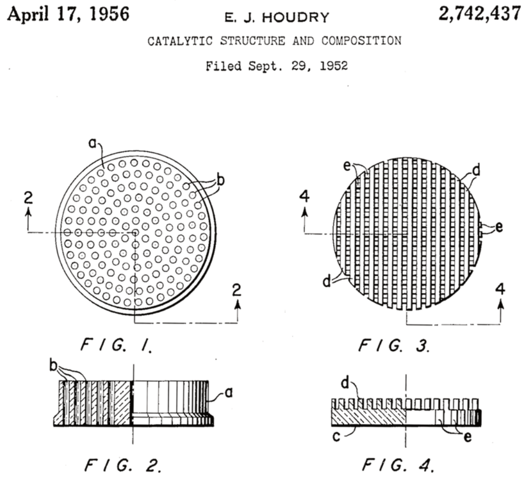

April 17, 1956 E. J. HOUDRY 2,742,437

CATALYTIC STRUCTURE AND COMPOSITION

Filed Sept. 29, 1952

Figure 1.3: Extract from the original patent for a catalytic converter, patented from Eugene J. Houdry in 1956[64].

While photocatalytic wastewater treatment still is in its early stage of development, removal of pollutants from exhaust gases already is a well-established process since decades. First catalytic converters for usage in automobiles were invented as early as the 1950s, when the production of vehicles with combustion engines increased drastically and first connections between extremely polluted air and road traffic were drawn[65,66]. The first patent for a catalytic converter for automotive application was obtained as early as 1956 by Eugene Houdry (Figure 1.3)[64]. However, due to low stability against fuel additives the first commercial application of such systems was not before the 1970s following the clean air act from 1963[67]. By then, more advanced and versatile systems were invented[68]. The main reactions in a modern catalytic converter are the reduction of nitrogen oxides to elemental nitrogen and the simultaneous oxidation of carbon monoxide and hydrocarbons to carbon dioxide (see Figure 1.4)[69].

$$2\,NO + 2\,CO \longrightarrow N_2 + 2\,CO_2$$

$$2\,CO + O_2 \longrightarrow 2\,CO_2$$

$$2\,C_2H_6 + 7\,O_2 \longrightarrow 4\,CO_2 + 6\,H_2O$$

Figure 1.4: Model reactions taking place in a modern three-way-catalyst.

To achieve adequate yields in these reactions, respectively to lower the emission of the pollutants matching the regulations discussed in chapter 1.1, utilization of a catalyst is crucial. While a catalyst solely for the oxidation reaction or the reduction in a model reactor can be easily found among transition metals, the demands in this particular case exacerbate the search[69,70]. Application in vehicles requires high activity of the catalytic converter in a broad range of temperatures, preferably from cold start up to 1000 °C. At low temperatures the activity is the factor that limits the scope of possible candidates, whereas high temperatures often cause sintering of the catalyst or much worse, oxidation of the catalyst to metal oxides that are volatile at elevated temperatures leading to a loss of precious material[71,72]. Since fuels often contain additives to increase their knock resistance or to alter their properties in other ways, the stability of the catalyst against these additional substances is also crucial. In fact, tetraethyl lead (TEL) in fuels for higher knock resistance was the main cause, why the oxidation catalyst invented by Houdry did not see commercial application[73]. The substance caused poisoning of the catalyst by deposition of lead on its surface, respectively the formation of an inactive metal alloy. Since the 1970s most countries regulated the use of TEL both due to possible health risks and for the successful introduction of catalytic converters into the automotive market[73]. Furthermore, the exhaust gas composition is not exactly the same for every vehicle and even within the drive cycle of one car, it changes substantially, depending on many parameters such as the temperature of the engine or the driving habits of the operator. Therefore such a catalyst must be even more resilient.

Since abundant metals like cobalt, nickel or copper, despite promising activity in oxidation reactions, were too sensitive to catalyst poisoning and sintering[74-78] research focused on platinum group metals (PGM). Here, as stated before, formation of oxidic species that are volatile at elevated temperatures can cause loss of the catalyst metal, which is the case for ruthenium[71]. Palladium and platinum were then chosen for the oxidative part, while a mixture of rhodium and platinum was selected for the reduction of nitrogen oxides. Since activity of the catalysts for both processes is strongly dependent on whether the conditions are oxidizing or reducing, the ratio of air to fuel (λ) introduced into the system plays a key role. A stoichiometric ratio of air to fuel means the point of total combustion, at least in theory, without any excess air or fuel. This ratio is defined as $\lambda = 1$. Excess air leads to oxidizing conditions in the exhaust gas stream and is often referred to as a *lean mixture* ($\lambda > 1$), whereas excess fuel is called *fat* or *rich* and results in more unburned fuel, hence reducing conditions ($\lambda < 1$). Because of the need for either a fat or a lean mixture (Figure 1.5), first both processes were kept separated[79]. The emissions from the combustion engine first entered the converter with ruthenium/platinum for *selective catalytic reduction* (SCR), then air was added to the gas mixture before entering the second part of the converter for the oxidation of CO and hydrocarbons. Later it was found, that, when running the engine close to the stoichiometric point of fuel to air ($\lambda = 1$), all three main reactions can take place simultaneously in one chamber, which is now known as the three-way-catalyst[70]. Introduction of the TWC to commercial automotive market was in the 1980s, first in the US and Canada, then in the EU and other parts of the world[80].

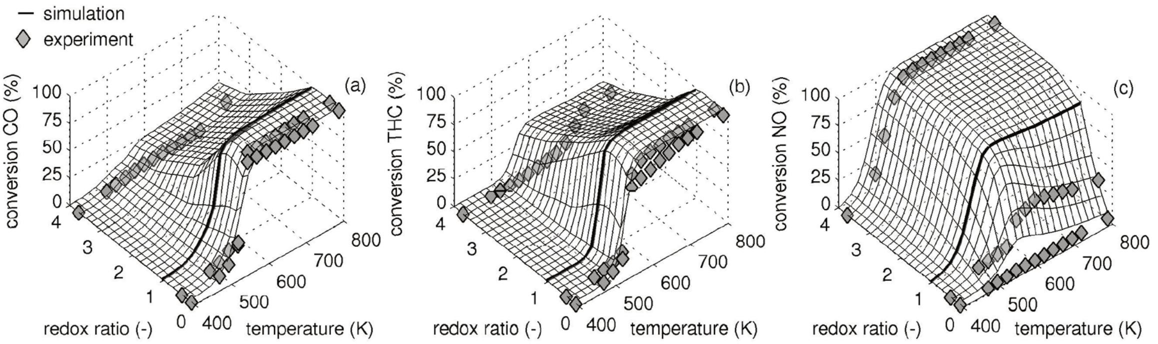

Figure 1.5: Experimental and modelled conversion curves of CO (left), hydrocarbons (middle) and NO (right) vs. temperature and redox ratio, respectively reciprocal lambda value, reprinted from Wurzenberger et al.[81].

As if all these considerations were not complex enough, they only apply for petrol engines, which can operate at the said stoichiometric lambda value. The also widely used diesel engine, however, operates mostly under lean conditions exacerbating the reduction of nitrogen oxides. Due to the lean air to diesel mixture emissions of hydrocarbons and carbon monoxide are usually lower than for petrol engines. Commonly a diesel oxidation catalyst (DOC) is deployed to further decrease them, usually by platinum as catalytically active species. Besides that, high amounts of PM and NO_x require special treatment. Modern cars with diesel engines are equipped with particulate filters (DPF)[82,83] to reduce PM emissions. To reduce nitrogen oxides, either NO_x storage/reduction catalysts (NSR)[84] or converters for SCR[85-88] are used. The latter works by addition of a reductant which promotes selective degeneration of the harmful nitrogen compounds. AdBlue® is the commonly used mixture, with which the required additive, urea, is introduced into the exhaust gas[89]. There urea is hydrolyzed to ammonia, which then works as the said reductant (Figure 1.6)[90].

$$1)\qquad (NH_2)_2CO + H_2O \longrightarrow 2\,NH_3 + CO_2$$

$$2)\qquad 4\,NO + 4\,NH_3 \longrightarrow 4\,N_2 + 6\,H_2O$$

$$3)\qquad 6\,NO_2 + 8\,NH_3 \longrightarrow 7\,N_2 + 12\,H_2O$$

$$4)\qquad NO_2 + NO + 2\,NH_3 \longrightarrow 2\,N_2 + 3\,H_2O$$

Figure 1.6: Main reactions correlated to selective catalytic reduction: 1) hydrolysis of urea to form ammonia; 2) reduction of NO with ammonia; 3) reduction of NO_2 with ammonia; 4) reduction of NO and NO_2 together[90].

While the SCR process requires the redesign of the infrastructure with a reservoir and an injector for the additive, sensors to control the amounts needed and a whole new compartment for the SCR catalyst, NSR can be applied in the standard converter. Therefore materials are introduced, that can store NO_2 in form of nitrates. Under lean conditions with excess air, NO is oxidized to NO_2, which is then incorporated into the storage material. In distinct time intervals the conditions are changed to a fat mixture. This promotes the release of NO_2 followed by its reduction by CO or HCs, just like in a three-way-catalyst[89]. Both of these strategies can also be applied in vehicles with modern petrol engines, as they are often operated under lean conditions ($\lambda > 1$) where a standard TWC does not work. Another approach is the direct reduction of NO_x by soot, which has been studied extensively by

Kagawa and co-workers on catalysts like manganese containing perovskites[91] or Co-Fe spinels[92] and by Kureti and co-workers on iron oxide catalysts such as $Fe_{1.9}K_{0.1}O_3$[93] and Fe_2O_3[94]. The commonly used catalysts in SCR are V_2O_5-WO_3/TiO_2 in which the vanadium oxide is the catalytically active species, tungsten trioxide a promoter and stabilizer and both are supported on titanium dioxide[86,95,96] or zeolites doped with iron[97-99] or copper[100,101]. The latter have the advantage of a higher temperature stability compared to the vanadium catalyst, which is beneficial for a possible coupling of SCR with DPF. Here the selective reduction could be accomplished by unburned hydrocarbons trapped in the DPF instead of an external reducing agent (urea) but the high temperatures needed for regeneration of the particulate filter lead to deactivation of vanadium oxide catalysts[98].

All of these countermeasures already show small positive effects with partly lowered emissions of pollutants from combustion engines[16]. However, there is still the need for enormous improvement to fulfill the thresholds set in the Kyoto protocol or the Paris agreement and even more if we want to fight global warming and save our ecosystem.

1.2.3 Carbon Monoxide Oxidation

The human body is an elegantly designed and yet complex construct. Bones, muscles, tendons, organs, cross-linked and working together in countless ways. Numerous chemical reactions and physical processes taking place at the same time, even while writing or reading this. Yet it is so delicate that when one small molecule, such as oxygen, is withheld, the balance of all processes is disrupted. Oxygen is essential for every cell of our body. It enters the circulatory system via the alveoli of our lung, it is then bound reversibly by hemoglobin of the erythrocytes responsible for its distribution in our body. Derogations in this cycle can lead to severe consequences, even death[102].

Despite the entirety of negative effects of pollutants from combustion engines, carbon monoxide still stands out due to its acute toxicity. CO is a colorless gas without any odor or taste and thus an insidious threat. Just like oxygen it can pass the blood-air-barrier via the alveoli of our lung. Dissolved in the blood it binds onto hemoglobin with a 210 times higher affinity than oxygen, hence inhibiting distribution of the latter[103]. The fast binding of CO by hemoglobin (Hb) and a very slow dissociation lead to a steadily increasing blood concentration of COHb and a simultaneously decreasing amount of HbO_2, when exposed to CO over a long period of time. Elevated amounts of COHb can lead to severe damages and even death through several mechanisms[103,104]. In the myocardium, the heart muscle, CO is transferred from hemoglobin to myoglobin, which is responsible for intramuscular oxygen transport. This way distribution of oxygen to the mitochondria is impaired, hence oxidative phosphorylation of adenosine monophosphate (AMP) or adenosine diphosphate (ADP) is blocked and no adenosine triphosphate (ATP) is being generated. Absence of the energy carrier ATP leads to a non-functioning heart muscle and thus a lack of blood circulation, without which all other tissue stays without oxygen supply. Consequences are malfunction of organs - including the brain - unconsciousness, coma, death, depending on the severity of the CO intoxication. But CO also poses a threat when the blood circulation with oxygen-containing blood is brought back. A lack of oxygen distribution leads to tissue hypoxia, thus to a degradation of ATP under the formation of hypoxanthine. Without ATP cellular ion pumps cannot work. Potassium ions are set free while calcium enters the cell followed by the degradation of xanthine dehydrogenase to xanthine oxidase, which, when the oxygen supply is restored, oxidizes hypoxanthine to xanthine and radical oxygen species. These radicals attack the cell membranes, causing visible damage to tissue such as myocardial fiber necrosis or damages on the central nervous system. This can lead to life-threatening malfunction of organs hereafter. Additionally, the direct damage to pulmonary tissue without prior transport of CO by hemoglobin is being discussed, again through reoxygenation injury.

The main source of carbon monoxide is incomplete combustion of fossil resources, which leads to vast emissions of CO. As mentioned in chapter 1.1 over 704 thousand tons were set free by road traffic in Germany (2017), although countermeasures such as TWC or DOC have already been optimized to keep emissions below the thresholds set by the EU. Obviously, the efficiency of the catalytic CO oxidation still has to be increased towards the point of “zero emissions”.

To improve catalytic activity a basic understanding of the oxidation of CO by elemental oxygen is crucial. Catalysis in general can be divided into heterogeneous and homogeneous catalysis. The latter describes processes, where the catalyst is present in the same physical state as the reactants. Such a process is often considered to be more efficient because it is not dependent on as much parameters as a heterogeneous catalyst, which, in contrast, is present in another phase than the reactants. For instance, a solid-state catalyst for a liquid or gas phase reaction. The benefits here are that the catalyst can easily be regained from the application (i. e. by simple filtration of a solid catalyst from a liquid phase reaction) or that the catalyst can be totally immobilized on a support surface, so that even the filtration step can be avoided. The handling of a heterogeneous catalyst often is more convenient, especially for automotive application, which will be discussed further in the following chapters.

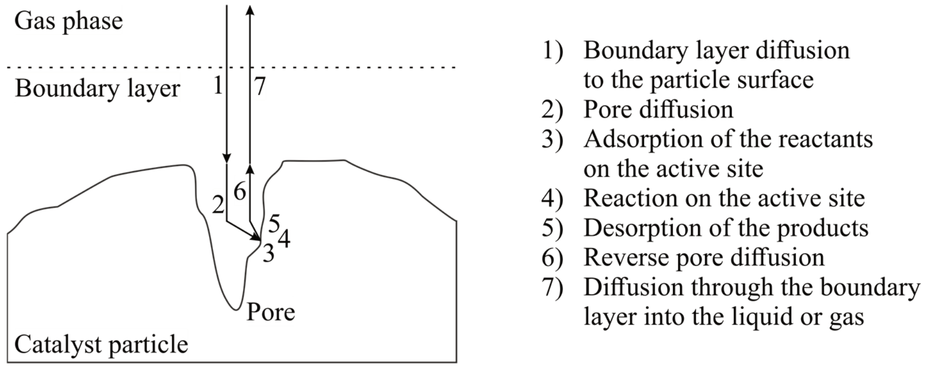

Figure 1.7: Conceptual scheme of the steps required from educts and products in heterogeneous catalysis.

The concept of heterogeneous catalysis often is described in 7 steps (Figure 1.7)[105]. In a reaction of gaseous reactants on a solid catalyst, like in a catalytic converter of a vehicle, the gas stream containing the educts surrounds the catalyst particles. In order to react, first the educts have to diffuse through the boundary layer to the particle surface (1), then through the pore to the actual active site (2), if the catalyst, respectively the catalyst support, is a porous material. Adsorption (3) is then required before the reaction of the reactants on the catalyst surface (4) after which the products desorb from the active site (5) and diffuse back through the pore (6) and the film diffusion layer back into the surrounding gas stream (7). Every heterogeneously catalyzed reaction, oxidation of CO included, can be described with these simple steps. It is desirable to minimize the effects of boundary layer and pore diffusion to prevent the overall process from being diffusion limited. Then CO oxidation can be described by adsorption on the active site, reaction of CO with oxygen and desorption of CO_2. The energetic scheme of this reaction, exemplary on a palladium catalyst, is shown in Figure 1.8[106,107].

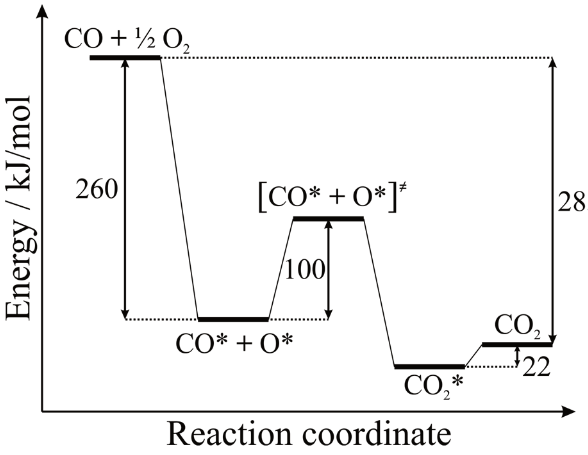

Figure 1.8: Energetic diagram of the oxidation of carbon monoxide on a platinum catalyst[106,107]; adsorbed species are marked with "" and the transition state with "≠"; numbers give the energy value of the respective step.*

The reaction of adsorbed CO and O on the catalyst surface is the rate determining step (RDS). The energy needed for dissociation of O_2 on the active site is neglectable, thus not shown here. However, in the gas phase without the interaction with a catalyst, the dissociation energy of O_2 is approx. 500 kJ/mol[107], hence this is the RDS for the gas phase reaction and at the same time the reason why the reaction does not take place spontaneously. A catalyst is indispensable to lower the energy demand of this reaction.

First publications of CO oxidation date back to over a century ago. In their *Handbuch der Anorganischen Chemie*, published in 1909, Abegg and Auerbach describe experiments of Colson[108], Nicloux[109], Gautier[110] and Phillips[111] about oxidation of carbon monoxide to CO_2 by noble metal halides of palladium, platinum and gold or by other compounds containing silver, osmium, ruthenium, manganese, chromium or cobalt[112]. In the early 20th century CO oxidation was subject of many investigations, even by military laboratories due to the ubiquitous problem of high emissions by fires in enclosed spaces in ships by or machine gun fire in tanks etc., but also due to the fear of CO being used as a warfare agent[113]. The number of different compounds tested in this regards shows the impact of this reaction over the whole century, be it because of fire as the main energy supply and indoor heater back in these days, because of the potential thread of CO as warfare agent or because of the tremendous emissions from traffic, as it is today. Figure 1.9 shows the periodic table of elements with an overview of the elements occurring in compounds tested in CO oxidation over the decades. And it also illustrates the sheer amount of possibilities when it comes to the preparation of such a catalytic material, from the choice of active species, to the support material or even the usage of promoters.

1.2.3.1 CO Oxidation Catalysts

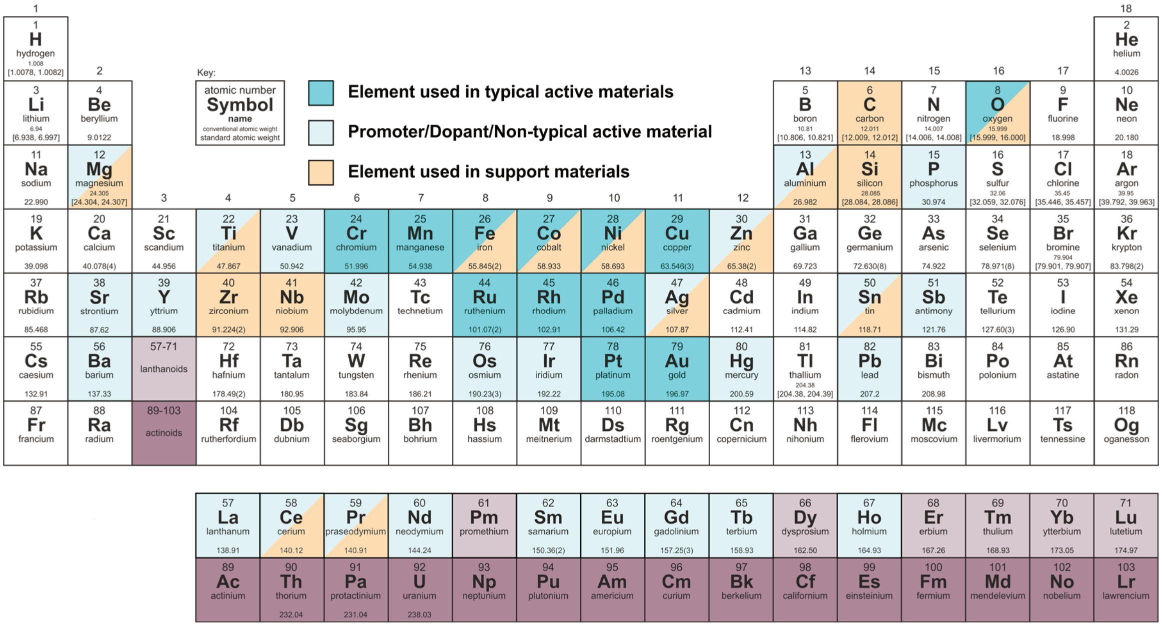

Figure 1.9: Periodic table of elements according to IUPAC[114]; common elements in the active species of CO oxidation catalysts are marked in cyan; common elements in support materials are marked in orange; other elements tested as active species, promoter or dopant are colored pale cyan; here "common" is defined as "commonly tested in CO oxidation experiment" or even "used in actual applications"; the colored markings of materials for CO oxidation were made during the research work for this thesis and were not included in the original periodic table of elements by IUPAC.

When referring to a "catalyst" in heterogeneous catalysis, this term does not solely denote the catalytically active species, but the whole construct that entails it. Numerous catalysts, especially in CO oxidation, comprise a support material on which the actual active site is immobilized. This support commonly makes up most of the catalyst weight and does feature no or only minor catalytic activity. The active species, as said, is immobilized on the support, either by adsorption or via chemical bond. To elevate certain properties of the catalyst, additional materials can be introduced, the so-called promoters. Their main purpose is to increase catalytic activity and/or the stability of the active sites. These three parts of a catalyst are not limited to solely one material, for example usage of two or more active species, like in a three-way-catalyst, is rather common. To connect the three parts to form a usable catalyst, the preparation technique plays an important role. By choice of the technique itself and its conditions, the final structure of the catalyst can be controlled and thus its activity, stability and selectivity. However, the selection of active species, support material, promoter and the numerous preparation techniques lead to a sheer endless number of possibilities. Therefore, these topics will be discussed in more detail in the next paragraphs.

1.2.3.2 Preparation Method

Almost as important as the choice of active site or the support material is the preparation method. It decides whether or not the final catalyst shows good activity in catalytic experiments. A few of the most relevant techniques for preparation of catalysts containing more than one species are briefly described in the following:

Mechanic Mixture: the simplest method of catalyst preparation is a mechanic mixture of the particular parts, either in their preliminary or their final form. Such mixtures can for example be achieved by pestle and mortar or, more advanced, with a ball mill[115,116]. This can be done with dry precursors as well as from solutions and is often followed by thermal treatment like annealing[117].

Precipitation/Co-Precipitation: the precursors are dissolved in an organic or aqueous solvent prior to addition of a precipitating agent. An excellent example is the synthesis of magnetite from iron(II) and iron(III) chloride[118,119]. Ammonia solution is added to a solution of both in water, forming Fe_3O_4 which instantaneously precipitates due to its insolubility in water. It can be removed by filtration or in this case with a magnet, making this method very convenient for upscaling[120,121].

Sol-Gel-Process: the sol-gel-process is a more complex method of catalyst preparation, in which a precursor solution is converted into a colloidal solution, the sol. Here the precursors form so-called micelles, for example by condensation reactions. These micelles can now polymerize to form a gel, which then, depending on the removal of the solvent, yields either a xero- or aerogel, whose main difference is that the xerogel loses volume by shrinkage while the aerogel retains its shape. By this, porous and light materials can be produced with various compositions and shapes. For example, the sol could consist of a precursor for the support material. The active material can now be added to the sol resulting in an excellent distribution over the final catalyst. The sol containing the support and active site precursor could even be impregnated on a honeycomb structure, as in a modern three-way-catalyst, by dip-coating. Also, the precursor of the active species itself could be turned into the sol to yield an unsupported catalyst with high porosity. Typically, metal alkoxides are used as precursors for metal oxide catalysts and their condensation controlled by the pH of the solution[120,122].

Flame Spray Pyrolysis: a precursor solution of either the active material or even both the active material and the support are sprayed through a nozzle into a compartment, where the aerosol is pyrolyzed to form the final oxidic nanopowder which is then caught or is directly applied on a surface as a coating. Through this method high quantities of metal oxides can be produced in only one step. It is possible to add multiple precursors in one solution or via separated nozzles simultaneously, depending on the setup. The flame of the ignited oxygen-solvent-mixture reaches temperatures up to over 2000 °C combusting the precursor solution. The vaporized oxides form nanoparticles or nanopowders upon cooling before being caught[123,124].

Grafting: the active species and the support material are attached to each other via chemical bond. Usually, the active part is introduced as a transition metal complex, that can undergo a chemical reaction with a respective functional group on the support surface. The term *grafting* is often used synonymously with *anchoring*, albeit the latter means a simple bond formation between metal complex and support while grafting describes a further alteration of the ligands or bond situation after the anchoring[117].

Incipient Wetness Impregnation: a facile and yet very potent method in which one part, usually the precursor of the active species, is dissolved in water or an organic solvent and introduced to a solid part, which is usually the support. Commonly drops of the dissolved material are added to the dry support, the mixture is then dried and annealed, if needed. For a good distribution of the solution, the drops can be added systematically to the flattened-out support material to cover as many particles as possible and then mixed well by stirring. To yield catalysts with the active species mostly located in the pores of the support, the total pore volume of the latter can be determined via N_2 physisorption. If the exact same volume of precursor solution is added, this solution should ideally be absorbed by the pores of the support material through capillary forces. A disadvantage is the relatively low volume of solvent used, limiting the amount of active material that can be added. An alteration of this method is the suspension of the solid support, usually in the solvent in which the active species or precursor of the active species is dissolved, and then mixing of both. A benefit of this technique is the better distribution of the precursor solution with the solid part. Major drawback of this technique are the rather high amounts of solvent that have to be removed. Here, high amounts of active species can be introduced while they are distributed both in the pores of the support material as well as on its outer surface. This method will be referred to as *wetness impregnation* in the following[117,121].

Each one of the above-mentioned techniques is described in hundreds and thousands of publications illustrating their complexity. Basic choices that must be made are whether or not a support material is used, and if so, which one out of the thousands of possibilities. The active material and its chemical and physical structure. Also, additional substances can be introduced to act as a promoter during catalysis. Many catalysts, for example transition metal oxides, have to undergo some kind of thermal treatment such as annealing, which comprises numerous variables itself. It can be done prior or after merging of the support and the active species, a constant gas stream can be applied, for example with reducing or oxidizing properties, the temperature has to be chosen and the heating ramp. These are just some of the endless choices that can be made upon catalyst preparation.

1.2.3.3 Support Material

A support material commonly is a solid on which the active sites can be immobilized. Its functions are to secure the catalytically active species against their emission from the system, to facilitate removal of a catalyst (e. g. solid catalysts from liquid phases) but also a promoting effect on the active sites during preparation and the actual catalysis. By use of a support material preparation of small active sites or even single site catalysts is possible and they can also prevent sintering of the active sites at elevated temperatures. Beneficial effects include the adsorption of reactants on the support surface or even storage, like the oxygen storage of ceria, prior to reaction on the catalytically active species[125-128]. Some of the most used support materials, besides CeO_2, include TiO_2, SiO_2 and Al_2O_3. While titania has more relevance in photocatalysis, silica and especially alumina are omnipresent in CO oxidation, mostly as support for 3d metal oxides[129,130]. Due to their high thermal stability and their ability to form high surface mesoporous materials they are prerequisite for the preparation of catalysts with finely dispersed isolated active sites[131]. This can lead to higher activities and better long-term stability of catalysts with rather low amounts of active material compared to pure active material. In modern TWCs metallic PGMs are immobilized on a cordierite support, a magnesium, aluminum and silicon containing oxidic material that combines thermal and chemical stability[68]. Zirconia is another support material often used[132,133] while also 3d metal oxides can be used, mainly when the active component is a noble metal[134,135].

1.2.3.4 Promoters

Besides the active site and, if one is used, the support material, also the introduction of a promoter can be decided on.

> "*Promoters are materials that enhance the effect of the catalyst*"[107]

Many different materials have been tested as a promoter for CO oxidation catalysts, mostly lanthanoids or transition metals in form of their oxides, but also alkaline earth metals have been used. Promoters can work in various ways. For example by affecting structural parameters of the active sites like facilitation of a high dispersion and stabilization against sintering or by electronical interactions of the promoters with the active sites or the reactants[105]. Ceria is a commonly used promoter to reduce sintering of the catalytically active species as well as for oxygen storage, as said above, but with no or only minor activity itself[136]. Several 3d metal oxides have been tested as promoters, both for PGMs and for other 3d metal oxides and also the usage of noble metals as promoters for 3d metal oxides has been discussed. However, often there is no differentiation between promoting the catalytic reaction on another active site and of the so-called promoters being active themselves.

1.2.3.5 Catalytically Active Species

Two groups of metals are mainly used for CO oxidation: non-noble 3d metals, especially the ones from chromium to copper, and noble metals such as gold and the PGMs ruthenium, rhodium, palladium and platinum. The latter can be used as catalytically active species in their metallic form or as oxides. Activity could even be shown for pure metallic wires, while their position in the electrochemical series displays their stability against oxidation under oxidative conditions. Only under elevated temperatures oxidation of these metals can take place, which in case of ruthenium and iridium leads to volatile compounds and thus a loss of active species when used in a catalytic converter. A good overview about CO oxidation experiments on transition metals was given by *Royer* and *Duprez* in 2011[137]. Palladium, platinum and sometimes rhodium are commonly used as the active part in oxidative catalysts, either pure in their metallic form or immobilized on a support material[138-152]. Gold also attracted many research groups and has been tested in numerous experiments for CO oxidation, with promising activity as well[135,153-158]. In contrast to these noble metals, base metals predominantly are used in their oxidic form such as Cr_2O_3, MnO_2, Mn_2O_3, Mn_3O_4, Fe_2O_3, Fe_3O_4, Co_3O_4, NiO, CuO or Cu_2O, which are their stable forms under oxidizing conditions. Especially manganese, cobalt and copper show extraordinarily high activity in catalytic tests, similar to PGMs, but with a higher tendency for deactivation by poisoning[159]. A broad screening of catalysts was carried out by *Yu Yao et al.* in the 1970s and 1980s in which they tested noble metals[140,160] as well as numerous non-noble metals in oxidation of CO and hydrocarbons. Amongst the tested catalysts were 3d metal oxides such as Cr_2O_3[75,76], MnO_2[161], Fe_2O_3[161], Co_3O_4[78], NiO[75,77], CuO[75,161], and mixed metal oxides like $CuCr_2O_4$[75,161] or perovskite-like structures[74]. Especially CuO and $CuCr_2O_4$ were mentioned as promising candidates due to a higher stability against poisoning and thermal sintering compared to Co_3O_4, which showed higher activities when no poisoning agents were present[161]. *Heck and Farrauto* as well as *Kummer et al.* also attributed excellent activity to copper and cobalt containing catalysts but with the drawback of high susceptibility to deactivation by water and sulfurous compounds[138,159,162]. As mentioned before, this high predisposition for catalyst poisoning and at the same time high amounts of potential poisoning agents in fossil fuels were the main reasons why more groups concentrated on precious metals for automotive purposes since the 1970s. Palladium, platinum and rhodium are the metals that were chosen for the oxidative part of TWCs and DOCs. A good review was given recently by *Rood et al.[163]*. Benchmarks of light-off temperatures, from now on defined as the temperature of 50 % conversion of CO (T_{50}), of modern catalysts lie between 100 and 110 °C for Pd containing catalysts[164-166], at 160 °C for mixed Pt-Rh catalysts[167] and between 210 and 230 °C for Pt or Rh containing TWCs[168,169]. However, for a comparison with non-noble metal catalysts described in this work it is noticeable that these Pd, Pt and Rh systems were investigated in catalytic experiments under rather realistic conditions in true three-way-catalysis with HC, CO and NO present in the gas stream. *Boubnov et al.* described Pt catalysts with a T_{50} of approx. 50 °C after activation by reduction prior to the actual CO oxidation experiment under model conditions with 1000 ppm CO, 10 vol% O_2 and no further reactant besides 5 % of water, which was denoted as a promoter on these catalysts. They showed even higher conversions of CO from start at 40 °C when NO was present[170].

Combination of two or more metals presents also a promising approach to combine catalytic and structural properties of different materials. Some of the most prominent examples are hopcalites, which are usually CuO and MnO_2 containing mixed oxide catalysts that are known for their activity in CO oxidation since almost a century[171]. *Gao et al.* tested hopcalite against various other mixed metal oxides with combinations such as Fe-Mn, Co-Mn, Ni-Mn and Cu-Mn where the second metal was used as a dopant for MnO_2 nanowires[172]. The highest activity in CO oxidation with a T_{50} of approx. 80 °C was obtained by the Cu-doped catalyst, while the activity of the remaining catalysts followed the order $CuO_{0.1}$-MnO_2 > $Co_{0.1}MnO_x$ > $Ni_{0.1}MnO_x$ > $Fe_{0.1}MnO_x$ > MnO_2, all of them with a T_{50} above 125 °C. They could also show that the combination of copper with manganese is relatively stable against moisture with only minor decreases in activity at 70 and 120 °C. A combination of nickel and cobalt was presented by *Yi et al.* in 2018 with temperatures of

50 % conversion between 80 and 120 °C depending on the ratio of Ni to Co[173]. These high activities could be assigned to the addition of cobalt, since pure nickel oxide did feature almost no CO conversion in their experiments. Various groups investigated the combination of iron oxides with copper. *Cao et al.* in 2008 and *Cui et al.* in 2019 showed significant increases in catalytic activity by addition of CuO to Fe_2O_3[174,175]. The T_{50} of the presented catalysts with both metals was between 60 and 80 °C. A further decrease of the T_{50} down below 40 °C could be obtained by doping of a Cu and Ce containing oxidic catalyst with iron[176]. Another highly active combination is iron with cobalt. *Biabani-Ravandi et al.* presented Fe-Co mixed oxides prepared by co-precipitation which featured over 25 % CO conversion at room temperature and a T_{50} of 50 °C[177]. Even higher activities were obtained by *G. Li et al.* with T_{50} below 20 °C and an initial conversion below -20 °C[178]. They also tested the influence of humidity in the gas stream on the catalytic activity. Surprisingly, iron seemed to increase the catalysts stability against water, so that almost no influence of moisture could be detected. A rather astounding full conversion of CO below -80 °C on Co-Fe catalysts was shown by *J. Li et al.*[179]. They compared the iron and cobalt containing oxidic catalysts with pure Co_3O_4 which also showed a surprisingly high activity in their tests with total conversion below -45 °C. They ascribe the even better activity of the mixed metal oxides partly to a higher ratio of Co^{3+} to Co^{2+} when iron was present, which is more efficient in the adsorption of CO. A trimetallic system containing Co, Cu and Fe was tested by *Veselovskii et al.* and later by *Ishchenko* et al.[180,181]. The mostly copper containing system was used in its pure form by *Veselovskii* in PROX experiments with a minimum T_{100} of the CO oxidation of 160 °C in presence of hydrogen, a T_{50} was not mentioned. *Ishchenko* impregnated carbon nanotubes and achieved a lower T_{100} of 95 °C, but without hydrogen in the gas stream. Both ascribe the good activity of the catalysts to the present $Cu_2(OH)_3NO_3$ species that is stabilized by iron and cobalt. Excellent activities in CO as well as propane oxidation were shown by *Faure et al.* using the combination of cobalt and manganese in a spinel structure[182]. From the start at 50 °C they featured a CO conversion over 85 % and total conversion of CO above 70 °C.

1.2.3.6 Iron in CO Oxidation

The resources of noble metals are very limited leading to high prices and due to an increasing demand they are expected to increase even further[183,184] while their depletion is problematic, hence their ecological impact is still not fully revealed[185-189]. The examples above show very promising results for non-noble metal catalysts in CO oxidation. However, the most active amongst them also have drawbacks, mostly due to poor thermal and long-term stability or, especially for cobalt, low stability against catalyst poisoning, mostly by water. Iron presents an auspicious alternative with good biocompatibility and high abundance, but so far rather low activities compared to the above-mentioned systems. Iron oxides have been tested for this purpose since the 1960s by *Hofer et al.*[190] and later during the broad screening of *Yu Yao et al.[191]* which both ascribed minor activity to iron oxides compared to other catalysts. *Walker et al.* were the first to try, besides others, Fe_2O_3 supported on γ-alumina in simultaneous CO and C_3H_6 oxidation in which a strong tendency to catalyst poisoning by sulfur dioxide or byproducts of the oxidation was shown[192]. The addition of only 40 ppm SO_2 to the gas feed increased the light-off temperature from 327 °C up to 446 °C for CO, respectively from 292 °C up to 327 °C for propene oxidation, by formation of sulfite and sulfate groups at the catalyst surface, blocking the active sites. Other inhibitors such as CO_2, HC or H_2O were also discussed, of which the latter nowadays still is one of the most challenging problems of iron oxide catalysts for CO oxidation. Due to the relatively low activities and rather high susceptibility against poisoning agents, iron oxides were not a choice for industrial applications which demanded the high performance of noble metals, thus pushing iron catalysts almost into oblivion until the 2000s. Then, increasing prices, respectively shrinking resources due to a high demand for PGMs fueled the research for cheap and harmless replacements leading to more and more publications on this topic (see Figure 1.10).

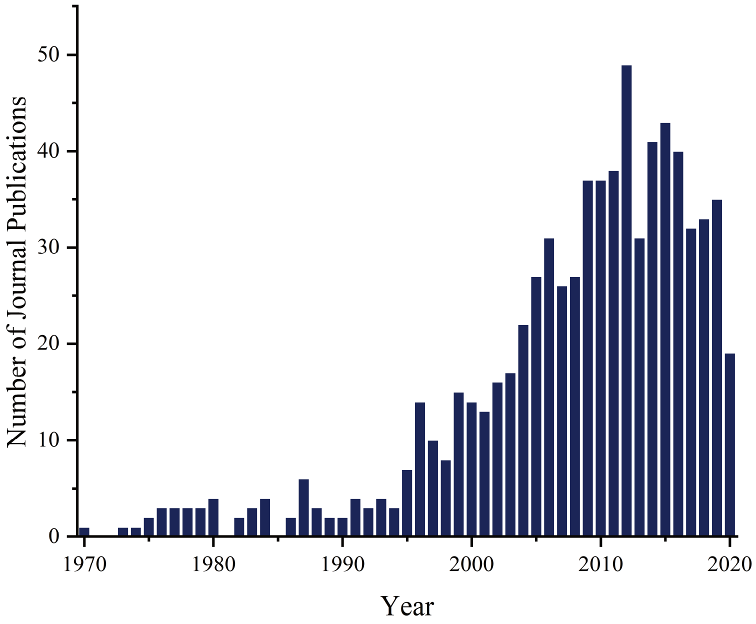

Figure 1.10: Number of publications in scientific journals per year about iron compounds in CO oxidation.

In 2003 *Li et al.* published a study in which they tested commercially available iron oxide, called NANOCAT®, featuring a high surface area of 250 m^2/g and very small particle diameters of 3 nm[193]. This catalyst was able to catalyze the oxidation of carbon monoxide at relatively low temperatures with a T_{50} of approximately 250 °C (Figure 1.11). It is important to note, that the conditions in which such a catalyst is tested can alter its activity substantially. Noteworthy are the amount of the catalyst used, the flow rate of the gas feed and its composition and also the volume of the catalyst bed (or the length of the catalyst bed and the inner diameter of the reactor) to calculate the gas hourly space velocity GHSV, if not already mentioned, for a better comparison of catalysts. The GHSV is defined as the flow rate of the gas feed divided by volume of the catalyst bed. However, many catalytic systems from literature cannot be compared objectively due to a lack of these, like for *Li et al.* 50 mg of NANOCAT® were tested with 3.44 vol% CO and 20.6 vol% oxygen in helium balance and a total gas feed of 1000 ml/min. The inner diameter of the reactor was 9 mm resulting in a gas velocity of 0.94 km/h, which can also be an important variable. This catalyst was compared to nanosized iron oxide catalysts with even higher surface areas up to 406 m^2/g and particle diameters below 4 nm by *Lin et al.* in 2005[194]. They measured 37 % of CO conversion at room temperature, the T_{50} as low as 32 °C and 60 % conversion at 100 °C, although the gas feed contained 0.6 vol% of water which would normally be expected to lower catalytic activity drastically. They conclude from XRD analysis that

Fe_3O_4 is the present phase of the active species and attribute the high activities to hydroxylated iron oxidic sites on the catalyst surface. Only a gas velocity of 30 km/h is given without further information of the amount of catalyst or the GHSV. While their gas velocity is substantially higher than the one of the compared NANOCAT® system, they only used 0.25 vol% of CO compared to 3.44 vol% of *Li et al.*

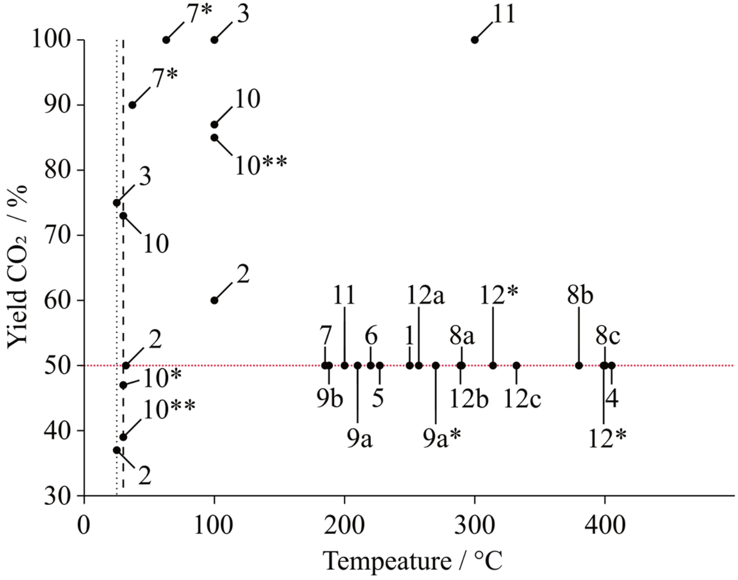

Figure 1.11: Benchmarks of iron catalysts in CO oxidation experiments from important references of the last 20 years; black dottet line: 25 °C; black stripes: 30 °C; red dotted line: 50 % CO_2 yield; Li et al.: 1[193]; Lin et al.: 2[194] with addition of water to the gas stream; Szegedi et al.: 3[195]; Carriazo et al.: 4[196]; Bao et al.: 5[197]; Ren et al.: 6[198]; Hnat et al.: 7[199] FeSiBEA as-prepared; 7 FeSiBEA reduced prior to CO oxidation; Gao et al.: 8[200] a = α-Fe_2O_3 nanorods, b = α-Fe_2O_3 nanocubes, c = α-Fe_2O_3 nanotubes; Tepluchin et al.: 9[201] a = prepared by IWI, b = prepared by FSP, 9a* = addition of water to gas stream; Kim et al.: 10[202] measurements at constant temperatures of 30 and 100 °C, 10 = start, 10* = after 6 h, 10** = after 33 h; Li et al.: 11[203]; Schoch et al.: 12[204] Fe_2O_3 on γ-Al_2O_3, a = 1 wt%, b = 5 wt%, c = 10 wt%, 12*[205] catalysts prepared by reduction of the iron(III) precursor prior to impregnation of the support and calcination.*

Also in 2005, *Szegedi et al.* published iron based catalysts with even higher catalytic activity[195]. Their systems showed yields over 75 % at room temperature and total conversion at 100 °C. These extraordinarily high yields can be assigned to reduction of the iron species with H_2 prior to the catalytic tests and their high surface area. By introduction of iron to MCM-41 via sol-gel-method surface areas up to 1000 m^2/g and by hydrothermal synthesis 1400 m^2/g could be obtained. Rather ineffective CO oxidation catalysts with a T_{50} higher than 400 °C were shown by Carriazo and coworkers, who deposited iron and cerium on naturally occurring bentonite clay[196]. However, the tested catalysts did show good activity in the oxidation of phenol in aqueous medium and also showed activity in the oxidation of 2-propanol in gas phase reaction, which emphasizes their versatility. *Bao et al.* carried out *in-situ* Raman spectroscopy on Fe_2O_3-CeO_2 composite materials with a T_{50} of 227 °C and showed a linear correlation between oxygen vacancies on the catalysts and their reaction rates, which gives strong evidence that the oxidation of CO on these systems follows a Mars-van-Krevelen mechanism (see Figure 1.12 right)[197]. In this mechanism CO diffuses to the catalyst surface and is adsorbed (1), prior to reaction with lattice oxygen to form CO_2 (2) which then desorbs and diffuses back into the gas phase (3). The resulting oxygen vacancy is refilled by oxygen from an oxygen molecule that is adsorbed (4). A second CO is then adsorbed (5), reacts with the remaining oxygen atom (6) and desorbs as a second CO_2 molecule (7). The catalyst is regained in its native form. Since by use of lattice oxygen said vacancies are formed throughout the reaction, their detection by Raman spectroscopy and their proportionality to the reaction rate is a strong indicator for this mechanism. A more common mechanism in heterogeneous catalysis is the Langmuir-Hinshelwood mechanism (Figure 1.12 left) in which no lattice oxygen is used. Here, CO and oxygen from the gas phase diffuse to the surface of the catalyst, where they both are adsorbed simultaneously (1). The oxygen molecule dissociates on the catalyst surface (2) and CO reacts with one of the adsorbed oxygen atoms to form CO_2 (3) which then desorbs and diffuses back into the gas phase (4). Then again, a CO molecule is adsorbed (5), reacts with the remaining adsorbed oxygen atom (6) and desorbs as CO_2 while the catalyst is regained. This mechanism was for example proposed for CO oxidation on metallic platinum, palladium or rhodium catalysts[137,140], while sometimes also the Eley-Rideal mechanism is discussed, in which one of the reactants does not adsorb on the catalyst surface but reacts directly from the gas phase with the second educt to form CO_2 (Figure 1.12 left)[206]. In 2008 *Wagloehner et al.* postulated the oxidation of CO on Fe_2O_3 to follow the Eley-Rideal mechanism after kinetic studies as well as DRIFT spectroscopic experiments and isotopic labeling[207]. They could also show that the reaction of dissociatively adsorbed oxygen with CO from the gas phase is the rate-determining step.

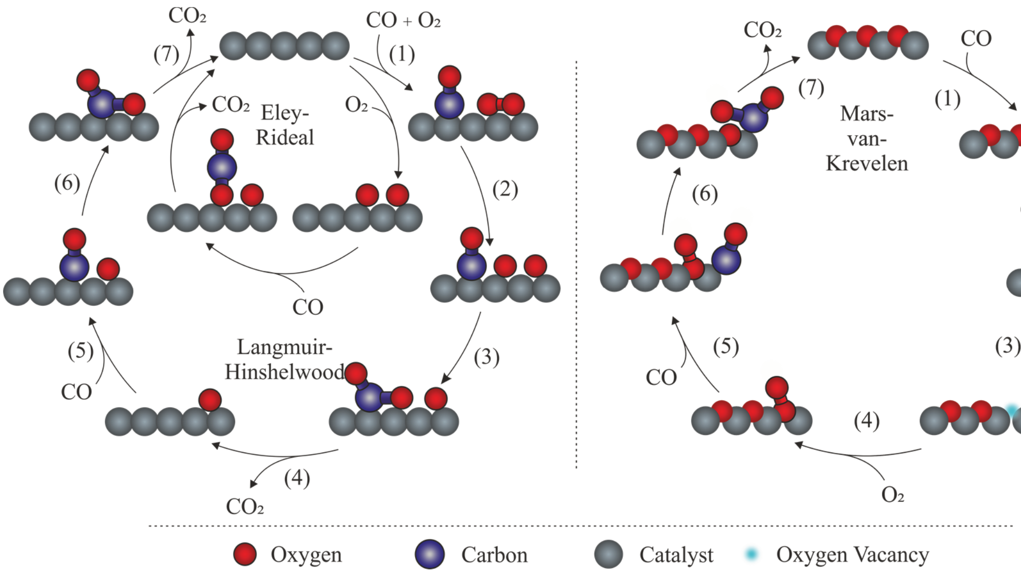

Figure 1.12: Schematic description of CO oxidation on a heterogenous catalyst following a Langmuir-Hinshelwood or Eley-Rideal mechanism (left) or a Mars-van-Krevelen mechanism (right); both mechanisms are simplified and do not show each elementary step that occurs during reaction.

In 2009 *Ren et al.* published their work in which they compared various commercially available mesoporous transition metal oxides with their corresponding bulk phase[198]. Surprisingly, bulk Fe_2O_3, despite a surface area of only 9 m^2/g, was found to be slightly more active than its mesoporous form with a surface of 139 m^2/g. The T_{50} for bulk Fe_2O_3 was approx. 220 °C while the one of mesoporous Fe_2O_3 was 10 °C higher. Catalysts with a very astounding activity were published by *Hnat et al.*, who also used zeolites as support material for the immobilization of iron oxides with a total iron content of 0.6 to 10 wt%[199]. The catalysts were prepared by impregnation of SiBEA with iron(III) nitrate in aqueous solution with addition of nitric acid followed by removal of the solvent and annealing of the dry solids at 500 °C in air. Additional annealing in oxygen atmosphere at 760 °C prior to catalytic tests lead to less active catalysts with a minimum T_{50} of 185 °C, whereas reduction with H_2 at 760 °C prior to the experiments resulted in extraordinarily high CO conversion of over 90 % from the start at 37 °C and total conversion at 63 °C. They concluded that with their preparation method mainly tetrahedrally coordinated and isolated iron oxide species were formed, which promoted the formation of Brønsted and Lewis acidic sites, which again were ideal for the adsorption of carbon monoxide. Also, lower iron content catalysts were found to be much more active in CO oxidation, which is due to the higher ratio of tetrahedrally coordinated iron sites compared to octahedral ones. α-Fe_2O_3 nanomaterials were investigated by *Gao et al.* in the form of iron oxide nanorods, nanocubes and nanotubes. A good comparison between activity of different crystal planes could be made. At the nanorods, mainly the (001) plane is visible, which seems to be much more active with a T_{50} of 290 °C while the nanotubes mainly comprise (010) sites on the surface exposed to the gas stream, resulting in a T_{50} of 400 °C. The nanocubes do not feature one main crystal plane, thus showing activity in between at 380 °C. *Tepluchin et al.* published a series of manuscripts in which they compared iron oxide and manganese oxide catalysts immobilized on a Al_2O_3 support prepared by incipient wetness impregnation to the respective catalysts made by flame spray pyrolysis[201,208,209]. IWI derived catalysts featured T_{50} of 210, 232 and 267 °C with a respective iron content of 20, 10 and 5 wt%, while FSP derived catalysts with the same contents converted 50 % of CO at 188, 217 and 270 °C[201]. Lower activities for the IWI derived catalysts at higher amounts of iron were assigned to a much higher content of bulk phase iron oxide. An addition of 5 vol% water to the gas stream lowered the activity of the 20 wt% IWI catalyst significantly to a T_{50} of 270 °C. Unfortunately, no other iron catalysts were tested under influence of moisture. For the experiments 500 mg of each catalyst were tested in a gas stream of 250 ml/min containing 500 ppm CO and 5 vol% O_2 in N_2 balance and a gas velocity of 0.3 km/h, while for the experiments with addition of water only 100 mg of catalyst were used under the same conditions. Hence, the substantial decrease of activity could also be the result of 80 % less active material. They also investigated the influence hydrothermal ageing on the above-mentioned catalysts, but now immobilized on a honeycomb carrier which is typical for automotive applications[209]. Here, the 20 wt% IWI derived catalyst showed better activity than the respective FSP catalyst, but after hydrothermal ageing at 700 °C in a gas stream containing 10 vol% H_2O and 10 wt% O_2 in N_2 balance the activity of the IWI catalyst decreased drastically, while the FSP derived samples showed almost no differences after 2 or 4 h of ageing. This high hydrothermal stability of the FSP derived catalysts was assigned to their much higher nanocrystallinity. *Kim et al.* prepared a very active iron oxide catalyst by chemical vapor deposition of ferrocene on a mesoporous Al_2O_3 support followed by annealing under atmospheric air[202]. The catalyst with an approximated amount of 7 wt% iron was able to convert 73 % of CO from the start at 30 °C but its activity decreased within 6 h down to 47 % and down to 39 % after 33 h. A rather stable activity could be shown at 100 °C with a starting conversion of 87 % and 85 % after 33 h. However, it is noteworthy that the catalytic experiments in this case were conducted with 2 g of the catalyst and a gas flow of only 10 ml/min. Since the catalyst was loaded into a glass tray in the reactor, only vague approximations can be made, resulting in a GHSV of 54 h^{-1} and a gas velocity of 0.0016 km/h. A very interesting route of catalyst preparation was published by *Li et al.* in 2018[203]. A reaction of iron(III) nitrate with sodium carbonate was carried out to form $NaNO_3$ and presumably an iron carbonate intermediate which is instable and reacts to $Fe(OH)_3$. The mixture was then vaporized and carried into a 600 °C oven by a constant oxygen stream to form Fe_2O_3 templated by the sodium nitrate. By this, so-called sponge-like Fe_2O_3 microspheres with a surface area of 216 m^2/g could be prepared. These catalysts featured 50 % CO conversion at 200 °C and total conversion at 300 °C, but under more realistic conditions with a GHSV between 36000 and 60000 h^{-1}. Significant publications on this topic were also made by *Schoch et al.* in 2014 and 2016[204,205]. Initially they presented a facile preparation technique for iron oxide catalysts on alumina support by wetness impregnation of iron(III) acetylacetonate on γ-Al_2O_3 followed by removal of the solvent and annealing under atmospheric air at 600 °C. They carried out a structure-activity-correlation of three catalysts with 1, 5 and 10 wt% of iron in which they correlated a high amount of isolated tetrahedrally coordinated iron oxidic species on the support surface of the 1 wt% catalyst with its higher activity in CO oxidation. Its T_{50} was 257 °C and it could catalyze 100 % of CO conversion at approx. 278 °C. The T_{50} of the 5 and 10 wt% catalysts were 298 respectively 332 °C. The lower activities of the latter could be attributed to high amounts of octahedrally coordinated iron species in small oligomers or even bulk phase. In a second manuscript they showed a completely different approach in which they reduced the $Fe(acac)_3$ precursor prior to impregnation with phenyllithium, phenylmagnesium bromide or triphenyl aluminum in inert atmosphere to form small core-shell-nanoparticles with Fe^{III} core and the respective metal of the reductant as its shell[205]. They describe an integrating effect of the organoaluminum species if an Al_2O_3 support is used due to the possible incorporation of the core-shell-nanoparticles into the support lattice, resulting in isolated and predominantly tetrahedrally coordinated iron species. In contrast to this, they ascribe an isolating effect to shells containing metals different than in the support as they tend to stay separated from the support and form larger particles of iron(III) oxide, which could also be correlated to their catalytic activity. The catalysts prepared with $AlPh_3$ showed significantly higher conversions at lower temperatures compared to the LiPh and PhMgBr derived samples. In contrast to the catalysts of the previous publication, here the 10 wt% catalysts were more active with a T_{50} of 314 °C and 399 °C for the samples prepared with $AlPh_3$ respectively PhMgBr, while the 1 wt% catalyst showed highest activity for the samples derived from LiPh with a T_{50} of 507 °C. Also, a higher thermal stability of the $AlPh_3$ derived catalysts could be shown by comparison of EXAFS analysis before and after usage in CO oxidation which could also be explained by incorporation or anchoring of the core-shell-nanoparticles into the support.

Albeit all of these publications and the work done on this topic, our knowledge about the working principles of these systems is still marginal. It is crucial to investigate these catalysts even further to understand how potent alternatives to noble metal catalysts can be prepared, especially for low temperature CO oxidation in the range of RT to 150 °C and with a high stability against catalyst poisons and thermal ageing.

2 AIM OF THIS WORK

To replace noble metal catalysts in automotive applications, iron oxides present a potent but abundant and biocompatible alternative. However, to keep up with state-of-the-art systems iron catalysts must be optimized by means of their catalytic activity as well as their stability. To do so, a better knowledge about these catalysts is crucial.

The aim of the herein presented work is a thorough structure-activity-correlation of basic iron oxide catalysts supported on γ-Al_2O_3 to enhance the understanding of their working principles. Therefore, a series of catalysts with varying weight-loading of iron should be prepared and investigated by mostly spectroscopic methods to elucidate their structural properties. Amongst the applied methods are powder X-ray diffractometry to determine the actual phase of the iron oxide species as well as diffuse reflectance UV/Vis spectroscopy and X-ray absorption spectroscopy for an extensive study of the coordination geometry of the active sites. These results should then be correlated to the catalytic activity of these catalysts to deduce a working hypothesis for the preparation of new iron oxide catalysts with enhanced structural and catalytic properties, which could potentially keep up with noble metal catalysts. For the preparation of these catalysts, two main routes should be evaluated, on one hand the improvement of the alumina-supported iron oxide catalysts themselves by an advanced preparation technique deduced from the structure-activity-correlation made hitherto, and on the other hand the addition of a second and third 3d metal. For the latter, manganese was chosen to elevate the stability of the catalysts against poisoning or thermal ageing and cobalt for low temperature activity. For each route a series of catalysts should be prepared and again investigated thoroughly regarding their structural parameters as well as their CO oxidation activity.

3 QUALITY OR QUANTITY?

How Structural Parameters Affect Catalytic Activity of Iron Oxides in CO Oxidation

Iron oxides present a potent, abundant and biocompatible alternative to commonly used PGMs for catalytic CO oxidation. Economic and ecological reasons consolidate their advocacy, but despite high activity, good stability against catalyst poisoning is required. Hitherto no iron-based system could fulfill the requirements. To successfully replace noble metals in catalytic converters, a better understanding of iron oxides regarding their working principles in CO oxidation is crucial. A structure-activity-correlation of iron oxide catalysts immobilized on γ-Al_2O_3 was carried out with different weight-loadings of iron to determine differences in the present iron species and how they affect catalytic activity. Therefore, the catalysts were investigated by various spectroscopic and microscopic methods and finally tested in CO oxidation experiments, aiming at the improvement of the preparation technique to yield catalysts that could potentially keep up with noble metals in the abatement of carbon monoxide from exhaust gases.

3.1 Results

A series of five catalysts was prepared according to *Schoch et al.*[204]. Therefore $Fe(acac)_3$ was dissolved in a mixture of NMP and THF (1:1) and added to γ-Al_2O_3 suspended in THF to yield mixtures of 1, 2.5, 5, 10 and 20 wt% of iron respective to alumina. The solvents were removed and the dried powders annealed under atmospheric air at 600 °C (for further information see chapter 8.2). The as-prepared catalysts were investigated by various spectroscopic and microscopic methods, such as PXRD, DRUVS, Mößbauer, STEM-EDX and XAS.

The catalytic activity of iron oxides strongly depends on structural parameters, such as the phase of iron oxide, its dispersion on the support surface and especially whether it is present in isolated species or in large clusters, respectively bulk phase. Often, basics like the surface area give important information about catalytic systems.

Table 3.1: Specific surface areas of Fe01 to Fe20 compared to the pure γ-Al_2O_3 support, obtained from N_2 physisorption via BET method.

Sample	**Surface [m^2/g]**
γ-Al_2O_3	169
Fe01	155
Fe025	164
Fe05	167
Fe10	152
Fe20	121

The pure support material has a surface area of 169 m^2/g which does not change significantly for Fe01 to Fe10 where it ranges between 152 and 167 m^2/g (Table 3.1). For Fe20 the area decreases to 121 m^2/g due to a higher amount of agglomeration.

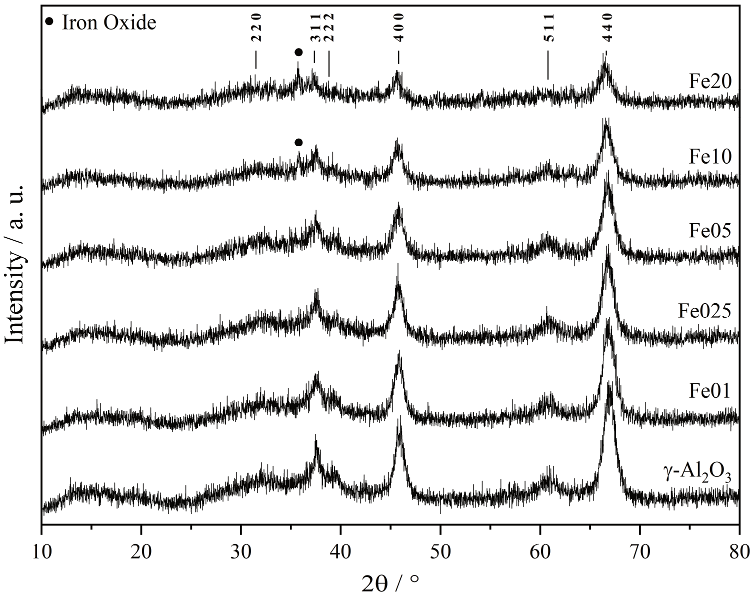

Figure 3.1: Powder X-ray diffractograms of Fe01 to Fe20 and the γ-Al_2O_3 support.

For determination of the phases of the support as well as the catalytic species, powder X-ray diffraction presents a potent tool. However, the in-house diffractometer only shows iron oxide reflexes for Fe10 and Fe20 at 2θ = 36° which could be attributed to both, the (110) plane of hematite or the (311) crystal plane of maghemite (Figure 3.1).

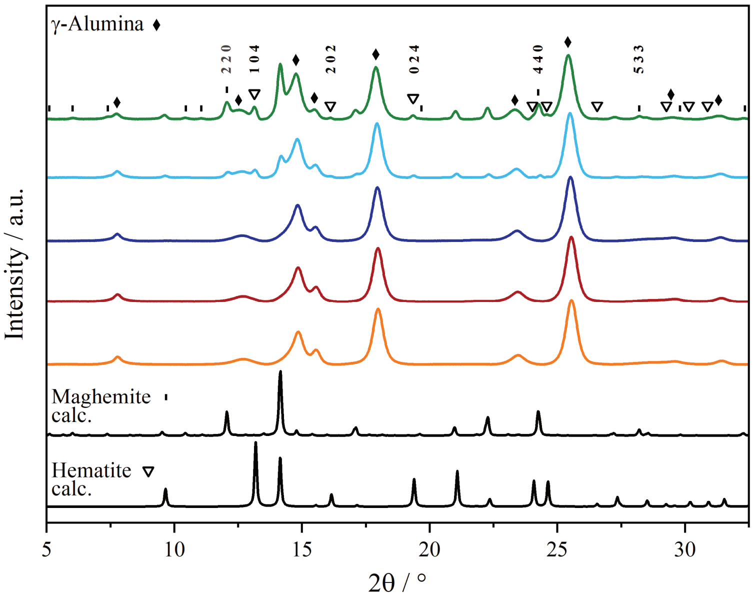

Figure 3.2: Experimental high-resolution powder X-ray diffractograms of catalyst Fe01 to Fe20 (orange to green) and calculated diffractograms of hematite (α-Fe_2O_3) and maghemite (γ-Fe_2O_3).

Besides that, no further signals for iron oxide can be detected. The remaining reflexes at approx. 37, 39, 46, 61 and 67 ° can be assigned to the powder pattern of pure

γ-Al_2O_3, respectively the (311), (222), (400), (511) and (440) crystal planes[210,211]. To maximize the detectability of the iron oxidic phase of these systems an increase of the signal-to-noise ratio and resolution by exchange of the in-house diffractometer to synchrotron X-ray radiation with a high resolution 2D detector is crucial. Hence, high resolution powder X-ray diffraction is carried out. The obtained diffractograms clearly show that both Fe10 and Fe20, besides the γ-Al_2O_3 support, consist of a mixed phase of α- and γ-Fe_2O_3 (see Figure 3.2). As an example, both samples show signals corresponding to the (104), (202) and (024) crystal planes of hematite (α-Fe_2O_3)[212] as well as the (220), (440) and (533) planes of maghemite (γ-Fe_2O_3)[213]. Comparison of the reflex positions in the high resolution PXRD data shows a clear trend for all γ-Al_2O_3 signals. With increasing iron loading peak positions shift to lower angles. The respective plane distances and hence the lattice parameters increase, which is a strong indicator for the incorporation of the iron species somehow into the γ-Al_2O_3 lattice. This correlation is shown in Figure 3.3 for the (311), (222), (400), (511) and (440) planes of the γ-Al_2O_3 support. The (111) and (220) planes were left out from this comparison, because their low intensity and interference with iron oxide reflexes lowered the validity of the results.

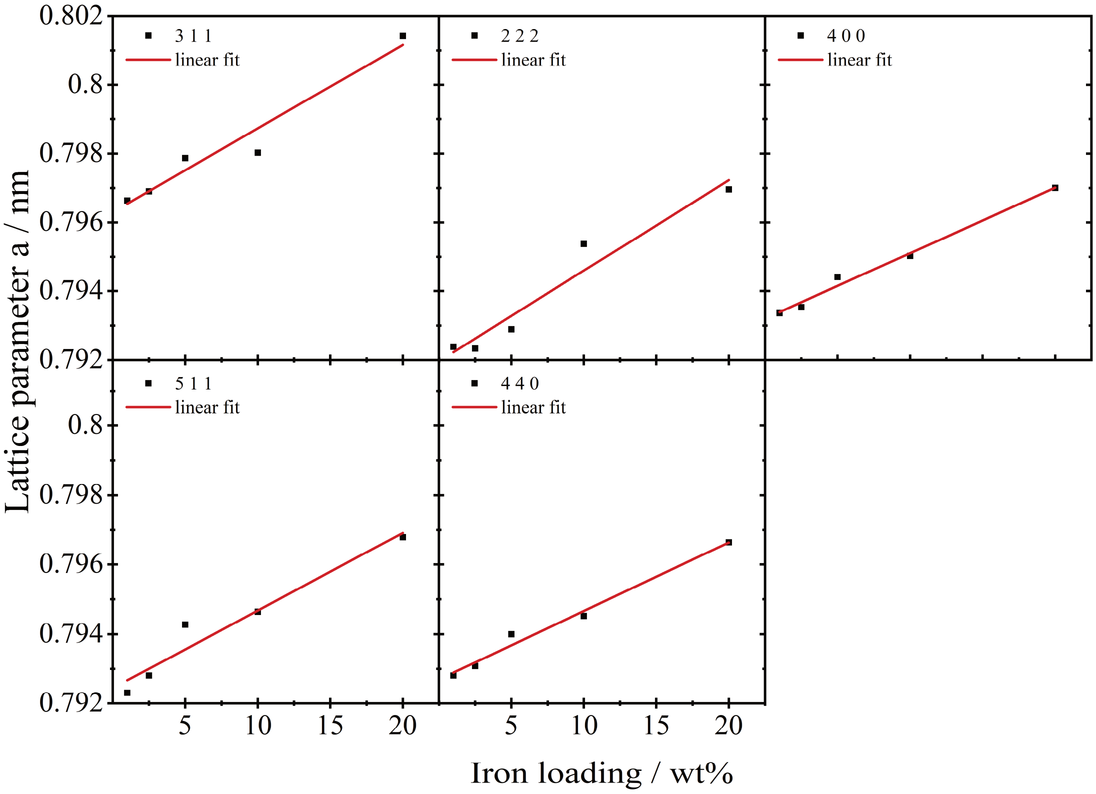

Figure 3.3: Lattice parameter a calculated from 2θ shifts of the (311), (222), (400), (511) and (440) crystal planes of the alumina support of catalyst Fe01 to Fe20, derived from high resolution PXRD data.

To gain insights into the cluster sizes of the iron oxide species, Mößbauer spectroscopy of the catalysts was carried out at ambient temperature (295 K) as well as at low temperature (77 K). Due to the small iron concentration in Fe01, no Mößbauer spectra at low temperature could be recorded for this catalyst. Isomer shifts δ of Fe01 to Fe20 together with their quadrupole splitting ΔE_Q verify that solely iron species in the oxidation state +III are present in the investigated catalysts (Figure 3.4).

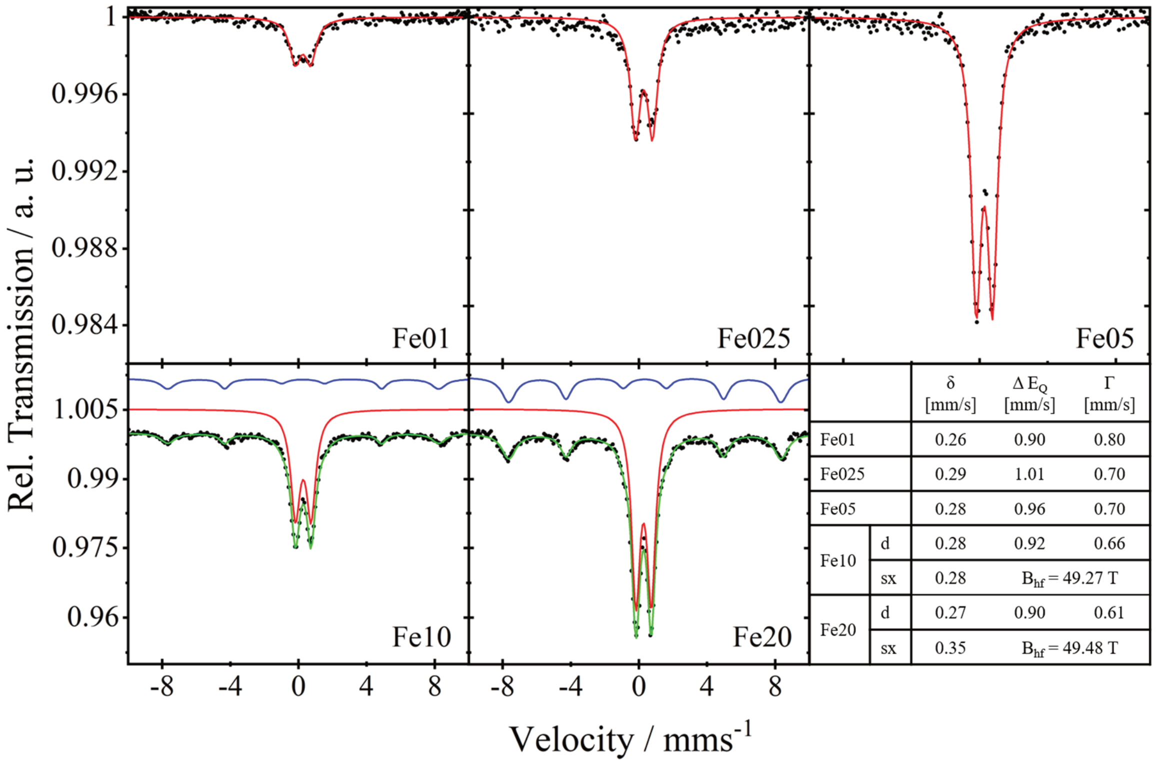

		δ [mm/s]	ΔE_Q [mm/s]	Γ [mm/s]
Fe01		0.26	0.90	0.80
Fe025		0.29	1.01	0.70
Fe05		0.28	0.96	0.70
Fe10	d	0.28	0.92	0.66
	sx	0.28	B_{hf} = 49.27 T	
Fe20	d	0.27	0.90	0.61
	sx	0.35	B_{hf} = 49.48 T	

Figure 3.4: Mößbauer spectra (black dots) of catalysts Fe01 to Fe20 with corresponding fits (red: doublet, blue: sextet, green: cumulative fit) and the resulting parameters (bottom right).

At ambient temperature, all of them show a doublet with an isomer shift of 0.26 to 0.29 mm/s and since a sextet is missing for Fe01 to Fe05 this can be assigned to particles with sizes below 13.5 nanometres[214]. The fact, that even at 77 K no additional sextet occurs for Fe025 and Fe05 (see Appendix: Figure SI 9.2 and Figure SI 9.3) indicates that the particles feature superparamagnetism, meaning that they are too small to induce magnetic splitting. In contrast, Fe10 and Fe20 show additional Zeeman lines due to magnetic splitting even at ambient temperature, which indicate particle sizes of the iron oxide species above 13.5 nm. Areas of the fitted spectra can directly be used to quantify the ratio of small to big particles. The ratio of doublet to sextet changes from 3.4:1 at catalyst Fe10 to 2.2:1 at Fe20, which means that the percentage of iron species present in particles above 13.5 nm is much higher at the 20 wt% catalyst.

For elucidation of variations of the iron oxide species present in the catalysts, meaning the ratio of tetrahedrally to octahedrally coordinated iron(III) and isolated vs. agglomerated iron oxide species, UV/Vis spectroscopy is carried out. The local geometry of Fe^{III} has a strong influence on the energy of the bonding and non-bonding orbitals, leading to characteristic absorption bands in the UV/Vis region originating from charge transfer (CT). Bands below approx. 300 nm can be assigned to isolated iron species, while CT bands of tetrahedrally coordinated iron species tend to occur at lower wavelengths compared to those of octahedrally coordinated metal centers[215-221]. Oligomers and small particles lead to additional bands at higher wavelengths up to 900 nm. The spectra of the presented catalysts (Figure 3.5) show strong variations in these regions with Fe01 having least contributions above 400 nm and its main feature at low wavelengths around 300 nm.

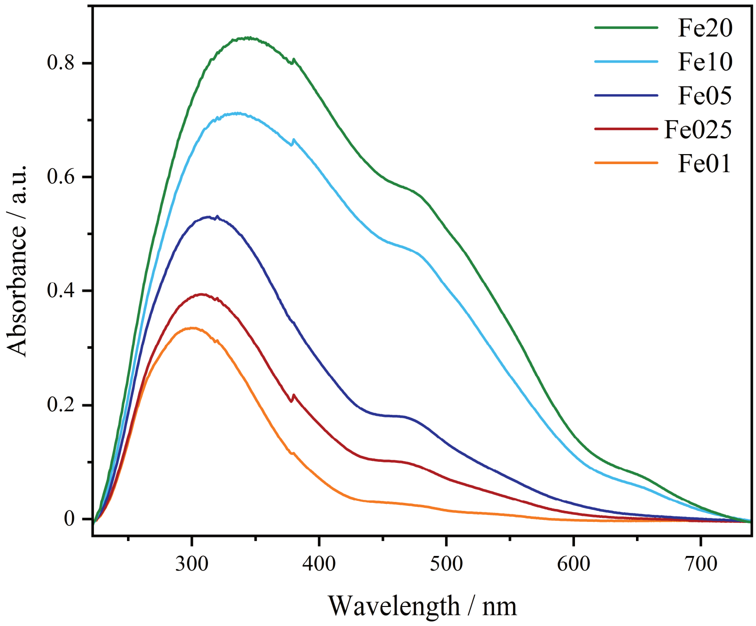

Figure 3.5: Background-corrected diffuse reflectance UV/Vis-spectra of Fe01 to Fe20.

This feature, despite growing, seems to shift to lower energies, respectively higher wavelengths, with increasing iron loading. Additionally, there is a strong increase of contributions above 400 nm from Fe01 to Fe20. These findings can be quantified to gather detailed information about the iron oxide structure. The structure of hematite contains solely iron oxide octahedrons while the maghemite structure consists of both octahedral and tetrahedral oxygen coordination, which means that the ratio of tetrahedrons to octahedrons is a good indicator for the actual iron phase.

Table 3.2: Percentual amounts of tetrahedral, octahedral, oligomeric and particulate iron species of Fe01 to Fe20, derived from peak deconvolution of the DRUV spectra.

Catalyst	**Fe_{tet} [%]**	**Fe_{oct} [%]**	**Fe_xO_y olig. [%]**	**Fe_xO_y particles [%]**
Fe01	12.0	37.3	50.3	0.44
Fe025	10.8	35.4	48.6	5.15
Fe05	7.30	22.7	60.5	9.52
Fe10	4.87	17.6	57.7	19.8
Fe20	4.20	15.2	65.7	14.9

Deconvolution of the experimental spectra (Figure 3.6) yields the area values given in Table 3.2. As can be seen in Figure 3.7 (left), the normalized area for tetrahedral coordinated isolated iron(III) species decreases from Fe01 to Fe20 and so does the area of isolated octahedrons, while the areas for small oligomers and especially for particles increase with increasing iron loading. For Fe01 only 12 % can be assigned to tetrahedrally with a 3.1 times higher amount of octahedrally coordinated Fe^{III} centers. Fe025 has a 3.3 times higher amount of octahedral iron species while this number is 3.1 again for Fe05. For Fe10 and Fe20 this number increases to 3.6. Since the crystal structure of hematite does not comprise tetrahedrally coordinated iron oxide species, this increase of the ratio of peak 2 to 1 in the 200 to 300 nm regime at higher iron loadings can be correlated to a decrease in the amount of maghemite compared to hematite.

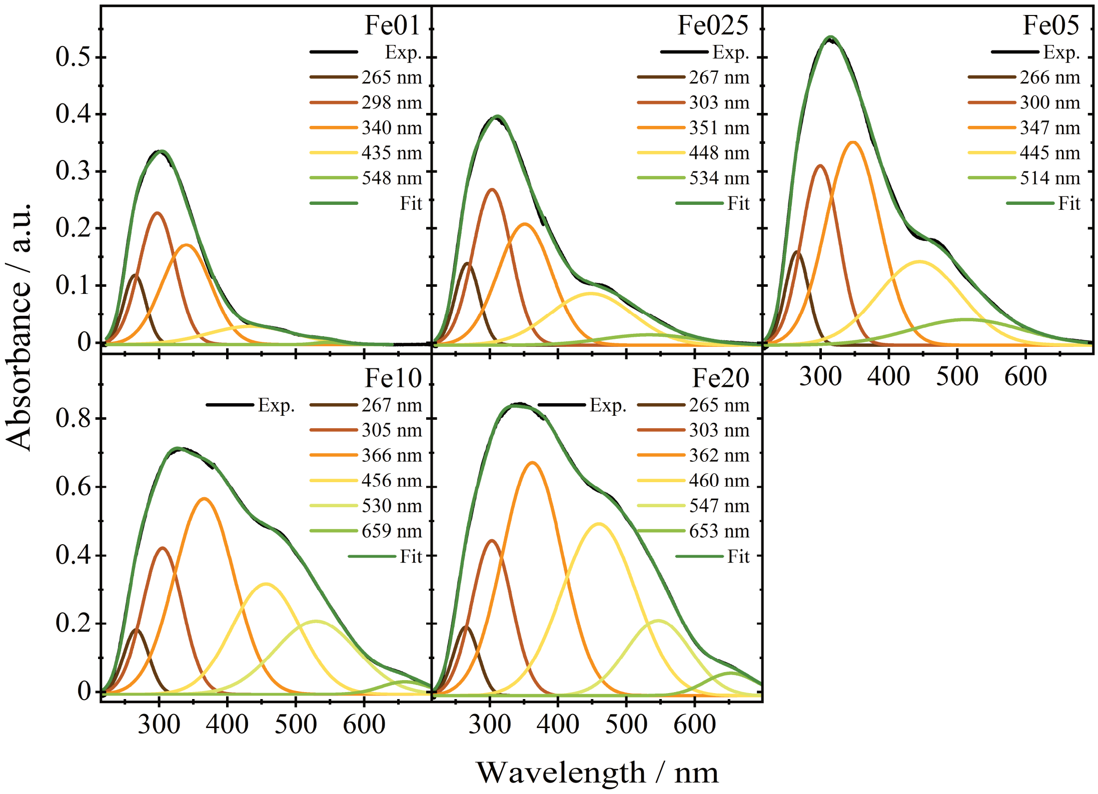

Figure 3.6: Results from peak deconvolution of the DRUV spectra of Fe01 to Fe20; experimental spectra after background subtraction (black) and the corresponding cumulative peak fit (dark green); the center of each peak is given in nanometers in the legend.

However, when the iron loading of each catalyst is taken into account (Figure 3.7 right), the overall amount of both, isolated tetrahedral and isolated octahedral species increases from Fe01 to Fe20 but so does the number of oligomers and bulk species.

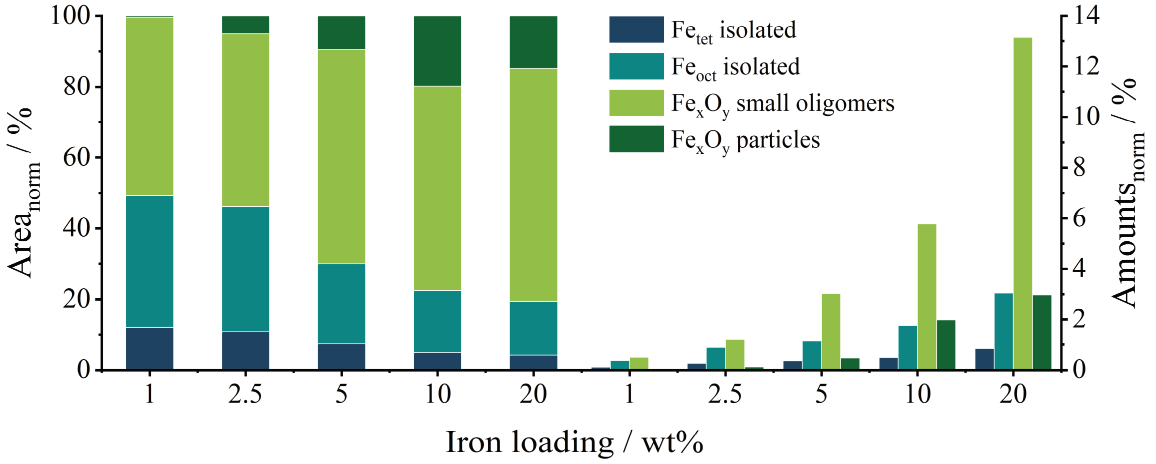

Figure 3.7: Visualization of the normalized percentual areas of tetrahedral, octahedral, oligomeric and particulate iron oxide species (left); amounts of these species relative to the overall mass of the catalysts (right).

To gain insights into the distribution of iron on the support and the iron oxide particle size, scanning transmission electron microscopy of Fe01 to Fe20 is utilized combined with energy dispersive X-ray mapping. Figure 3.8 shows the HAADF images of a confined domain of each observed catalyst, together with the filtered images for oxygen, aluminum and iron. The catalyst particles have a rough, irregular appearance with a broad particle size distribution, which derives from the used support. The HAADF image of catalyst Fe20 shows bright spots with diameters up to 50 nm, which correspond to bright spots on the iron signal. These are isolated clusters of iron oxide. The signals of oxygen, aluminum and iron on the remaining parts of the observed domain are finely distributed. For Fe10, a smaller number of isolated iron oxide clusters is found. Fe05 displays almost no visible clusters and at Fe025 only small dots of iron can be seen if the intensity of the signal is increased. At Fe01 almost no iron signal can be seen.

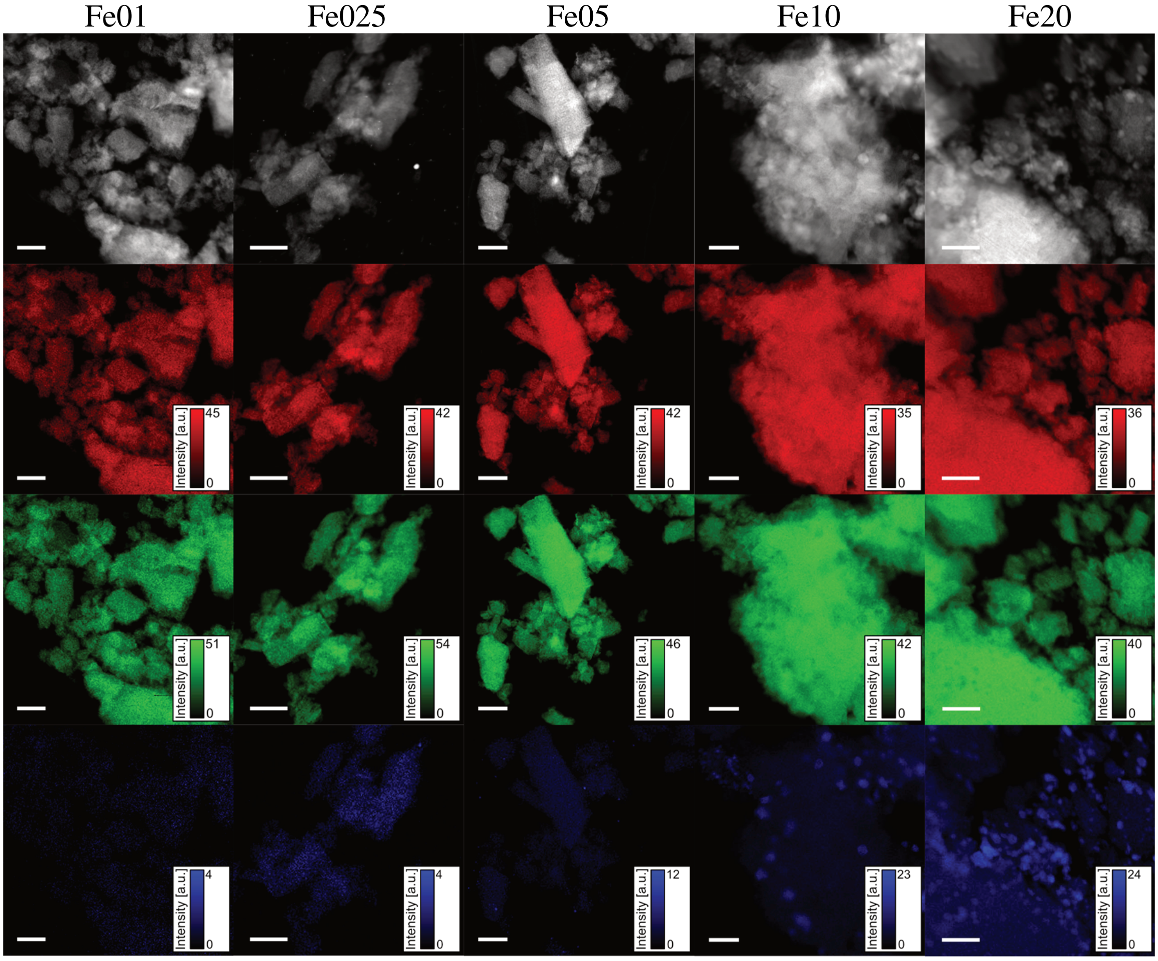

Figure 3.8: HAADF images (top row) and STEM-EDX images (red: oxygen K signal; green: aluminum K signal; blue: iron K signal) of Fe01 to Fe20 (left to right); scale bar 200 nm.

All of the observed domains of Fe01, Fe025 and Fe05 show a very homogeneous distribution of oxygen, aluminum and iron signal, indicating very finely dispersed iron oxidic species with almost no detectable agglomerates.

In addition to UV/Vis spectroscopy, X-ray absorption spectroscopy (XAS) provides an additional tool to probe the oxidation state and local geometry of the iron centers in the catalysts. The iron K-edge X-ray absorption near edge structure (XANES) shown in Figure 3.9 can be divided into two main features, pre-peak (approx. 7110 eV to 7120 eV) and the main edge (approx. 7120 eV to 7135 eV).

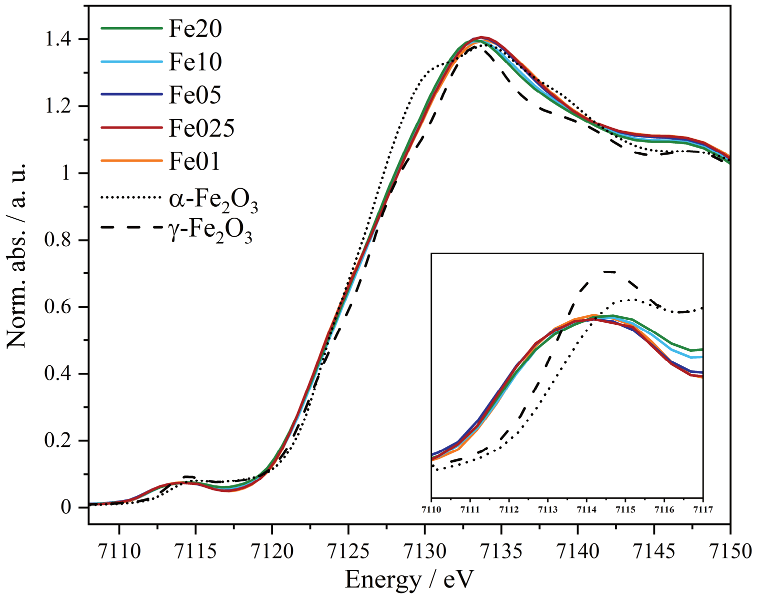

Figure 3.9: XANES region of the X-ray absorption spectra of Fe01 to Fe20 and α-Fe_2O_3 and zoomed in pre-peak of the respective samples.

The pre-peak originates from excitation of 1s electrons to the localized 3d/4p hybrid orbitals. It is therefore sensitive to the symmetry of the probed atom and even its oxidation state. The pre-peak energies of the catalysts are between 7113.9 and 7114.1 eV (Table 3.3) while their intensities are roughly the same. In comparison to that, the pre-peak of α- and γ-Fe_2O_3 have slightly higher energies with 7114.6 and 7114.3 eV for the first maximum with a less broadened and more intense shape.

Table 3.3: Pre-peak and edge positions of Fe01 to Fe20 and the α- and γ-Fe_2O_3 references; for the references, the pre-peak was fitted by two Gaussian-type functions; for the catalysts Fe01 to Fe20 only one fit function was applied; edge positions were obtained by halved maximum of the edge jump.

Catalyst	**Pre-peak [eV]**	**Edge position [eV]**
Fe01	7114.0	7126.0
Fe025	7113.9	7125.7
Fe05	7113.9	7125.4
Fe10	7114.1	7125.6
Fe20	7114.0	7125.4
α-Fe_2O_3	7114.6 7117.5	7125.1
γ-Fe_2O_3	7114.3 7117.1	7125.9

However, the spectra of catalysts Fe01 to Fe20 and the references were measured with different beamline parameters, which could contribute to a broadening in the case of Fe01 to Fe20. The main edge shows transitions of 1s electrons into the continuum, making it an accurate descriptor for the oxidation state of the probed species. The edge positions of Fe01 to Fe20 range between 7125.4 and 7126 eV (Table 3.3), α- and γ-Fe_2O_3 have edge energies of 7125.1 respectively 7125.9 eV. While the pre-peaks of Fe01 to Fe20 are slightly shifted to lower energies, compared to the references, the edge positions are almost the same. Differences in the positions are minor and can be neglected. All obtained energies are in good agreement to the literature and confirm together with the Mößbauer data the presence of iron in the oxidation state of +III.

A more detailed view of the local short-range structure of the iron centers can be achieved by analysis of the extended X-ray absorption fine structure, short EXAFS. By application of a model structure[205], two main coordination spheres can be fitted to the Fourier transformation of the experimental spectra (Figure 3.10). The first region, from 1.8 to 2.2 Å, containing the oxygen neighbours, allows a discrimination of tetrahedral and octahedral coordination sites. The region from 2.2 to 4 Å contains the nearest iron and aluminum backscatterers. Fitting the experimental data with the EXAFS equation yields structural parameters summarized inTable 3.4.

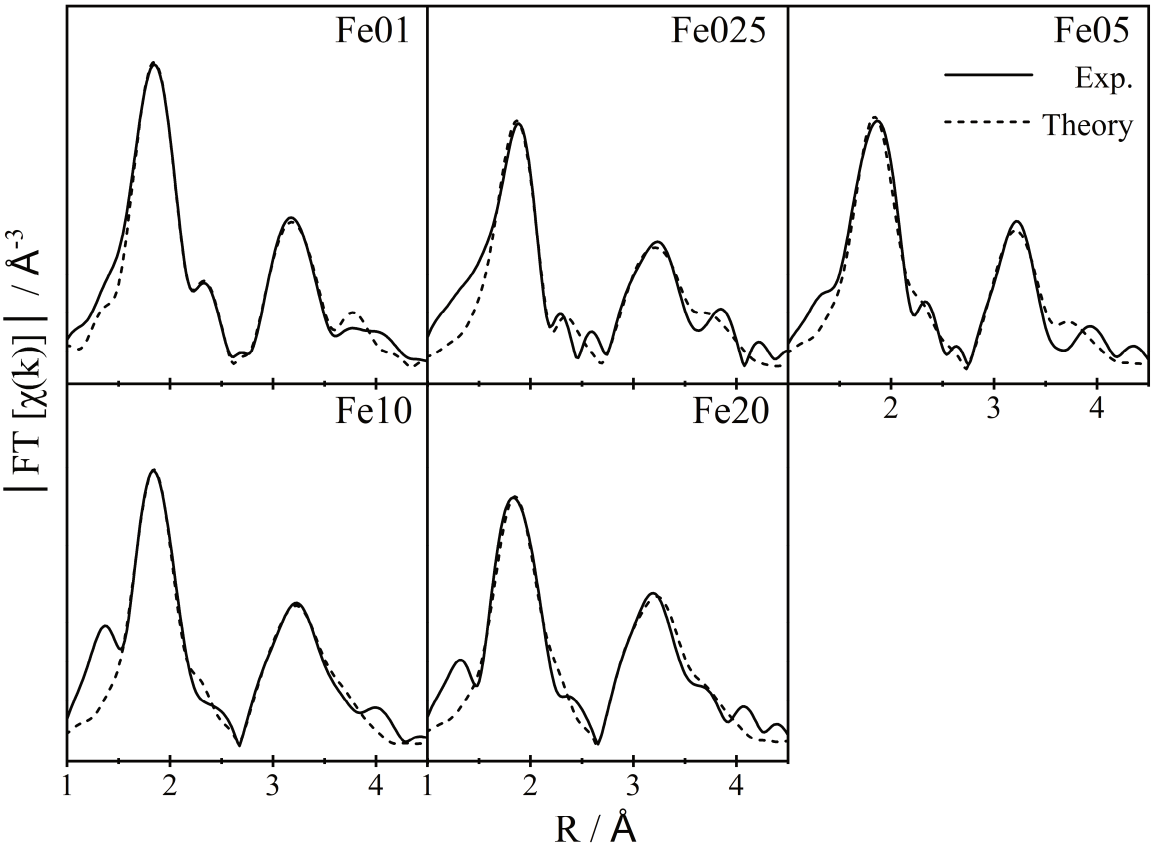

Figure 3.10: Fourier transformed EXAFS spectra of Fe01 to Fe20 and the corresponding fits.

Comparison of the first region clearly shows a trend from a coordination of 2.5 oxygen backscatterers at 1.9 Å and 3.9 at 2 Å to the observed iron center of catalyst Fe20, over 3.6 oxygen atoms at 1.9 Å and 3.1 at 2.1 Å at catalyst Fe05, towards a ratio of 4.8 oxygen atoms at 1.9 Å to 1.1 atoms at 2.2 Å for Fe01. If the crystallographic data of the presumed phases of iron[212,213], maghemite and hematite, are taken into consideration, these numbers can be correlated to tetrahedral and octahedral iron oxide species. While an octahedral coordination in maghemite as well as in hematite has Fe-O distances between 1.9 and 2.2 Å, tetrahedrons from maghemite also introduce Fe-O distances between 1.7 and 1.9 Å. Since the averaged Fe-O distance of the octahedrons is approx. 2 Å and they are only slightly distorted, which means that the coordination is still somewhat symmetrical, only a contribution of low R Fe-O distances from tetrahedrons could lead to a coordination number higher than 3 at 1.94 Å. Thus, the high coordination number of 4.8 oxygen backscatterers of Fe01 can be attributed to a high amount of tetrahedrally coordinated iron species. Fe025 seems to be identical, while the coordination changes over 3.6:3.1 for Fe05 to 2.5:3.9 for Fe20, indicating that here the ratio of tetrahedral to octahedral iron(III) coordination is decreased, which is in excellent agreement to the information obtained from DRUVS data (Figure 3.7). However, compared to the α-Fe_2O_3 reference the Fe-O distances of Fe20 are still smaller, ascertaining that there is still a certain amount of γ-Fe_2O_3 as also shown by XRD. The second region, as stated before, contains the nearest iron and aluminum atoms, which can be an indicator for particle size as well as the incorporation of the active site into the support lattice. In this particular case there are no major changes or trends detectable. All of them have a minor coordination sphere of iron at 3 Å and a larger amount of aluminum followed by iron backscatterers at around 3.4 Å.

Table 3.4: Structural parameters obtained by EXAFS analysis of the catalysts Fe01 to Fe20 Fe20 as well as the α- and γ-Fe_2O_3 reference; Abs = absorbing atom; Bs = backscattering atom; n(Bs) = number of backscattering atoms; r(Abs-Bs) = distance of absorbing to backscattering atom; σ = Debye-Waller-like factor; R = fit index; E_f = Fermi energy; Afac = amplitude reducing factor.

Catalyst	**Abs-Bs**	**n(Bs)**	**r(Abs-Bs) [Å]**	**σ [Å^{-1}]**	
Fe01	Fe-O	4.8 ± 0.24	1.944 ± 0.019	0.089 ± 0.008	**R** = 28.29 %
	Fe-O	1.1 ± 0.05	2.157 ± 0.021	0.045 ± 0.004	**E_f** = 3.655 eV
	Fe-Fe	1.0 ± 0.10	3.059 ± 0.030	0.112 ± 0.011	**Afac** = 0.9072
	Fe-Al	8.1 ± 0.81	3.426 ± 0.034	0.112 ± 0.011	
	Fe-Fe	5.0 ± 0.50	3.439 ± 0.034	0.112 ± 0.011	
Fe025	Fe-O	4.6 ± 0.23	1.944 ± 0.019	0.095 ± 0.009	**R** = 38.80 %
	Fe-O	1.6 ± 0.08	2.169 ± 0.021	0.087 ± 0.008	**E_f** = 3.137 eV
	Fe-Fe	1.1 ± 0.11	3.047 ± 0.030	0.107 ± 0.010	**Afac** = 0.9477
	Fe-Al	7.9 ± 0.79	3.455 ± 0.034	0.112 ± 0.011	
	Fe-Fe	5.6 ± 0.56	3.463 ± 0.034	0.112 ± 0.011	
Fe05	Fe-O	3.6 ± 0.18	1.911 ± 0.019	0.087 ± 0.008	**R** = 34.13 %
	Fe-O	3.1 ± 0.15	2.076 ± 0.020	0.112 ± 0.011	**E_f** = 4.013 eV
	Fe-Fe	0.8 ± 0.08	3.063 ± 0.030	0.105 ± 0.010	**Afac** = 0.8896
	Fe-Al	7.4 ± 0.74	3.397 ± 0.033	0.112 ± 0.011	
	Fe-Fe	4.7 ± 0.47	3.414 ± 0.034	0.112 ± 0.011	
Fe10	Fe-O	3.4 ± 0.17	1.907 ± 0.019	0.081 ± 0.008	**R** = 33.88 %
	Fe-O	3.0 ± 0.15	2.065 ± 0.020	0.112 ± 0.011	**E_f** = 2.925 eV
	Fe-Fe	0.5 ± 0.05	2.983 ± 0.029	0.092 ± 0.009	**Afac** = 0.8896
	Fe-Al	6.2 ± 0.62	3.354 ± 0.033	0.112 ± 0.011	
	Fe-Fe	4.0 ± 0.40	3.403 ± 0.034	0.112 ± 0.011	
Fe20	Fe-O	2.5 ± 0.12	1.898 ± 0.018	0.077 ± 0.007	**R** = 33.35 %
	Fe-O	3.9 ± 0.19	2.025 ± 0.020	0.110 ± 0.011	**E_f** = 4.384 eV
	Fe-Fe	0.5 ± 0.05	2.962 ± 0.029	0.081 ± 0.008	**Afac** = 0.8217
	Fe-Al	9.0 ± 0.90	3.360 ± 0.033	0.112 ± 0.011	
	Fe-Fe	5.7 ± 0.57	3.394 ± 0.033	0.112 ± 0.011	

α-Fe_2O_3	Fe–O	3.2 ± 0.16	1.961 ± 0.019	0.081 ± 0.008	**R** = 27.77 %
	Fe–O	3.3 ± 0.16	2.134 ± 0.021	0.110 ± 0.011	$\mathbf{E_f}$ = 2.584 eV
	Fe–Fe	6.3 ± 0.31	2.983 ± 0.029	0.112 ± 0.011	**Afac** = 0.9735
	Fe–Fe	2.9 ± 0.29	3.317 ± 0.033	0.112 ± 0.011	
	Fe–Fe	1.2 ± 0.12	3.706 ± 0.037	0.063 ± 0.006	
γ-Fe_2O_3	Fe–O	0.7 ± 0.03	1.868 ± 0.018	0.032 ± 0.003	**R** = 24.68 %
	Fe–O	4.8 ± 0.14	2.003 ± 0.020	0.105 ± 0.010	$\mathbf{E_f}$ = 3.112 eV
	Fe–Fe	4.4 ± 0.44	3.019 ± 0.030	0.112 ± 0.011	**Afac** = 0.8219
	Fe–Fe	2.1 ± 0.21	3.467 ± 0.034	0.087 ± 0.008	
	Fe–Fe	3.6 ± 0.36	5.128 ± 0.051	0.112 ± 0.011	

The CO oxidation activity of each catalyst was both measured under a constant heating ramp with 2 °C/min up to 600 °C (Figure 3.11 left) as well as at static temperatures in 50 °C steps starting from 150 °C (Figure 3.11 right). In the continuous measurements the temperatures of 10 % conversion for Fe01, Fe025, Fe05, Fe10 and Fe20 are 170, 109, 86, 88 and 94 °C, respectively 362, 211, 169, 177 and 177 °C for 50 % of CO-conversion (Table 3.5). Here Fe01 shows the lowest activity, followed by Fe025. Fe05, Fe10 and Fe20 only show minor differences in their curves of conversion, with Fe05 being the most active. Fe10 is slightly better than Fe20 below 177 °C which changes at higher temperatures due to the steeper incline in the conversion curve of Fe20. The temperatures corresponding to 90 and 95 % CO-conversion for Fe01 to Fe20 are 449, 307, 240, 283 and 248 °C, respectively 467, 332, 259, 340 and 272 °C. Here Fe05 is again superior to the other catalysts, followed by Fe20. Fe10 has a lower temperature than Fe025 for 90 % conversion but due to a drop in activity of Fe10 this is inverted for 95 % CO_2 yield.

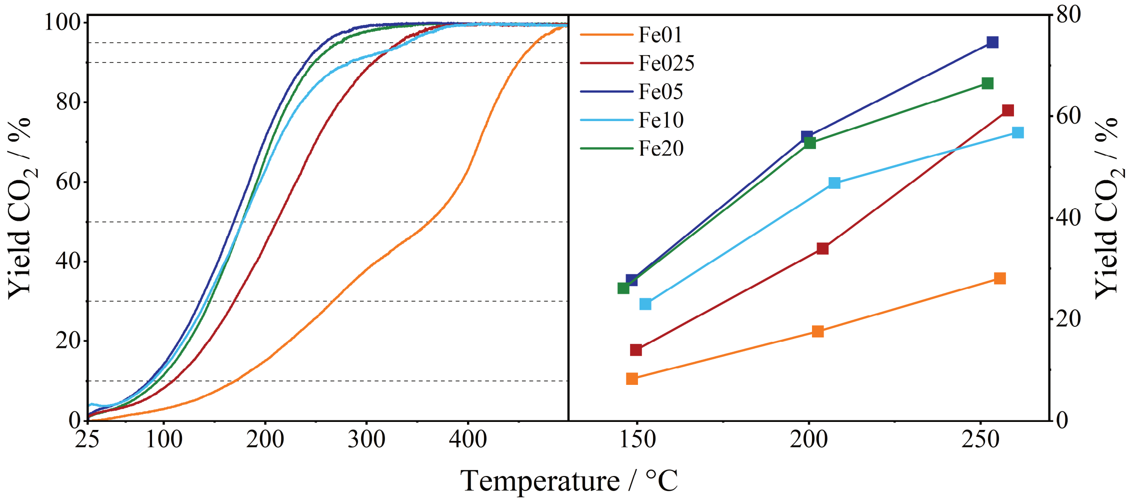

Figure 3.11: Percentual CO_2 yield of Fe01 to Fe20 in continuous CO oxidation experiments (left) and at static temperatures (right).

Fe01 shows the lowest activity over the whole measurement, including a large drop of activity between 300 and 400 °C. The same trends can be seen in the measurements at static temperatures. Here also Fe01 shows lowest activity, followed by Fe025, at least at 150 and 200 °C. Fe05 displays the highest conversion at all temperatures, while Fe10 is less active and shows even lower activity than Fe025 at 250 °C. Fe20 features only slightly lower activities than Fe05, as in the continuous measurements. The CO_2 yields of Fe01 to

Fe20 from continuous measurements at 100, 150, 200, 250 and 300 °C were converted into the turnover frequencies shown in Figure 3.12 (left).

Table 3.5: Temperatures of Fe01 to Fe20 corresponding to 10 %, 30 %, 50 %, 90 % and 95 % CO conversion, respectively CO_2 yield, obtained from measurements with continuous heating.

Catalyst	**T_{10} [°C]**	**T_{30} [°C]**	**T_{50} [°C]**	**T_{90} [°C]**	**T_{95} [°C]**
Fe01	170	267	362	449	467
Fe025	109	169	211	307	332
Fe05	86	136	169	240	259
Fe10	88	142	177	283	340
Fe20	94	146	177	248	272

Here the catalysts with low iron loadings Fe01, Fe025 and Fe05 are superior to Fe10 and Fe20 at 100, 150 and 200 °C. Above that the turnover frequencies of Fe01 and Fe025 abscond to almost twice the TOF of Fe05, while the values for Fe05, Fe10 and Fe20 stagnate. Turnover frequencies obtained from CO oxidation experiments at static temperatures show a similar trend, where at 150 °C Fe01 has a slightly higher TOF than Fe025 and Fe05 (Figure 3.12 right). Fe10 has a much lower value, followed by Fe20. The turnover frequency of Fe01 doubles to 200 °C and increases with the same amount up to 250 °C with Fe025 being slightly less active at both temperatures.

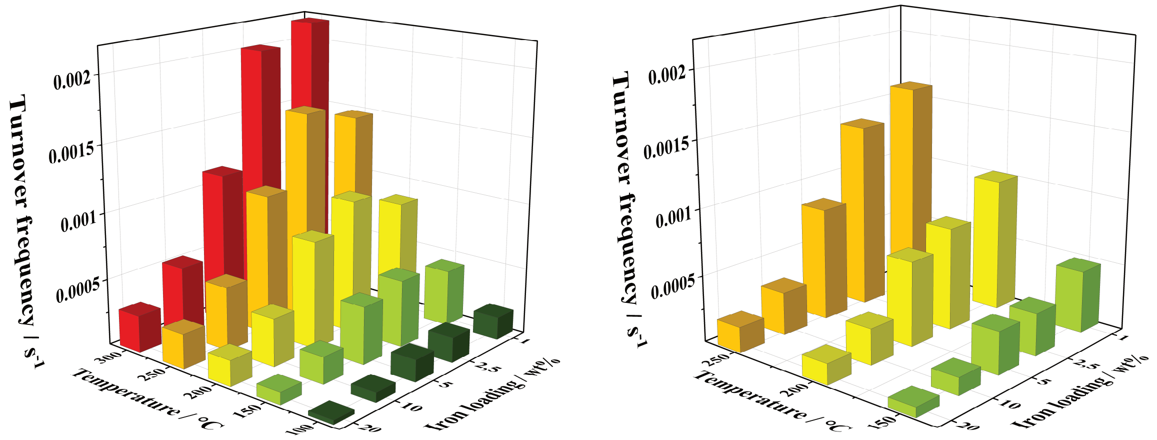

Figure 3.12: Turnover frequencies of Fe01 to Fe20 in CO oxidation experiments with continuous heating (left) and at static temperatures (right).

Fe05 can almost keep up at 200 °C but has a much lower TOF than Fe025 at 250 °C. The values of Fe10 are much lower at all temperatures and Fe20 shows even worse turnover frequencies. It is noteworthy, that for these static measurements a decay in conversion for each step could be detected after reaching the desired temperature. This decrease in CO conversion can be quantified as high as 10 to 15 % and derives most certainly from carbon dioxide poisoning of the active sites. Nonetheless, at these stationary measurements the superiority of low iron loadings can be visualized even further by comparison of turnover frequencies (Figure 3.12). If the whole amount of iron is taken into the calculation, the TOF of catalyst Fe01 at 250 °C is 5 times higher than Fe10 and more than 8 times higher than Fe20. However, since the number of iron oxidic sites that take actively part in the reaction cannot be quantified, the TOF can only be calculated for the overall amount of iron.

3.2 Summary and Discussion

Catalysts with iron oxide immobilized on a γ-Al_2O_3 support with varying weight-loadings of iron were prepared to perform a multidimensional structure-activity-correlation. All of the catalysts could be ascribed to iron oxide with iron in the oxidation state +III as confirmed by isomer shift and quadrupole splitting of the Mößbauer spectra as well as the pre-peak and edge positions of the XANES analysis. The surface area of the pure support and the catalysts Fe01 to Fe20 was obtained via the BET method, which showed that only minor changes occur for Fe01 to Fe10 when compared to γ-Al_2O_3, whereas the surface area drops from approx. 160 m^2/g to 121 m^2/g for Fe20. This can be explained by the higher amount of agglomeration of Fe20 when compared to the other samples, as indicated by UV/Vis, Mößbauer as well as the STEM-EDX mapping. XRD analysis showed increasing γ-Al_2O_3 lattice parameters for increasing Fe loadings, which is due to either incorporation of Fe ions into the support lattice or interaction with the latter. While Fe10 and Fe20 could be ascertained to a mixture of both α- and γ-Fe_2O_3, respectively hematite and maghemite, Fe01, Fe025 and Fe05 did not show any iron oxide related signals which is either due to poor crystallinity or crystallite sizes too small to be detected by high-resolution XRD. Latter fits to the information gained by Mößbauer spectroscopy, in which Fe01 to Fe05 were assigned to particles less than 13.5 nm, whereas Fe10 and Fe20 do also contain particles above this value. The superparamagnetism of Fe025 and Fe05 deduced from low temperature Mößbauer analysis underlines the conjecture of very small particle sizes. STEM-EDX mapping of Fe01 to Fe20 also showed large variations in the iron oxide particle sizes. For Fe20 a number of large clusters of iron oxide with diameters up to 50 nm could be detected. The amount of these clusters decreases with decreasing iron oxide loading. For Fe01 to Fe05, none of these large clusters are visible. Besides these agglomerates, a fine dispersion of iron oxide species with sizes below the resolution of the microscope could be shown on all observed γ-Al_2O_3 particles of Fe01, Fe025, Fe05, Fe10 and Fe20, which is again in good agreement to the Mößbauer data. Peak deconvolution of diffuse reflectance UV/Vis spectra also shows an increase in the amount of oligomers (Fe_xO_y) and bigger particles from Fe01 to Fe20. Quantification of the peak areas below 330 nm led to a trend of octahedrally vs. tetrahedrally coordinated iron oxide species. This ratio is 3.1 respectively 3.3 and 3.1 for Fe01, Fe025 and Fe05 and increases to 3.6 for both Fe10 and Fe20. X-ray absorption spectroscopy of the catalysts was carried out at the iron K-edge. While analysis of the near edge region did not show any differences throughout the samples, EXAFS analysis also led to a clear trend of more tetrahedrally coordinated iron oxide species with Fe-O distances of approx. 1.94 Å for Fe01 and Fe025, to more Fe-O contributions at distances above 2 Å with increasing iron loading. This can be assigned to a higher amount of octahedrally coordinated iron species for Fe10 and Fe20 as also shown by the above-mentioned peak deconvolution of the DRUV spectra. The catalysts showed good to excellent activity during CO oxidation experiments, dependent on the approach taken for comparison. Fe05, Fe10 and Fe20 showed high activity at much lower temperatures than Fe01 and Fe025 in the continuous measurements and also at static temperatures with the exception of Fe10 being less active than Fe025 at high temperatures. Over the whole experiment Fe05 was superior to the other catalysts, followed by Fe20 and Fe10. Fe025 and Fe01 appeared to be least active when comparing the temperatures needed for a certain amount of CO_2 yield. However, when converted into turnover frequencies, the catalysts with lower weight-loadings of iron were superior to the other catalysts at distinct temperatures, in the continuous as well as the static measurements. The much higher turnover frequencies of Fe01 and Fe025 can be explained by a higher ratio of more active tetrahedral to less active octahedral iron oxide species, as it could be proven by the deconvolution of the DRUVS data as well as the EXAFS analysis. In addition to this, Fe01 and Fe025 did not show any agglomerates (Fe_xO_y) in STEM-EDX mapping, while with increasing iron loading large clusters of iron oxide up to 50 nm could be detected. This can be emphasized by the information gathered throughout Mößbauer analysis as well as the DRUVS data which both showed large contributions of iron oxide oligomers and small particles. This means that an increasing amount of iron oxide is present in bulk phase with increasing iron loading, which is likely to be less accessible for catalytic purposes. Nevertheless, Fe05 to Fe20 showed curves of conversion at much lower temperatures than Fe01 and Fe025. While the ratio of tetrahedral to octahedral iron oxide species of Fe10 and Fe20 is lower than that of Fe01 and Fe025, the overall amount of tetrahedrally coordinated Fe^{III} still increases with increasing iron loading (Figure 3.7). The fact of Fe05 showing the highest activity by means of the lowest temperatures needed leads to the assumption, that Fe05 is the best compromise between high amounts of more active tetrahedral iron oxide species and the amount of iron oxide present in less or non-active bulk phase. The latter is higher for Fe10 and Fe20, which is most probably the reason why they are not better than Fe05.

Taking all of these findings into consideration, Fe05 presents an excellent starting point for the optimization of such systems. An iron oxide catalyst with high amount of iron present in tetrahedral coordination geometry that is finely dispersed and easily accessible for catalysis without any agglomeration, respectively without iron oxide in bulk phase, could exhibit outstanding catalytic activity in CO oxidation. Since the process of agglomeration is a problem most likely occurring during the annealing process and could probably even be linked to the formation of higher amounts of hematite, respectively solely octahedrally coordinated iron oxide species, this is what should be addressed. Potential solutions comprise either the alteration of the annealing process itself, by variation of the temperature ramp applied or a stepwise temperature program, or the successive annealing of small amounts of iron precursor impregnated on the support. Such a multi-step impregnation-calcination process would benefit from the fact that iron oxide is less mobile than the non-annealed $Fe(acac)_3$ precursor, potentially hindering agglomeration on the support surface.

To conclude, the structure-activity-correlation of the presented catalysts led to crucial insights into the dependence of catalytic activity of iron oxide catalysts for CO oxidation from their structural parameters and the working hypothesis derived thereof aims towards the optimization of such systems and hence the potential replacement of state-of-the-art noble metal catalysts in industrial applications.

4 KEEP IT SIMPLE!

A New Preparation Technique for Iron Oxide Catalysts with Outstanding Structural Properties for CO Oxidation

Since catalysts with low iron loadings exhibit all attributes of highly dispersed, isolated iron oxidic species with high amounts of tetrahedrally coordinated iron species, which also show a superiority to catalysts with high amounts of iron regarding their turnover frequencies, the obvious next step is to take advantage of this. On the assumption, that the precursor, respectively iron(III) acetylacetonate, has a high mobility on the support surface compared to the final iron oxide, a new synthetic strategy to hinder agglomeration and obtain a high amount of finely dispersed tetrahedral iron oxide species was developed. It was assumed, that a multi-step impregnation-calcination procedure, where the iron species is added successively in 1 wt% steps, could inhibit agglomeration through immobilization of the iron species in form of iron oxides on the support surface.

4.1 Results

For proof of principle of this multi-step impregnation-calcination procedure, a range of iron oxide catalysts immobilized on γ-Al_2O_3 was prepared with iron loadings of 1 to 10 wt% in steps of 1 wt% (MI01 to MI10). Therefore Fe(acac)$_3$ was impregnated on the alumina support via wetness impregnation and annealed in atmospheric air at 600 °C after removal of the solvent. As a reference, a single-step impregnated catalyst with 10 wt% of iron was prepared (SI10).

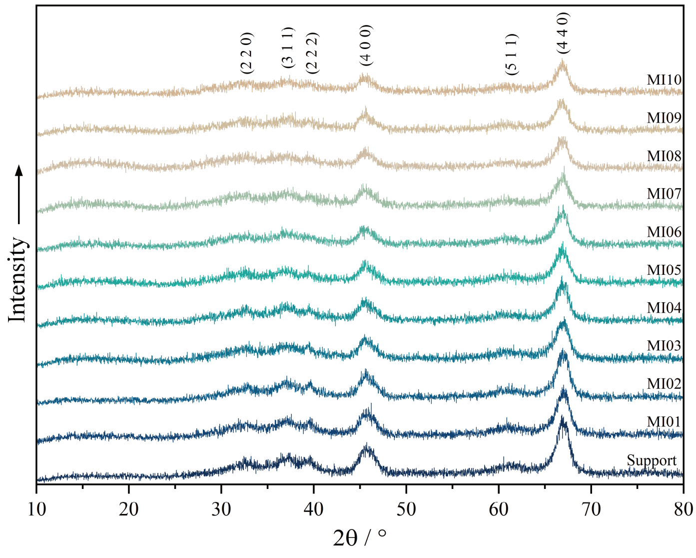

Figure 4.1: Powder X-ray diffractograms of the catalysts MI01 to MI10 and the pure γ-Al_2O_3 support.

The as-prepared catalysts are investigated with various spectroscopic methods to gain structural insights and for comparison to Fe01 - Fe20 (Chapter 1). The data obtained by powder X-ray diffractometry for catalysts MI01 to MI10 shows the pattern of the γ-alumina support, without further reflexes of the iron species, either due to low crystallite sizes or amorphism (Figure 4.1). However, a comparison of the 2θ values of the alumina reflexes gives important insights into the influence of the iron loading on the support material of the catalysts. The reflexes shift to lower 2θ values with increasing iron loading, which means that the plane distances of the support are increasing. Similar to Fe01 to Fe20 (Figure 3.3), the lattice parameter *a* shows a linear correlation to the iron loading (Figure 4.2). This linear correlation of the lattice parameter to the iron loading, analogous to Fe01 to Fe20, is an indicator for the incorporation of iron somehow into the lattice of the γ-Al_2O_3 support or for the interaction of both. Due to the high signal-to-noise ratio of the obtained diffractograms, only the two most intense signals (400) and (440) are considered for these calculations.

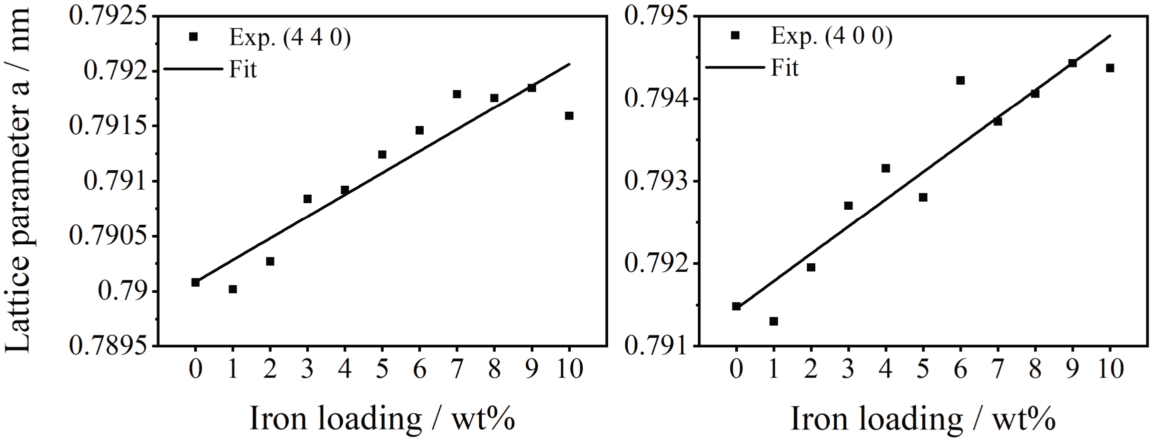

Figure 4.2: Lattice parameter a calculated from PXRD reflexes of the lattice planes (440) and (400) of catalysts MI01 - MI10 and the pure support material and their linear fit.

Diffuse reflectance UV/Vis spectroscopy of MI01 to MI10 and the reference catalyst SI10 is carried out to probe the coordinative and spatial geometry of the present iron species. With increasing iron loading the overall intensity of the background-corrected spectra increases up to a maximum for MI06, accompanied with an increase of contributions above 300 nm and the growth of an additional feature above 400 nm. From MI07 to MI10 the maximum intensity decreases again, while the contributions above 400 nm continue to increase. These trends can be explained by an increase in the formation of small iron oxide oligomers or particulates with increasing iron loading. For a quantification of these effects the spectra of the investigated catalysts are processed by manual subtraction of a Lorentzian-type function as a baseline followed by peak deconvolution, each with 3, respectively 4, 5 or 6 peaks, depending on the shape of the experimental spectrum (Figure 4.3).

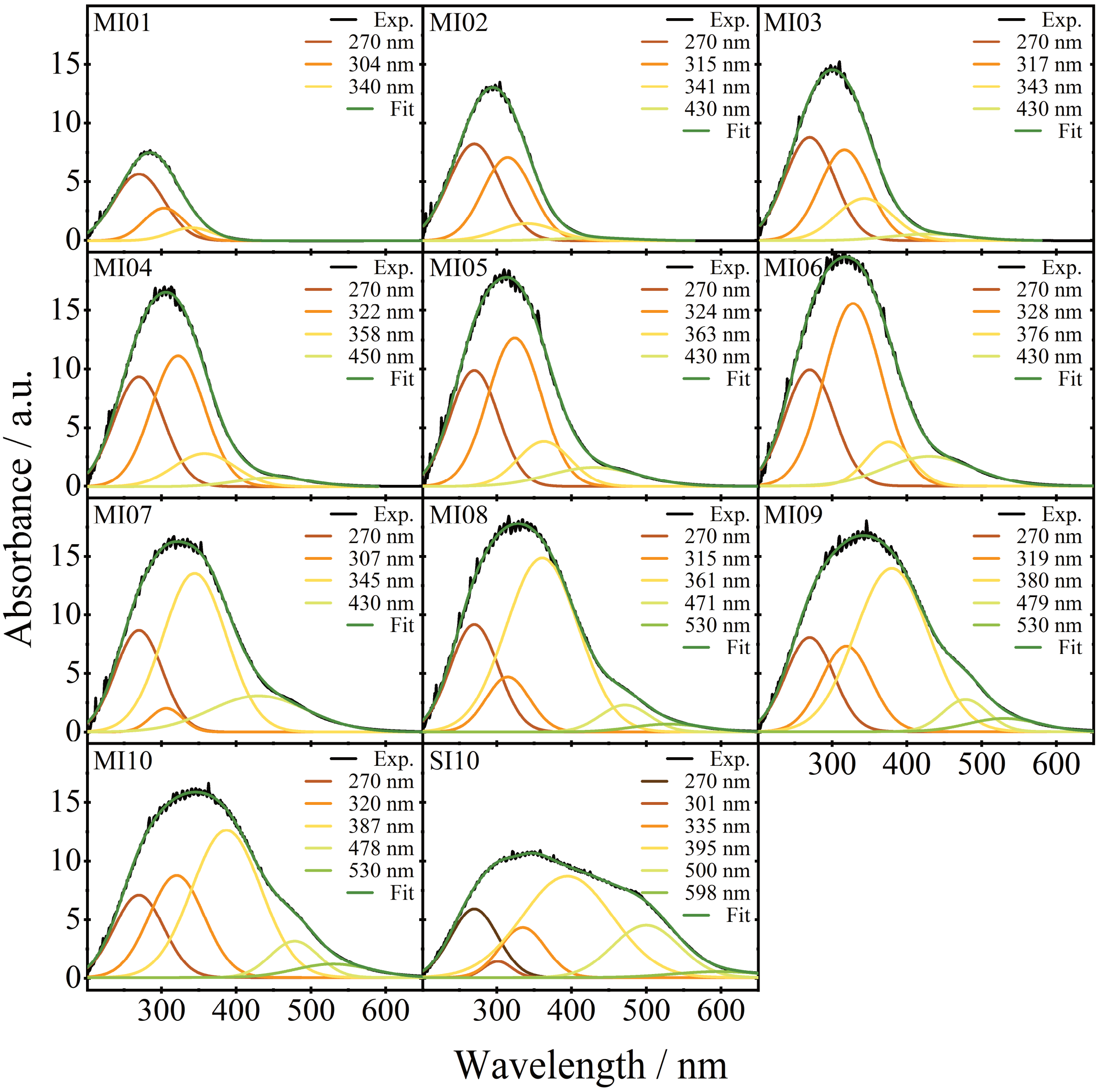

Figure 4.3: DRUV spectra of catalysts MI01 - MI10 and SI10 and resulting peak deconvolution with the respective peak centers and their convoluted fit.

The peaks below 330 nm represent contributions of isolated iron oxide species, peak 1 from tetrahedrally coordinated iron at lower wavelengths and peak 2 from octahedrons around 320 nm. Small oligomers, as mentioned in the previous chapter, lead to signals between approximately 330 and 500 nm, bigger agglomerates lead to bands above 500 nm. Figure 4.4 shows the percentages of each contribution derived from peak areas of the deconvolution (left) respective to the normalized overall areas of the spectra and their percentual amount respective to the as-prepared catalysts, when iron loading and the support are taken into calculation (right). From MI01 to MI10 the percentage of isolated tetrahedrally coordinated iron species decreases, accompanied with an increase of isolated octahedral species from MI01 to MI06 and, after a drop, again from MI07 to MI10. The percentual number of small oligomers increases from MI01 to MI03, then stays roughly at the same level up to MI06. From MI06 to MI07 there is a steep increase in oligomeric iron species, which causes the drop in the percentage of octahedral species. Up to MI10 the percentage of oligomers decreases slightly, while from MI08 to MI10 an additional increasing contribution of large oligomers, respectively particulates, arises.

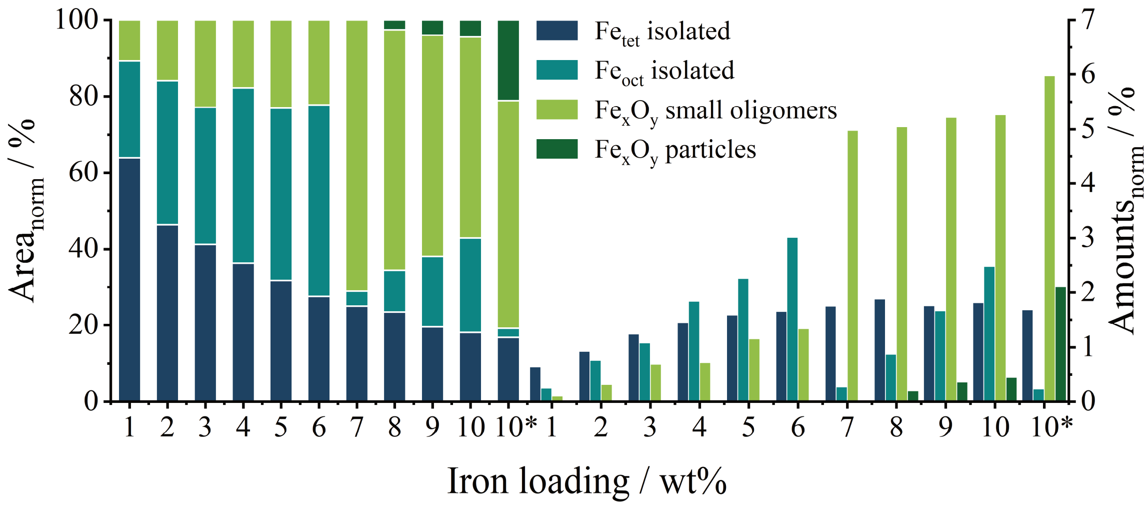

Figure 4.4: Visualization of the normalized percentual areas of tetrahedral, octahedral, oligomeric and particulate iron oxide species (left) gained from peak deconvolution of the DRUV spectra of SI10 and MI01-MI10 and amounts of these species relative to the overall mass of the respective catalyst (right).

If the whole mass of the catalysts is taken into consideration, the trends are clearer. The amount of tetrahedrally coordinated isolated iron species increases from MI01 up to MI08 and then stagnates to MI10, while the number of octahedrons increases from MI01 to MI06 and then, due to the inversion of the ratio of octahedrally coordinated isolated iron species to small oligomers, drops as the amount of oligomers increases harshly.

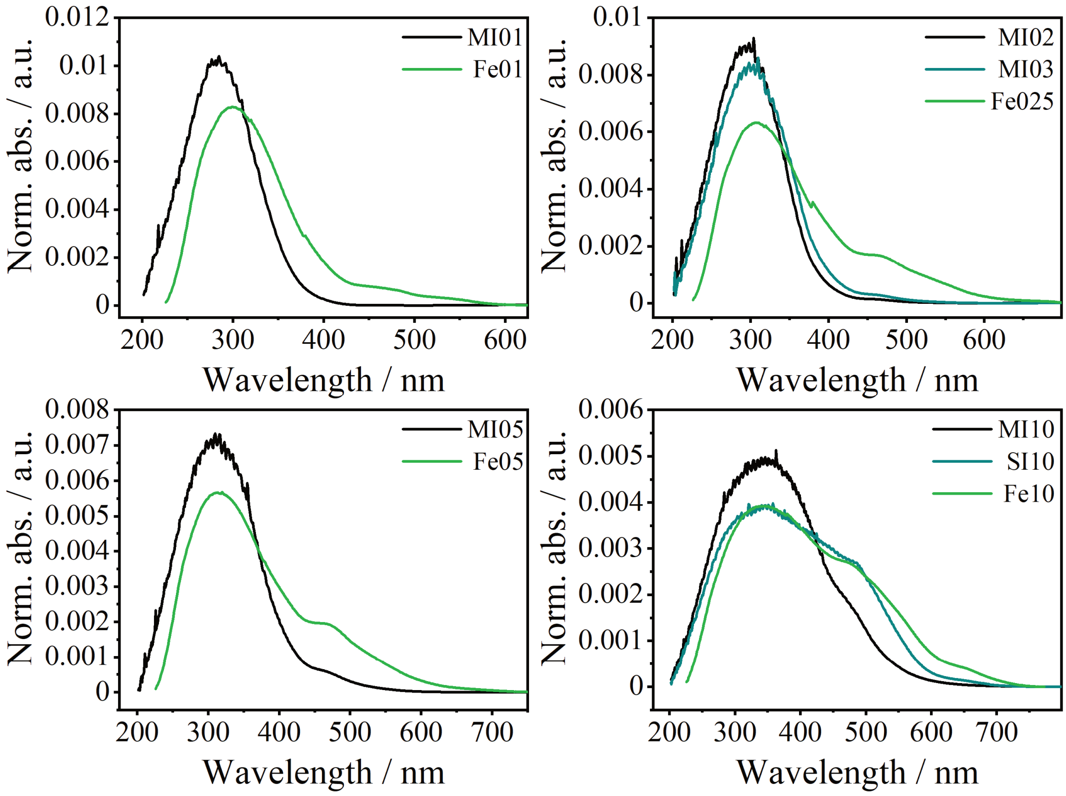

Figure 4.5: Comparison of the area-normalized DRUV spectra of the multi-step impregnated catalysts MI01, MI02, MI03, MI05 and MI10 with the respective single-step catalysts Fe01, Fe025, Fe05 and Fe10 and the reference catalyst SI10.

From MI07 up to MI10 there is a huge, slightly increasing number of oligomers and from MI08 to MI10 an increasing contribution of particles can be seen. The reference catalyst SI10 contains a higher number of oligomers and a much lower amount of octahedrally coordinated isolated iron oxide species, while the number of particulates is over four times higher than at MI10. The advantage of the multi-step impregnation-calcination procedure comes to view if the UV/Vis spectra are compared to Fe01, Fe025, Fe05 and Fe10 with the respective iron loading (Figure 4.5). Clearly the MI catalysts contain less agglomerates in form of oligomers or particles, leading to less broadened bands and lower or zero contributions above 400 nm (for further information including the summarized results of peak deconvolution see Appendix: Figure SI 9.11 to Figure SI 9.21).

To probe the spatial geometry of the present iron species and their oxidation state, X-ray absorption spectroscopy was carried out at the iron K-edge (7112 eV). Catalysts MI01 to MI03 were investigated in fluorescence mode, while higher weight-loadings of iron were measured in transmission to minimize the influence of self-absorption. The so-called pre-peak derives from transitions of the excited 1s electron into 3d or hybridized 3d/4p orbitals[222]. Because 1s to 3d is dipole forbidden, only quadrupole transitions can be accounted which are far less intense but whose probability increases by 3d-4p-hybridization resulting of a deviation from centrosymmetry, e. g. in tetrahedral systems. The pre-peak intensities of the herein described catalysts increase from MI01 to MI04, then staying roughly at the same intensity. The increase from MI01 to MI04 is an indicator that the amount of non-centrosymmetric, respectively tetrahedral, iron centers increases in this ascending order which is not in accordance with the decreasing peak areas of lower wavelength transitions in the UV/Vis data with increasing iron loading. This indicates that the areas obtained from peak deconvolution of the DRUV spectra could probably be too low for isolated tetrahedral iron oxide species and the missing of information about tetrahedrally coordinated iron species in oligomers and particles.

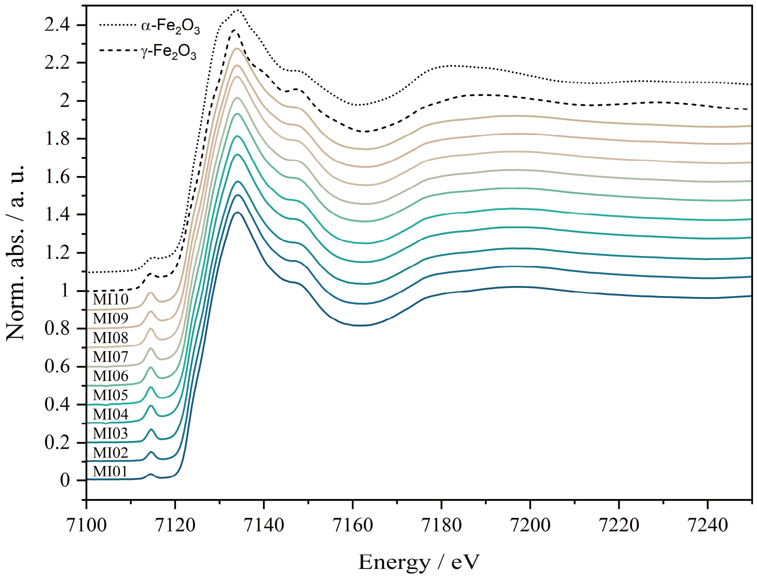

Figure 4.6: XANES spectra of MI01 - MI10, SI10 and the references α-Fe_2O_3 and γ-Fe_2O_3 at the Fe K-edge (7112 eV).

Also, the presence of distorted octahedrally coordinated iron species could be a factor increasing the peak intensity of the pre-peak. The position of the pre-peaks as well as the actual edge position, shown in Table 4.1, are roughly the same for all systems as they all can clearly be assigned to iron III. The centers of the pre-peaks for all investigated samples lie at approximately 7114.5 eV without any visible trend.

Table 4.1 Pre-peak and edge positions of MI01 - MI10, SI10 and α-Fe_2O_3 and γ-Fe_2O_3; pre-peak positions were obtained by baseline correction of the XANES spectra followed by fit of a Gaussian-type function; edge positions obtained from halved maximum of the edge jump.

Catalyst	**Pre-peak [eV]**		**Edge position [eV]**
MI01	7114.46		7126.43
MI02	7114.57		7126.36
MI03	7114.57		7126.20
MI04	7114.49		7126.22
MI05	7114.48		7126.20
MI06	7114.47		7126.12
MI07	7114.48		7126.13
MI08	7114.47		7126.07
MI09	7114.49		7126.03
MI10	7114.42		7125.97
SI10	7114.21	7117.18	7125.72
α-Fe_2O_3	7114.60	7117.47	7125.11
γ-Fe_2O_3	7114.34	7117.11	7125.86

The edge positions of MI01 to MI10 are between 7126.4 eV and 7126.0 eV and, as mentioned above, fit perfectly to iron in the oxidation state +III. Although the changes in the edge position seem to be only minor, a clear trend is visible. The edge positions shift to lower energies from MI01 to MI10.

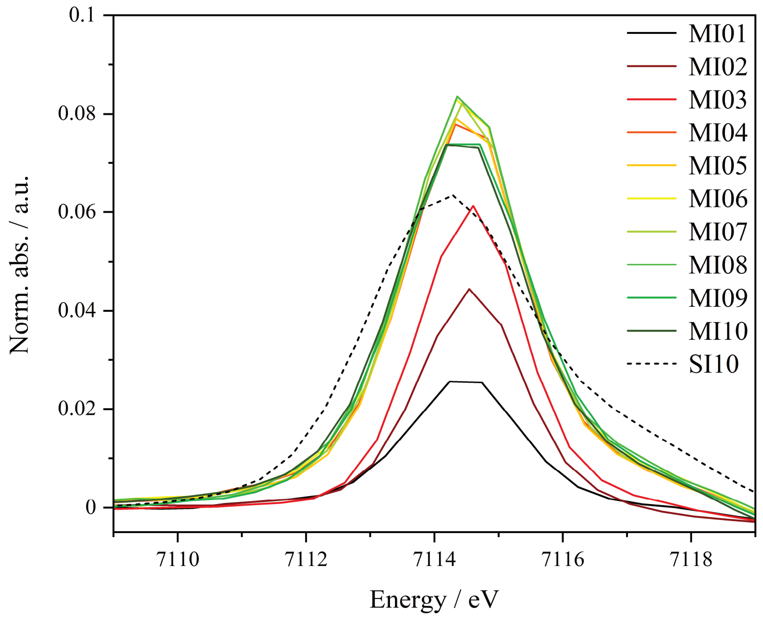

Figure 4.7: Baseline corrected pre-peaks of MI01 - MI10 and SI10 obtained from XANES spectra at the Fe K-edge.

Since the edge energy of α-Fe_2O_3 is much lower than that of γ-Fe_2O_3, this shift could potentially be correlated to an increased amount of α-Fe_2O_3 with increasing iron loading of the catalysts. The edge position of the reference sample SI10 is shifted to an even lower energy, thus showing that the single-step impregnation led to a higher amount of α-Fe_2O_3 compared to the MI catalysts.

A more detailed view of the coordination geometry of iron and its neighboring atoms can be achieved by EXAFS analysis, for which the spectra are processed as described before. The results are shown in Table 4.2. In contrast to catalysts Fe01 to Fe20, for which two oxygen shells were fitted, here three groups of oxygen backscatterers were fitted in close proximity to the observed iron center, as this led to the most adequate results. Since a high amount of maghemite was expected, the first Fe-O distance was fitted at approx. 1.8 Å. The second shell was fitted above 1.9 Å and the third above 2 Å to describe the possible hematite phase and the Fe-O contributions of maghemite at higher distances, according to its crystal structure. From MI01 to MI05 an increase in the first coordination sphere can be seen, which would also match the increase in pre-peak intensities, as this first coordination is characteristic of Fe-O tetrahedrons. This coordination number stays roughly at the same level with increasing iron loading, except for MI08, which hast the highest number with 1.9 oxygen backscatterers. The second coordination number does not show a clear trend, but a shift in the Fe-O distance from 1.92 Å for MI01 to 1.99 Å for MI08 and MI09 and 1.97 Å for MI10, which could also indicate a higher amount of α-Fe_2O_3 with a higher averaged Fe-O distance or more iron present in bulk phase, which would mean more iron in octahedral oxygen coordination. For the third oxygen shell no trend can be deduced, since both maghemite and hematite contain oxygen backscatterers at Fe-O distances of approx. 2.1 Å. According to Fe01 to Fe20, two Fe-Fe shells at 3 and 3.4 Å were fitted, together with a Fe-Al shell in between. While the numbers and distances do not follow any clear trend, the ratio of iron to aluminum backscatterers shows a rather drastic increase from MI06 to MI07. The ratio lies between 0.57 and 0.71 for MI01to MI06 with a slight decrease with increasing iron loading, then increases up to 0.80 for MI07 and even further at MI08 to MI10. This can be attributed to a drastic increase of oligomers from MI06 to MI07, which is in good agreement to the results obtained from peak deconvolution of the DRUV spectra. Compared to MI10 the reference sample SI10 shows increased Fe-O distances in the second and third shell, which is most likely due to more bulk iron oxide, in which mostly an octahedral coordination geometry with higher distances is present. Also, the ratio of iron to aluminum backscatterers increases to 1.05 what can be assigned to a high amount of oligomers or small particles present. While the first two shells of the as-prepared catalysts can be compared to the two oxygen shells of maghemite, the third oxygen coordination of the samples seems to resemble the second Fe-O coordination of the hematite phase at higher distances, also being a good indicator for this iron oxide phase, especially with increasing iron loading of the catalysts.

Table 4.2: Structural parameters obtained by EXAFS analysis of the catalysts MI01 - MI10, SI10 and the α- and γ-Fe_2O_3 reference; Abs = absorbing atom; Bs = backscattering atom; n(Bs) = number of backscattering atoms; r(Abs-Bs) = distance of absorbing to backscattering atom; σ = Debye-Waller-like factor; R = fit index; E_f = Fermi energy; Afac = amplitude reducing factor.

Catalyst	Abs-Bs	n(Bs)	r(Abs-Bs) [Å]	σ [Å^{-1}]	
MI01	Fe–O	0.1 ± 0.01	1.876 ± 0.018	0.032 ± 0.003	**R** = 24.94 %
	Fe–O	3.0 ± 0.15	1.923 ± 0.019	0.067 ± 0.006	**E_f** = 1.649 eV
	Fe–O	3.1 ± 0.15	2.074 ± 0.020	0.107 ± 0.010	**Afac** = 0.9477
	Fe–Fe	0.4 ± 0.04	3.016 ± 0.030	0.063 ± 0.006	**n(Fe)/n(Al)** = 0.67
	Fe–Al	5.7 ± 0.57	3.430 ± 0.034	0.112 ± 0.011	
	Fe–Fe	3.4 ± 0.34	3.447 ± 0.034	0.110 ± 0.011	
MI02	Fe–O	0.2 ± 0.01	1.807 ± 0.018	0.032 ± 0.003	**R** = 26.51 %
	Fe–O	4.4 ± 0.22	1.954 ± 0.019	0.081 ± 0.008	**E_f** = 1.160 eV
	Fe–O	2.1 ± 0.10	2.164 ± 0.021	0.110 ± 0.011	**Afac** = 0.9477
	Fe–Fe	0.3 ± 0.03	3.039 ± 0.030	0.032 ± 0.003	**n(Fe)/n(Al)** = 0.71
	Fe–Al	4.9 ± 0.49	3.441 ± 0.034	0.112 ± 0.011	
	Fe–Fe	3.3 ± 0.33	3.457 ± 0.034	0.110 ± 0.011	
MI03	Fe–O	0.5 ± 0.02	1.836 ± 0.018	0.032 ± 0.003	**R** = 22.14 %
	Fe–O	3.7 ± 0.18	1.946 ± 0.019	0.071 ± 0.007	**E_f** = 2.170 eV
	Fe–O	1.4 ± 0.07	2.134 ± 0.021	0.059 ± 0.005	**Afac** = 0.9477
	Fe–Fe	0.2 ± 0.02	3.053 ± 0.030	0.032 ± 0.003	**n(Fe)/n(Al)** = 0.67
	Fe–Al	4.6 ± 0.46	3.386 ± 0.033	0.110 ± 0.011	
	Fe–Fe	2.9 ± 0.29	3.407 ± 0.034	0.112 ± 0.011	
MI04	Fe–O	0.9 ± 0.04	1.836 ± 0.018	0.045 ± 0.004	**R** = 22.12 %
	Fe–O	2.8 ± 0.14	1.946 ± 0.019	0.032 ± 0.003	**E_f** = 1.934 eV
	Fe–O	1.7 ± 0.08	2.134 ± 0.021	0.032 ± 0.003	**Afac** = 0.9477
	Fe–Fe	0.4 ± 0.04	3.053 ± 0.030	0.112 ± 0.011	**n(Fe)/n(Al)** = 0.63
	Fe–Al	4.3 ± 0.43	3.386 ± 0.033	0.112 ± 0.011	
	Fe–Fe	2.3 ± 0.23	3.407 ± 0.034	0.102 ± 0.010	
MI05	Fe–O	1.4 ± 0.07	1.803 ± 0.018	0.032 ± 0.003	**R** = 32.88 %
	Fe–O	3.2 ± 0.16	1.959 ± 0.019	0.045 ± 0.004	**E_f** = 3.491 eV
	Fe–O	1.5 ± 0.07	2.128 ± 0.021	0.059 ± 0.005	**Afac** = 0.9477
	Fe–Fe	0.4 ± 0.03	3.075 ± 0.030	0.100 ± 0.010	**n(Fe)/n(Al)** = 0.64
	Fe–Al	4.4 ± 0.44	3.345 ± 0.034	0.112 ± 0.011	
	Fe–Fe	2.4 ± 0.24	3.373 ± 0.037	0.112 ± 0.011	
MI06	Fe–O	1.3 ± 0.06	1.758 ± 0.017	0.032 ± 0.003	**R** = 25.88 %
	Fe–O	3.8 ± 0.19	1.944 ± 0.019	0.032 ± 0.003	**E_f** = 3.917 eV
	Fe–O	1.4 ± 0.07	2.128 ± 0.021	0.032 ± 0.003	**Afac** = 0.9477
	Fe–Fe	0.3 ± 0.03	3.087 ± 0.030	0.050 ± 0.005	**n(Fe)/n(Al)** = 0.57
	Fe–Al	4.7 ± 0.47	3.318 ± 0.033	0.112 ± 0.011	
	Fe–Fe	2.4 ± 0.24	3.342 ± 0.033	0.110 ± 0.011	

Catalyst	Abs-Bs	n(Bs)	r(Abs-Bs) [Å]	σ [Å^{-1}]	
MI07	Fe–O	1.4 ± 0.07	1.800 ± 0.018	0.032 ± 0.003	**R** = 28.83 %
	Fe–O	3.5 ± 0.17	1.960 ± 0.019	0.032 ± 0.003	**E**$_f$ = 2.651 eV
	Fe–O	1.7 ± 0.08	2.153 ± 0.021	0.032 ± 0.003	**Afac** = 0.9477
	Fe–Fe	0.6 ± 0.03	2.986 ± 0.029	0.112 ± 0.011	**n(Fe)/n(Al)** = 0.80
	Fe–Al	4.4 ± 0.44	3.383 ± 0.033	0.100 ± 0.010	
	Fe–Fe	2.9 ± 0.29	3.404 ± 0.034	0.105 ± 0.010	
MI08	Fe–O	1.9 ± 0.09	1.825 ± 0.018	0.032 ± 0.003	**R** = 25.58 %
	Fe–O	3.0 ± 0.15	1.986 ± 0.019	0.032 ± 0.003	**E**$_f$ = 3.788 eV
	Fe–O	1.3 ± 0.06	2.188 ± 0.021	0.095 ± 0.009	**Afac** = 0.9477
	Fe–Fe	0.9 ± 0.09	3.093 ± 0.030	0.112 ± 0.011	**n(Fe)/n(Al)** = 0.85
	Fe–Al	5.5 ± 0.55	3.359 ± 0.033	0.112 ± 0.011	
	Fe–Fe	3.8 ± 0.38	3.377 ± 0.033	0.112 ± 0.011	
MI09	Fe–O	1.4 ± 0.07	1.841 ± 0.018	0.032 ± 0.003	**R** = 25.24 %
	Fe–O	2.5 ± 0.12	1.986 ± 0.019	0.045 ± 0.004	**E**$_f$ = 1.610 eV
	Fe–O	1.5 ± 0.07	2.146 ± 0.021	0.089 ± 0.008	**Afac** = 0.9477
	Fe–Fe	0.7 ± 0.07	3.032 ± 0.030	0.100 ± 0.010	**n(Fe)/n(Al)** = 0.86
	Fe–Al	4.2 ± 0.42	3.394 ± 0.033	0.107 ± 0.010	
	Fe–Fe	2.9 ± 0.29	3.405 ± 0.034	0.112 ± 0.011	
MI10	Fe–O	1.2 ± 0.06	1.829 ± 0.018	0.032 ± 0.003	**R** = 25.64 %
	Fe–O	3.0 ± 0.15	1.968 ± 0.019	0.050 ± 0.005	**E**$_f$ = 1.764 eV
	Fe–O	1.9 ± 0.09	2.152 ± 0.021	0.089 ± 0.008	**Afac** = 0.9477
	Fe–Fe	0.7 ± 0.07	3.014 ± 0.030	0.105 ± 0.010	**n(Fe)/n(Al)** = 0.86
	Fe–Al	3.7 ± 0.37	3.396 ± 0.033	0.112 ± 0.011	
	Fe–Fe	2.5 ± 0.25	3.416 ± 0.034	0.112 ± 0.011	
SI10	Fe–O	1.7 ± 0.08	1.855 ± 0.018	0.032 ± 0.003	**R** = 20.64 %
	Fe–O	3.0 ± 0.15	2.010 ± 0.020	0.032 ± 0.003	**E**$_f$ = 0.1510 eV
	Fe–O	1.3 ± 0.06	2.201 ± 0.022	0.032 ± 0.003	**Afac** = 0.9261
	Fe–Fe	1.7 ± 0.08	2.983 ± 0.029	0.112 ± 0.011	**n(Fe)/n(Al)** = 1.05
	Fe–Al	4.4 ± 0.44	3.389 ± 0.033	0.112 ± 0.011	
	Fe–Fe	2.9 ± 0.29	3.414 ± 0.034	0.100 ± 0.010	
α-Fe_2O_3	Fe–O	3.2 ± 0.16	1.961 ± 0.019	0.081 ± 0.008	**R** = 27.77 %
	Fe–O	3.3 ± 0.16	2.134 ± 0.021	0.110 ± 0.011	**E**$_f$ = 2.584 eV
	Fe–Fe	6.3 ± 0.31	2.983 ± 0.029	0.112 ± 0.011	**Afac** = 0.9735
	Fe–Fe	2.9 ± 0.29	3.317 ± 0.033	0.112 ± 0.011	
	Fe–Fe	1.2 ± 0.12	3.706 ± 0.037	0.063 ± 0.006	
γ-Fe_2O_3	Fe–O	0.7 ± 0.03	1.868 ± 0.018	0.032 ± 0.003	**R** = 24.68 %
	Fe–O	4.8 ± 0.14	2.003 ± 0.020	0.105 ± 0.010	**E**$_f$ = 3.112 eV
	Fe–Fe	4.4 ± 0.44	3.019 ± 0.030	0.112 ± 0.011	**Afac** = 0.8219
	Fe–Fe	2.1 ± 0.21	3.467 ± 0.034	0.087 ± 0.008	
	Fe–Fe	3.6 ± 0.36	5.128 ± 0.051	0.112 ± 0.011	

Carbon monoxide oxidation experiments of the presented catalysts were carried out, according to the procedure described in chapter 8.5, with continuous heating as well as at static temperatures to assess their catalytic activity in both scenarios. Curves of conversion for all catalysts under continuous heating are shown in Figure 4.8 and the respective temperatures of 10, 30, 50, 90 and 95 % CO conversion in Table 4.3.

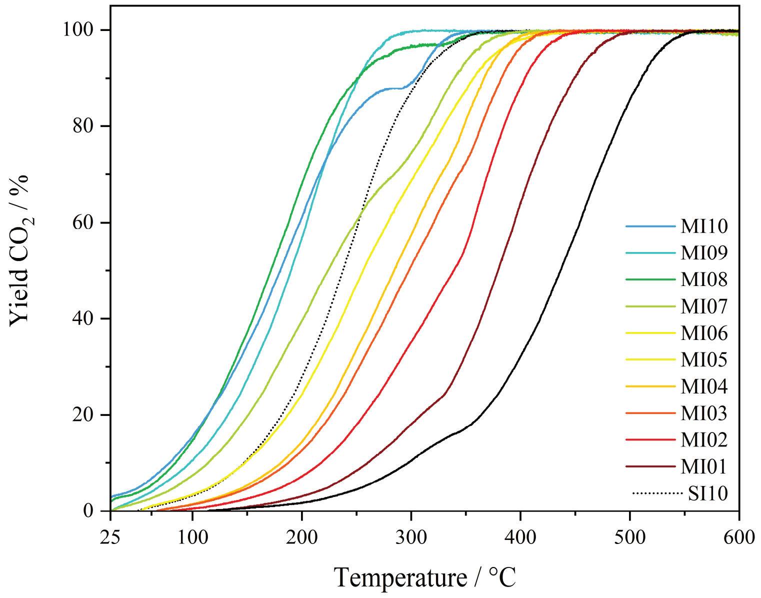

Figure 4.8: Graphs of conversion from CO oxidation experiments of MI01-MI10 and SI10 under continuous heating with 2 °C/min up to 600 °C.

With a light-off temperature of 297 °C MI01 shows the lowest activity, followed by MI02 to MI08 in ascending order, respectively decreasing T_{10}. MI08 shows a conversion of 10 % at 85 °C while the respective temperature of MI09 is slightly higher. MI10 has the lowest T_{10} of all investigated catalysts with 79 °C, while the reference catalyst SI10 needs 147 °C for the same activity. T_{30} and T_{50} follow almost the same order. Here MI08 is most active with a T_{30} of 136 °C and a T_{50} of 172 °C, respectively 140 °C and 180 °C for MI10.

Table 4.3: Respective temperatures of 10, 30, 50, 90 and 95 % CO conversion, obtained from catalytic experiments under continuous heating with 2 °C/min.

Catalyst	**T_{10} [°C]**	**T_{30} [°C]**	**T_{50} [°C]**	**T_{90} [°C]**	**T_{95} [°C]**
MI01	297	395	436	511	525
MI02	260	345	380	449	464
MI03	218	286	339	404	418
MI04	188	252	298	382	395
MI05	181	242	284	367	380
MI06	148	214	256	357	377
MI07	114	177	224	340	356
MI08	85	136	172	250	280
MI09	98	155	190	252	265
MI10	79	140	180	304	318
SI10	147	204	237	308	327

The respective temperatures are 155 °C and 190 °C for MI09 and 204 °C and 237 °C for the reference catalyst. T_{90} and T_{95} decrease from 511 °C and 525 °C for MI01 with increasing iron loading to a minimum T_{90} of 250 °C for MI08 and a minimum T_{95} for MI09 at 265 °C. MI10 has a significant incline drop in its curve of conversion, with a T_{90} of 304 °C and a T_{95} of 318 °C, while they are 308 °C, respectively 327 °C for SI10. To conclude, the activity of the catalysts increases with increasing iron loading up to 8 wt% of iron. At low temperatures, MI10 is most active. Above 100 °C up to 250 °C the activity of MI08 and above that MI09 is superior to the rest of the samples.

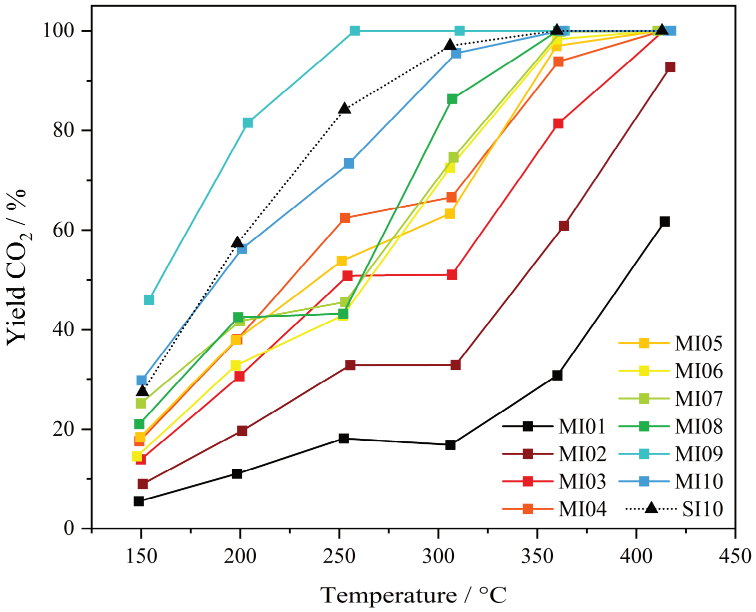

Figure 4.9: CO_2 yields of MI01 to MI10 and SI10 obtained from CO oxidation experiments at static temperatures.

In the experiments at static temperatures MI01 also shows the lowest catalytic activity with conversion below 20 % for temperatures up to 300 °C and even a slight drop from 250 to 300 °C. Activity increases to MI04, all of them featuring a stagnation in activity in the same temperature range as MI01. MI05 shows the same conversion as MI04 at 150 and 200 °C, lower activity at 250 and 300 °C but better conversion at 350 °C. MI06 is slightly better than MI05 untill full conversion at 400 °C but features a lower activity than MI04 at 250 °C. CO_2 yields of MI07 and MI08 roughly lie in the same area but with a stagnation from 200 to 250 °C so that their activity at 250 °C is even below that of MI03. MI10 and SI10 feature a higher activity at all investigated temperatures with SI10 being slightly better at 250 °C. MI09 shows a much higher catalytic activity than the rest of the samples, with full conversion at 250 °C. A CO_2 yield of 100 % is only achieved by MI06 to MI10 and SI10 above 350 °C and above 400 °C by MI03 to MI05, while MI01 and MI02 do not reach the point of full conversion in these experiments.

Again, the obtained numbers of conversion at distinct temperatures can be transformed into turnover frequencies, which, in this case without knowledge of the exact amount of active sites, display the averaged number of conversions per iron atom of the as-prepared catalyst.

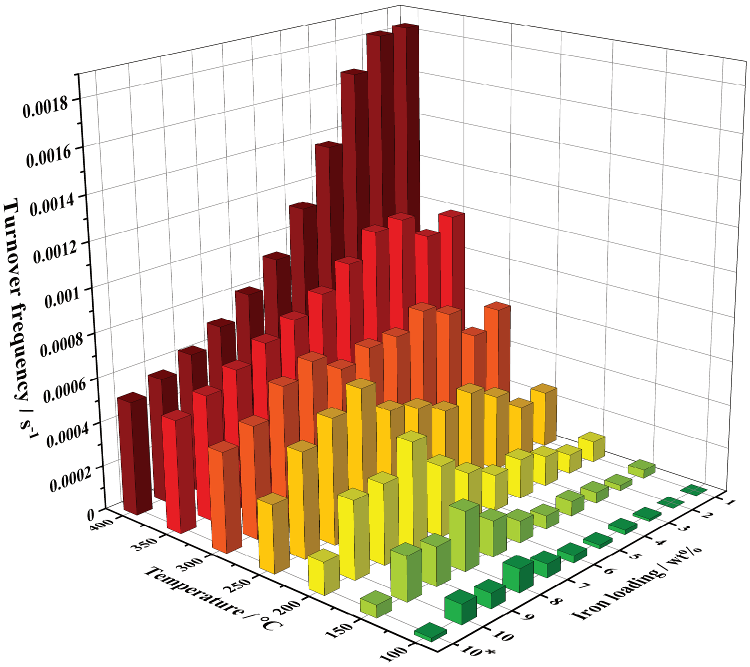

*Figure 4.10: Turnover frequencies of MI01 to MI10 and SI10 (marked with *) calculated from CO oxidation experiments under continuous heating with 2 °C/min.*

At low temperatures up to 250 °C the TOFs obtained by catalytic experiments under continuous heating can be divided into two regions. Catalysts with lower iron loadings, respectively MI01 to MI06, are rather inactive and show very low turnover frequencies with a maximum at MI04 and increasing TOFs with increasing temperature. MI07 to MI10 have higher turnover frequencies at these temperatures with the maximum TOFs at MI08. They also increase with increasing temperature up to 300 °C. The reference catalyst here is approx. at the same level as MI04. At more elevated temperatures, however, catalysts with less iron display superior activity in terms of turnover frequencies. While at 300 °C the two regions can still be seen with the maxima of MI04 and MI08, TOFs of both regions are now similar and above that the numbers increase with decreasing iron loading. The maximum TOF at 350 °C is reached at MI03, with a slight drop for MI02 and MI01, and at 400 °C MI01 shows the highest rate of conversion. Here the TOF obtained from MI01 is more than three times higher than that of MI09 and MI10. The TOFs of SI10 follow the same trend as the catalysts with higher iron loading, an increase with increasing temperatures up to 300 °C and then they stagnate because they reach the point of total conversion.

The trends in the turnover frequencies from static measurements are different. At all temperatures an increase can be seen with decreasing iron loading. MI08 and MI09 here are exceptional, while the TOFs of MI08 are lower than expected from the ascending order at low temperatures, MI09 shows numbers similar to MI01 at 150 and 200 °C and shows still a local maximum at 250 and 300 °C. At 350 °C the trend is clearest but mostly due to the fact that except MI01 and MI02, all of the catalysts reached full conversion.

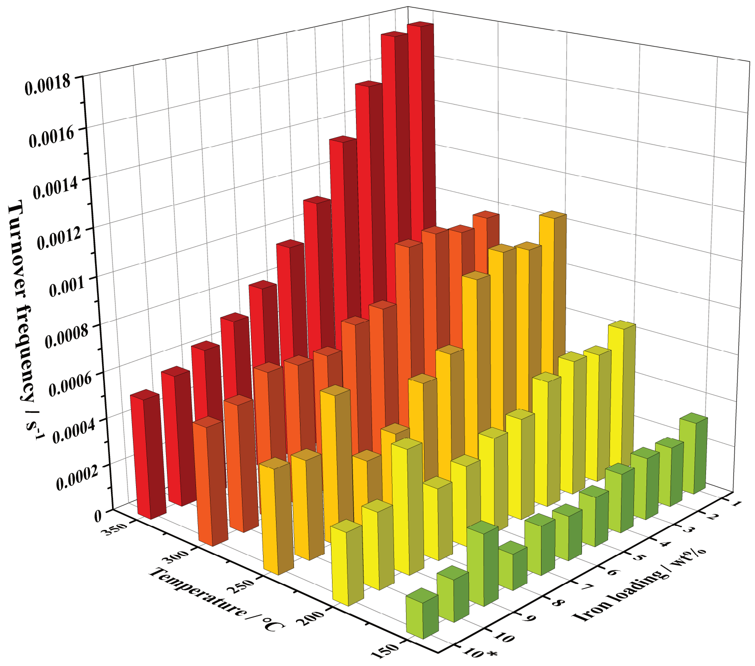

*Figure 4.11: TOFs of SI10 (marked with *) and MI01 - MI10, obtained from CO oxidation experiments at static temperatures of 150, 200, 250, 300 and 350 °C.*

4.2 Summary and Discussion

Based on the working hypothesis derived from Fe01 to Fe20, a new facile technique for the preparation of iron oxide catalysts with outstanding properties was introduced and tested. The scope of catalysts was prepared by a multi-step impregnation-calcination procedure with iron loadings from 1 to 10 wt% in steps of 1 wt%. They were characterized with multiple spectroscopic methods such as powder X-ray diffractometry, diffuse reflectance UV/Vis spectroscopy or X-ray absorption spectroscopy.

In this case, powder X-ray diffractometry only showed reflexes of the γ-Al_2O_3 support without any additional signals of iron oxide, which means that the latter forms either amorphous structures non-visible by diffractometry or that the present iron oxide crystallites are rather small and below the detection limit of the used diffractometer. Like for the previous catalysts Fe01 to Fe20, 2θ values of the γ-Al_2O_3 reflexes decrease with increasing iron loading, indicating that iron is somehow incorporated into the support lattice or interferes with it in a way, that the plane distances of the support material increase. Peak deconvolution of the DRUV spectra shows a decrease of the percentages of isolated iron oxide species with tetrahedral coordination geometry throughout the scope of catalysts with increasing iron loading, but an increase of octahedrally coordinated iron species from MI01 to MI06. From MI06 to MI07 a drop in octahedrally coordinated isolated iron species occurs, accompanied with a drastic increase in small oligomers. The percentage of octahedrons then increases again with increasing iron loading, while the percentual amount of oligomers decreases. From MI08 to MI10 an additional contribution above 500 nm indicates an increasing number of particles. In comparison, SI10 has a slightly lower amount of isolated tetrahedrally coordinated iron species than MI10 but a much lower percentage of octahedrons and at the same time a much higher amount of oligomers and especially particulates. The trends of the total amounts of the respective species are even clearer. The total number of isolated tetrahedral as well as octahedral iron species and those in form of small oligomers increase with increasing iron loading from MI01 to MI06. For MI01 to MI03 most iron seems to be present in tetrahedral coordination, then octahedral and then oligomers. For MI04 to MI06 octahedrally coordinated iron species are the majority while the increase in tetrahedrons recedes. Alike the percentual amounts, there is a drastic increase in the total number of oligomers from MI06 to MI07 and consequently a drop of octahedrally coordinated iron species. The latter then increase again up to MI10 with the number of oligomers almost staying at the same level. The total amount of particles increases from MI08 to MI10 but stays below 0.5 % of the total catalyst mass in contrast to SI10, whose total number of particles makes over 2 % of the catalyst. Also, the amount of oligomers is roughly 1 % higher than for MI10 but with a much lower content of isolated octahedrally coordinated iron species. To summarize the data obtained by DRUVS, the maximum total number of isolated tetrahedrally coordinated iron oxide centers is reached at MI08, a local maximum for isolated octahedrons at MI10 and the global maximum at MI06 while MI10 also has the highest number of oligomers and particulates, hence bulk iron oxide, if SI10 is not taken into consideration. Comparison of the DRUV spectra of the MI samples with the respective catalysts from Fe01 to Fe10 shows that through multi-step impregnation-calcination procedure a scope of iron oxide catalysts can be prepared with considerably less contributions of small oligomers and especially particles. XANES analysis of MI01 to MI10 ascertains that all iron species are present in the oxidation state +III with minor variations in shape and energy of the pre-peak or the absorption edge. A small increase in pre-peak intensity from MI01 to MI04 can be seen, which is not in accordance with the decreasing percentual amounts of non-centrosymmetric tetrahedrally coordinated iron species. However, the oligomers and particles of γ-Fe_2O_3 do also contain tetrahedrons and their octahedrons can be distorted, which would also result in an increase of pre-peak intensity. A slight shift in the edge positions to lower energies could be observed with increasing iron loading, which could indicate an increasing ratio of α-Fe_2O_3 to γ-Fe_2O_3. EXAFS analysis showed an increase of small distance oxygen backscatterers, which can be translated into an increase of tetrahedral oxygen coordination of the observed iron centers for MI01 to MI05. This number stays roughly at the same level from MI05 to MI10, except for an increase at MI08 which also matches the highest pre-peak intensity of MI08. A shift in the Fe-O distance of the second coordination sphere shows an increase in octahedrons or oligomeric iron oxide species, which matches the increasing amounts of bulk iron oxide in form of oligomers and particles from DRUVS analysis. In addition, a drastic increase in the ratio of iron to aluminum backscatterers can be seen from MI06 to MI07 which also ascertains the steep increase of oligomeric iron oxide species obtained from peak deconvolution of the DRUV spectra. The reference catalyst showed enhanced Fe-O distances as well as a further increase of the Fe-Al ratio, which is due to a higher amount of α-Fe_2O_3 in bulk phase, respectively oligomers and particles. Catalytic tests of the presented samples can be correlated to their structural properties in terms of their amount of isolated tetrahedrally coordinated iron oxide species, of which MI08 contains the most. The CO oxidation experiments with continuous heating followed this trend. The catalysts show increasing activity, respectively decreasing values of T_{10}, T_{30}, T_{50}, T_{90} and T_{95} with only few exceptions. Over a wide temperature range, MI08 is the most active catalyst of the tested. At low temperatures MI10 is slightly more active, at higher temperatures MI09, which both have only minor deficits in tetrahedrally coordinated isolated iron species but a higher number of isolated octahedral ones. The reference catalyst SI10, whose overall amounts of isolated species are similar to MI07 but with additional oligomers and particles, lies between MI06 and MI07 from low to medium temperatures but is more active than MI07 at high temperatures because it features no recede in activity as MI07 does. The turnover frequencies show similar results that, at lower temperatures from 100 to 250 °C, can also be correlated to the amount of isolated tetrahedral iron species with an increase from MI01 to MI08. TOFs then decrease to MI10 because of the stagnation in the amount of tetrahedrons but a further increase in less or non-active oligomers and particles. The TOFs of SI10 are similar to MI05 up to 250 °C. From 300 °C on catalysts with low iron loadings show further increasing TOFs while MI08 to MI10 already reached the point of total conversion and hence their maximum turnover frequency. The catalytic experiments at static temperatures show different trends. While there is also an increase in activity from MI01 to MI04 the catalysts MI04 to MI08 all display a roughly equal activity. MI10 shows higher numbers of conversion while the activity of the reference catalyst is even higher from 200 to 300 °C. In these experiments MI09 clearly is superior with full conversion at 250 °C and over 80 % CO_2 yield at 200 °C. The turnover frequencies calculated from these measurements show roughly a decrease with increasing iron loading up to MI08 at lower temperatures up to 250 °C, a drastic increase to MI09 and then MI10 and SI10 at approx. the same level as MI08. At 300 °C MI01, MI03 and MI04 have the highest TOFs and again, at 350 °C, MI01 has the highest TOF slightly higher than MI02, since all other samples have reached their points of total conversion.

To conclude, the amount of isolated tetrahedrally coordinated iron oxide is highest for MI08, which also showed the highest catalytic activity over the largest temperature range of the CO oxidation experiments with continuous heating. However, in static measurements MI09 displays a superior activity that cannot be explained by the herein presented results. Therefore, additional information is required, hence Mößbauer spectroscopy as well as STEM-EDX mapping should be conducted to investigate these systems even further. Also, the rather high activity of SI10, respectively the low activities of MI01 to MI10 cannot be explained. Since tetrahedrally coordinated and isolated iron oxide species are known to be more active than oligomers and particles with iron in bulk phase, the herein presented catalysts should be superior to Fe01 - Fe20 since their structural parameters display all the required properties for a highly active CO oxidation catalyst.

Nevertheless, a facile preparation technique was presented which leads to catalysts with outstanding structural properties. With the multi-step impregnation-calcination procedure catalysts with very fine dispersion of a high amount of isolated iron oxide species could be prepared, especially in tetrahedral coordination geometry. The successive impregnation of iron precursor onto the γ-Al_2O_3 support in 1 wt% steps followed by calcination steps seems to hinder agglomeration, hence much less oligomers and particulates were detected, compared to Fe01 to Fe10. From MI01 to MI07 no particles are formed and until MI06 even the number of small oligomers is low compared to the isolated iron oxide species. Although the presented catalysts did not display outstanding catalytic activity, the multi-step impregnation-calcination technique enables the preparation of new heterogeneous catalysts with finely dispersed isolated active sites, potentially also with other 3d metals, that could lead to the replacement of noble metal catalysts, may it be in CO oxidation for the automotive industry or in other heterogeneously catalyzed reactions.

5 BI- AND TRIMETALLIC 3D-METAL CATALYSTS FOR CO OXIDATION

Catalytic activity of iron oxide catalysts for CO oxidation is still not on a level to keep up with state-of-the-art noble metal catalysts. Although the investigation of such systems continues with an enormous effort, other possible solutions should not be left out. As mentioned before, other 3d metals such as manganese, cobalt, nickel and copper show very promising CO oxidation properties, but with drawbacks such as bad stability against catalyst poisoning. By addition of highly active cobalt oxide to the previously presented iron oxide catalysts, their minor activity at low temperatures should be elevated and through addition of manganese oxide, long term stability, especially against water, should be achieved, latter being an enormous problem for iron oxide catalysts.

5.1 Results

Herein a scope of bi- and trimetallic catalysts containing iron, cobalt and manganese immobilized on γ-Al_2O_3 are presented. Their structural properties are investigated by various analytic methods such as N_2 physisorption, PXRD, DRUVS and XAS. Since the focus should remain on iron oxide, the Fe content is held constant while the weight loadings of manganese are decreased from 6 to 0 wt%, respectively increased for cobalt in the same steps (Table 5.1). This way two bimetallic and three trimetallic 3d metal catalysts were prepared via multi-step impregnation-calcination procedure.

Table 5.1: Composition of the multi metal (MM) catalysts containing iron, manganese and cobalt; average pore diameter d_{pore}; total pore volume V_{pores}; BET surface area.

Catalyst	**Fe [wt%]**	**Mn [wt%]**	**Co [wt%]**	**d_{pore} [nm]**	**V_{pores} [cc/g]**	**Surface [m^2/g]**
MM01	6	6	0	10.1	0.37	106
MM02	6	4	2	10.1	0.39	109
MM03	6	3	3	10.3	0.38	107
MM04	6	2	4	10.2	0.39	111
MM05	6	0	6	10.1	0.38	106
Support	0	0	0	11.3	0.49	132

To gain basic knowledge about structural parameters of the presented catalysts, nitrogen physisorption was conducted. The average pore diameter obtained via BJH method is 11.3 nm for the pure support and between 10.1 and 10.3 nm for MM01 to MM05. These values, together with a decrease of the total pore volume of 0.1 cc/g from support to the as-prepared catalysts indicates, that the metal oxides are not only immobilized on the support surface, but also in the pores. The surface area obtained by BET method is 132 m^2/g for the pure support and decreases to 106 to 111 m^2/g for the catalysts, showing that the surface area stays relatively high although a total of 12 wt% of mixed metal oxides was immobilized on the surface of the support material for each catalyst.

Powder X-ray diffractograms of MM01 to MM05 only show reflexes that can be assigned to the γ-Al_2O_3 support. No additional signals of the 3d metal oxides can be seen, either because they form amorphous structures that cannot be detected by X-ray diffractometry, or because their crystallite sizes are below the detection limit of the used diffractometer. However, a small shift in the alumina reflexes can be seen. This shift is quantified for the (440) crystal plane, because its signal at 66.7 ° is the most intense, hence leading to the lowest error. The intensity of the residual reflexes is too low to ascertain that no additional signals of the 3d metal oxides are beneath them and cause unwanted shifts of the alumina reflexes.

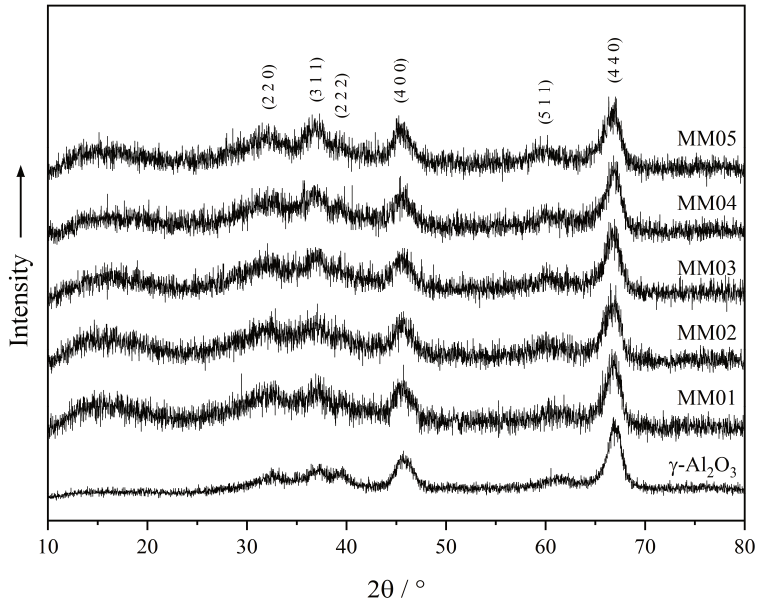

Figure 5.1: PXRD of MM01 to MM05 and the respective support material.

The reflex of the (440) lattice plane shifts from a 2θ value of 66.93 ° for the pure support material to lower values between 66.61 and 66.76 ° for MM01 to MM05 (Table 5.2). The resulting lattice parameter *a* is 0.79 nm for the support and increases through addition of the iron, cobalt and manganese oxides.

Table 5.2: 2θ values of the (440) crystal plane and the resulting plane distances d and lattice parametes a obtained for pure γ-Al_2O_3 and MM01 - MM05.

Catalyst	**$2\theta_{440}$ [°]**	**d_{440} [nm]**	***a* [nm]**
MM01	66.74	0.1400	0.792
MM02	66.65	0.1402	0.793
MM03	66.70	0.1401	0.793
MM04	66.76	0.1400	0.792
MM05	66.61	0.1403	0.794
Support	66.93	0.1397	0.790

The lattice parameter is 0.792 nm for MM01 and MM04, 0.793 nm for MM02 and MM03 and 0.794 nm for MM05. The increase in *a* is a strong indicator of interaction of the active sites with the support lattice or even incorporation of the 3d metals into it. This interaction or incorporation is lowest for MM01, which only contains iron and manganese and MM04, and highest for MM05 which only contains iron and cobalt, but without any visible trend. For further structural investigation of MM01 to MM05 DRUV spectroscopy is carried out since it is a potent tool for qualitative and quantitative analysis of the present metal species. However, due to the presence of multiple 3d metals with absorption bands in the same energy range, no peak deconvolution can be carried out in a reliable manner.

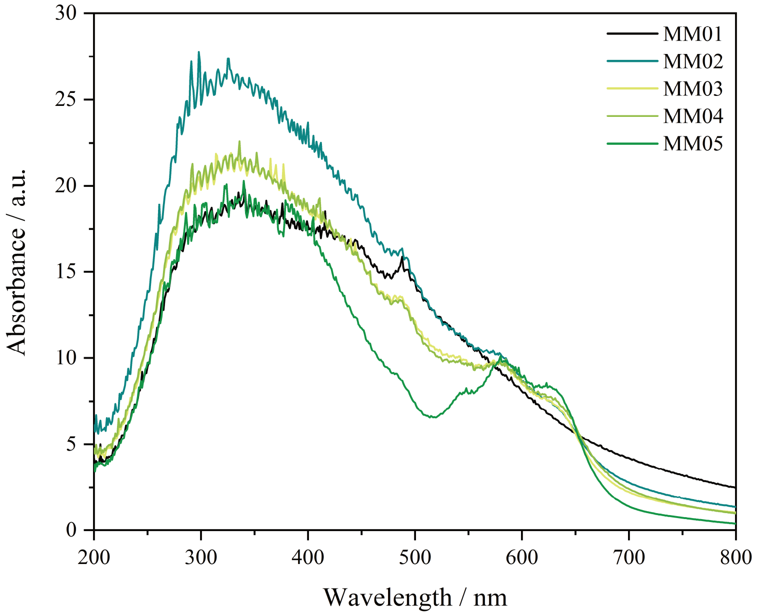

Figure 5.2: DRUV spectra of MM01 to MM05.

All catalysts show a broad band with high intensity and a maximum between 300 and 400 nm and additional contributions at higher wavelengths. The main feature of MM01 is very broadened and a second large band can be seen above 400 nm. As for all of the catalysts, a narrow feature between 480 and 500 nm can be observed, hence it is assigned to the iron species indicating some form of oligomers. To higher wavelengths the spectrum decreases in absorbance. The spectrum of MM02 shows increased absorbance with two distinct shoulders at 575 and 625 nm respectively. Interestingly, MM03 and MM04 show almost the identical spectrum, with an additional shoulder at 540 nm which, as the bands at 575 and 625 nm, is much more distinct at MM05. Hence, these three shoulders are attributed to the cobalt species, since they are not present for MM01 and most distinct for MM05 which has the highest amount of Co.

To probe the oxidation state of the active sites and gain information about their coordination geometry, hence their actual phase, X-ray absorption spectroscopy at the respective K-edges is carried out. The XANES spectra of MM01 to MM04 at the manganese K-edge are shown in Figure 5.3 compared to a $LiMn_2O_4$ reference, in which Mn is present in the oxidation states +III and +IV. The pre-peak is fitted by two Gaussian functions after subtraction of a Lorentzian-type function as a background. The centers of both functions are at 6541 and 6543 eV for MM01 to MM04, while the energies are 6540 and 6542 eV for the $Mn^{+III/+IV}$ reference (Table 5.3).

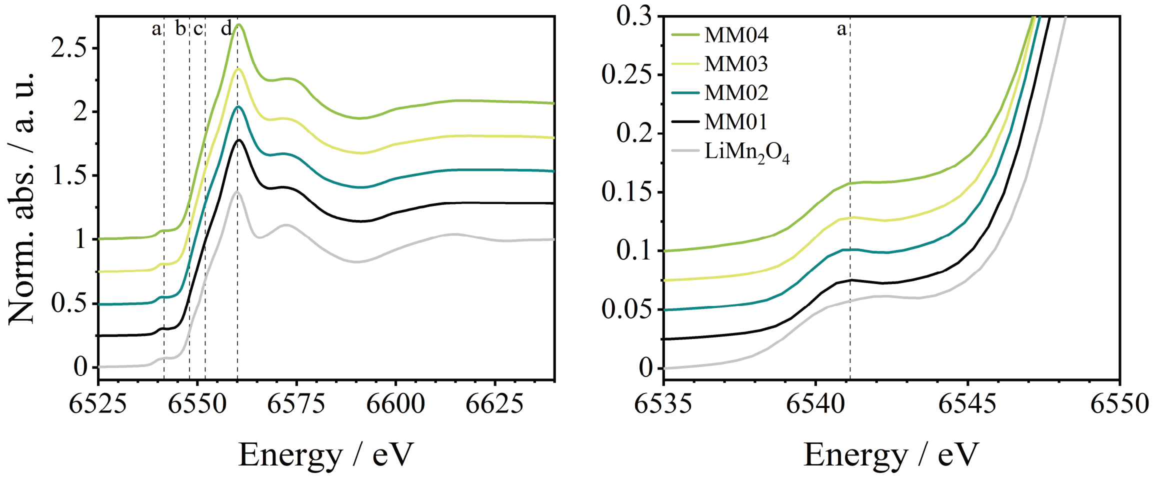

Figure 5.3: XANES spectra of MM01 to MM04 at the Mn K-edge and of $LiMn_2O_4$ as a reference (left) and zoomed pre-peak region (right); pre-peak (a), first maximum of the edge (b), E_0 by halved whiteline intensity (c) and maximum of the whiteline (d) are highlighted with dotted lines.

Depending on how E_0 is defined, either by the first maximum in the derivative of the jump (second maximum if the pre-peak is included), or as center of the jump, E_0 of MM01 to MM04 is between 6547.9 and 6549.1 eV, respectively 6551.8 and 6552.3 eV. E_0 of $LiMn_2O_4$ is 6548.8 or 6549.0 eV. Thus, it is proposed that the manganese species in MM01 to MM04 are present in the same oxidation state as in $LiMn_2O_4$ or even solely in +IV as in MnO_2. Interestingly, the shape of the spectra resembles the spectrum of the $LiMn_2O_4$ reference, hence Mn could also be present in a spinel structure analogous to the reference sample.

Table 5.3: Mn K-edge pre-peak positions of MM01 to MM04 and $LiMn_2O_4$ as a reference, obtained by fit of two Gaussian functions a and b; E_0 of MM01 to MM04 and the reference obtained from the first maximum of the absorption edge (*) and at half maximum of the whiteline (**).

Catalyst	Pre-peak a [eV]	Pre-peak b [eV]	E_0^* [eV]	E_0^{**} [eV]
MM01	6540.94	6543.28	6547.88	6552.23
MM02	6540.84	6543.17	6548.48	6551.84
MM03	6540.95	6543.26	6548.82	6551.92
MM04	6541.09	6543.31	6549.14	6552.28
$LiMn_2O_4$	6540.06	6542.09	6548.82	6549.02

The XANES spectra at the Fe K-edge of the five catalysts as well as α- and γ-Fe_2O_3 as references are shown in Figure 5.4. The pre-peak positions, again obtained by subtraction of a Lorentzian-type function as background and fit of two Gaussian-type functions, lie at approx. 7114.3 and 7117.3 eV for MM01 to MM05 (Table 5.4). For hematite and maghemite the pre-peak energies are 7114.6 and 7117.5 eV, respectively 7114.3 and 7117.1 eV. E_0 of the investigated catalysts is approx. 7123 eV or 7126 eV with only minor differences, again depending on the method used to obtain E_0. They are 7123.4 eV and 7122.6 eV for α- and γ-Fe_2O_3, respectively 7125.5 eV and 7125.9 eV. This, in addition to the shape, indicates that the present iron oxide species are a mixture of maghemite and hematite, and thus, in the oxidation state +III.

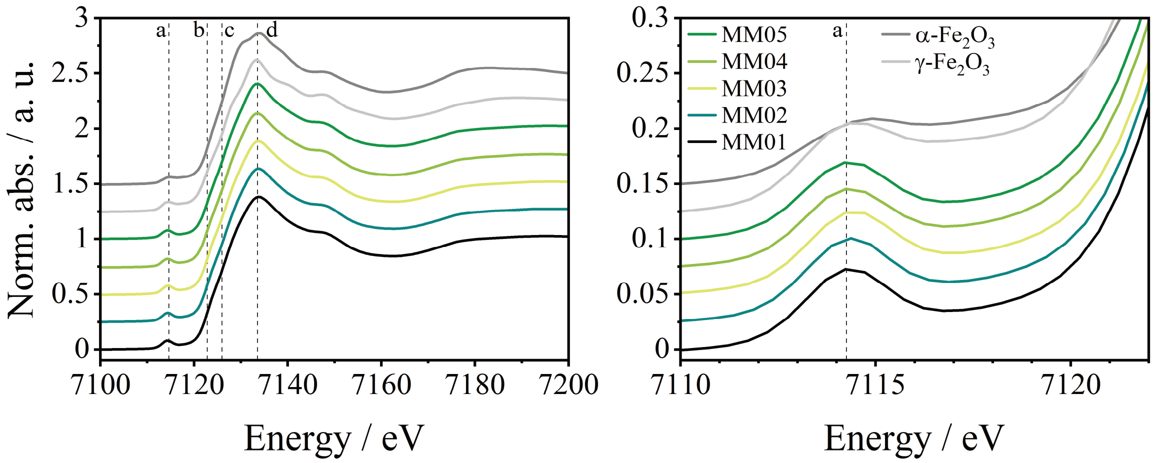

Figure 5.4: XANES spectra of MM01 to MM05 at the Fe K-edge and of α-Fe_2O_3 and γ-Fe_2O_3 as references (left) and zoomed pre-peak region (right); pre-peak (a), first maximum of the edge (b), E_0 by halved whiteline intensity (c) and maximum of the whiteline (d) are highlighted with dotted lines.

Table 5.4: Fe K-edge pre-peak positions of MM01 to MM05 and α- and γ-Fe_2O_3 as references, obtained by fit of two Gaussian functions a and b; E_0 of MM01 to MM05 and the references obtained from the first maximum of the absorption edge (*) and at half maximum of the whiteline (**).

Catalyst	**Pre-peak a [eV]**	**Pre-peak b [eV]**	**E_0^*[eV]**	**E_0^{**} [eV]**
MM01	7114.29	7117.25	7123.00	7125.80
MM02	7114.31	7117.26	7122.91	7125.88
MM03	7114.40	7117.41	7122.95	7125.96
MM04	7114.28	7117.23	7122.91	7125.93
MM05	7114.27	7117.23	7122.85	7126.01
α-Fe_2O_3	7114.60	7117.47	7123.37	7125.11
γ-Fe_2O_3	7114.34	7117.11	7122.59	7125.86

At the Co K-edge the catalysts do not show any differences (Figure 5.5). The shape of the spectra, as well as the pre-peak and edge positions are almost identical (Table 5.5). Their pre-peak energy is approx. 7709 eV and their E_0 obtained from the first maximum of the jump lies at 7717 eV. Only E_0 from half maximum of the whiteline differs slightly, from 7718.15 eV for MM02 to 7718.79 eV for MM05. Nevertheless, these are only minor differences that can be neglected. In comparison, E_0 of $CoBr_2$ is 7714.2 eV, respectively 7718.5 eV, indicating that in MM02 to MM05 Co is present in the oxidation state +II and/or +III.

Table 5.5: Co K-edge pre-peak positions of MM01 to MM04 and $CoBr_2$ as a reference, obtained by fit of a Gaussian function; E_0 of MM02 to MM05 and the reference obtained from the first maximum of the absorption edge (*) and at half maximum of the whiteline (**).

Catalyst	**Pre-peak a [eV]**	**E_0^*[eV]**	**E_0^{**} [eV]**
MM02	7709.06	7717.15	7718.15
MM03	7709.00	7717.08	7718.16
MM04	7708.96	7717.06	7718.43
MM05	7709.08	7717.17	7718.70
$CoBr_2$	7708.29	7714.03	7718.50

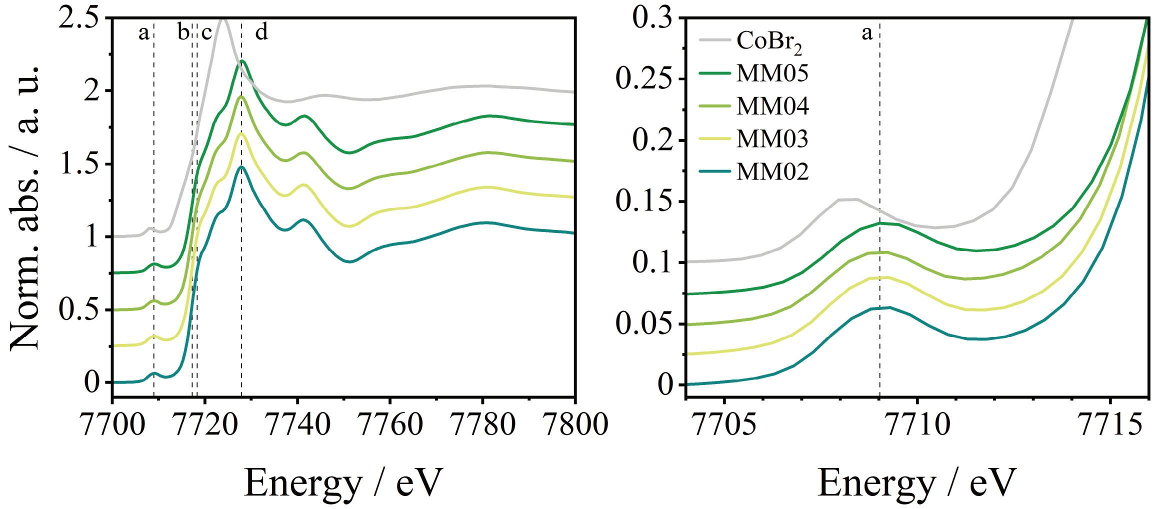

Figure 5.5: XANES spectra of MM02 to MM05 at the Co K-edge and of CoBr$_2$ as a reference (left) and zoomed pre-peak region (right); pre-peak (a), first maximum of the edge (b), E$_0$ by halved whiteline intensity (c) and maximum of the whiteline (d) are highlighted with dotted lines.

Analysis of the extended X-ray absorption fine structure of the manganese K-edge spectra is carried out under the conjecture of Mn being present in an oxidation state of +III or higher, as deduced from XANES analysis and comparison to a LiMn$_2$O$_4$ reference. All of the investigated samples show a Mn-O shell at small distances around 1.9 Å and Mn backscatterers at 2.85 Å (Table 5.6).

Table 5.6: Structural parameters obtained by EXAFS analysis of the catalysts MM01 – MM04 at the Mn K-edge; Abs = absorbing atom; Bs = backscattering atom; n(Bs) = number of backscattering atoms; r(Abs-Bs) = distance of absorbing to backscattering atom; σ = Debye-Waller-like factor; R = fit index; E$_f$ = Fermi energy; Afac = amplitude reducing factor.

Catalyst	**Abs-Bs**	**n(Bs)**	**r(Abs-Bs) [Å]**	**σ [Å^{-1}]**	
MM01	Mn–O	5.8 ± 0.29	1.900 ± 0.019	0.089 ± 0.008	**R** = 38.96 %
	Mn–Mn	0.4 ± 0.02	2.845 ± 0.028	0.067 ± 0.006	**E$_f$** = 10.24 eV
	Mn–Mn	7.1 ± 0.07	3.400 ± 0.034	0.112 ± 0.011	**Afac** = 0.5080
	Mn–O	16.6 ± 1.66	3.541 ± 0.035	0.095 ± 0.009	
MM02	Mn–O	5.6 ± 0.28	1.897 ± 0.018	0.092 ± 0.009	**R** = 40.13 %
	Mn–Mn	0.6 ± 0.03	2.851 ± 0.029	0.097 ± 0.009	**E$_f$** = 10.36 eV
	Mn–Mn	4.6 ± 0.46	3.390 ± 0.033	0.112 ± 0.011	**Afac** = 0.5226
	Mn–O	13.8 ± 1.38	3.529 ± 0.035	0.105 ± 0.010	
MM03	Mn–O	6.0 ± 0.30	1.897 ± 0.018	0.089 ± 0.008	**R** = 43.04 %
	Mn–Mn	0.5 ± 0.02	2.849 ± 0.028	0.097 ± 0.009	**E$_f$** = 10.63 eV
	Mn–Mn	5.1 ± 0.51	3.380 ± 0.033	0.112 ± 0.011	**Afac** = 0.4348
	Mn–O	16.7 ± 1.67	3.526 ± 0.035	0.112 ± 0.011	
MM04	Mn–O	5.3 ± 0.26	1.903 ± 0.019	0.084 ± 0.008	**R** = 38.88 %
	Mn–Mn	0.3 ± 0.01	2.843 ± 0.028	0.039 ± 0.003	**E$_f$** = 9.766 eV
	Mn–Mn	7.9 ± 0.79	3.405 ± 0.034	0.112 ± 0.011	**Afac** = 0.4474
	Mn–O	17.6 ± 1.76	3.555 ± 0.035	0.095 ± 0.009	

Especially the low distance Mn-O shell and the absence of an oxygen shell at 2 Å or higher indicates, that the present manganese oxide cannot be Mn_2O_3 or Mn_3O_4. Thus, the proposed phase of Mn in MM01 to MM04 is MnO_2 with manganese in the oxidation state +IV. Since in between the catalysts only minor changes can be seen, the same structure can be concluded for all of them.

EXAFS analysis of the spectra obtained at the iron K-edge is carried out considering α- and/or γ-Fe_2O_3 as the present species (Table 5.7). For all of the catalysts a low distance Fe-O shell below 1.9 Å can be fitted, which represents the tetrahedral oxygen coordination only present in γ-Fe_2O_3. However, besides the oxygen shell above 1.9 Å an additional third Fe-O shell is present above 2.05 Å, hence also α-Fe_2O_3 seems to be present. As for Fe01 to Fe20 as well as MI01 to MI10, two Fe-Fe shells and a Fe-Al shell are fitted, resulting in an iron-aluminum ratio of 0.47 to 0.67. This ratio increases from MM01 to MM03 and then decreases again to MM05. This ratio can be an indicator for the size of the particles, as a smaller ratio of iron to aluminum means that less iron backscatterers are present compared to aluminum backscatterers of the alumina support, hence the iron oxide species seems to contain less iron atoms as in smaller particles. Therefore it can be concluded, that the particle size of the iron oxidic species increases from MM01 to MM03 and decreases again to MM05.

Table 5.7: Structural parameters obtained by EXAFS analysis of the catalysts MM01 - MM05 and the α- and γ-Fe_2O_3 references at the Fe K-edge; Abs = absorbing atom; Bs = backscattering atom; n(Bs) = number of backscattering atoms; r(Abs-Bs) = distance of absorbing to backscattering atom; σ = Debye-Waller-like factor; R = fit index; E_f = Fermi energy; Afac = amplitude reducing factor.

Catalyst	**Abs-Bs**	**n(Bs)**	**r(Abs-Bs) [Å]**	**σ [Å^{-1}]**	
MM01	Fe–O	0.5 ± 0.02	1.878 ± 0.018	0.032 ± 0.003	**R** = 34.50 %
	Fe–O	2.9 ± 0.14	1.934 ± 0.019	0.063 ± 0.006	**E_f** = 5.575 eV
	Fe–O	1.2 ± 0.06	2.096 ± 0.020	0.059 ± 0.005	**Afac** = 0.7864
	Fe–Fe	0.3 ± 0.03	3.179 ± 0.031	0.112 ± 0.011	**n(Fe)/n(Al)** = 0.47
	Fe–Al	6.0 ± 0.60	3.304 ± 0.033	0.112 ± 0.011	
	Fe–Fe	2.5 ± 0.25	3.341 ± 0.034	0.112 ± 0.011	
MM02	Fe–O	0.6 ± 0.03	1.853 ± 0.018	0.032 ± 0.003	**R** = 36.94 %
	Fe–O	2.5 ± 0.12	1.922 ± 0.019	0.055 ± 0.005	**E_f** = 6.229 eV
	Fe–O	1.4 ± 0.07	2.064 ± 0.020	0.050 ± 0.005	**Afac** = 0.7864
	Fe–Fe	0.8 ± 0.08	3.231 ± 0.032	0.077 ± 0.007	**n(Fe)/n(Al)** = 0.59
	Fe–Al	6.4 ± 0.64	3.308 ± 0.033	0.112 ± 0.011	
	Fe–Fe	3.0 ± 0.30	3.384 ± 0.033	0.112 ± 0.011	
MM03	Fe–O	0.5 ± 0.02	1.877 ± 0.018	0.032 ± 0.003	**R** = 34.02 %
	Fe–O	1.9 ± 0.09	1.909 ± 0.019	0.039 ± 0.003	**E_f** = 5.650 eV
	Fe–O	1.5 ± 0.07	2.052 ± 0.020	0.032 ± 0.003	**Afac** = 0.7864
	Fe–Fe	0.9 ± 0.09	3.252 ± 0.032	0.087 ± 0.008	**n(Fe)/n(Al)** = 0.67
	Fe–Al	6.7 ± 0.67	3.315 ± 0.033	0.112 ± 0.011	
	Fe–Fe	2.8 ± 0.28	3.390 ± 0.033	0.110 ± 0.011	

MM04	Fe–O	0.6 ± 0.03	1.896 ± 0.018	0.032 ± 0.003	**R** = 34.16 %
	Fe–O	1.9 ± 0.09	1.906 ± 0.019	0.032 ± 0.003	**E_f** = 5.755 eV
	Fe–O	1.7 ± 0.08	2.056 ± 0.020	0.032 ± 0.003	**Afac** = 0.7864
	Fe–Fe	1.2 ± 0.12	3.246 ± 0.032	0.092 ± 0.009	**n(Fe)/n(Al)** = 0.63
	Fe–Al	7.1 ± 0.71	3.311 ± 0.033	0.112 ± 0.011	
	Fe–Fe	3.3 ± 0.33	3.389 ± 0.033	0.112 ± 0.011	
MM05	Fe–O	0.5 ± 0.02	1.862 ± 0.018	0.039 ± 0.003	**R** = 35.87 %
	Fe–O	2.9 ± 0.14	1.935 ± 0.019	0.063 ± 0.006	**E_f** = 6.329 eV
	Fe–O	1.3 ± 0.06	2.084 ± 0.021	0.050 ± 0.005	**Afac** = 0.7864
	Fe–Fe	0.4 ± 0.04	3.161 ± 0.030	0.112 ± 0.011	**n(Fe)/n(Al)** = 0.49
	Fe–Al	6.1 ± 0.61	3.302 ± 0.034	0.112 ± 0.011	
	Fe–Fe	2.6 ± 0.26	3.348 ± 0.037	0.112 ± 0.011	
α-Fe_2O_3	Fe–O	3.2 ± 0.16	1.961 ± 0.019	0.081 ± 0.008	**R** = 27.77 %
	Fe–O	3.3 ± 0.16	2.134 ± 0.021	0.110 ± 0.011	**E_f** = 2.584 eV
	Fe–Fe	6.3 ± 0.31	2.983 ± 0.029	0.112 ± 0.011	**Afac** = 0.9735
	Fe–Fe	2.9 ± 0.29	3.317 ± 0.033	0.112 ± 0.011	
	Fe–Fe	1.2 ± 0.12	3.706 ± 0.037	0.063 ± 0.006	
γ-Fe_2O_3	Fe–O	0.7 ± 0.03	1.868 ± 0.018	0.032 ± 0.003	**R** = 24.68 %
	Fe–O	4.8 ± 0.14	2.003 ± 0.020	0.105 ± 0.010	**E_f** = 3.112 eV
	Fe–Fe	4.4 ± 0.44	3.019 ± 0.030	0.112 ± 0.011	**Afac** = 0.8219
	Fe–Fe	2.1 ± 0.21	3.467 ± 0.034	0.087 ± 0.008	
	Fe–Fe	3.6 ± 0.36	5.128 ± 0.051	0.112 ± 0.011	

CoO, Co_2O_3 as well as Co_3O_4 are taken into consideration for EXAFS analysis of the cobalt species of MM02 to MM05, since an oxidation state of +II and/or +III is concluded from XANES analysis. Interestingly, the most common cobalt oxidic structure Co_3O_4 can be excluded. This structure comprises a rather high number of Co backscatterers at 2.85 Å, which cannot be found in the Fourier transformations of MM02 to MM05 (Table 5.8). CoO does only contain Co-O distances above 2.1 Å but since all of the catalysts show a significant amount of oxygen backscattering atoms between 1.90 and 1.95 Å also CoO can be ruled out. Therefore cobalt in a Co_2O_3 or $CoAlO_3$ phase is proposed for the investigated catalysts, of which the distances of all shells decrease from MM02 to MM05 and also a shift in the ratio of the oxygen backscatterers from 2.4 to 3.4 at MM02 to 3.3 to 1.7 for MM05 can be seen. This indicates that the structure changes slightly throughout the catalysts.

Table 5.8: Structural parameters obtained by EXAFS analysis of the catalysts MM02 – MM05 at the Co K-edge; Abs = absorbing atom; Bs = backscattering atom; n(Bs) = number of backscattering atoms; r(Abs-Bs) = distance of absorbing to backscattering atom; σ *= Debye-Waller-like factor; R = fit index;* E_f *= Fermi energy; Afac = amplitude reducing factor.*

Catalyst	**Abs-Bs**	**n(Bs)**	**r(Abs-Bs) [Å]**	**σ [Å^{-1}]**	
MM02	Co–O	2.4 ± 0.12	1.958 ± 0.019	0.032 ± 0.003	**R** = 31.75 %
	Co–O	3.4 ± 0.17	2.087 ± 0.020	0.112 ± 0.011	**E_f** = 0.4107 eV
	Co–Co	3.8 ± 0.38	3.075 ± 0.030	0.112 ± 0.011	**Afac** = 0.8140
	Co–Co	3.8 ± 0.38	3.523 ± 0.035	0.097 ± 0.009	
	Co–Co	2.8 ± 0.28	4.050 ± 0.040	0.112 ± 0.011	
MM03	Co–O	2.5 ± 0.12	1.902 ± 0.019	0.032 ± 0.003	**R** = 33.54 %
	Co–O	2.7 ± 0.13	2.039 ± 0.020	0.039 ± 0.003	**E_f** = 2.859 eV
	Co–Co	3.3 ± 0.33	3.062 ± 0.030	0.112 ± 0.011	**Afac** = 0.7961
	Co–Co	5.6 ± 0.56	3.496 ± 0.034	0.100 ± 0.010	
	Co–Co	2.0 ± 0.20	4.000 ± 0.040	0.095 ± 0.009	
MM04	Co–O	2.5 ± 0.12	1.909 ± 0.019	0.032 ± 0.003	**R** = 31.32 %
	Co–O	2.4 ± 0.12	2.039 ± 0.020	0.039 ± 0.003	**E_f** = 3.384 eV
	Co–Co	2.5 ± 0.25	3.027 ± 0.030	0.112 ± 0.011	**Afac** = 0.7893
	Co–Co	3.7 ± 0.37	3.483 ± 0.034	0.092 ± 0.009	
	Co–Co	2.6 ± 0.26	4.005 ± 0.040	0.105 ± 0.010	
MM05	Co–O	3.3 ± 0.16	1.898 ± 0.018	0.059 ± 0.005	**R** = 34.15 %
	Co–O	1.7 ± 0.08	2.018 ± 0.020	0.032 ± 0.003	**E_f** = 6.000 eV
	Co–Co	1.9 ± 0.09	2.994 ± 0.029	0.112 ± 0.011	**Afac** = 0.7961
	Co–Co	4.1 ± 0.41	3.459 ± 0.034	0.095 ± 0.009	
	Co–Co	3.3 ± 0.33	3.968 ± 0.039	0.112 ± 0.011	

CO oxidation experiments of MM01 to MM05 were carried out according to the procedure described for MI01 to MI10, both under continuous heating (Figure 5.6) as well as at static temperatures of 150, 200, 250 and 300 °C (Figure 5.7). In the experiments with a constant heating ramp MM01 starts with 6.5 % CO conversion below 30 °C and increases up to 27 % at 115 °C, followed by a drop in activity down to 23 % at 145 °C (Table 5.9). The temperatures of 30 % and 50 % CO conversion are 166 °C, respectively 190 °C, T_{90} is 234 °C and T_{95} 245 °C. When cobalt is added to the catalysts, full conversion at room temperature can be reached. MM02 shows a conversion of 98 % at 30 °C but drops down to a minimum of 62 % at 176 °C. After that, 90 % are reached again at 234 °C and the T_{95} is 245 °C alike MM01. MM03 and MM04 both feature total conversion of CO at 30 °C but also accompanied with a drop in activity. Conversion decreases to 92 % at a temperature of 200 °C for MM03 and to 81 % at 206 °C for MM04. T_{95} of MM03 is 249 °C, while T_{90} and T_{95} of MM04 are 232 and 243 °C. MM05 displays 99 % CO_2 yield at 30 °C but a decrease down to a minimum of 57 % at 190 °C. T_{90} and T_{95} are the highest for MM05 with 293 °C, respectively 308 °C.

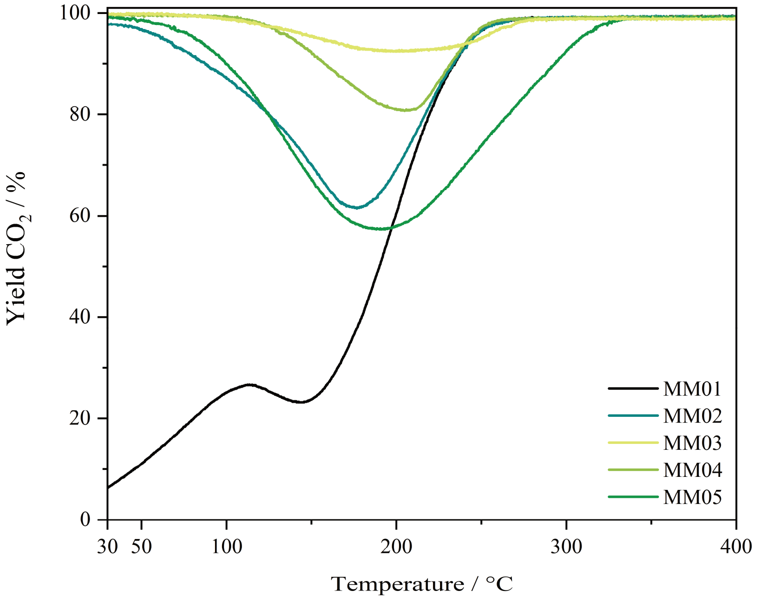

Figure 5.6: CO oxidation experiments of MM01 to MM05 under continuous heating.

As Figure 5.6 shows, MM01 is the only catalyst that does not feature CO_2 yields close to 100 % from the start at 30 °C. For all catalysts a drop in activity is detected, which decreases in intensity from MM01 to MM03 and then increases again to MM05. The latter shows the broadest activity drop in a temperature range from 50 °C up to over 300 °C. The minimum of this drop also shifts from 145 °C at MM01 to 200 and 206 °C for MM03 and MM04 and then decreases to 190 °C for MM05.

Table 5.9: Resulting values of CO oxidation experiments under continuous heating of MM01 to MM05; Y_{30} *=* CO_2 *yield at 30 °C;* Y_{min} *=* CO_2 *yield at the minimum of the activity drop;* T_{min} *= corresponding temperature of the minimum;* T_{10} *= temperature of 10 %* CO_2 *yield;* T_{30}*,* T_{50}*,* T_{90}*,* T_{95}*: temperatures of 30, 50, 90 and 95 %* CO_2 *yield.*

Catalyst	Y_{30} (CO_2) [%]	Y_{min} [%]	T_{min} [°C]	T_{10} [°C]	T_{30} [°C]	T_{50} [°C]	T_{90} [°C]	T_{95} [°C]
MM01	6.5	23	145	46	166	190	234	245
MM02	98	62	176	-	-	-	234	245
MM03	100	92	200	-	-	-	-	249
MM04	100	81	206	-	-	-	232	243
MM05	99	57	190	-	-	-	293	308

Similar trends can be observed in the measurements at static temperatures. While MM01 shows approx. 40 % CO conversion at 150 °C, CO_2 yield is over 70 % for MM02. MM03 to MM05 show 95 - 96 % CO_2. Except MM01, all catalysts display less activity at 200 °C, analogous to the drop in activity in continuous measurements. At 200 °C MM01 and MM02 both show roughly 60 % activity, MM04 70 % and then MM05 and MM03 with 88 and 90 % CO conversion. From 200 °C with increasing temperature, CO_2 yield increases for MM01 to MM04, while it decreases even more for MM05, which is also according to the broad drop of MM05 in the continuous measurements, when compared to the others.

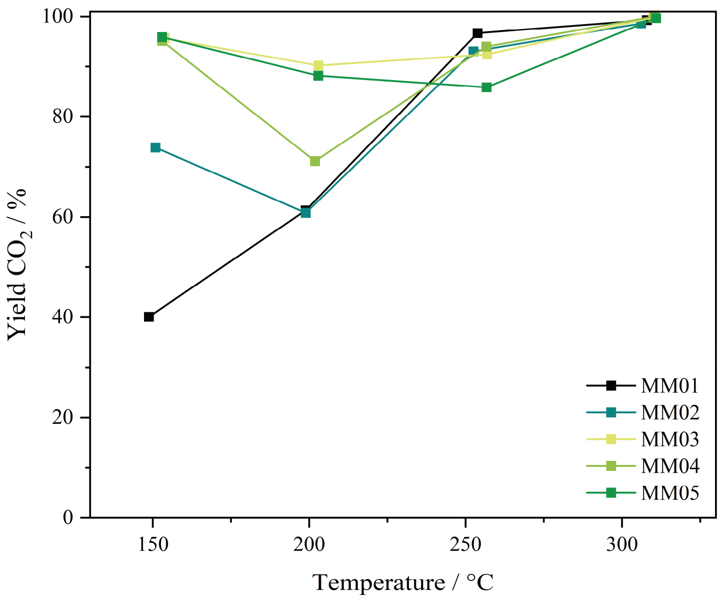

Figure 5.7: CO$_2$ yields of MM01 - MM05 obtained from CO oxidation experiments at static temperatures.

All of the catalysts feature conversion close to 100 % at 300 °C. In both continuous and static measurements MM03 is superior to the rest of the tested catalysts with a much smaller decrease in catalytic activity in the so-called drop, 100 % conversion at 30 °C and almost total conversion at 150 °C during the static measurements. Only at approx. 250 °C it shows a slightly smaller activity than MM01, MM02 and MM04.

To test the influence of manganese on the catalysts regarding their stability, long-term experiments at the static temperatures of 100 and 200 °C are carried out (Figure 5.8). Therefore MM03, the catalyst with highest activity, is investigated as well as MM05 as a reference without manganese content since the premise of the addition of manganese was to enhance the catalysts stability.

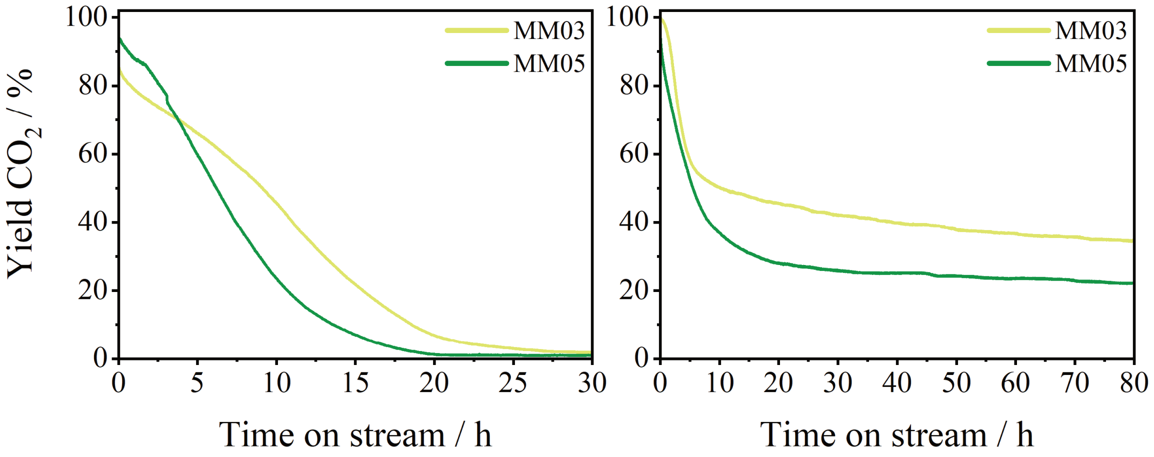

Figure 5.8: Long-term stability experiments of MM03 and MM05 at 100 °C (left) and 200 °C (right).

At 100 °C MM03 starts with approx. 85 % yield while MM05 shows even higher CO conversion. The activity of MM05 drops relatively fast, with a conversion below 20 % after 10 hours and close to zero activity after 20 h. The catalyst containing 3 wt% Mn shows a less steep decrease for the first 10 hours. Its activity falls below 20 % after 15 hours on stream and drops to zero after 30 h. At 200 °C the initial conversion of MM05 is 95 % while MM03 starts at full conversion. Both show a steep decrease in the first 10 hours on stream, that flattens below 50 % for MM03 and below 30 % conversion for MM05. The decrease continues linearly to 34 % for MM03 and 21 % for MM05 after 80 hours. In both experiments MM03 shows a higher long-term stability compared to the catalyst without manganese. However, the activity still decreases drastically within the first 10 to 20 hours.

From the catalytic experiments with continuous heating it can be approximated, that the perfect cobalt to manganese ratio lies between those of MM03 and MM04. For a more precise assertion, the molar amount of unoxidized CO, respectively the area under the negated curves of conversion, is plotted against the Co loading of the catalysts (Figure 5.9). The minimum of the respective cubic fit function is obtained at 3.67 wt% (for fit parameters see Table SI 9-105). Hence, a catalyst MM06, again with 6 wt% of iron, but with 3.5 wt% of cobalt, to simplify the parameters, and 2.5 wt% of manganese is proposed as the ideal mixture. The catalyst was prepared analogous to MM01 - MM05 and tested in CO oxidation experiments to provide proof for the above-made conjecture.

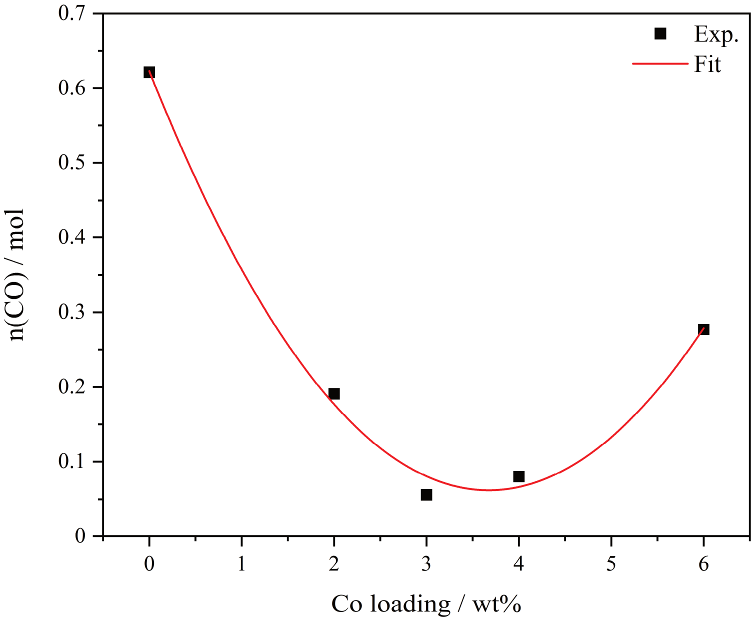

Figure 5.9: Molar amount of unoxidized CO over the whole catalytic experiment with continuous heating from 30 to 600 °C against Co loading of the catalysts MM01 - MM05.

In experiments under continuous heating MM06 shows a drop in activity shifted to lower temperatures, which means that it does not feature full conversion of CO at room temperature (Figure 5.10). It starts at approximately 86 % of CO_2 yield at 30 °C and displays a total conversion of CO at 150 °C. The superiority of MM06 comes to display when the experiments at static temperatures are compared (Figure 5.11). Here the optimized catalyst shows higher activity at 150 °C and at 200 °C with almost full conversion at both temperatures. All other investigated catalysts show a bigger drop in activity at 200 °C.

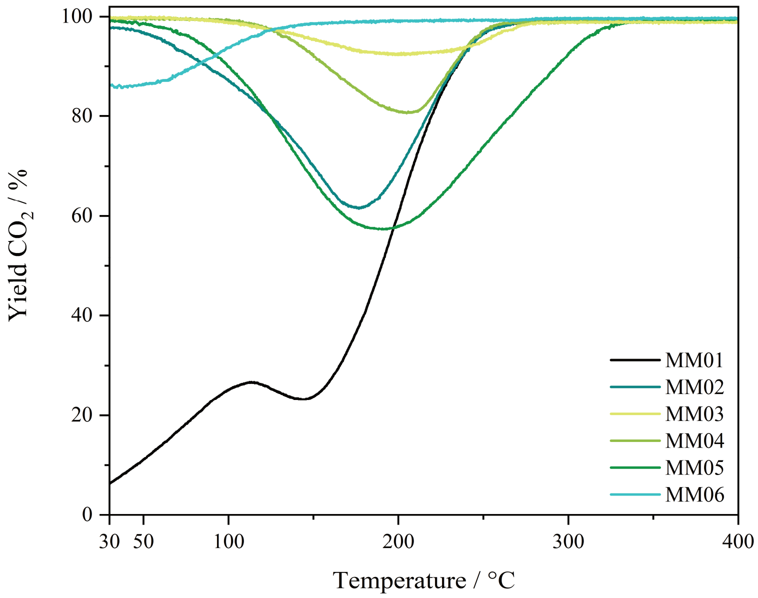

Figure 5.10: CO oxidation experiments of MM01 to MM06 under continuous heating.

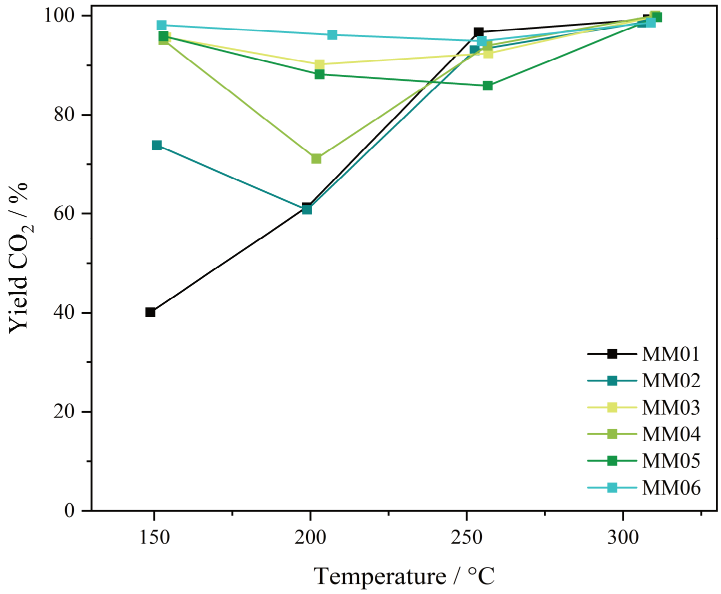

Figure 5.11: CO₂ yields of MM01 - MM06 at static temperatures.

MM06 was also tested in long-term studies both at 100 °C and 200 °C. In contrast to MM03 and MM05, it starts at almost full conversion at the lower of both temperatures. Although it also features drastic decreases in activity directly from the start, its incline is not as steep as for MM05. The activity of MM06 decreases analogous to the one of MM03 but due to its higher starting conversion its curve is shifted to the right. At 200 °C MM06 starts with constant full conversion for approx. 7.5 hours, then decreasing steeply down to below 60 % conversion after 12.5 hours. After that the curve flattens, just like for MM03 and MM05, with a rather constant decrease of approx. 5 % per 10 hours. Despite these decreases in CO oxidation activity MM06 does feature a better long-term stability compared to MM03 and MM05. Especially the constant total conversion at the beginning of the measurement at 200 °C is outstanding and very promising.

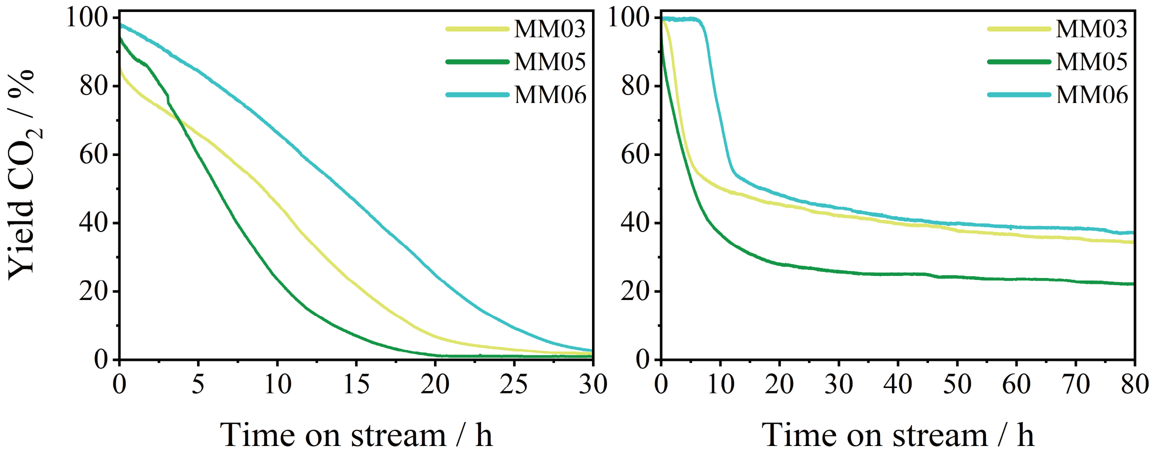

Figure 5.12: Long-term stability experiments of MM03, MM05 and MM06 at 100 °C (left) and 200 °C (right).

5.2 Summary and Discussion

Since iron oxide catalysts could not be optimized to a level comparable to state-of-the-art noble metal catalysts, the addition of other 3d metals was proposed to elevate their catalytic properties. To increase catalytic activity, especially at low temperatures close to room temperature, cobalt was introduced and to enhance their long-term stability manganese was chosen. For first tests a series of catalysts with a total of 12 wt% of the 3d metals immobilized on a γ-Al_2O_3 support was prepared by the multi-step impregnation-calcination procedure described in chapter 3. The as-prepared catalysts MM01 to MM05 were investigated by various characterization techniques and finally tested in CO oxidation experiments.

By N_2 physisorption it could be shown, that for all of the catalysts the BET surface area as well as the average pore volume and diameter of the particles decrease, compared to the pure γ-Al_2O_3 support. This indicates that the 3d metal oxides are present on the outer surface of the support as well as in its actual pores. Powder X-ray diffraction did not feature any additional reflexes other than the expected signals of the support. This again indicates that all 3d metal species are X-ray amorphous or too small to be detected. For the reflex corresponding to the (440) crystal plane a shift to lower values could be shown, resulting in higher plane distances, which means that the 3d metals somehow interact with the support lattice and/or are even incorporated into it somehow. The signals in the DRUV spectra unfortunately are mostly superimposed by all two or three metals, so that only minor results could be derived. All of the catalysts show a broad band from 220 up to 500 nm and an additional sharp signal at 500 nm that can be assigned to iron oxide oligomers. From 500 to 700 nm three relatively sharp signals can be seen for the Co containing catalysts MM02 to MM05, indicating that these bands can be attributed to cobalt oxidic species. More detailed insights could be obtained by X-ray absorption spectroscopy. XANES spectra at the Mn K-edge showed that the manganese species of MM01 to MM04 are present in oxidation state +III to +IV without any major differences between the catalysts. From the iron K-edge spectra, an oxidation state of +III could be constituted for the iron species of all of the catalysts. Also, a mixture of α- and γ-Fe_2O_3 can be presumed. The spectra obtained at the K-edge of cobalt showed pre-peak and edge energies close to the ones of a $CoBr_2$ reference, indicating cobalt in the oxidation state +II or higher. Analysis of the EXAFS region at the Mn K-edge showed that MnO_2 with manganese in the oxidation state +IV is the most presumable structure present at MM01 to MM04, while a mixture of α- and γ-Fe_2O_3 could be ascertained for the iron oxide species in all investigated samples. Despite Co_3O_4 being the most common structure for oxidic cobalt catalysts, EXAFS led to the conclusion that the catalysts MM02 to MM05 all contain Co_2O_3 or $CoAlO_3$ with cobalt in the oxidation state +III.

The catalysts were tested in CO oxidation experiments and featured extraordinarily high activities both during continuous heating and at static temperatures. While the catalyst without cobalt, MM01, only displayed 7 % CO conversion at 30 °C, the samples containing cobalt showed approx. 100 % CO_2 yield at 30 °C. All of the catalysts show a more or less distinct drop in activity at medium temperatures, that is most pronounced for MM01 and MM05 and least for MM03. These findings can also be seen in the measurements at static temperatures and provide evidence, that cobalt increases the catalytic activity drastically. From the continuous measurements a method for the optimization of these systems was derived, in which the overall amount of unoxidized CO was plotted against the Co loading. A cubic fit was applied and the x-value of the minimum derived thereof used as the ideal parameter for an optimized catalyst. Based on this conjecture a catalyst MM06 with 3.5 wt% of Co and 2.5 wt% of Mn was prepared and tested successfully in CO oxidation experiments. While MM06 did not show full conversion at room temperature due to the shifted drop in activity to lower temperatures, it featured a total conversion of CO above 150 °C and a CO_2 yield close to 100 % over the whole temperature range of the static experiments. To prove the hypothesis, that manganese increases the long-term stability of such systems, MM03 and MM05 were tested at 100 °C and 200 °C over a prolonged time. It could be shown that at both temperatures the catalyst containing manganese displayed higher rates of conversion for the most part of the experiments. Additionally, MM06 was tested in these long-term experiments featuring even higher activity than MM03.

To conclude, a series of bi- and trimetallic catalysts containing manganese, iron and cobalt supported on γ-Al_2O_3 were prepared by multi-step impregnation-calcination procedure and investigated regarding their structural properties. It could be shown, that by addition of cobalt to such systems, a tremendous increase in activity can be achieved and that addition of manganese leads to a higher long-term stability. From these catalytic experiments the ideal Co-Mn ratio was determined, a catalyst MM06 with this ideal composition prepared and again tested in CO oxidation experiments. While the drop in activity for MM06 was shifted to lower temperatures around room temperature, it featured full conversion of CO above 150 °C and especially high activities during the experiments at static temperatures. Also, in long-term measurements MM06 showed outstanding performance compared to MM03 and MM05.

6 REACTION PARAMETER OPTIMIZATION

For a correct evaluation of the catalytic activity of a catalyst and its comparison to other systems, the parameters with which the experiments are carried out are of topmost relevance. A number which is often used for such purposes is the *gas hourly space velocity*. The *GHSV* is defined as:

$$GHSV = \tau^{-1} = \frac{\dot{V}_{gas}}{V_{cat.}} \qquad \text{Eq. 5.1}$$

It is the reciprocal value of the residence time τ and describes the volume of gas streaming over the volume of the catalyst bed in a certain amount of time. When $\dot{V}$ is replaced with the volume of gas V_{gas} per time t (Eq. 5.2) and this volume of gas is substituted by $V_{gas} = A_{reactor} \cdot x_{gas}$ with the cross-section of the reactor $A_{reactor}$ and the way x_{gas} the gas travels in the time t, the equations are as follows:

$$GHSV \quad = \frac{V_{gas}}{t \cdot V_{cat.}} \qquad \text{Eq. 5.2}$$

$$= \frac{A_{reactor} \cdot x_{gas}}{t \cdot V_{cat.}} \qquad \text{Eq. 5.3}$$

The way x the gas travels in the time t can be replaced by the velocity v of the gas stream multiplied by the time t:

$$GHSV \quad = \frac{A_{reactor} \cdot v_{gas} \cdot t}{t \cdot V_{cat.}} \qquad \text{Eq. 5.4}$$

$$= \frac{A_{reactor} \cdot v_{gas}}{V_{cat.}} \qquad \text{Eq. 5.5}$$

This means, that the GHSV is directly proportional to the velocity of the gas stream. At a constant volume of the catalyst bed the GHSV increases when the velocity v of the gas stream increases. At the same time, when the volume of the catalyst bed is increased proportionally to the velocity, the GHSV stays the same.

The ratio of diffusion to convection in a reactor is defined by the Reynolds number:

$$Re = \frac{v_{gas} \cdot d_{particle}}{\nu_{kin}} \qquad \text{Eq. 5.6}$$

In the catalytic CO oxidation experiments described herein, the velocity of the gas stream was between 0.166 m/s (Fe01-Fe20) and 0.236 m/s (MI01-MI10 & MM01-MM05) and the particle sizes of the granulated catalyst between 125 and 250 µm. If the kinematic viscosity ν_{kin} of the gas is approximated by the kinematic viscosity of Ar[223] since the gas stream consists of 80 vol% of argon:

$$\nu_{Ar}^{20} = 1.35 \cdot 10^{-5}\ \frac{m^2}{s} \qquad \text{Eq. 5.7}$$

$$Re_{min} = \frac{0.166\ \frac{m}{s} \cdot 125 \cdot 10^{-6}\ m}{1.35 \cdot 10^{-5}\ \frac{m^2}{s}} = 1.54 \qquad \text{Eq. 5.8}$$

$$Re_{max} = \frac{0.236\ \frac{m}{s} \cdot 250 \cdot 10^{-6}\ m}{1.35 \cdot 10^{-5}\ \frac{m^2}{s}} = 4.37 \qquad \text{Eq. 5.9}$$

For the catalytic experiments a Reynolds number between 1.54 and 4.37 can be calculated (even lower at elevated temperatures because of an increase of the viscosity), which means that the gas stream in the catalyst bed is laminar (Re < 2000[224]). In a gas stream, a boundary layer forms on the outside of a catalyst particle in which the concentration of the educts decreases from gas phase to the particle. The educts have to diffuse through this BL in order to get to the catalyst surface (Figure 6.1). If the thickness of the boundary layer δ is above a certain threshold the reaction is faster than the diffusion, hence not enough educts are present on the catalyst surface, the reaction is limited by diffusion of the educts through the BL.

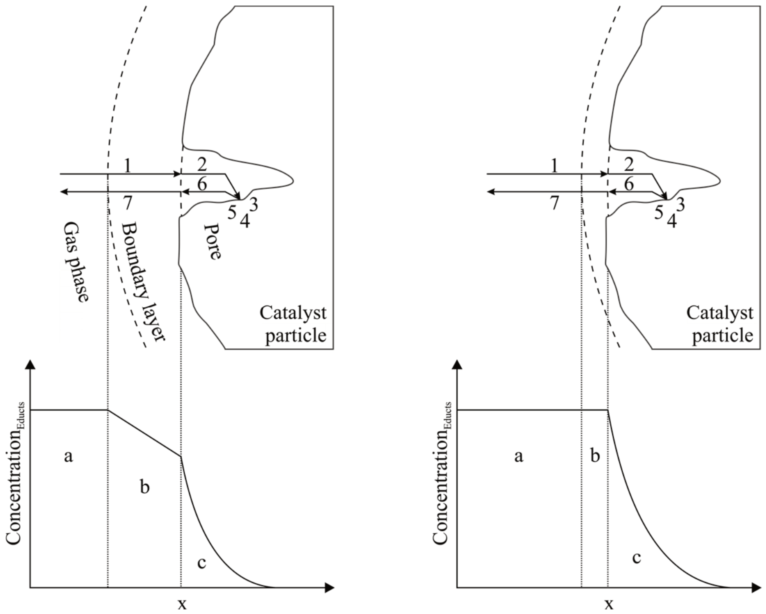

Figure 6.1: Schematic description of the boundary layer on a catalyst particle, depending on the outer gas velocity, and the concentration gradient of the educts in the outer gas stream (a), the boundary layer (b) and the pore system of the catalyst (c); left: low velocity; right: high velocity; concentration gradients simplified.

In a laminar gas flow the BL thickness δ is inversely proportional to the square root of the Reynolds number[224]:

$$d \sim \frac{1}{\sqrt{Re}} \qquad \text{Eq. 5.10}$$

This can be transformed into:

$$\delta \sim \frac{1}{\sqrt{\frac{v_{gas} \cdot d_{particle}}{\nu_{kin}}}} \qquad \text{Eq. 5.11}$$

Hence, the thickness of the BL is inversely proportional to the outer gas velocity. This means that the catalytic experiments carried out below a certain velocity threshold are diffusion limited, while above this value they become limited by the reaction rate. Hence the velocity has to be higher than this threshold to measure a catalysts actual activity. To achieve this, tests were carried out with variation of the gas velocity but with a constant GHSV. Therefore, the velocity and the catalyst volume, respectively the volumetric gas flow and the catalyst mass, were varied proportionally to obtain a GHSV close to 60000 h^{-1} for each experiment. As can be seen in Figure 6.2 for Fe10, the curve of conversion shifts significantly to lower temperatures when the gas feed is increased to 500 ml/min.

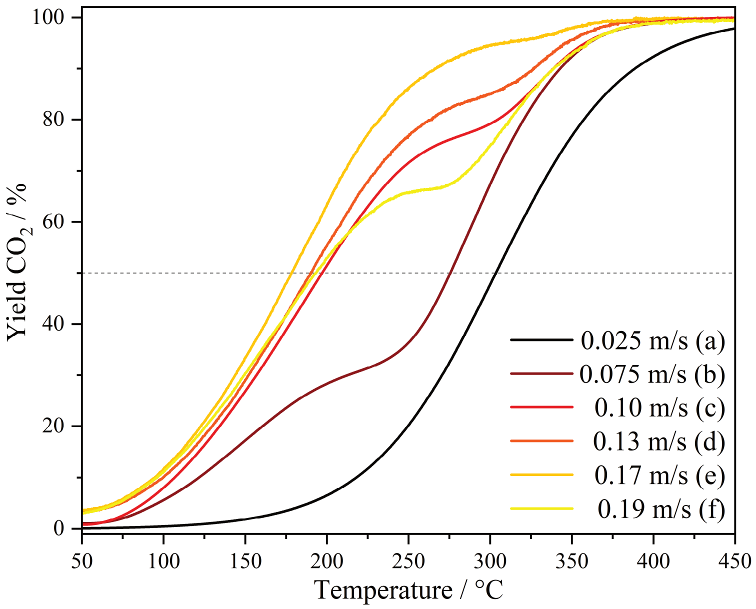

Figure 6.2: Diffusion limitation experiments in CO oxidation of Fe10 with the following amount of catalyst used, the applied gas feed and resulting gas velocity: 50 mg, 75 ml/min & 0.025 m/s (a); 150 mg, 225 ml/min & 0.075 m/s (b); 200 mg, 300 ml/min & 0.10 m/s (c); 267 mg, 400 ml/min & 0.13 m/s (d); 333 mg, 500 ml/min & 0.17 m/s (e); 375 mg, 560 ml/min & 0.19 m/s (f); gas composition: 1000 ppm CO (1 vol% CO in N_2*), 10 vol%* O_2*, Ar balance,* $d_{reactor}$ *= 8 mm.*

Since the lowest T_{50} was achieved with 333 mg catalyst in a gas feed of 500 ml/min for Fe10 in a reactor with inner diameter of 8 mm, these parameters were used in the catalytic experiments of Fe01 to Fe20, resulting in an outer gas velocity of 0.166 m/s. Since the density of the catalysts increases by addition of iron the volume of the catalyst bed is dependent on the iron loading. With an average bed length of 10 mm a GHSV of 59643 h^{-1} was achieved. However, MI01 to MI10 as well as MM01 to MM05 were prepared by impregnation of SCFa140 instead of the self-prepared γ-Al_2O_3 support of Fe01-Fe20. Therefore, different structural parameters were expected and thus again tests carried out regarding diffusion limitation (Figure 6.3). For MI07 the lowest T_{50} was obtained at

400 ml/min with 267 mg of catalyst, but now in a reactor with an inner diameter of 6 mm resulting in a gas velocity of 0.236 m/s. The GHSV remains the same as for Fe01-Fe20.

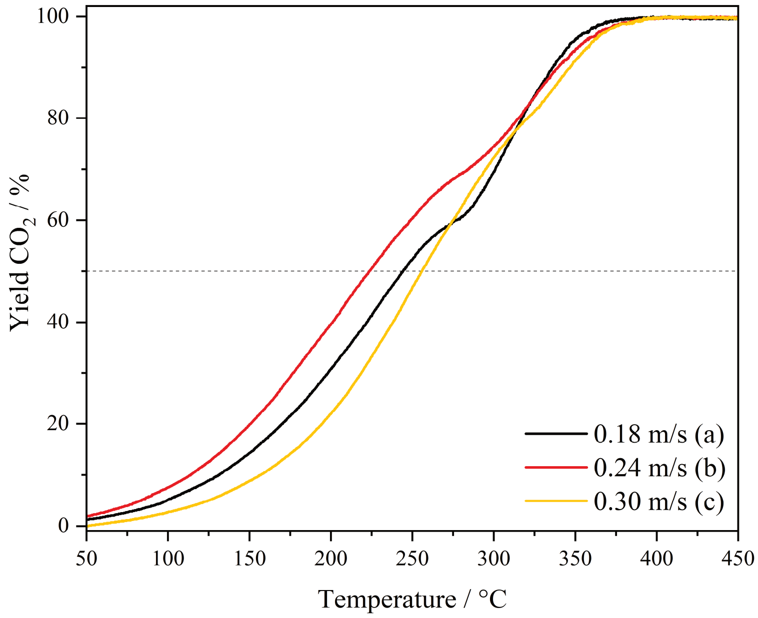

Figure 6.3: Diffusion limitation experiments in CO oxidation of MI07 with the following amount of catalyst used and the applied gas feed: 200 mg, 300 ml/min & 0.18 m/s (a); 267 mg, 400 ml/min & 0.24 m/s (b); 333 mg, 500 ml/min & 0.30 m/s (c); gas composition: 1000 ppm CO (1 vol% CO in N_2*), 10 vol%* O_2*, Ar balance,* $d_{reactor}$ *= 6 mm.*

These investigations illustrate the importance of these parameters, not only for comparison between different systems, but also for a single catalytic experiment. As shown, a simple variation of the gas velocity can lead to the reaction being diffusion limited and not by kinetics. By increase or decrease of the inner diameter of the reactor, the velocity can be altered significantly, even without changing the amount of catalyst used. Therefore, diffusion limitation experiments are crucial if a new system is tested, to ascertain that the activities measured are limited by the kinetics of the reaction.

7 CONCLUSION & OUTLOOK

The oxidation of CO is one of the key reactions in the removal of toxic emissions from automotive exhaust systems. In contrast to the typical platinum, palladium and ruthenium catalysts, iron is abundant and biocompatible. It can be considered superior on an economical as well as on an ecological level. However, the needed activity for automotive application still cannot be reached with iron oxide catalysts, since we lack a basic understanding of their working principles and mechanisms. The present work aimed at contributing to this by correlation of structural properties of simple iron oxide catalysts immobilized on a γ-alumina support to their catalytic activity in CO oxidation. The gained insights should then be transformed into a working hypothesis for the preparation and optimization of catalysts that could potentially compete with state-of-the-art noble metal catalyst.

Various analytical methods such as powder X-ray diffractometry, diffuse reflectance UV/Vis spectroscopy, Mößbauer spectroscopy and X-ray absorption spectroscopy were applied to gain structural insights into a series of iron oxide catalysts with different weight loadings of iron, synthesized by simple wetness impregnation of a Fe^{III} precursor on γ-Al_2O_3 as a support material followed by annealing under atmospheric air. The resulting oxidic species showed strong structural variations dependent on the iron loading. Lower amounts of iron led to smaller clusters of iron oxide on the support surface that are finely dispersed with less iron oxide in bulk phase. Also, lower amounts of iron oxide seem to form γ-Fe_2O_3 preferably, which comprises tetrahedrally coordinated iron species that are predestined for high CO oxidation activity. In catalytic experiments higher conversion of CO was displayed by the catalysts with 5, 10 and 20 wt% of iron due to the amount of potentially active iron centers. The turnover frequencies, however, showed that Fe01 and Fe025 display much higher activities, which can be correlated to their higher percentual amounts of isolated iron species in tetrahedral oxygen coordination.

Based on these findings a new working hypothesis was deduced: a catalyst comprising a high amount of iron up to 10 wt%, but with finely dispersed and isolated iron oxide species in tetrahedral oxygen coordination could show outstanding catalytic activity. Since Fe01 showed the highest ratio of tetrahedrally to octahedrally coordinated iron with almost no oligomers or particles, it was concluded that a multi-step impregnation-calcination procedure with successive impregnation of 1 wt% of iron(III) precursor followed by annealing could hinder agglomeration drastically, and hence the formation of clusters or bulk iron oxide.

This technique was utilized for the preparation of a series of catalysts from 1 to 10 wt% of iron on a γ-Al_2O_3 support. It could be shown that by this facile technique an increasing amount of isolated iron species was obtained for catalysts up to 6 wt% with almost no oligomers or particles. The amount of tetrahedrally coordinated isolated iron species increased even further to MI08, which could be correlated to the high activity in CO oxidation experiments under continuous heating. MI08 showed the lowest temperatures of conversion in the largest temperature range. However, in experiments at static temperatures MI09 was superior to MI08, which could not be explained by any of the analytical methods carried out and will need further investigation. Also, the overall activity of the MI catalysts compared to a single-step prepared catalyst SI10 and to Fe01 - Fe20 did not show any improvement, which is contrary to our expectations. The outstanding structural parameters obtained by this new facile preparation technique should lead to catalysts with higher activities due to the higher amounts of tetrahedrally coordinated iron species that are finely dispersed on the support surface, which should promote higher activities.

To increase catalytic activity, especially at low temperatures, additional 3d metals were introduced. To obtain better long-term stability and resistance against poisoning of the catalysts, manganese was chosen and for the enhancement of low temperature activity cobalt was used. Five catalysts, each with 6 wt% of iron and a varying ratio of Mn to Co, were prepared by the multi-step impregnation-calcination procedure described before and investigated thoroughly. Hereby catalysts with outstanding performance in CO oxidation could be obtained, with conversion close to 100 % from the start at room temperature for the samples containing Co. All of the catalysts showed a more or less pronounced drop in activity between 100 and 300 °C which was least intense for MM03 with 3 wt% of Mn and 3 wt% of Co. A method for the extrapolation to an ideal Co-Mn ratio was derived thereof resulting in a ratio of 3.5:2.5. A catalyst MM06 with the said ratio was prepared analogous to MM01 - MM05 and tested in CO oxidation experiments, with superior activity compared to the others. For this catalyst the drop in activity was shifted to lower temperatures around room temperature. The catalyst showed full conversion of CO at 150 °C but with a minimum yield of 85 % throughout the drop in the continuous measurements and approx. 95 % at static temperatures. Also, long-term stability tests were carried out at 100 and 200 °C. Here, the catalyst with manganese, MM03, showed a better stability at both temperatures compared to MM05, without Mn. However, MM06 with the optimized ratio of Co to Mn featured even increased long-term stability, especially at 200 °C where it showed full conversion of CO constantly over the first 7.5 hours.

In the last part of the herein presented work the importance of the parameters used in catalytic experiments was emphasized by tests in which the limitation of the measured curves of conversion by diffusion processes could be shown. Since in heterogeneously catalyzed processes with a constant flow of the reactant over a solid catalyst a so-called boundary layer is formed between the catalyst surface and the constant gas or liquid feed, the diffusion of the reactants through this layer can be the rate determining step of the overall process, if the thickness of this layer exceeds a certain threshold. Therefore, catalytic experiments with constant GHSV but variation of the amount of catalyst and the flow rate of the gas feed were carried out. For Fe01 to Fe20 the optimal working conditions were obtained for 333 mg of the catalyst with a gas feed of 500 ml/min in a reactor with an inner diameter of 8 mm, whereas for the catalysts supported on commercial alumina 267 mg of the catalyst in a gas stream of 400 ml/min were found to show the best results in a reactor with an inner diameter of 6 mm. For these parameters it can be expected that the activities measured are the actual activities of the catalysts themselves and that the influence of diffusion through the boundary layer can be neglected due to a minimum thickness of the latter.

Altogether a facile new preparation technique was derived from a structure-activity-correlation and applied on a new series of catalysts, resulting in outstanding structural parameters with finely dispersed active sites. Although this series of catalysts did not feature noticeably better activities, the working hypothesis for the prevention of agglomeration by multi-step impregnation-calcination procedure could be proven successfully and then applied on a series of catalysts with additional Mn and Co. Hereby, catalysts with outstanding catalytic activities were prepared, for which the enhancement in activity by Co and an increase in long-term stability by Mn were established as well as a simple method for the optimization of the Co-Mn ratio that improved the activities even further, to a level at which a comparison to state-of-the-art noble metal catalysts is definitely possible. Additionally, an optimization of the experimental parameters was carried out to limit the influence of diffusion on the catalytic tests and with which the importance of the reaction parameters could be emphasized.

Based on the herein presented work, further investigation of the MI systems should be carried out to investigate why their structural properties prerequisite for high activities in catalytic experiments did not fulfill these expectations. Therefore, *in-situ* X-ray absorption and X-ray emission spectroscopy could be carried out. By modulation-excitation experiments, XAS could help to identify the number of actual active sites during CO oxidation and possibly even to distinguish between activity of tetrahedrally and octahedrally coordinated iron species. *In-situ* XES could then show how CO and O_2 adsorb on the catalyst surface and where. This would give important insights into the mechanism of the reaction on iron oxide catalysts, since this is still unknown. As mentioned in the introduction, both Eley-Rideal as well as Mars-van-Krevelen seem to be possible mechanisms. Therefore, experiments regarding the reaction kinetics are crucial. Preliminary results of such tests indicate the reaction being of first order regarding CO and of zero order for O_2, which would advocate for a MvK mechanism in which oxygen from the iron oxide lattice or even the support material is used, hence being independent of the O_2 concentration. Although these systems did not comprise better activities than the previous catalysts, they should also be tested regarding their long-term stability as well as their thermal stability and resistance against poisoning by water. These could potentially be enhanced by the optimized structural properties obtained through the new preparation technique, and if so, the catalysts could already be potential alternatives to noble metals. Since the multi-metallic catalysts feature outstanding catalytic activities and promising long-term stability, they should also be investigated further. With a good stability against catalyst poisoning by water, they would even be superior to state-of-the-art noble metal catalysts used in automotive applications nowadays. Although Co containing catalysts with similar activity have been published, most of them are bulk catalysts without immobilization on a support material, hence the herein described catalysts are prerequisite to feature higher thermal stability compared to catalysts containing solely the active material. For further improvement, the iron content should be optimized with a steady ratio of Co to Mn of 3.5:2.5 and even the overall amount of 3d metals could be varied to find the best parameters. A manifold of parameters can be tuned to enhance these catalysts properties emphasizing the potential of this new system. The next step should also involve experimental tests under realistic conditions with moisture and then also with NO_x or even HCs. Definitely, the next step towards replacement of noble metal catalysts has been made.

8 EXPERIMENTAL

8.1 Preparation of the γ-Al_2O_3 support

The γ-Al_2O_3 support was synthesized by calcination of PuralBT® (Sasol Germany GmbH) in a furnace under atmospheric air. Heating with a ramp of 5 °C/min was carried out up to 600 °C, where the sample was further calcined for 3 hours. Phase purity was checked by X-ray diffraction measurements in a 2θ range of 15 to 80 degrees (Appendix: Figure SI 9.1).

8.2 Preparation of Fe01 to Fe20

Table 8.1: Parameters for the catalyst preparation of Fe01 to Fe20.

Catalyst	**Iron loading [wt%]**	**m(Fe) [mg]**	**n(Fe(acac)$_3$) [mmol]**	**m(γ-Al_2O_3) [g]**
Fe01	1	20	0.358	1.98
Fe025	2.5	50	0.895	1.95
Fe05	5	100	1.79	1.90
Fe10	10	200	3.58	1.80
Fe20	20	400	7.16	1.60

A 0.25 M solution of iron (III) acetylacetonate in a mixture of *N*-Methyl-2-pyrrolidone and tetrahydrofuran (1:1) was prepared and added to a suspension of previously synthesized γ-Al_2O_3 in tetrahydrofuran. Details are given in Table 8.1. After stirring for 30 minutes, the mixture was heated to 140 °C and the solvents were slowly removed under vacuum. The dry reddish powders were then annealed in a furnace under air with a heating ramp of 2 °C/min up to 600 °C and held at this temperature for 3 hours. The reported weight-loadings of iron refer to the mass of iron inserted during synthesis. The amounts of iron and γ-Al_2O_3 were calculated to add up to 100 wt%.

8.3 Preparation of MI01 to MI10 and SI10

Commercially available SCFa140 (Sasol®) was used as γ-Al_2O_3 support and Fe(acac)$_3$ (Sigma Aldrich) as precursor. For preparation, a 0.25 M solution of the iron precursor in acetone was added to a suspension of SCFa140 in acetone, stirred for 10 minutes before removal of the solvent at 40 °C under reduced pressure. The obtained reddish powder was then annealed under atmospheric air, heating with 2 °C/min up to 600 °C and keeping this temperature constant for 3 hours. This procedure was repeated for each percent of iron loading up to a total amount of 10 wt% iron. The amounts of pure iron and γ-Al_2O_3, respectively pure iron and the obtained catalyst from the previous step, were calculated to add up to 100 wt% (Table 8.2).

Table 8.2: Total amounts used in the preparation of MI01 to MI10 and SI10.

Catalyst	**Iron loading [wt%]**	**m(Fe) [mg]**	**n(Fe(acac)$_3$) [mmol]**	**m(γ-Al$_2$O$_3$) [g]**
MI01	1	20	0.358	1.98
MI02	2	40	0.716	1.96
MI03	3	60	1.07	1.94
MI04	4	80	1.43	1.92
MI05	5	100	1.79	1.90
MI06	6	120	2.15	1.88
MI07	7	140	2.51	1.86
MI08	8	160	2.86	1.84
MI09	9	180	3.22	1.82
MI10	10	200	3.58	1.80
SI10	10	200	3.58	1.80

8.4 Preparation of MM01 to MM06

MM01 to MM06 were prepared by Jennifer Klaucke between August 24th and October 26th 2020 as objective of her bachelor thesis[225]. The catalysts were prepared analogous to the MI catalysts in 1 wt% steps, if applicable. $Fe(NO_3)_3{\cdot}9H_2O$, $Mn(NO_3)_2{\cdot}4H_2O$ and $Co(NO_3)_2{\cdot}6H_2O$ were used as precursors and for better solubility ethanol was used as a solvent. The weightloadings impregnated in each step before calcination at 600 °C in atmospheric air are shown in Table 8.3.

Table 8.3: Weightloadings of each 3d metal impregnated on the support material or the respective previous stage in each step of the preparation of MM01 - MM06.

	Metal	**MM01**	**MM02**	**MM03**	**MM04**	**MM05**	**MM06**
Step 1	Mn:Fe:Co [wt%]	1:1:0	0:1:0	0:1:0	0:1:0	0:1:1	0:1:0
Step 2	Mn:Fe:Co [wt%]	1:1:0	0:1:0	0:1:0	0:1:0	0:1:1	0:1:0
Step 3	Mn:Fe:Co [wt%]	1:1:0	1:1:0	0:1:0	0:1:1	0:1:1	0:1:0.5
Step 4	Mn:Fe:Co [wt%]	1:1:0	1:1:0	1:1:1	0:1:1	0:1:1	0.5:1:1
Step 5	Mn:Fe:Co [wt%]	1:1:0	1:1:1	1:1:1	1:1:1	0:1:1	1:1:1
Step 6	Mn:Fe:Co [wt%]	1:1:0	1:1:1	1:1:1	1:1:1	0:1:1	1:1:1
Overall	Mn:Fe:Co [wt%]	6:6:0	4:6:2	3:6:3	2:6:4	0:6:6	2.5:6:3.5

8.5 Catalytic experiments

For catalytic experiments the samples were homogenized in a mortar, pressed to a pellet and then granulated and sieved to a fraction of 125 to 250 µm. In case of Fe01 to Fe20, 333 mg of the catalyst were filled in a quartz glass tube with an inner diameter of 8 mm. The filling was plugged on both sides with quartz wool and the reactor was mounted into a clamshell oven. K-type thermocouples were inserted from both sides to log the exact temperatures at the gas entrance and exit of the packed bed. Continuous measurements were carried out during heating with a rate of 2 °C/min up to 600 °C with a permanent gas feed of 1000 ppm CO and 10 vol% O_2 in inert gas balance to a total flow of 500 ml/min resulting in a GHSV of 59642 h^{-1}. For activation, the catalysts were heated under a constant argon flow of 500 ml/min up to 600 °C with a heating rate of 5 °C/min and cooled down again to room temperature. For static experiments the catalysts were cooled down to 150 °C in inert gas after the continuous measurement. Then the above-mentioned gas feed was applied and the catalytic activity measured at 150, 200 and 250 °C, each for 2 hours. The values measured after these 2 h were used as the amount of conversion at the respective temperature.

For the MI, SI and MM catalysts a total of 267 mg of the granulated sample were used in a reactor with 6 mm inner diameter and a total gas flow of 400 ml/min but with the same GHSV and same composition of CO and O_2 in inert gas. The activation of these catalysts was carried out by heating with 5 °C/min up to 450 °C under a constant Ar flow of 400 ml/min before the actual catalytic experiment.

The long-term stability tests were carried out with the same parameters, after activation of the catalysts analogous to the measurements with continuous heating. The experiments at 100 °C were carried out until zero conversion of CO was reached. Since at 200 °C the experiments would take up to 30 days to reach the point of zero conversion, they were aborted after 80 h.

Catalytic experiments were conducted with 1 vol% CO (1.9 purity) in nitrogen (5.0), oxygen (4.5) and argon (5.0). The pressures were reduced by double stage reducing valves (GCE druva®) to a constant rate of 5 bar. The final gas mixture was set by mass flow controllers (ANALYT-MTC Messtechnik GmbH) to yield a lean composite of 1000 ppm CO and 10 vol% oxygen in inert gas with a total flow rate of 400, respectively 500 ml/min. The packed bed plug flow reactor was heated by a clamshell furnace (HORST GmbH, equipped with a JUMO dTron 304 controller) in a range of 200 mm (packed bed length approx. 10 mm) to ensure a uniform heating of the gas stream and the packed bed. The composition of the exhaust gas was analyzed by a NDIR analyzer (Infralyt 50, SAXON Junkalor® GmbH) equipped with two separate channels, one for carbon monoxide and one for carbon dioxide, both calibrated for a range of 0 to 1000 ppm.

8.6 Analytics

8.6.1 N_2 Physisorotion

The surface areas, average pore diameters and total pore volumes were obtained from nitrogen physisorption, which was carried out at 77 K using a Quantachrome Autosorb 6 after degassing the samples for 12 h at 120 °C. ASWin was used for processing of the data[226]. Surface areas were obtained via Brunauer-Emmett-Teller method and pore diameters via Barrett-Joyner-Halenda method.

8.6.2 PXRD

Powder X-ray diffractometry was carried out at a Bruker AXS D8 Advance with an incident Cu K_α radiation ($\lambda = 1.54$ Å), a step size of $2\theta = 0.02°$, time per step of 3 s and a wide-angle range of 10° to 80°.

8.6.3 HRPXRD

High resolution powder X-ray diffractometry was carried out at beamline P24 at DESY (Hamburg/Germany) with an incident radiation of 20 keV ($\lambda = 0.619$ Å) and a MarCCD 165 detector. For processing of the obtained Bragg circles respectively the transformation into a diffractogram the free software Datasqueeze[227] was used. For calibration of the spectra lanthanum hexaboride was used as a reference.

The plane distances resulting from PXRD as well as HRPXRD were calculated according to Bragg´s by

$$d = \frac{\lambda}{2\sin\left(\frac{\theta\pi}{180}\right)} \qquad \text{Eq. 7.1}$$

These parameters can further be transformed into the lattice parameter *a* for each plane using its Miller or Laue indices by the following formula:

$$d = \frac{a}{\sqrt{h^2 + k^2 + l^2}} \qquad \text{Eq. 7.2}$$

8.6.4 Mößbauer

Fe025-Fe20 (RT) and Fe025/Fe10 (77 K): ^{57}Fe Mößbauer spectra were obtained in transmission geometry using a constant acceleration spectrometer (WissEl GmbH) with a 512-channel analyzer and a ^{57}Co source implemented in a Rh matrix. The spectrometer was calibrated against α-iron at room temperature. A continuous flow cryostat (OptistatDN, Oxford Instruments) was utilized to perform experiments at variable temperatures. For further analysis, spectroscopic data were transferred from the multi-channel analyzer to a PC. The spectra were analyzed, employing the public domain program Vinda[228] running on an Excel 2003® platform, by least-squares fits using Lorentzian line shapes. In addition to the Mößbauer parameters isomer shift δ, quadrupole splitting ΔE_Q and the line width at half maximum Γ, the area and area ratios of the components to each other were determined. The spectra were measured and analyzed by A. Omlor (AK Schünemann, TU Kaiserslautern).

Fe01 (RT) and Fe01/Fe05/Fe20 (77 K): ^{57}Fe Mößbauer spectra were taken on a spectrometer (WissEl GmbH) with movable 100 mCi ^{57}Co source implemented in a Rh matrix and fixed sample holder. The analyses were carried out in constant acceleration mode in the velocity range between -10 mm/s and 10 mm/s without external magnetic field. The temperature of the samples was controlled by an MBBC-HE0106 Mößbauer He/N_2 cryostat within an accuracy of ±0.3 K. Transmitted radiation was measured by a proportional counter. The collected spectra were analysed by WinNormos[229] software using least-square fitting procedure assuming Lorentzian peak shapes. The obtained correlation coefficients were always above 0.95 indicating appropriate accuracy of the deconvolution. Isomer shift δ, quadrupole splitting ΔE_Q and hyperfine field B are reported relative to a α-Fe reference. The spectra were measured and analysed by C. Singer (AK Kureti, TU BA Freiberg)

8.6.5 DRUVS

Fe01-Fe20: diffuse reflectance UV/Vis spectroscopy of Fe01 to Fe20 was carried out at a Lambda 18 (Perkin Elmer) in the range of 200 to 900 nm. For background correction a Lorentz-type function was fitted to the regions of 200 to 215 nm and 700 to 900 nm and then subtracted from the spectrum. Deconvolution was carried out with NLFit function of Origin 2020b[230] via manual selection of 5 (respectively 6) initial wavelengths as starting points for the fit. Lower limits were set for peak 1 at 260 nm, peak 3 at 340 nm and y_0 according to the lowest point of the spectrum to keep the fit within these boundaries.

MI01-MI10/SI10/MM01-MM05: diffuse reflectance UV/Vis spectroscopy of the MI and MM catalysts was carried out in the range of 200 to 800 nm at a Lambda 850 spectrometer (Perkin Elmer) equipped with a Praying Mantis diffuse reflectance accessory (Harric Scientific). The samples were investigated at ambient conditions with the SCFa140 support material as reference. The spectra were converted using the Kubelka-Munk function defined as following:

$$F(R) = \frac{(1-R)^2}{2R} \qquad \text{Eq. 7.3}$$

For background correction a Lorentz-type function was fitted to the starting point of the spectra at 200 nm and the first zero value at higher energies, and then subtracted from the spectrum. Deconvolution was carried out with NLFit function of Origin 2020b[230] via manual selection of 3 to 6 initial wavelengths as starting points for the fit. The range of the fitted area was kept between the first zero value for absorption in both lower and higher energy direction. Lower limits were set for peak 1 at 270 nm, peak 3 at 340 nm, peak 4 at 430 nm, peak 5 at 530 nm and y_0 according to the lowest point of the spectrum to keep the fit within these boundaries.

8.6.6 HAADF/STEM-EDX

Scanning transmission electron microscopy (STEM) images were obtained using a probe-side C_s-corrected JEOL JEM-ARM200F, equipped with a cold field emission gun and a JEOL SDD detector for the acquisition of energy dispersive x-ray spectra (EDS). TEM specimen of all catalysts are prepared by dispersing the synthesis products in isopropyl alcohol and placing a droplet of the dispersion on a Lacey grid. The analysis of all specimen is conducted with a high tension of 200 kV, a semi-convergence angle of 25 mrad and a maximum resolution of 70 pm owing to the C_s-correction. High angle annular dark-field (HAADF) images are acquired on an annular dark-field detector with a collection angle ranging from (51 ± 2) mrad and (180 ± 2) at a used camera length of 12 cm. At these settings the intensity contrasts in HAADF images can be explained within the well-known Z-contrast model by Pennycook[231], in which the contrast is proportional to the atomic number $Z^{\sim 2\text{-}x}$ (x between 0.3 and 0.7, accounting for inelastically scattered electrons)[232]. Dwell-time and image resolution of EDS mappings are chosen to keep specimen drift while acquisition as small as possible. Elemental maps of iron, aluminium and oxygen are obtained using K-edges. The images were obtained and processed by J. Bürger (AK Lindner, Paderborn University).

8.6.7 XAS

X-ray absorption spectroscopy experiments of Fe01 to Fe20 at the Fe K-edge (7112 eV) were performed at PETRA III beamline P65 at Deutsches Elektronen-Synchrotron DESY (Hamburg/Germany) using a Si(111) double crystal monochromator at a maximum beam current of 100 mA. Energy calibration of the monochromator was controlled using a Fe foil. The samples were diluted with cellulose (Sigma-Aldrich), homogenized in a mortar and then pressed to a pellet. Fe01 was measured in fluorescence mode using a PIPS detector (**p**assivated **i**mplanted **p**lanar **s**ilicon). Fe025 to Fe20 were measured in transition mode using ionization chambers in front of and behind the sample. The spectra were measured in step scan mode, which means that the spectra are divided in regions with different step sizes (Table 8.4).

Table 8.4: Step scan parameters used in X-ray absorption spectroscopy of the presented catalysts at the iron K-edge (7112 eV).

Energy [eV]	Step size	Time per point [s]
6962 - 7062	5 eV	0.2
7062 - 7092	3 eV	0.2
7092 - 7142	0.5 eV	0.2
7142 - 8112	0.5 $Å^{-1}$	0.2

MI09, MI10, SI10 and MM01 to MM05 were measured at the same beamline with the same setup in transmission mode at the respective edges (Mn K, Fe K or Co K) but with continuous scanning, which means that the spectra are measured with equal step sizes from start to finish, which is usually from -200 to +1000 eV according to E_0 of the reference metal (Mn: 6539 eV, Fe: 7112 eV, Co: 7709 eV). The time per point was 0.1 s and the overall time per spectrum 180 s. The step size results from the energy range, the time per point and the time per spectrum.

MI01 to MI08 were measured at beamline P64 at DESY with a similar setup and also with continuous mode. The spectra of MI01 to MI03 were obtained in fluorescence mode while MM04 to MM08 were measured in transmission.

The processing of the raw data including calibration of the spectra to the Fe reference, deglitching, normalization and background removal the program Athena of the Demeter software package was used[233].

E_0 was defined as the center of the jump, obtained at the halved maximum of the maximum intensity of the jump. For EXAFS analysis the background was subtracted from the obtained spectra as a Victoreen-type polynomial[234,235], followed by determination of the smooth part of the spectrum by a piecewise polynomial, optimized to yield minimal low-R components for the resulting Fourier transformation. After division by the smoothed part, the photon energy was transformed into the photoelectron wavenumber k. $\chi(k)$ was weighted with k3 for the fitting with the program Excurve 9.26[236], which utilizes the EXAFS equation (Eq. 7.4) in the form of pseudo-radial distribution functions.

$$\chi(k) = \sum_j s_0^2\,(k)\frac{N_j}{kr_j^2}F_j(k)e^{-2\sigma_j^2 k^2}e^{\frac{2r_j}{\lambda(k)}}\sin\left[2kr_j + \varphi_{ij}(k)\right] \qquad \text{Eq. 7.4}$$

Here inelastic effects are represented by the amplitude reducing factor $s_0^2(k)$ and λ, the mean free path length, while the number of backscattering atoms N_j, their distance to the observed atom r_j and the Debye-Waller like factor σ^2 take structural parameters into account.

References

[1] Royal College of Physicians, *Every breath we take: the lifelong impact of air pollution. Report of a working party*, RCP, London, **2016**.

[2] L. J. Puckett, *Environ. Sci. Technol.* **1995**, *29*, 408A-414A. https://doi.org/10.1021/es00009a743

[3] P. Williams, *Anim. Feed Sci. Tech.* **1995**, *53*, 135-144. https://doi.org/10.1016/0377-8401(95)02017-T

[4] A. E. V. Evans, J. Mateo-Sagasta, M. Qadir, E. Boelee, A. Ippolito, *Curr. Opin. Env. Sust.* **2019**, *36*, 20-27. https://doi.org/10.1016/j.cosust.2018.10.003

[5] S. Harrison, C. McAree, W. Mulville, T. Sullivan, *Sci. Total Environ.* **2019**, *677*, 700-717. https://doi.org/10.1016/j.scitotenv.2019.04.169

[6] V. J. P. D. Martinho, *Sci. Total Environ.* **2019**, *688*, 346-360. https://doi.org/10.1016/j.scitotenv.2019.06.199

[7] A. Zwolak, M. Sarzyńska, E. Szpyrka, K. Stawarczyk, *Water Air Soil Pollut.* **2019**, *230*. https://doi.org/10.1007/s11270-019-4221-y

[8] P. Longobardi, A. Montenegro, H. Beltrami, M. Eby, *PloS one* **2016**, *11*, 1-34. https://doi.org/10.1371/journal.pone.0153357

[9] R. A. Houghton, A. A. Nassikas, *Glob. Chang. Biol.* **2018**, *24*, 350-359. https://doi.org/10.1111/gcb.13876

[10] C. G. Solomon, R. C. LaRocque, *N. Engl. J. Med.* **2019**, *380*, 209-211. https://doi.org/10.1056/NEJMp1817067

[11] P. Stott, *Science* **2016**, *352*, 1517-1518. https://doi.org/10.1126/science.aaf7271

[12] S. N. Jorgenson, J. C. Stephens, B. White, *J. Environ. Educ.* **2019**, *50*, 160-171. https://doi.org/10.1080/00958964.2019.1604478

[13] T. R. Anderson, E. Hawkins, P. D. Jones, *Endeavour* **2016**, *40*, 178-187. https://doi.org/10.1016/j.endeavour.2016.07.002

[14] S. E. Schwartz, *Am. J. Phys.* **2018**, *86*, 645-656. https://doi.org/10.1119/1.5045577

[15] M. Meinshausen, N. Meinshausen, W. Hare, S. C. B. Raper, K. Frieler, R. Knutti, D. J. Frame, M. R. Allen, *Nature* **2009**, *458*, 1158-1162. https://doi.org/10.1038/nature08017

[16] IEA - International Energy Agency, *CO_2 Emissions from Fuel Combustion*, **2019**.

[17] Intergovernmental Panel on Climate Change, *Climate Change 2013: The Physical Science Basis*, Cambridge University Press, Cambridge, New York, **2013**.

[18] United Nations Framework Convention on Climate Change, *Kyoto Protocol to the United Nations Framework Convention on Climate Change*, Kyoto, Japan, **1997**.

[19] United Nations Framework Convention on Climate Change, *Paris Agreement to the United Nations Framework Convention on Climate Change*, Paris, France, **2016**.

[20] Bundesministerium für Transport und Digitale Infrastruktur, *Verkehr in Zahlen,* 47th ed., **2018/2019**.

[21] Bundesministerium für Transport und Digitale Infrastruktur, *Verkehr in Zahlen,* 48th ed., **2019/2020**.

[22] T. Bourdrel, M.-A. Bind, Y. Béjot, O. Morel, J.-F. Argacha, *Arch. Cardiovasc. Dis.* **2017**, *110*, 634-642. https://doi.org/10.1016/j.acvd.2017.05.003

[23] D. Ye, M. Klein, H. H. Chang, J. A. Sarnat, J. A. Mulholland, E. S. Edgerton, A. Winquist, P. E. Tolbert, S. E. Sarnat, *Epidemiology* **2017**, *28*, 197-206. https://doi.org/10.1097/EDE.0000000000000607

[24] O. K. Kurt, J. Zhang, K. E. Pinkerton, *Curr. Opin. Pulm. Med.* **2016**, *22*, 138-143. https://doi.org/10.1097/MCP.0000000000000248

[25] S. Ha, R. Sundaram, G. M. Buck Louis, C. Nobles, I. Seeni, S. Sherman, P. Mendola, *Fertil. Steril.* **2018**, *109*, 148-153. https://doi.org/10.1016/j.fertnstert.2017.09.037

[26] Z. J. Andersen et al., *Neuro-oncology* **2018**, *20*, 420-432. https://doi.org/10.1093/neuonc/nox163

[27] L. Stabile, A. Massimo, V. Rizza, M. D'Apuzzo, A. Evangelisti, M. Scungio, A. Frattolillo, G. Cortellessa, G. Buonanno, *Sci. Total Environ.* **2019**, *656*, 1032-1042. https://doi.org/10.1016/j.scitotenv.2018.11.432

[28] European Community, *Commission Decision 70/220/EWG*, **1970**.

[29] European Community, *Commission Decision 77/102/EWG*, **1977**.

[30] European Community, *Commission Decision 88/436/EWG*, **1988**.

[31] European Community, *Commission Decision 715/2007*, **2007**.

[32] K. Inagaki, T. Fuyuto, K. Nishikawa, K. Nakakita, I. Sakata in *SAE Technical Paper Series*, SAE International 400 Commonwealth Drive, Warrendale, PA, United States, **2006**.

[33] P. W. Bessonette, C. H. Schleyer, K. P. Duffy, W. L. Hardy, M. P. Liechty in *SAE Technical Paper Series*, SAE International 400 Commonwealth Drive, Warrendale, PA, United States, **2007**.

[34] D. Splitter, R. Reitz, R. Hanson, *SAE Int. J. Fuels Lubr.* **2010**, *3*, 742-756

[35] A. Gerini, G. Monnier, R. Bonetto in *SAE Technical Paper Series*, SAE International400 Commonwealth Drive, Warrendale, PA, United States, **1996**.

[36] B.-Q. He, *Renew. Sust. Energ. Rev.* **2016**, *60*, 570-586. https://doi.org/10.1016/j.rser.2016.01.093

[37] M. Sellnau, W. Moore, J. Sinnamon, K. Hoyer, M. Foster, H. Husted, *SAE Int. J. Fuels Lubr.* **2015**, *8*, 775-790

[38] J. J. Berzelius (Ed.) *Annual Report on the Progress in Physics and Chemistry*, Royal Swedish Academy of Sciences, **1835**.

[39] P. E. McGovern et al., *Proc. Natl. Acad. Sci. U. S. A.* **2004**, *101*, 17593-17598. https://doi.org/10.1073/pnas.0407921102

[40] W. Ostwald, *Z. Phys. Chem.* **1894**, *15U*, 699-708. https://doi.org/10.1515/zpch-1894-1548

[41] J. W. Erisman, M. A. Sutton, J. Galloway, Z. Klimont, W. Winiwarter, *Nature Geosci.* **2008**, *1*, 636-639. https://doi.org/10.1038/ngeo325

[42] W. Ostwald, US858904, **1902**.

[43] J. Dwyer, D. J. Rawlence, *Catal. Today* **1993**, *18*, 487-507. https://doi.org/10.1016/0920-5861(93)80065-9

[44] R. Sadeghbeigi, *Fluid catalytic cracking handbook. An expert guide to the practical operation, design, and optimization of FCC units,* 4th ed., Butterworth-Heinemann, Amsterdam, **2020**.

[45] H. Schulz, *Appl. Catal. A: Gen.* **1999**, *186*, 3-12. https://doi.org/10.1016/S0926-860X(99)00160-X

[46] M. E. Dry, *Catal. Today* **2002**, *71*, 227-241. https://doi.org/10.1016/S0920-5861(01)00453-9

[47] A. P. Steynberg in *Studies in Surface Science and Catalysis*, *Vol. 152* (Eds.: A. Steynberg, M. Dry), Elsevier, Amsterdam, **2006**.

[48] B. Cornils, J. Hibbel, P. Ruprecht, J. Langhoff, R. Dürrfeld, *Fuel Process. Technol.* **1984**, *9*, 251-264.
https://doi.org/10.1016/0378-3820(84)90045-6

[49] J. R. van Veen, *Catal. Today* **2017**, *292*, 2-25.
https://doi.org/10.1016/j.cattod.2016.09.027

[50] J. K. Stille, R. Divakaruni, *J. Organomet. Chem.* **1979**, *169*, 239-248.
https://doi.org/10.1016/S0022-328X(00)81163-8

[51] R. Jira, *Angew. Chem. Int. Ed.* **2009**, *48*, 9034-9037.
https://doi.org/10.1002/anie.200903992

[52] J. A. Keith, P. M. Henry, *Angew. Chem. Int. Ed.* **2009**, *48*, 9038-9049.
https://doi.org/10.1002/anie.200902194

[53] M. G. Kulkarni, Y. B. Shaikh, A. S. Borhade, S. W. Chavhan, A. P. Dhondge, D. D. Gaikwad, M. P. Desai, D. R. Birhade, N. R. Dhatrak, *Tetrahedron Lett.* **2013**, *54*, 2293-2295.
https://doi.org/10.1016/j.tetlet.2013.01.082

[54] R. L. Pruett in *Advances in Organometallic Chemistry*, *Vol. 17* (Eds.: F. G. A. Stone, B. Bogdanovich), Elsevier, **1979**.

[55] B. Cornils, W. A. Herrmann, M. Rasch, *Angew. Chem. Int. Ed.* **1994**, *33*, 2144-2163.
https://doi.org/10.1002/anie.199421441

[56] F. G. Ciapetta, D. N. Wallace, *Catal. Rev.* **1972**, *5*, 67-158.
https://doi.org/10.1080/01614947208076866

[57] M. J. Sterba, V. Haensel, *Ind. Eng. Chem. Prod. Res. Dev.* **1976**, *15*, 2-17.
https://doi.org/10.1021/i360057a002

[58] M.-O. Coppens, G. F. Froment, *Chem. Eng. Sci.* **1996**, *51*, 2283-2292.
https://doi.org/10.1016/0009-2509(96)00085-1

[59] H. Sinn, W. Kaminsky in *Advances in Organometallic Chemistry*, *Vol. 18* (Eds.: F. G. A. Stone, R. West), Academic Press, New York, **1980**.

[60] K. Soga, *Prog. Polym. Sci.* **1997**, *22*, 1503-1546.
https://doi.org/10.1016/S0079-6700(97)00003-8

[61] M. Röper, *Chemie in unserer Zeit* **2006**, *40*, 126-135.
https://doi.org/10.1002/ciuz.200600373

[62] N. Miranda-García, M. I. Maldonado, J. M. Coronado, S. Malato, *Catal. Today* **2010**, *151*, 107-113. https://doi.org/10.1016/j.cattod.2010.02.044

[63] N. Yahya, F. Aziz, N. A. Jamaludin, M. A. Mutalib, A. F. Ismail, W. N. W. Salleh, J. Jaafar, N. Yusof, N. A. Ludin, *J. Environ. Chem. Eng.* **2018**, *6*, 7411-7425. https://doi.org/10.1016/j.jece.2018.06.051

[64] E. J. Houdry, US2742437, **1952**.

[65] Maga J. A., Goldsmith, J., R., *J. Air Pollut. Control Assoc.* **1960**, *10*, 453-455. https://doi.org/10.1080/00022470.1960.10467958

[66] Maga J. A., Hass, G., C., *J. Air Pollut. Control Assoc.* **1960**, *10*, 393-396. https://doi.org/10.1080/00022470.1960.10467949

[67] 88th United States Congress, *Clean Air Act*. *88-206*, **1963**.

[68] O. Deutschmann, J.-D. Grunwaldt, *Chem. Ing. Tech.* **2013**, *85*, 595-617. https://doi.org/10.1002/cite.201200188

[69] M. V. Twigg, *Philos. Trans. A Math. Phys. Eng. Sci.* **2005**, *363*, 1013-33; discussion 1035-40. https://doi.org/10.1098/rsta.2005.1547

[70] J. Kašpar, P. Fornasiero, N. Hickey, *Catal. Today* **2003**, *77*, 419-449. https://doi.org/10.1016/S0920-5861(02)00384-X

[71] M. Shelef, Gandhi, H., S., *Platin. Met. Rev.* **1974**, *18*, 2-14

[72] Graham, A., G., S. E. Wanke, *J. Catal.* **1981**, *68*, 1-8. https://doi.org/10.1016/0021-9517(81)90032-4

[73] D. Seyferth, *Organometallics* **2003**, *22*, 5154-5178. https://doi.org/10.1021/om030621b

[74] Y.-F. Y. Yao, *J. Catal.* **1975**, *36*, 266-275. https://doi.org/10.1016/0021-9517(75)90036-6

[75] Y.-F. Y. Yao, *J. Catal.* **1977**, *46*, 388-401. https://doi.org/10.1016/0021-9517(77)90223-8

[76] Y.-F. Y. Yao, *J. Catal.* **1973**, *28*, 139-149. https://doi.org/10.1016/0021-9517(73)90187-5

[77] Y.-F. Y. Yao, J. T. Kummer, *J. Catal.* **1973**, *28*, 124-138. https://doi.org/10.1016/0021-9517(73)90186-3

[78] Y.-F. Y. Yao, *J. Catal.* **1974**, *33*, 108-122. https://doi.org/10.1016/0021-9517(74)90250-4

[79] B. J. K. Acres, B. J. Cooper, *Platin. Met. Rev.* **1972**, *16*, 74-86

[80] M. V. Twigg, *Platin. Met. Rev.* **1999**, *43*, 168-171

[81] J. C. Wurzenberger, G. Auzinger, R. Heinzle, R. Wanker in *SAE Technical Paper Series*, SAE International400 Commonwealth Drive, Warrendale, PA, United States, **2006**.

[82] B. A. A. L. van Setten, M. Makkee, J. A. Moulijn, *Catal. Rev.* **2001**, *43*, 489-564. https://doi.org/10.1081/CR-120001810

[83] D. Fino, *Sci. Technol. Adv. Mater.* **2007**, *8*, 93-100. https://doi.org/10.1016/j.stam.2006.11.012

[84] W. S. Epling, L. E. Campbell, A. Yezerets, N. W. Currier, J. E. Parks, *Catal. Rev.* **2004**, *46*, 163-245. https://doi.org/10.1081/CR-200031932

[85] D. Klukowski, P. Balle, B. Geiger, S. Wagloehner, S. Kureti, B. Kimmerle, A. Baiker, J.-D. Grunwaldt, *Appl. Catal. B: Environ.* **2009**, *93*, 185-193. https://doi.org/10.1016/j.apcatb.2009.09.028

[86] P. G. Kompio, A. Brückner, F. Hipler, G. Auer, E. Löffler, W. Grünert, *J. Catal.* **2012**, *286*, 237-247. https://doi.org/10.1016/j.jcat.2011.11.008

[87] M. Goldbach, A. Roppertz, P. Langenfeld, M. Wackerhagen, S. Füger, S. Kureti, *Chem. Eng. Technol.* **2017**, *40*, 2035-2043. https://doi.org/10.1002/ceat.201700261

[88] P. Forzatti, L. Lietti, I. Nova, E. Tronconi, *Catal. Today* **2010**, *151*, 202-211. https://doi.org/10.1016/j.cattod.2010.02.025

[89] T. Johnson, A. Joshi, *SAE Int. J. Engines* **2018**, *11*, 1307-1330. https://doi.org/10.4271/2018-01-0329

[90] W. Weisweiler, *Chem. Ing. Tech.* **2000**, *72*, 441-449. https://doi.org/10.1002/1522-2640(200005)72:5%3C441::AID-CITE441%3E3.0.CO;2-R

[91] Y. Teraoka, K. Kanada, S. Kagawa, *Appl. Catal. B: Environ.* **2001**, *34*, 73-78. https://doi.org/10.1016/S0926-3373(01)00202-8

[92] Y. Teraoka, W. F. Shangguan, S. Kagawa, *Res. Chem. Intermed.* **2000**, *26*, 201-206. https://doi.org/10.1163/156856700X00246

[93] S. Kureti, K. Hizbullah, W. Weisweiler, *Chem. Eng. Technol.* **2003**, *26*, 1003-1006. https://doi.org/10.1002/ceat.200301759

[94] H. Bockhorn, S. Kureti, D. Reichert, *Top. Catal.* **2007**, *42-43*, 283-286. https://doi.org/10.1007/s11244-007-0192-0

[95] I. Nova, C. Ciardelli, E. Tronconi, D. Chatterjee, M. Weibel, *AIChE J.* **2009**, *55*, 1514-1529. https://doi.org/10.1002/aic.11750

[96] S. Djerad, M. Crocoll, S. Kureti, L. Tifouti, W. Weisweiler, *Catal. Today* **2006**, *113*, 208-214. https://doi.org/10.1016/j.cattod.2005.11.067

[97] M. Schwidder, S. M. Kumar, K. Klementiev, M. M. Pohl, A. Brückner, W. Grünert, *J. Catal.* **2005**, *231*, 314-330. https://doi.org/10.1016/j.jcat.2005.01.031

[98] P. Balle, B. Geiger, D. Klukowski, M. Pignatelli, S. Wohnrau, M. Menzel, I. Zirkwa, G. Brunklaus, S. Kureti, *Appl. Catal. B: Environ.* **2009**, *91*, 587-595. https://doi.org/10.1016/j.apcatb.2009.06.031

[99] M. T. Jan, S. Kureti, K. Hizbullah, N. Jan, *Chem. Eng. Technol.* **2007**, *30*, 1440-1444. https://doi.org/10.1002/ceat.200700076

[100] T. Günter, D. E. Doronkin, A. Boubnov, H. W. P. Carvalho, M. Casapu, J.-D. Grunwaldt, *Top. Catal.* **2016**, *59*, 866-874. https://doi.org/10.1007/s11244-016-0561-7

[101] M. Jabłońska, R. Palkovits, *Appl. Catal. B: Environ.* **2016**, *181*, 332-351. https://doi.org/10.1016/j.apcatb.2015.07.017

[102] R. F. Anderson, D. C. Allensworth, W. J. DeGroot, *Ann. Intern. Med.* **1967**, *67*, 1172-1182. https://doi.org/10.7326/0003-4819-67-6-1172

[103] L. D. Prockop, R. I. Chichkova, *J. Neurol. Sci.* **2007**, *262*, 122-130. https://doi.org/10.1016/j.jns.2007.06.037

[104] J. A. Raub, M. Mathieu-Nolf, N. B. Hampson, S. R. Thom, *Toxicology* **2000**, *145*, 1-14. https://doi.org/10.1016/s0300-483x(99)00217-6

[105] G. Ertl, *Handbook of heterogeneous catalysis,* 2nd, completely rev. and enl. ed. ed., Wiley-VCH, Weinheim, Chichester, **2008**.

[106] T. Engel, G. Ertl, *J. Chem. Phys.* **1978**, *69*, 1267. https://doi.org/10.1063/1.436666

[107] I. Chorkendorff, J. W. Niemantsverdriet, *Concepts of modern catalysis and kinetics*, Wiley-VCH, Weinheim, **2003**.

[108] A. Colson, *Compt. rend.* **1901**, *132*, 467

[109] M. Nicloux, *Compt. rend.* **1898**, *126*, 746

[110] A. Gautier, *Compt. rend.* **1898**, *126*, 793, 931

[111] F. C. Phillips, *Z. anorg. Chem.* **1894**, *6*, 243

[112] R. Abegg, F. Auerbach (Eds.) *Handbuch der Anorganischen Chemie in vier Bänden. Die Elemente der vierten Gruppe des periodischen Systems*, S. Hirzel, Leipzig, **1909**, *Vol. 3*

[113] A. B. Lamb, W. C. Bray, J. C. W. Frazer, *J. Ind. Eng. Chem.* **1920**, *12*, 213-221. https://doi.org/10.1021/ie50123a007

[114] *Chemistry International* **2019**, *41*, 1-60. https://doi.org/10.1515/ci-2019-0100

[115] D. Fejes, L. Forró, K. Hernadi, *phys. stat. sol. (b)* **2010**, *247*, 2713-2716. https://doi.org/10.1002/pssb.201000235

[116] C. Zhang, S. Li, G. Wu, J. Gong, *Catal. Today* **2014**, *233*, 53-60. https://doi.org/10.1016/j.cattod.2013.08.013

[117] G. Ertl, H. Knözinger, J. Weitkamp, *Preparation of Solid Catalysts*, Wiley, Weinheim, **2008**.

[118] T. Ahn, J. H. Kim, H.-M. Yang, J. W. Lee, J.-D. Kim, *J. Phys. Chem. C* **2012**, *116*, 6069-6076.
https://doi.org/10.1021/jp211843g

[119] H. Rashid, M. A. Mansoor, B. Haider, R. Nasir, S. B. Abd Hamid, A. Abdulrahman, *Sep. Sci. Technol.* **2020**, *55*, 1207-1215. https://doi.org/10.1080/01496395.2019.1585876

[120] G. Ertl (Ed.) *Handbook of heterogeneous catalysis,* 2nd, completely rev. and enl. ed. ed., Wiley-VCH, Weinheim, Chichester, **2008**.

[121] K. P. de Jong, *Synthesis of solid catalysts*, Wiley-VCH, Weinheim, **2009**.

[122] L. L. Hench, J. K. West, *Chem. Rev.* **1990**, *90*, 33-72. https://doi.org/10.1021/cr00099a003

[123] L. Mädler, H. K. Kammler, R. Mueller, S. E. Pratsinis, *J. Aerosol Sci.* **2002**, *33*, 369-389.
https://doi.org/10.1016/S0021-8502(01)00159-8

[124] W. Y. Teoh, R. Amal, L. Mädler, *Nanoscale* **2010**, *2*, 1324-1347. https://doi.org/10.1039/c0nr00017e

[125] S. Kacimi, J. Barbier, R. Taha, D. Duprez, *Catal. Lett.* **1993**, *22*, 343-350. https://doi.org/10.1007/BF00807243

[126] M. Kang, *Appl. Catal. A: Gen.* **2003**, *251*, 143-156. https://doi.org/10.1016/S0926-860X(03)00324-7

[127] J. Luo, M. Meng, X. Li, Y. Zha, T. Hu, Y. Xie, J. Zhang, *J. Catal.* **2008**, *254*, 310-324. https://doi.org/10.1016/j.jcat.2008.01.007

[128] B. M. Reddy, K. N. Rao, P. Bharali, *Ind. Eng. Chem. Res.* **2009**, *48*, 8478-8486. https://doi.org/10.1021/ie900755b

[129] G. Pantaleo, L. F. Liotta, A. M. Venezia, G. Deganello, E. M. Ezzo, M. A. El Kherbawi, H. Atia, *Mat. Chem. Phys.* **2009**, *114*, 604-611. https://doi.org/10.1016/j.matchemphys.2008.10.006

[130] R. Prasad, P. Singh, *Catal. Rev.* **2012**, *54*, 224-279. https://doi.org/10.1080/01614940.2012.648494

[131] J. T. Richardson, *Principles of Catalyst Development*, Springer US, Boston, MA, s.l., **1989**.

[132] J.-D. Grunwaldt, C. Kiener, C. Wögerbauer, A. Baiker, *J. Catal.* **1999**, *181*, 223-232. https://doi.org/10.1006/jcat.1998.2298

[133] M. Maciejewski, P. Fabrizioli, J.-D. Grunwaldt, O. Sven Becker, A. Baiker, *Phys. Chem. Chem. Phys.* **2001**, *3*, 3846-3855. https://doi.org/10.1039/b101184g

[134] M. Haruta, S. Tsubota, T. Kobayashi, H. Kageyama, M. J. Genet, B. Delmon, *J. Catal.* **1993**, *144*, 175-192. https://doi.org/10.1006/jcat.1993.1322

[135] X. Xu, J. Li, Z. Hao, W. Zhao, C. Hu, *Mater. Res. Bull.* **2006**, *41*, 406-413. https://doi.org/10.1016/j.materresbull.2005.08.003

[136] A. Törncrona, M. Skoglundh, P. Thormählen, E. Fridell, E. Jobson, *Appl. Catal. B: Environ.* **1997**, *14*, 131-145. https://doi.org/10.1016/S0926-3373(97)00018-0

[137] S. Royer, D. Duprez, *ChemCatChem* **2011**, *3*, 24-65. https://doi.org/10.1002/cctc.201000378

[138] J. T. Kummer in *Advances in Chemistry*, *Vol. 143* (Ed.: J. E. McEvoy), American Chemical Society, WASHINGTON, D. C., **1975**.

[139] N. W. Cant, *J. Catal.* **1980**, *62*, 173-175.
https://doi.org/10.1016/0021-9517(80)90434-0

[140] Y.-F. Y. Yao, *J. Catal.* **1984**, *87*, 152-162.
https://doi.org/10.1016/0021-9517(84)90178-7

[141] E. C. Akubuiro, X. E. Verykios, L. Lesnick, *Appl. Catal.* **1985**, *14*, 215-227.
https://doi.org/10.1016/S0166-9834(00)84356-0

[142] B. Harrison, af Diwell, C. Hallett, *Platinum Metals Review* **1988**, *32*, 73-83

[143] G. Ertl, *Science* **1991**, *254*, 1750-1755.
https://doi.org/10.1126/science.254.5039.1750

[144] S. H. Oh, C. C. Eickel, *J. Catal.* **1991**, *128*, 526-536.
https://doi.org/10.1016/0021-9517(91)90310-Z

[145] J. Barbier, D. Duprez, *Appl. Catal. B: Environ.* **1993**, *3*, 61-83.
https://doi.org/10.1016/0926-3373(93)80069-P

[146] R. Imbihl, G. Ertl, *Chem. Rev.* **1995**, *95*, 697-733.
https://doi.org/10.1021/cr00035a012

[147] M. Kolodziejczyk, R. E. Colen, M. Berdau, B. Delmon, J. H. Block, *Surf. Sci.* **1997**, *375*, 235-249.
https://doi.org/10.1016/S0039-6028(96)01297-6

[148] J. Dicke, H. H. Rotermund, J. Lauterbach, *Surf. Sci.* **2000**, *454-456*, 352-357.
https://doi.org/10.1016/S0039-6028(00)00189-8

[149] S. Abbet, U. Heiz, H. Häkkinen, U. Landman, *Physical review letters* **2001**, *86*, 5950-5953.
https://doi.org/10.1103/PhysRevLett.86.5950

[150] Y. J. Mergler, A. van Aalst, J. van Delft, B. E. Nieuwenhuys, *Appl. Catal. B: Environ.* **1996**, *10*, 245-261.
https://doi.org/10.1016/S0926-3373(96)00017-3

[151] M. E. Günay, R. Yildirim, *ChemCatChem* **2013**, *5*, 1395-1406.
https://doi.org/10.1002/cctc.201200665

[152] J. Lin, X. Wang, T. Zhang, *Chin. J. Catal.* **2016**, *37*, 1805-1813.
https://doi.org/10.1016/S1872-2067(16)62513-5

[153] D. A. H. Cunningham, T. Kobayashi, N. Kamijo, M. Haruta, *Catal. Lett.* **1994**, *25*, 257-264.
https://doi.org/10.1007/BF00816305

[154] M. Dekkers, M. Lippits, B. Nieuwenhuys, *Catal. Today* **1999**, *54*, 381-390. https://doi.org/10.1016/S0920-5861(99)00201-1

[155] K. Qian, W. Huang, Z. Jiang, H. Sun, *J. Catal.* **2007**, *248*, 137-141. https://doi.org/10.1016/j.jcat.2007.02.010

[156] W. Liu, M. Flytzani-Stephanopoulos, *J. Catal.* **1995**, *153*, 304-316. https://doi.org/10.1006/jcat.1995.1132

[157] W. Liu, M. Flytzani-Stephanopoulos, *J. Catal.* **1995**, *153*, 317-332. https://doi.org/10.1006/jcat.1995.1133

[158] K. Christmann, S. Schwede, S. Schubert, W. Kudernatsch, *ChemPhysChem* **2010**, *11*, 1344-1363. https://doi.org/10.1002/cphc.200900769

[159] R. Ferrauto, *J. Catal.* **1974**, *33*, 249-255. https://doi.org/10.1016/0021-9517(74)90268-1

[160] Y.-F. Yu-Yao, J. T. Kummer, *J. Catal.* **1987**, *106*, 307-312. https://doi.org/10.1016/0021-9517(87)90237-5

[161] Y.-F. Y. Yao, *J. Catal.* **1975**, *39*, 104-114. https://doi.org/10.1016/0021-9517(75)90286-9

[162] R. M. Heck, R. J. Farrauto, S. T. Gulati, *Catalytic air pollution control. Commercial technology,* 2. ed. ed., Wiley-Interscience, New York, **2002**.

[163] S. Rood, S. Eslava, A. Manigrasso, C. Bannister, *P. I. Mech. Eng. D: J. Automot. Eng.* **2020**, *234*, 936-949. https://doi.org/10.1177/0954407019859822

[164] L. Yang, S. Lin, X. Yang, W. Fang, R. Zhou, *J. Hazard. Mater.* **2014**, *279*, 226-235. https://doi.org/10.1016/j.jhazmat.2014.06.076

[165] L. Yang, X. Yang, S. Lin, R. Zhou, *Catal. Sci. Technol.* **2015**, *5*, 2688-2695. https://doi.org/10.1039/C5CY00117J

[166] L. Lan, S. Chen, Y. Cao, M. Zhao, M. Gong, Y. Chen, *J. Colloid Interface Sci.* **2015**, *450*, 404-416. https://doi.org/10.1016/j.jcis.2015.03.042

[167] J. Guo, Z. Shi, D. Wu, H. Yin, M. Gong, Y. Chen, *J. Alloys Compd.* **2015**, *621*, 104-115. https://doi.org/10.1016/j.jallcom.2014.09.189

[168] A. Papavasiliou, A. Tsetsekou, V. Matsouka, M. Konsolakis, I. V. Yentekakis, *Appl. Catal. A: Gen.* **2010**, *382*, 73-84. https://doi.org/10.1016/j.apcata.2010.04.025

[169] M. Haneda, Y. Tomida, T. Takahashi, Y. Azuma, T. Fujimoto, *Catal. Commun.* **2017**, *90*, 1-4. https://doi.org/10.1016/j.catcom.2016.11.009

[170] A. Boubnov, S. Dahl, E. Johnson, A. P. Molina, S. B. Simonsen, F. M. Cano, S. Helveg, L. J. Lemus-Yegres, J.-D. Grunwaldt, *Appl. Catal. B: Environ.* **2012**, *126*, 315-325. https://doi.org/10.1016/j.apcatb.2012.07.029

[171] G.-M. Schwab, G. Drikos, *Z. Phys. Chem.* **1939**, *185A*. https://doi.org/10.1515/zpch-1939-18531

[172] J. Gao, C. Jia, L. Zhang, H. Wang, Y. Yang, S.-F. Hung, Y.-Y. Hsu, B. Liu, *J. Catal.* **2016**, *341*, 82-90. https://doi.org/10.1016/j.jcat.2016.06.009

[173] Y. Yi, P. Zhang, Z. Qin, C. Yu, W. Li, Q. Qin, B. Li, M. Fan, X. Liang, L. Dong, *RSC Adv.* **2018**, *8*, 7110-7122. https://doi.org/10.1039/C7RA12635B

[174] J.-L. Cao, Y. Wang, X.-L. Yu, S.-R. Wang, S.-H. Wu, Z.-Y. Yuan, *Appl. Catal. B: Environ.* **2008**, *79*, 26-34. https://doi.org/10.1016/j.apcatb.2007.10.005

[175] Y. Cui, L. Xu, M. Chen, C. Lv, X. Lian, C. Wu, B. Yang, Z. Miao, F. Wang, X. Hu, *Catalysts* **2019**, *9*, 724. https://doi.org/10.3390/catal9090724

[176] S. Ma, G. Lu, Y. Shen, Y. Guo, Y. Wang, Y. Guo, *Catal. Sci. Technol.* **2011**, *1*, 669. https://doi.org/10.1039/c1cy00049g

[177] A. Biabani-Ravandi, M. Rezaei, *Chem. Eng. J.* **2012**, *184*, 141-146. https://doi.org/10.1016/j.cej.2012.01.017

[178] G. Li, L. Li, Y. Li, J. Shi, *New J. Chem.* **2015**, *39*, 1742-1748. https://doi.org/10.1039/C4NJ01919A

[179] J. Li, G. Lu, G. Wu, D. Mao, Y. Guo, Y. Wang, Y. Guo, *RSC Adv.* **2013**, *3*, 12409. https://doi.org/10.1039/c3ra41272e

[180] V. L. Veselovskii, V. K. Yatsimirskii, O. V. Ishchenko, S. V. Gaidai, B. G. Mischanchuk, M. I. Zakharenko, *Powder Metall. Met. Ceram.* **2012**, *50*, 744-748. https://doi.org/10.1007/s11106-012-9384-7

[181] E. V. Ishchenko, S. V. Gaidai, A. A. Byeda, T. M. Zakharova, A. G. Dyachenko, E. V. Prilutskiy, *J. Superhard Mater.* **2017**, *39*, 336-342.
https://doi.org/10.3103/S1063457617050057

[182] B. Faure, P. Alphonse, *Appl. Catal. B: Environ.* **2016**, *180*, 715-725.
https://doi.org/10.1016/j.apcatb.2015.07.019

[183] Y. Sun, M. Delucchi, J. Ogden, *Int. J. Hydrog. Energy* **2011**, *36*, 11116-11127.
https://doi.org/10.1016/j.ijhydene.2011.05.157

[184] A. B. Laursen, J. Sehested, I. Chorkendorff, P. C. Vesborg, *Chin. J. Catal.* **2018**, *39*, 16-26.
https://doi.org/10.1016/S1872-2067(17)62979-6

[185] J. Kielhorn, C. Melber, D. Keller, I. Mangelsdorf, *Int. J. Hyg. Environ. Health* **2002**, *205*, 417-432.
https://doi.org/10.1078/1438-4639-00180

[186] K. Ravindra, L. Bencs, R. van Grieken, *Sci. Total Environ.* **2004**, *318*, 1-43.
https://doi.org/10.1016/S0048-9697(03)00372-3

[187] S. Rauch, G. M. Morrison, *Elements* **2008**, *4*, 259-263.
https://doi.org/10.2113/GSELEMENTS.4.4.259

[188] A. Turner, S. Price, *Environ. Sci. Technol.* **2008**, *42*, 9443-9448.
https://doi.org/10.1021/es801189q

[189] C. L. S. Wiseman, F. Zereini, *Sci. Total Environ.* **2009**, *407*, 2493-2500.
https://doi.org/10.1016/j.scitotenv.2008.12.057

[190] L. J. E. Hofer, P. Gussey, R. B. Anderson, *J. Catal.* **1964**, *3*, 451-460.
https://doi.org/10.1016/0021-9517(64)90148-4

[191] Y.-F. Y. Yao, *J. Catal.* **1975**, *39*, 104-114.
https://doi.org/10.1016/0021-9517(75)90286-9

[192] J. S. Walker, G. I. Straguzzi, W. H. Manogue, G. C. A. Schuit, *J. Catal.* **1988**, *110*, 298-309.
https://doi.org/10.1016/0021-9517(88)90321-1

[193] P. Li, D. E. Miser, S. Rabiei, R. T. Yadav, M. R. Hajaligol, *Appl. Catal. B: Environ.* **2003**, *43*, 151-162.
https://doi.org/10.1016/S0926-3373(02)00297-7

[194] H.-Y. Lin, Y.-W. Chen, W.-J. Wang, *J. Nanopart. Res.* **2005**, *7*, 249-263.
https://doi.org/10.1007/s11051-005-4717-9

[195] A. Szegedi, M. Hegedus, J. L. Margitfalvi, I. Kiricsi, *Chem. Commun.* **2005**, 1441-1443.
https://doi.org/10.1039/b416852f

[196] J. G. Carriazo, M. A. Centeno, J. A. Odriozola, S. Moreno, R. Molina, *Appl. Catal. A: Gen.* **2007**, *317*, 120-128.
https://doi.org/10.1016/j.apcata.2006.10.009

[197] H. Bao, X. Chen, J. Fang, Z. Jiang, W. Huang, *Catal. Lett.* **2008**, *125*, 160-167.
https://doi.org/10.1007/s10562-008-9540-3

[198] Y. Ren, Z. Ma, L. Qian, S. Dai, H. He, P. G. Bruce, *Catal. Lett.* **2009**, *131*, 146-154.
https://doi.org/10.1007/s10562-009-9931-0

[199] I. Hnat, I. Kocemba, J. Rynkowski, T. Onfroy, S. Dzwigaj, *Catal. Today* **2011**, *176*, 229-233.
https://doi.org/10.1016/j.cattod.2010.12.052

[200] Q.-X. Gao, X.-F. Wang, J.-L. Di, X.-C. Wu, Y.-R. Tao, *Catal. Sci. Technol.* **2011**, *1*, 574.
https://doi.org/10.1039/c1cy00080b

[201] M. Tepluchin, M. Casapu, A. Boubnov, H. Lichtenberg, Di Wang, S. Kureti, J.-D. Grunwaldt, *ChemCatChem* **2014**, *6*, 1763-1773.
https://doi.org/10.1002/cctc.201301040

[202] I. H. Kim, H. O. Seo, E. J. Park, S. W. Han, Y. D. Kim, *Scientific reports* **2017**, *7*, 40497.
https://doi.org/10.1038/srep40497

[203] W. Li, Y. Hu, H. Jiang, Y. Jiang, Y. Wang, S. Huang, P. Biswas, C. Li, *Appl. Surf. Sci.* **2018**, *444*, 763-771.
https://doi.org/10.1016/j.apsusc.2018.02.095

[204] R. Schoch, H. Huang, V. Schünemann, M. Bauer, *ChemPhysChem* **2014**, *15*, 3768-3775.
https://doi.org/10.1002/cphc.201402551

[205] R. Schoch, M. Bauer, *ChemSusChem* **2016**, *9*, 1996-2004.
https://doi.org/10.1002/cssc.201600508

[206] I. Manuel, J. Chaubet, C. Thomas, H. Colas, N. Matthess, G. Djéga-Mariadassou, *J. Catal.* **2004**, *224*, 269-277.
https://doi.org/10.1016/j.jcat.2004.03.011

[207] S. Wagloehner, D. Reichert, D. Leon-Sorzano, P. Balle, B. Geiger, S. Kureti, *J. Catal.* **2008**, *260*, 305-314.
https://doi.org/10.1016/j.jcat.2008.09.018

[208] M. Tepluchin, D. K. Pham, M. Casapu, L. Mädler, S. Kureti, J.-D. Grunwaldt, *Catal. Sci. Technol.* **2015**, *5*, 455-464.
https://doi.org/10.1039/C4CY00727A

[209] M. Tepluchin, S. Kureti, M. Casapu, E. Ogel, S. Mangold, J.-D. Grunwaldt, *Catal. Today* **2015**, *258*, 498-506.
https://doi.org/10.1016/j.cattod.2015.01.010

[210] G. Gutiérrez, A. Taga, B. Johansson, *Phys. Rev. B* **2001**, *65*.
https://doi.org/10.1103/PhysRevB.65.012101

[211] L. Smrcok, V. Langer, J. Krestan, *Acta Crystallogr., Sect. C: Cryst. Struct. Commun.* **2006**, *62*, i83-i84.
https://doi.org/10.1107/S0108270106026850

[212] Blake, R. L., Hessevick, R. E., *The American Mineralogist* **1966**, *51*, 123-129

[213] C. Greaves, *J. Solid State Chem.* **1983**, *49*, 325-333.
https://doi.org/10.1016/S0022-4596(83)80010-3

[214] W. Kündig, H. Bömmel, G. Constabaris, R. H. Lindquist, *Phys. Rev.* **1966**, *142*, 327-333.
https://doi.org/10.1103/PhysRev.142.327

[215] J. Pérez-Ramírez, J. C. Groen, A. Brückner, M. Kumar, U. Bentrup, M. N. Debbagh, L. Villaescusa, *J. Catal.* **2005**, *232*, 318-334.
https://doi.org/10.1016/j.jcat.2005.03.018

[216] J. Pérez-Ramírez, A. Gallardo-Llamas, *J. Phys. Chem. B* **2005**, *109*, 20529-20538.
https://doi.org/10.1021/jp054447b

[217] E. Hensen, Q. Zhu, M. Hendrix, A. R. Overweg, P. J. Kooyman, M. V. Sychev, R. A. van Santen, *J. Catal.* **2004**, *221*, 560-574.
https://doi.org/10.1016/j.jcat.2003.09.024

[218] M. Schwidder, M. S. Kumar, K. Klementiev, M. Pohl, A. Brückner, W. Grünert, *J. Catal.* **2005**, *231*, 314-330.
https://doi.org/10.1016/j.jcat.2005.01.031

[219] M. S. Kumar, M. Schwidder, W. Grünert, A. Brückner, *J. Catal.* **2004**, *227*, 384-397.
https://doi.org/10.1016/j.jcat.2004.08.003

[220] J. Pérez-Ramírez, M. S. Kumar, A. Brückner, *J. Catal.* **2004**, *223*, 13-27.
https://doi.org/10.1016/j.jcat.2004.01.007

[221] J. Janas, J. Gurgul, R. P. Socha, T. Shishido, M. Che, S. Dzwigaj, *Appl. Catal. B: Environ.* **2009**, *91*, 113-122.
https://doi.org/10.1016/j.apcatb.2009.05.013

[222] T. E. Westre, P. Kennepohl, J. G. DeWitt, B. Hedman, K. O. Hodgson, E. I. Solomon, *J. Am. Chem. Soc.* **1997**, *119*, 6297-6314. https://doi.org/10.1021/ja964352a

[223] J. P. Abulencia, L. Theodore, *Fluid flow for the practicing chemical engineer*, Wiley, Hoboken, NJ, **2010**, *v.11*

[224] H. Schlichting, K. Gersten, *Boundary-Layer Theory,* Ninth edition ed., Springer Berlin Heidelberg, Berlin, Heidelberg, **2017**.

[225] Jennifer Klaucke, bachelor thesis, Paderborn University, Paderborn, **2020**.

[226] ASWin, Quantachrome Instruments, **2012**.

[227] Paul Heiney, Datasqueeze, Pennsylvania, **2018**.

[228] H. P. Gunnlaugsson, *Hyperfine Interact.* **2016**, *237*. https://doi.org/10.1007/s10751-016-1271-z

[229] WinNormos, WissEl GmbH, **2008**.

[230] Origin 2020b, OriginLab Corporation, Northampton, MA, USA, **2020**.

[231] S. J. Pennycook, P. D. Nellist (Eds.) *Scanning Transmission Electron Microscopy. Imaging and Analysis*, Springer Science+Business Media LLC, New York, NY, **2011**.

[232] N. Tanaka, *Scanning transmission electron microscopy of nanomaterials. Basics of imaging and analysis*, Imperial College Press, London, **2015**.

[233] B. Ravel, M. Newville, *J. Synchrotron Radiat.* **2005**, *12*, 537-541. https://doi.org/10.1107/S0909049505012719

[234] Newville, Livins, Yacoby, Rehr, Stern, *Phys. Rev. B* **1993**, *47*, 14126-14131. https://doi.org/10.1103/PhysRevB.47.14126

[235] T. S. Ertel, H. Bertagnolli, S. Hückmann, U. Kolb, D. Peter, *Appl. Spectrosc.* **1992**, *46*, 690-698. https://doi.org/10.1366/0003702924125069

[236] N. Binsted, *CLRC Daresbury Laboratory Program* **1998**

[237] C. F. Macrae et al., *J. Appl. Crystallogr.* **2020**, *53*, 226-235. https://doi.org/10.1107/S1600576719014092

Abbreviations

A	*Reactor cross-section*
Abs	*Absorbing atom*
ADP	*Adenosine diphosphate*
Afac	*Amplitude reducing factor*
AMP	*Adenosine monophosphate*
AOP	*Advanced oxidation process*
ATP	*Adenosine triphosphate*
BET	*Brunauer-Emmett-Teller*
BJH	*Barrett-Joyner-Halenda*
BL	*Boundary layer*
Bs	*Backscattering atom*
CARB	*California Air Resources Board*
COHb	*Carboxyhemoglobin*
DPF	*Diesel particulate filter*
DRUVS	*Diffuse reflectance UV/Vis spectroscopy*
EC	*European Community*
EDX	*Energy dispersive X-ray spectroscopy*
E_f	*Fermi energy*
EU	*European Union*
EXAFS	*Extended X-ray absorption fine structure*
FSP	*Flame spray pyrolysis*
GHSV	*Gas hourly space velocity*
HAADF	*High angle annular dark-field*
Hb	*Hemoglobin*
HbO_2	*Oxyhemoglobin*
HC	*Hydrocarbons*
IWI	*Incipient wetness impregnation*
MI	*Multi-Step Impregnation*
MM	*Multi metal*
MvK	*Mars-van-Krevelen*
NMHC	*Non-methane hydrocarbons*
NMP	*N-Methyl-2-pyrrolidone*
NSR	NO_x *storage-reduction*
PGM	*Platinum group metals*
PIPS	*Passivated implanted planar silicone*
PM	*Particulate matter*
PN	*Particle number*
PROX	*Preferential oxidation (of HC or CO when* H_2 *is present)*
PXRD	*Powder X-ray diffractometry*
RDS	*Rate-determining step*
Re	*Reynolds number*
RT	*Room temperature*
SCR	*Selective catalytic reduction*
SI	*Single-Step Impregnation*
STEM	*Scanning transmission electron microscopy*
t	*Time*
TEL	*Tetraethyl lead*
THF	*Tetrahydrofuran*
TWC	*Three-way-catalyst*
USA	*United States of America*
v	*Velocity*
$\dot{V}$	*Volumetric gas flow*
VOC	*Volatile organic compounds*
WLTP	*Worldwide harmonized light vehicles test procedure*
XANES	*X-ray absorption near edge structure*
XAS	*X-ray absorption spectroscopy*
δ	*Boundary layer thickness*
ν	*Kinematic viscosity*
ν_{kin}	*Kinematic viscosity*
τ	*Residence time*

Figures

Figure 1.1: German road traffic 2017; numbers of registered vehicles by categories (left) and emissions resulting from road traffic (right) per year[21]..2

Figure 1.2: Extract of the patent W. Ostwald obtained for his process of nitric acid synthesis in 1907[42]..4

Figure 1.3: Extract from the original patent for a catalytic converter, patented from Eugene J. Houdry in 1956[64]. 5

Figure 1.4: Model reactions taking place in a modern three-way-catalyst. 5

Figure 1.5: Experimental and modelled conversion curves of CO (left), hydrocarbons (middle) and NO (right) vs. temperature and redox ratio, respectively reciprocal lambda value, reprinted from Wurzenberger et al.[81]..7

Figure 1.6: Main reactions correlated to selective catalytic reduction: 1) hydrolysis of urea to form ammonia; 2) reduction of NO with ammonia; 3) reduction of NO_2 with ammonia; 4) reduction of NO and NO_2 together[90]..7

Figure 1.7: Conceptual scheme of the steps required from educts and products in heterogeneous catalysis...9

Figure 1.8: Energetic diagram of the oxidation of carbon monoxide on a platinum catalyst[106,107]; adsorbed species are marked with "*" and the transition state with "≠"; numbers give the energy value of the respective step..10

Figure 1.9: Periodic table of elements according to IUPAC[114]; common elements in the active species of CO oxidation catalysts are marked in cyan; common elements in support materials are marked in orange; other elements tested as active species, promoter or dopant are colored pale cyan; here "common" is defined as "commonly tested in CO oxidation experiment" or even "used in actual applications"; the colored markings of materials for CO oxidation were made during the research work for this thesis and were not included in the original periodic table of elements by IUPAC..11

Figure 1.10: Number of publications in scientific journals per year about iron compounds in CO oxidation...17

Figure 1.11: Benchmarks of iron catalysts in CO oxidation experiments from important references of the last 20 years; black dottet line: 25 °C; black stripes: 30 °C; red dotted line: 50 % CO_2 yield; Li et al.: 1[193]; Lin et al.: 2[194] with addition of water to the gas stream; Szegedi et al.: 3[195]; Carriazo et al.: 4[196]; Bao et al.: 5[197]; Ren et al.: 6[198]; Hnat et al.: 7[199] FeSiBEA as-prepared; 7* FeSiBEA reduced prior to CO oxidation; Gao et al.: 8[200] a = α-Fe_2O_3 nanorods, b = α-Fe_2O_3 nanocubes, c = α-Fe_2O_3 nanotubes; Tepluchin et al.: 9[201] a = prepared by IWI, b = prepared by FSP, 9a* = addition of water to gas stream; Kim et al.: 10[202] measurements at constant temperatures of 30 and 100 °C, 10 = start, 10* = after 6 h, 10** = after 33 h; Li et al.: 11[203]; Schoch et al.: 12[204] Fe_2O_3 on γ-Al_2O_3, a = 1 wt%, b = 5 wt%, c = 10 wt%, 12*[205] catalysts prepared by reduction of the iron(III) precursor prior to impregnation of the support and calcination..18

Figure 1.12: Schematic description of CO oxidation on a heterogenous catalyst following a Langmuir-Hinshelwood or Eley-Rideal mechanism (left) or a Mars-van-Krevelen mechanism (right); both mechanisms are simplified and do not show each elementary step that occurs during reaction...19

Figure 3.1: Powder X-ray diffractograms of Fe01 to Fe20 and the γ-Al_2O_3 support........26

Figure 3.2: Experimental high-resolution powder X-ray diffractograms of catalyst Fe01 to Fe20 (orange to green) and calculated diffractograms of hematite (α-Fe_2O_3) and maghemite (γ-Fe_2O_3). 26

Figure 3.3: Lattice parameter a calculated from 2θ shifts of the (311), (222), (400), (511) and (440) crystal planes of the alumina support of catalyst Fe01 to Fe20, derived from high resolution PXRD data. 27

Figure 3.4: Mößbauer spectra (black dots) of catalysts Fe01 to Fe20 with corresponding fits (red: doublet, blue: sextet, green: cumulative fit) and the resulting parameters (bottom right)...28

Figure 3.5: Background-corrected diffuse reflectance UV/Vis-spectra of Fe01 to Fe20. .29

Figure 3.6: Results from peak deconvolution of the DRUV spectra of Fe01 to Fe20; experimental spectra after background subtraction (black) and the corresponding cumulative peak fit (dark green); the center of each peak is given in nanometers in the legend...30

Figure 3.7: Visualization of the normalized percentual areas of tetrahedral, octahedral, oligomeric and particulate iron oxide species (left); amounts of these species relative to the overall mass of the catalysts (right). 30

Figure 3.8: HAADF images (top row) and STEM-EDX images (red: oxygen K signal; green: aluminum K signal; blue: iron K signal) of Fe01 to Fe20 (left to right); scale bar 200 nm. 31

Figure 3.9: XANES region of the X-ray absorption spectra of Fe01 to Fe20 and α-Fe_2O_3 and zoomed in pre-peak of the respective samples...32

Figure 3.10: Fourier transformed EXAFS spectra of Fe01 to Fe20 and the corresponding fits. 33

Figure 3.11: Percentual CO_2 yield of Fe01 to Fe20 in continuous CO oxidation experiments (left) and at static temperatures (right)...35

Figure 3.12: Turnover frequencies of Fe01 to Fe20 in CO oxidation experiments with continuous heating (left) and at static temperatures (right). 36

Figure 4.1: Powder X-ray diffractograms of the catalysts MI01 to MI10 and the pure γ-Al_2O_3 support...39

Figure 4.2: Lattice parameter a calculated from PXRD reflexes of the lattice planes (440) and (400) of catalysts MI01 - MI10 and the pure support material and their linear fit. ...40

Figure 4.3: DRUV spectra of catalysts MI01 - MI10 and SI10 and resulting peak deconvolution with the respective peak centers and their convoluted fit. 41

Figure 4.4: Visualization of the normalized percentual areas of tetrahedral, octahedral, oligomeric and particulate iron oxide species (left) gained from peak deconvolution of the DRUV spectra of SI10 and MI01-MI10 and amounts of these species relative to the overall mass of the respective catalyst (right)..42

Figure 4.5: Comparison of the area-normalized DRUV spectra of the multi-step impregnated catalysts MI01, MI02, MI03, MI05 and MI10 with the respective single-step catalysts Fe01, Fe025, Fe05 and Fe10 and the reference catalyst SI10............................42

Figure 4.6: XANES spectra of MI01 - MI10, SI10 and the references α-Fe_2O_3 and γ-Fe_2O_3 at the Fe K-edge (7112 eV)..43

Figure 4.7: Baseline corrected pre-peaks of MI01 - MI10 and SI10 obtained from XANES spectra at the Fe K-edge...44

Figure 4.8: Graphs of conversion from CO oxidation experiments of MI01-MI10 and SI10 under continuous heating with 2 °C/min up to 600 °C. 48

Figure 4.9: CO_2 yields of MI01 to MI10 and SI10 obtained from CO oxidation experiments at static temperatures...49

Figure 4.10: Turnover frequencies of MI01 to MI10 and SI10 (marked with *) calculated from CO oxidation experiments under continuous heating with 2 °C/min. 50

Figure 4.11: TOFs of SI10 (marked with *) and MI01 - MI10, obtained from CO oxidation experiments at static temperatures of 150, 200, 250, 300 and 350 °C..............................51

Figure 5.1: PXRD of MM01 to MM05 and the respective support material.....................56

Figure 5.2: DRUV spectra of MM01 to MM05..57

Figure 5.3: XANES spectra of MM01 to MM04 at the Mn K-edge and of $LiMn_2O_4$ as a reference (left) and zoomed pre-peak region (right); pre-peak (a), first maximum of the edge (b), E_0 by halved whiteline intensity (c) and maximum of the whiteline (d) are highlighted with dotted lines. 58

Figure 5.4: XANES spectra of MM01 to MM05 at the Fe K-edge and of α-Fe_2O_3 and γ-Fe_2O_3 as references (left) and zoomed pre-peak region (right); pre-peak (a), first maximum of the edge (b), E_0 by halved whiteline intensity (c) and maximum of the whiteline (d) are highlighted with dotted lines. 59

Figure 5.5: XANES spectra of MM02 to MM05 at the Co K-edge and of $CoBr_2$ as a reference (left) and zoomed pre-peak region (right); pre-peak (a), first maximum of the edge (b), E_0 by halved whiteline intensity (c) and maximum of the whiteline (d) are highlighted with dotted lines. 60

Figure 5.6: CO oxidation experiments of MM01 to MM05 under continuous heating 64

Figure 5.7: CO_2 yields of MM01 - MM05 obtained from CO oxidation experiments at static temperatures. 65

Figure 5.8: Long-term stability experiments of MM03 and MM05 at 100 °C (left) and 200 °C (right). 65

Figure 5.9: Molar amount of unoxidized CO over the whole catalytic experiment with continuous heating from 30 to 600 °C against Co loading of the catalysts MM01 - MM05. 66

Figure 5.10: CO oxidation experiments of MM01 to MM06 under continuous heating 67

Figure 5.11: CO_2 yields of MM01 - MM06 at static temperatures. 67

Figure 5.12: Long-term stability experiments of MM03, MM05 and MM06 at 100 °C (left) and 200 °C (right). 68

Figure 6.1: Schematic description of the boundary layer on a catalyst particle, depending on the outer gas velocity, and the concentration gradient of the educts in the outer gas stream (a), the boundary layer (b) and the pore system of the catalyst (c); left: low velocity; right: high velocity; concentration gradients simplified. 72

Figure 6.2: Diffusion limitation experiments in CO oxidation of Fe10 with the following amount of catalyst used, the applied gas feed and resulting gas velocity: 50 mg, 75 ml/min & 0.025 m/s (a); 150 mg, 225 ml/min & 0.075 m/s (b); 200 mg, 300 ml/min & 0.10 m/s (c); 267 mg, 400 ml/min & 0.13 m/s (d); 333 mg, 500 ml/min & 0.17 m/s (e); 375 mg, 560 ml/min & 0.19 m/s (f); gas composition: 1000 ppm CO (1 vol% CO in N_2), 10 vol% O_2, Ar balance, $d_{reactor}$ = 8 mm. 73

Figure 6.3: Diffusion limitation experiments in CO oxidation of MI07 with the following amount of catalyst used and the applied gas feed: 200 mg, 300 ml/min & 0.18 m/s (a); 267 mg, 400 ml/min & 0.24 m/s (b); 333 mg, 500 ml/min & 0.30 m/s (c); gas composition: 1000 ppm CO (1 vol% CO in N_2), 10 vol% O_2, Ar balance, $d_{reactor}$ = 6 mm. 74

9 APPENDIX

9.1 Phase Purity of the γ-Al_2O_3 Support

Phase purity of the γ-Al_2O_3 support used for catalysts Fe01 to Fe20 was ascertained by powder X-ray diffractometry and comparison to a calculated diffractogram as follows.

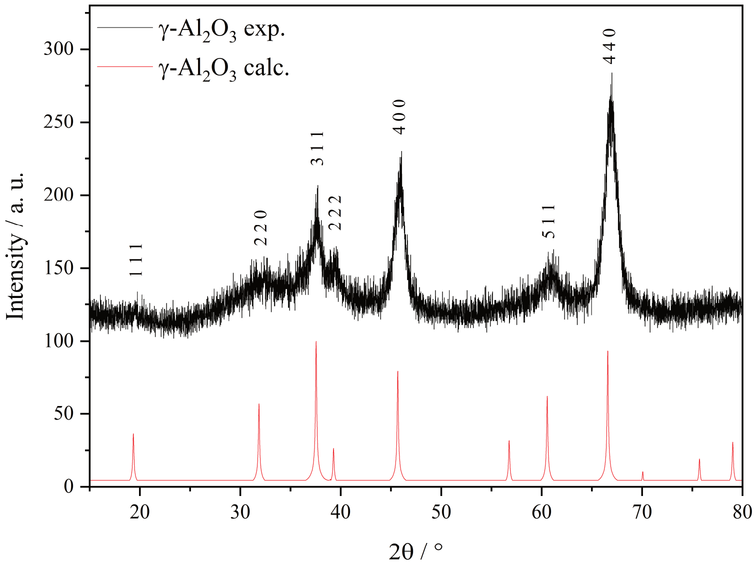

Figure SI 9.1: Experimental powder X-ray diffractogram of the as-prepared γ-Al_2O_3 support compared to a calculated powder pattern, obtained via the program Mercury[237] *from a crystal structure*[210,211].

9.2 Low Temperature Mößbauer Spectroscopy

Fe025

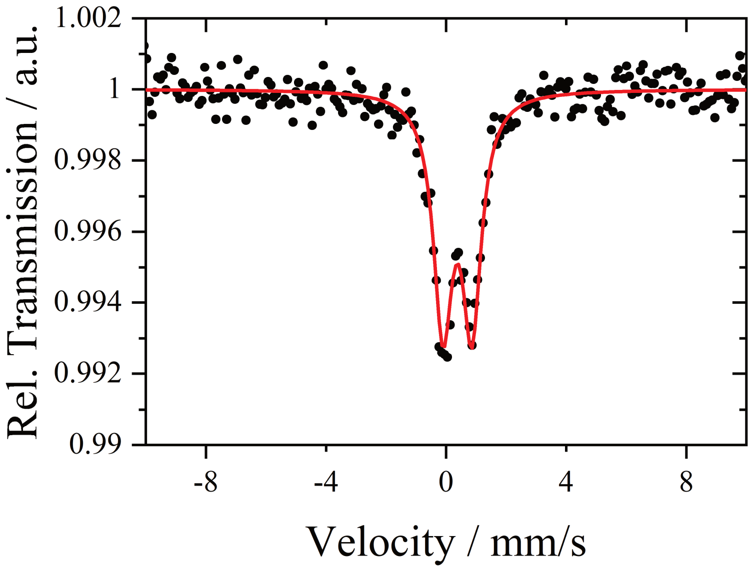

Figure SI 9.2: Mößbauer spectrum of Fe025 (black dots) obtained at 77 K and corresponding fit of the doublet (red).

Table SI 9-1: Parameters obtained by Mößbauer spectroscopy of Fe025 at 77 K.

δ [mm/s]	ΔE_Q [mm/s]	Γ [mm/s]
0.38	0.97	0.76

Fe05

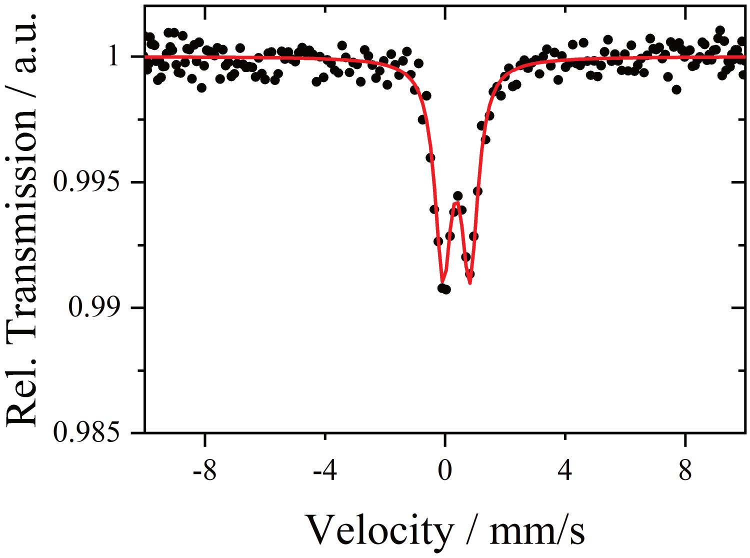

Figure SI 9.3: Mößbauer spectrum of Fe05 (black dots) obtained at 77 K and corresponding fit of the doublet (red).

Table SI 9-2: Parameters obtained by Mößbauer spectroscopy of Fe05 at 77 K.

δ [mm/s]	ΔE_Q [mm/s]	Γ [mm/s]
0.38	0.89	0.66

Fe10

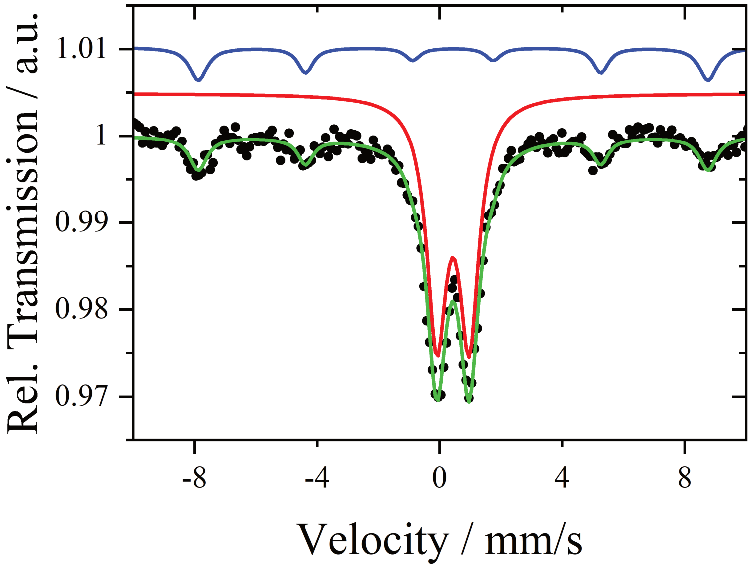

Figure SI 9.4: Mößbauer spectrum of Fe10 (black dots) obtained at 77 K and corresponding fit of the sextett (blue), doublet (red) and cumulative fit (green).

Table SI 9-3: Parameters obtained by Mößbauer spectroscopy of Fe10 at 77 K.

	δ [mm/s]	ΔE_Q [mm/s]	Γ [mm/s]
d	0.44	1.06	0.77
sx	0.44	B_{hf} = 51.5 T	

Fe20

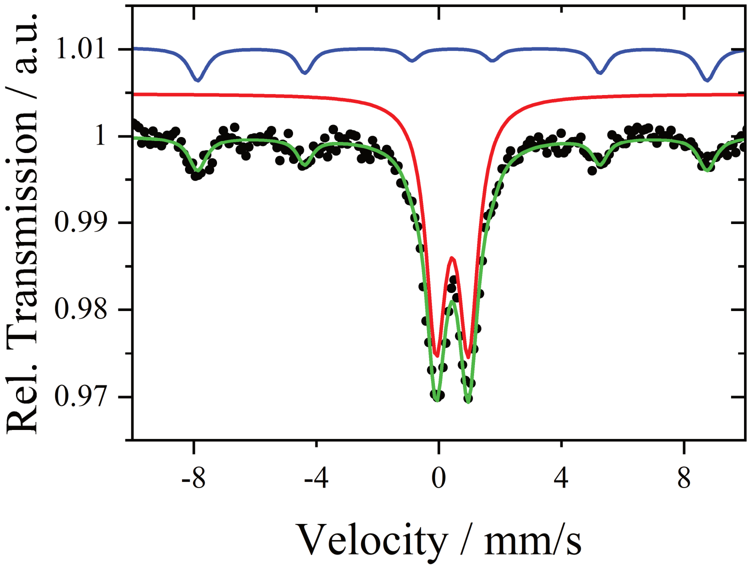

Figure SI 9.5: Mößbauer spectrum of Fe20 (black dots) obtained at 77 K and corresponding fit of the sextett (blue), doublet (red) and cumulative fit (green).

Table SI 9-4: Parameters obtained by Mößbauer spectroscopy of Fe20 at 77 K.

	δ [mm/s]	ΔE_Q [mm/s]	Γ [mm/s]
d	0.39	0.91	0.59
sx	0.46	B_{hf} = 52.3 T	

9.3 UV/Vis-Spectroscopy

9.3.1 Peak Deconvolution: Fe01 - Fe20

Fe01

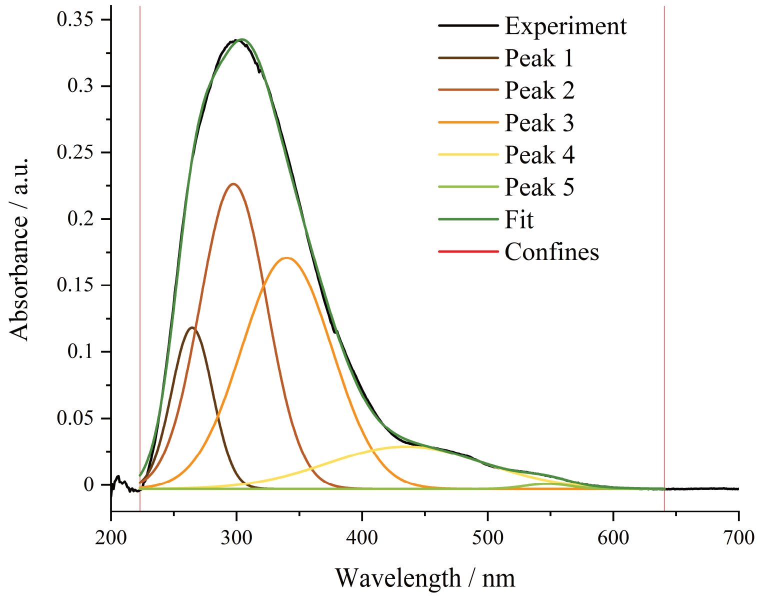

Figure SI 9.6: DRUV spectrum and deconvolution of Fe01.

Table SI 9-5: Parameters of the peak deconvolution of Fe01; for peak 4 a lower limit of 435 nm was set.

Model	Gaussian				
Function	y=y0 + (A/(w*sqrt(pi/2)))*exp(-2*((x-xc)/w)^2)				
	Peak 1	Peak 2	Peak 3	Peak 4	Peak 5
y_0	-0.003 ± 8.1973E-4	-0.003 ± 8.1973E-4	-0.003 ± 8.1973E-4	-0.003 ± 8.1973E-4	-0.003 ± 8.1973E-4
x_c	264.5944 ± 0.4482	297.5430 ± 1.9196	340 ± 13.1892	435 ± 23.4728	547.5522 ± 4.1119
Area	4.9403 ± 1.1736	15.3148 ± 7.6336	15.7082 ± 8.3174	4.9547 ± 2.1619	0.1794 ± 0.1520
χ^2_{red}	8.64457E-6				
r^2_{corr}	0.99934				

Table SI 9-6: Assignment of the peaks and their normalized areas to tetrahedral, octahedral and oligomerized iron oxide. Percentual amounts of the respective iron species of the overall amount of catalyst, calculated from the percentual areas multiplied by the iron loading.

X_C [nm]	Area [a.u.]	$\text{Area}_{\text{norm}}$ [%]	$\text{Area}_{\text{norm}}$ [%]		$\text{Amount}_{\text{norm}}$ [%]
265	4.94	12.0	Fe_{tet}	12.0	0.120
298	15.31	37.3	Fe_{oct}	37.3	0.373
340	15.71	38.2	Fe_xO_y olig.	50.3	0.503
435	4.95	12.0			
548	0.18	0.438	Fe_xO_y particles	0.44	0.00438

Fe025

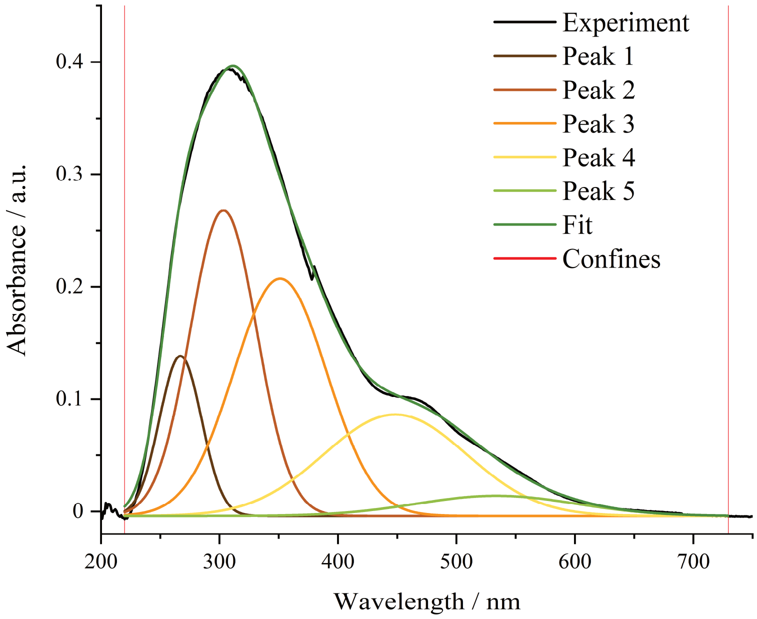

Figure SI 9.7: DRUV spectrum and deconvolution of Fe025.

Table SI 9-7: Parameters of the peak deconvolution of Fe025.

Model	Gaussian				
Function	y=y0 + (A/(w*sqrt(pi/2)))*exp(-2*((x-xc)/w)^2)				
	Peak 1	Peak 2	Peak 3	Peak 4	Peak 5
y_0	-0.004 ± 0.00123	-0.004 ± 0.00123	-0.004 ± 0.00123	-0.004 ± 0.00123	-0.004 ± 0.00123
x_c	267.0679 ± 0.8395	303.3725 ± 1.9892	351.2364 ± 14.8879	448.3542 ± 47.7532	533.7167 ± 475.1373
Area	6.3315 ± 1.9676	19.1931 ± 11.6177	20.7902 ± 15.6331	13.6395 ± 35.6409	3.0249 ± 30.0896
χ^2_{red}	1.27031E-5				
r^2_{corr}	0.99923				

Table SI 9-8: Assignment of the peaks and their normalized areas to tetrahedral, octahedral and oligomerized iron oxide. Percentual amounts of the respective iron species of the overall amount of catalyst, calculated from the percentual areas multiplied by the iron loading.

X_C [nm]	Area [a.u.]	$Area_{norm}$ [%]	$Area_{norm}$ [%]		$Amount_{norm}$ [%]
267	6.33	10.8	Fe_{tet}	10.8	0.270
303	20.8	35.4	Fe_{oct}	35.4	0.886
351	14.9	25.4	Fe_xO_y olig.	48.6	1.22
448	13.6	23.2			
534	3.02	5.15	Fe_xO_y particles	5.15	0.129

Fe05

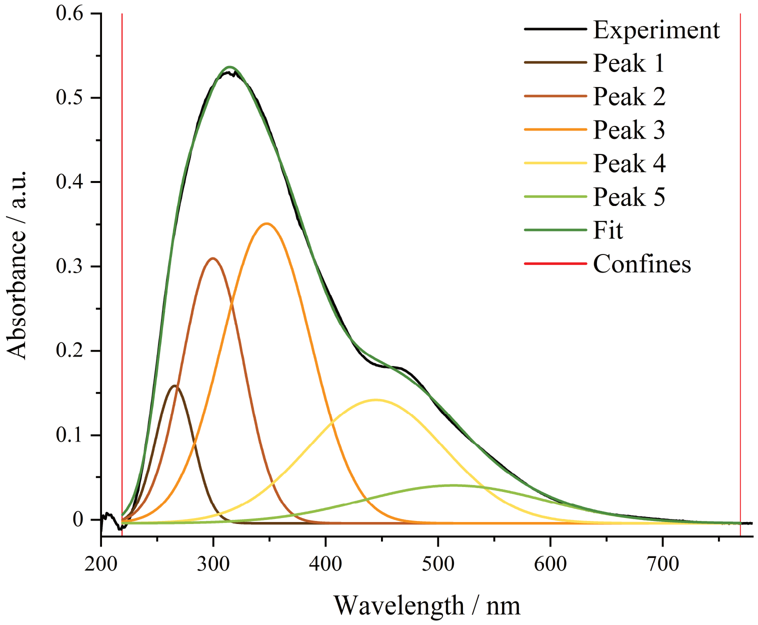

Figure SI 9.8: DRUV spectrum and deconvolution of Fe05.

Table SI 9-9: Parameters of the peak deconvolution of Fe05.

Model	Gaussian				
Function	y=y0 + (A/(w*sqrt(pi/2)))*exp(-2*((x-xc)/w)^2)				
	Peak 1	Peak 2	Peak 3	Peak 4	Peak 5
y_0	-0.004 ± 0.00147	-0.004 ± 0.00147	-0.004 ± 0.00147	-0.004 ± 0.00147	-0.004 ± 0.00147
x_c	265.5110 ± 0.7747	299.5955 ± 1.5577	347.4462 ± 8.9343	444.7809 ± 6.7279	513.9394 ± 334.2752
Area	6.9185 ± 2.2258	21.4682 ± 11.9875	35.0961 ± 14.2335	22.2702 ± 50.5516	9.0160 ± 47.9250
χ^2_{red}	1.85126E-5				
r^2_{corr}	0.9994				

Table SI 9-10: Assignment of the peaks and their normalized areas to tetrahedral, octahedral and oligomerized iron oxide. Percentual amounts of the respective iron species of the overall amount of catalyst, calculated from the percentual areas multiplied by the iron loading.

X_C [nm]	Area [a.u.]	$Area_{norm}$ [%]	$Area_{norm}$ [%]		$Amount_{norm}$ [%]
266	6.92	7.30	Fe_{tet}	7.30	0.365
300	21.5	22.7	Fe_{oct}	22.7	1.13
347	35.1	37.0	Fe_xO_y olig.	60.5	3.03
445	22.3	23.5			
514	9.02	9.52	Fe_xO_y particles	9.52	0.476

Fe10

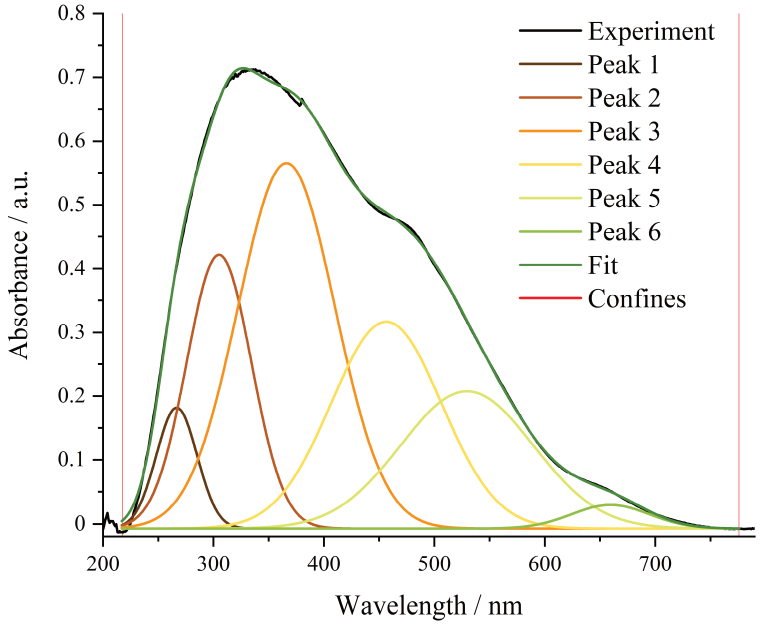

Figure SI 9.9: DRUV spectrum and deconvolution of Fe10.

Table SI 9-11: Parameters of the peak deconvolution of Fe10.

Model	Gaussian					
Function	y=y0 + (A/(w*sqrt(pi/2)))*exp(-2*((x-xc)/w)^2)					
	Peak 1	Peak 2	Peak 3	Peak 4	Peak 5	Peak 6
y_0	-0.007 ± 9.4064E-4	-0.007 ± 9.4064E-4	-0.007 ± 9.4064E-4	-0.007 ± 9.4064E-4	-0.007 ± 9.4064E-4	-0.007 ± 9.4064E-4
x_c	266.7093 ± 1.0371	305.0514 ± 1.3806	366.1235 ± 8.6004	456.4909 ± 7.1748	529.5326 ± 26.9542	659.4903 ± 10.0261
Area	8.7137 ± 2.6543	31.4941 ± 18.3908	62.94732 ± 51.6049	40.4059 ± 182.6243	32.1960 ± 151.9598	3.2282 ± 2.9828
χ^2_{red}	1.97494E-5					
r^2_{corr}	0.99971					

Table SI 9-12: Assignment of the peaks and their normalized areas to tetrahedral, octahedral and oligomerized iron oxide. Percentual amounts of the respective iron species of the overall amount of catalyst, calculated from the percentual areas multiplied by the iron loading.

X_C [nm]	Area [a.u.]	$Area_{norm}$ [%]	$Area_{norm}$ [%]		$Amount_{norm}$ [%]
267	8.71	4.87	Fe_{tet}	4.87	0.487
305	31.49	17.6	Fe_{oct}	17.6	1.76
366	62.95	35.2	Fe_xO_y olig.	57.7	5.77
456	40.41	22.6			
530	32.2	18.0	Fe_xO_y particles	19.8	1.98
659	3.23	1.80			

Fe20

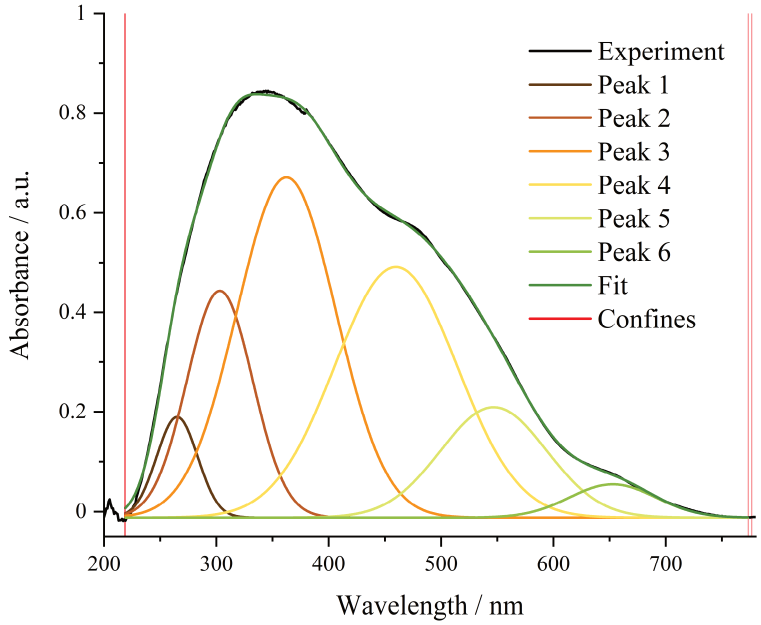

Figure SI 9.10: DRUV spectrum and deconvolution of Fe20.

Table SI 9-13: Parameters of the peak deconvolution of Fe20.

Model	Gaussian					
Function	y=y0 + (A/(w*sqrt(pi/2)))*exp(-2*((x-xc)/w)^2)					
	Peak 1	Peak 2	Peak 3	Peak 4	Peak 5	Peak 6
y_0	-0.012 ± 0.00103	-0.012 ± 0.00103	-0.012 ± 0.00103	-0.012 ± 0.00103	-0.012 ± 0.00103	-0.012 ± 0.00103
x_c	265.0813 ± 0.9056	303.0614 ± 1.1813	362.3565 ± 6.2809	459.8329 ± 15.1712	546.8148 ± 39.8440	652.8155 ± 5.6990
Area	9.2129 ± 2.5005	33.3372± 15.7789	75.5165± 43.3858	68.4914 ± 72.7927	26.1852± 44.3067	6.4027 ± 1.3589
χ^2_{red}	2.15064E-5					
r^2_{corr}	0.99976					

Table SI 9-14: Assignment of the peaks and their normalized areas to tetrahedral, octahedral and oligomerized iron oxide. Percentual amounts of the respective iron species of the overall amount of catalyst, calculated from the percentual areas multiplied by the iron loading.

X_C [nm]	Area [a.u.]	$Area_{norm}$ [%]	$Area_{norm}$ [%]		$Amount_{norm}$ [%]
265	9.21	4.20	Fe_{tet}	4.20	0.841
303	33.3	15.2	Fe_{oct}	15.2	3.04
362	75.5	34.5	Fe_xO_y olig.	65.7	13.1
460	68.5	31.3			
547	26.2	12.0	Fe_xO_y particles	14.9	2.97
653	6.40	2.92			

9.3.2 Peak Deconvolution: MI01 - MI10 and SI10

MI01

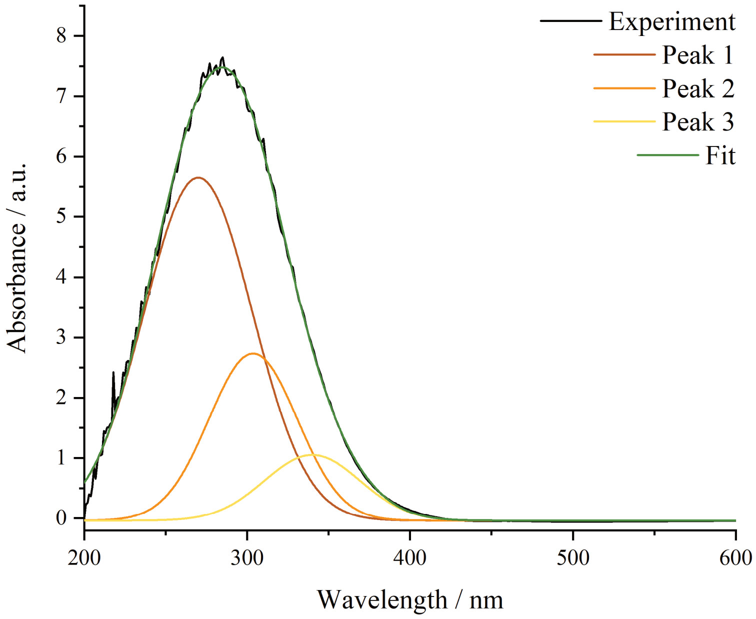

Figure SI 9.11: Experimental DRUV spectrum of MI01 and the peaks and fit obtained by peak deconvolution.

Table SI 9-15: Parameters of DRUVS peak deconvolution of MI01.

Model	Gauss		
Equation	y=y0 + (A/(w*sqrt(pi/2)))*exp(-2*((x-xc)/w)^2)		
Plot	Peak 1	Peak 2	Peak 3
y_0	-0.0372 ± 0.0037	-0.0372 ± 0.0037	-0.0372 ± 0.0037
x_c	270 ± 16.3596	303.6551 ± 8.5012	340 ± 50.5060
Area	475.1875 ± 307.3783	188.8935 ± 486.2429	80.1654 ± 202.8419
χ^2_{red}	0.00508		
r^2_{corr}	0.99901		

Table SI 9-16: Assignment of the peaks and their normalized areas to tetrahedral, octahedral and oligomerized iron oxide. Percentual amounts of the respective iron species of the overall amount of catalyst, calculated from the percentual areas multiplied by the iron.

X_C [nm]	Area [a.u.]	$Area_{norm}$ [%]	$Area_{norm}$ [%]		$Amount_{norm}$ [%]
270	475	63.9	Fe_{tet}	63.9	0.638
304	189	25.4	Fe_{oct}	25.4	0.254
347	80.2	10.8	Fe_xO_y olig.	10.8	0.108

MI02

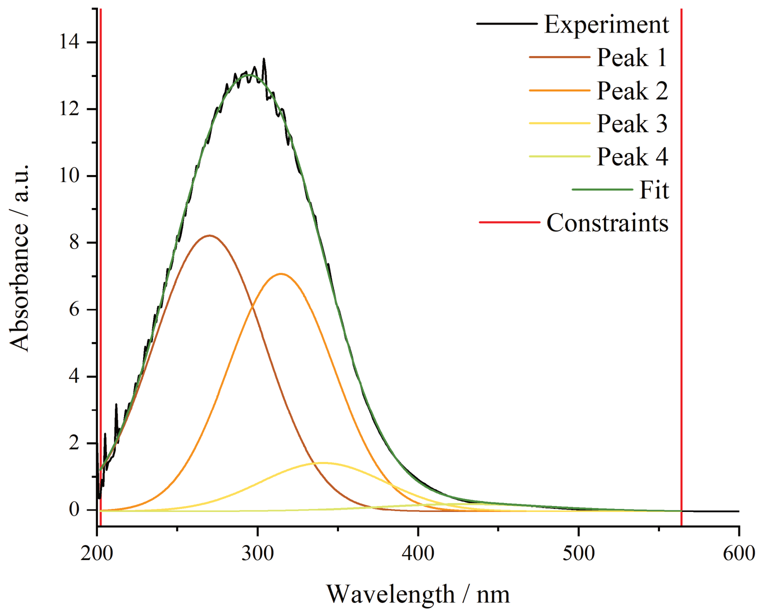

Figure SI 9.12: Experimental DRUV spectrum of MI02 and the peaks and fit obtained by peak deconvolution.

Table SI 9-17: Parameters of DRUVS peak deconvolution of MI02.

Model	Gauss			
Equation	y=y0 + (A/(w*sqrt(pi/2)))*exp(-2*((x-xc)/w)^2)			
Plot	Peak 1	Peak 2	Peak 3	Peak 4
y_0	-0.04 ± 0.113	-0.04 ± 0.113	-0.04 ± 0.113	-0.04 ± 0.113
x_c	270 ± 25.2117	314.6213 ± 39.2455	340.7059 ± 2271.8009	430 ± 448.7582
Area	720.0898 ± 855.7440	586.9530 ± 12678.2392	141.3488 ± 13151.6093	30 ± 286.594
χ^2_{red}	0.02114			
r^2_{corr}	0.99902			

Table SI 9-18: Assignment of the peaks and their normalized areas to tetrahedral, octahedral and oligomerized iron oxide. Percentual amounts of the respective iron species of the overall amount of catalyst, calculated from the percentual areas multiplied by the iron.

X_C [nm]	Area [a.u.]	$Area_{norm}$ [%]	$Area_{norm}$ [%]		$Amount_{norm}$ [%]
270	720	46.3	Fe_{tet}	46.3	0.926
315	587	37.7	Fe_{oct}	37.7	0.755
341	141	9.08	Fe_xO_y olig.	16.0	0.320
430	107	6.91			

MI03

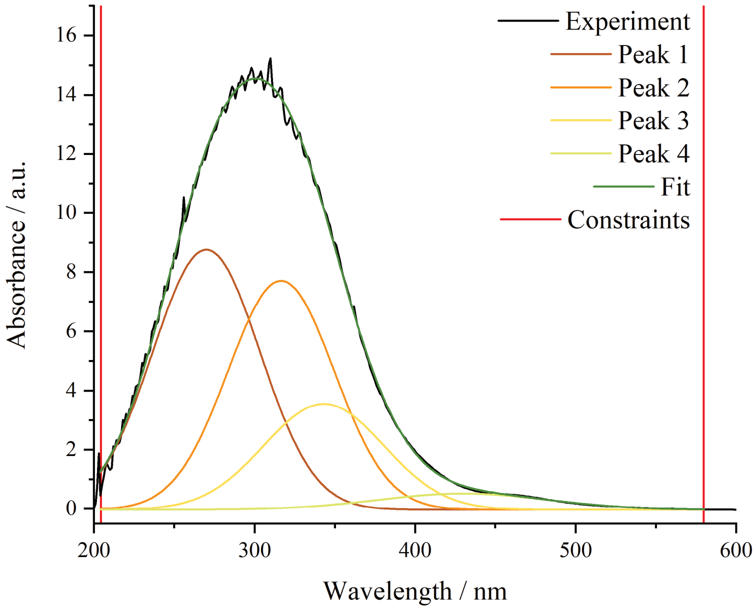

Figure SI 9.13: Experimental DRUV spectrum of MI03 and the peaks and fit obtained by peak deconvolution.

Table SI 9-19: Parameters of DRUVS peak deconvolution of MI03.

Model	Gauss			
Equation	y=y0 + (A/(w*sqrt(pi/2)))*exp(-2*((x-xc)/w)^2)			
Plot	Peak 1	Peak 2	Peak 3	Peak 4
y_0	-0.03 ± 0.0679	-0.03 ± 0.0679	-0.03 ± 0.0679	-0.03 ± 0.0679
x_c	270 ± 28.3187	316.5367 ± 100.5642	343.1960 ± 1168.6612	430 ± 145.0375
Area	737.7647 ± 962.9163	642.4903 ± 18661.2369	335.9280 ± 18149.3735	73.1068 ± 221.7451
χ^2_{red}	0.02483			
r^2_{corr}	0.99909			

Table SI 9-20: Assignment of the peaks and their normalized areas to tetrahedral, octahedral and oligomerized iron oxide. Percentual amounts of the respective iron species of the overall amount of catalyst, calculated from the percentual areas multiplied by the iron.

X_C [nm]	Area [a.u.]	$Area_{norm}$ [%]	$Area_{norm}$ [%]		$Amount_{norm}$ [%]
270	738	41.2	Fe_{tet}	41.2	1.24
317	642	35.9	Fe_{oct}	35.9	1.08
343	336	18.8	Fe_xO_y olig.	22.9	0.686
430	73.1	4.09			

MI04

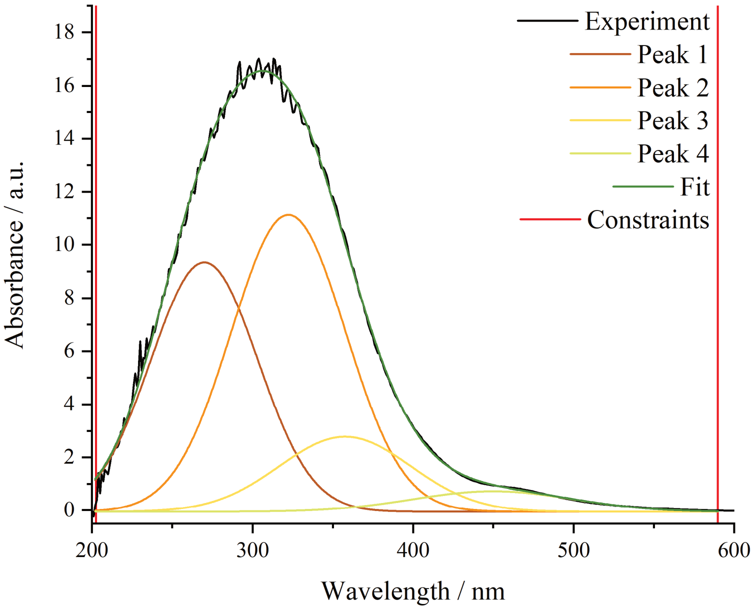

Figure SI 9.14: Experimental DRUV spectrum of MI04 and the peaks and fit obtained by peak deconvolution.

Table SI 9-21: Parameters of DRUVS peak deconvolution of MI04.

Model	Gauss			
Equation	y=y0 + (A/(w*sqrt(pi/2)))*exp(-2*((x-xc)/w)^2)			
Plot	Peak 1	Peak 2	Peak 3	Peak 4
y_0	-0.05 ± 0.0935	-0.05 ± 0.0935	-0.05 ± 0.0935	-0.05 ± 0.0935
x_c	270 ± 21.7463	322.3730 ± 76.1232	357.6623 ± 1272.8350	449.8710 ± 167.8575
Area	787.7098 ± 934.3251	998.1415 ± 14524.6895	290.8962 ± 14092.8611	96.7359 ± 378.0704
χ^2_{red}	0.04268			
r^2_{corr}	0.99879			

Table SI 9-22: Assignment of the peaks and their normalized areas to tetrahedral, octahedral and oligomerized iron oxide. Percentual amounts of the respective iron species of the overall amount of catalyst, calculated from the percentual areas multiplied by the iron.

X_C [nm]	Area [a.u.]	$Area_{norm}$ [%]	$Area_{norm}$ [%]		$Amount_{norm}$ [%]
270	788	36.2	Fe_{tet}	36.2	1.45
322	998	45.9	Fe_{oct}	45.9	1.84
358	291	13.4	Fe_xO_y olig.	17.8	0.713
450	96.7	4.45			

MI05

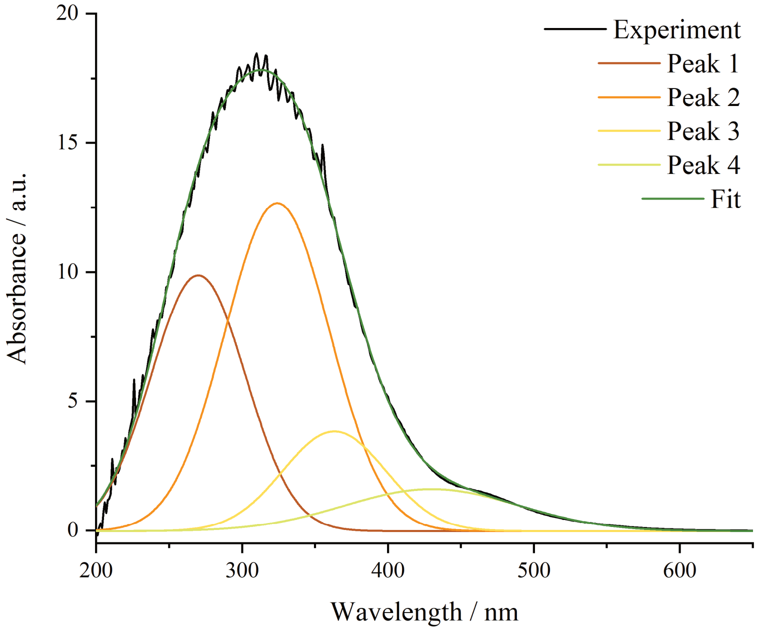

Figure SI 9.15: Experimental DRUV spectrum of MI05 and the peaks and fit obtained by peak deconvolution.

Table SI 9-23: Parameters of DRUVS peak deconvolution of MI05.

Model	Gauss			
Equation	y=y0 + (A/(w*sqrt(pi/2)))*exp(-2*((x-xc)/w)^2)			
Plot	Peak 1	Peak 2	Peak 3	Peak 4
y_0	-0.0266 ± 0.0159	-0.0266 ± 0.0159	-0.0266 ± 0.0159	-0.0266 ± 0.0159
x_c	270 ± 29.791	324.1526 ± 215.2770	363.2467 ± 597.6221	430 ± 47.2628
Area	805.3799 ± 1774.5549	1146.4344 ± 15044.5462	340.4321 ± 13484.924	245.1838 ± 201.9851
χ^2_{red}	0.04643			
r^2_{corr}	0.99872			

Table SI 9-24: Assignment of the peaks and their normalized areas to tetrahedral, octahedral and oligomerized iron oxide. Percentual amounts of the respective iron species of the overall amount of catalyst, calculated from the percentual areas multiplied by the iron.

X_C [nm]	Area [a.u.]	$Area_{norm}$ [%]	$Area_{norm}$ [%]		$Amount_{norm}$ [%]
270	805	31.7	Fe_{tet}	31.7	1.59
324	1146	45.2	Fe_{oct}	45.2	2.26
363	340	13.4	Fe_xO_y olig.	23.1	1.13
430	245	9.66			

MI06

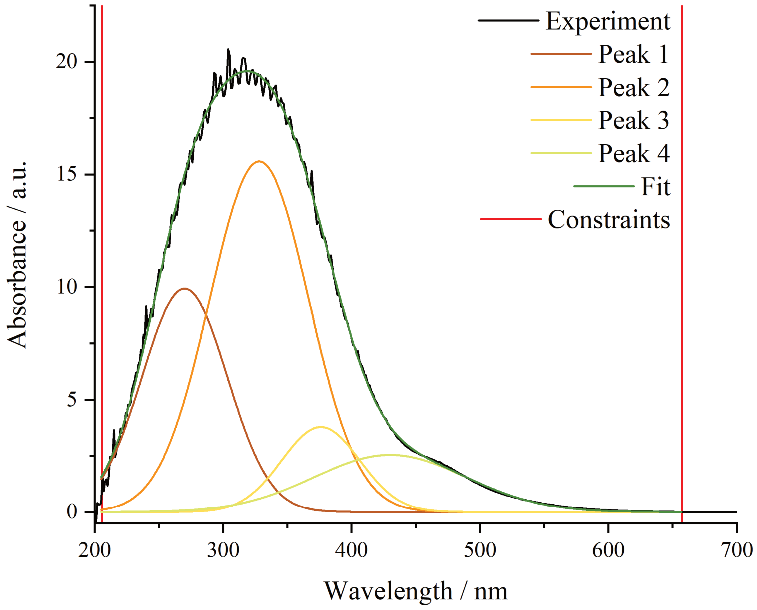

Figure SI 9.16: Experimental DRUV spectrum of MI06 and the peaks and fit obtained by peak deconvolution.

Table SI 9-25: Parameters of DRUVS peak deconvolution of MI06.

Model	Gauss			
Equation	y=y0 + (A/(w*sqrt(pi/2)))*exp(-2*((x-xc)/w)^2)			
Plot	Peak 1	Peak 2	Peak 3	Peak 4
y_0	0.0058 ± 0.0366	0.0058 ± 0.0366	0.0058 ± 0.0366	0.0058 ± 0.0366
x_c	270 ± 50.8728	328.0568 ± 49.5679	376.0429 ± 104.5992	430 ± 26.8617
Area	825.8000 ± 3373.6043	1505.8197 ± 8666.7054	288.4187 ± 5190.1680	379.0693 ± 182.9030
χ^2_{red}	0.063			
r^2_{corr}	0.99874			

Table SI 9-26: Assignment of the peaks and their normalized areas to tetrahedral, octahedral and oligomerized iron oxide. Percentual amounts of the respective iron species of the overall amount of catalyst, calculated from the percentual areas multiplied by the iron.

X_C [nm]	Area [a.u.]	$Area_{norm}$ [%]	$Area_{norm}$ [%]		$Amount_{norm}$ [%]
270	826	27.5	Fe_{tet}	27.5	1.65
328	1506	50.2	Fe_{oct}	50.2	3.01
376	288	9.62	Fe_xO_y olig.	22.3	1.34
430	379	12.6			

MI07

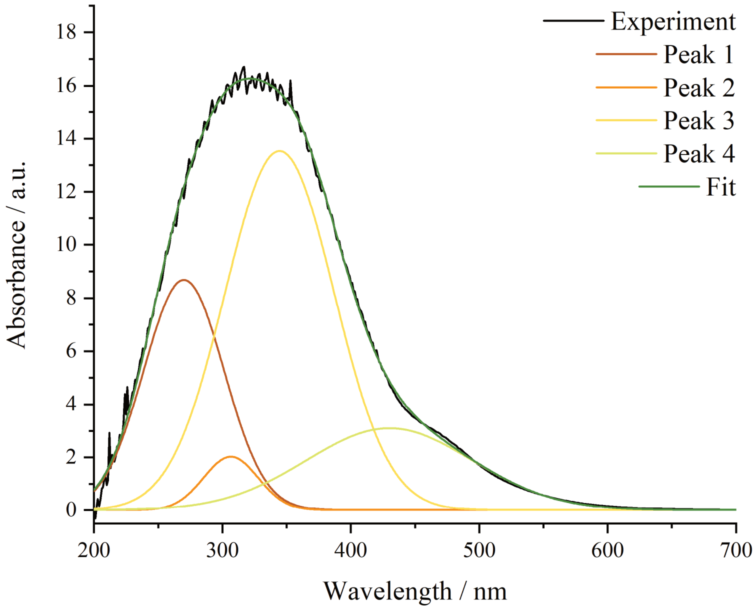

Figure SI 9.17: Experimental DRUV spectrum of MI07 and the peaks and fit obtained by peak deconvolution.

Table SI 9-27: Parameters of DRUVS peak deconvolution of MI07.

Model	Gauss			
Equation	y=y0 + (A/(w*sqrt(pi/2)))*exp(-2*((x-xc)/w)^2)			
Plot	Peak 1	Peak 2	Peak 3	Peak 4
y_0	0.0121 ± 0.0135	0.01208 ± 0.0135	0.0121 ± 0.0135	0.0121 ± 0.0135
x_c	270 ± 3.1348	306.6009 ± 2.9822	344.5069 ± 2.6163	430 ± 13.5454
Area	681.1547 ± 81.7874	107.2227 ± 92.3639	1437.5746 ± 200.3454	501.4843 ± 106.5360
χ^2_{red}	0.03161			
r^2_{corr}	0.99904			

Table SI 9-28: Assignment of the peaks and their normalized areas to tetrahedral, octahedral and oligomerized iron oxide. Percentual amounts of the respective iron species of the overall amount of catalyst, calculated from the percentual areas multiplied by the iron.

X_C [nm]	Area [a.u.]	$Area_{norm}$ [%]	$Area_{norm}$ [%]		$Amount_{norm}$ [%]
270	681	25.0	Fe_{tet}	25.0	1.75
307	107	3.93	Fe_{oct}	3.93	0.275
345	1438	52.7	Fe_xO_y olig.	71.1	4.98
430	501	18.4			

MI08

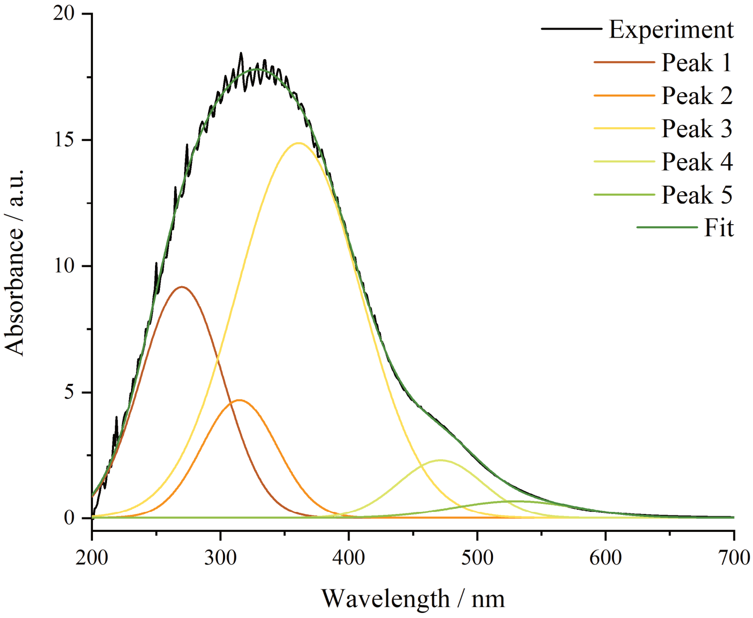

Figure SI 9.18: Experimental DRUV spectrum of MI08 and the peaks and fit obtained by peak deconvolution.

Table SI 9-29: Parameters of DRUVS peak deconvolution of MI08.

Model	Gauss				
Equation	y=y0 + (A/(w*sqrt(pi/2)))*exp(-2*((x-xc)/w)^2)				
Plot	Peak 1	Peak 2	Peak 3	Peak 4	Peak 5
y_0	0.0148 ± 0.0179	0.0148 ± 0.0179	0.0148 ± 0.0179	0.0148 ± 0.0179	0.0148± 0.0179
x_c	270 ± 7.3813	314.8246 ± 8.9298	360.9527 ± 23.1377	471.4822 ± 7.3835	530 ± 63.0564
Area	738.0563 ± 234.7684	343.2201 ± 821.6483	1793.5903 ± 995.6671	188.8770 ± 180.1028	80.7736 ± 109.1492
χ^2_{red}	0.03951				
r^2_{corr}	0.99901				

Table SI 9-30: Assignment of the peaks and their normalized areas to tetrahedral, octahedral and oligomerized iron oxide. Percentual amounts of the respective iron species of the overall amount of catalyst, calculated from the percentual areas multiplied by the iron.

X_C [nm]	Area [a.u.]	Area$_{norm}$ [%]	Area$_{norm}$ [%]		Amount$_{norm}$ [%]
270	738	23.5	Fe_{tet}	23.5	1.88
315	343	10.9	Fe_{oct}	10.9	0.873
361	1794	57.0	Fe_xO_y olig.	63.0	5.04
471	189	6.01			
530	80.8	2.57	Fe_xO_y particles	2.57	0.206

MI09

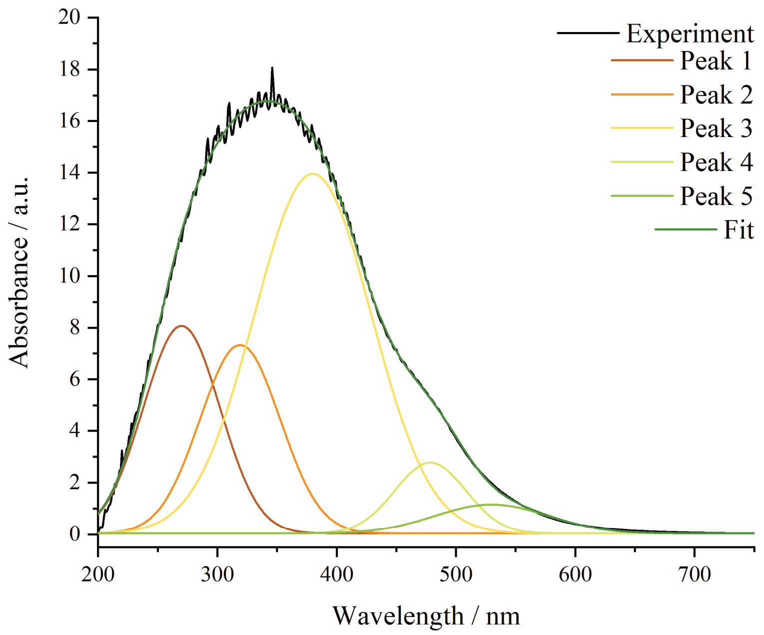

Figure SI 9.19: Experimental DRUV spectrum of MI09 and the peaks and fit obtained by peak deconvolution.

Table SI 9-31: Parameters of DRUVS peak deconvolution of MI09.

Model	Gauss				
Equation	y=y0 + (A/(w*sqrt(pi/2)))*exp(-2*((x-xc)/w)^2)				
Plot	Peak 1	Peak 2	Peak 3	Peak 4	Peak 5
y_0	0.0412 ± 0.0162	0.0412 ± 0.0162	0.0412 ± 0.0162	0.0412 ± 0.0162	0.0412 ± 0.0162
x_c	270 ± 12.7100	318.9988 ± 9.5170	379.9827 ± 29.7134	478.5759 ± 5.9409	530 ± 31.1803
Area	646.5139 ± 386.2515	612.9440 ± 1446.2040	1715.0089 ± 1248.1316	204.3287 ± 183.0333	133.8143 ± 88.1595
χ^2_{red}	0.03287				
r^2_{corr}	0.99912				

Table SI 9-32: Assignment of the peaks and their normalized areas to tetrahedral, octahedral and oligomerized iron oxide. Percentual amounts of the respective iron species of the overall amount of catalyst, calculated from the percentual areas multiplied by the iron.

X_C [nm]	Area [a.u.]	Area$_{norm}$ [%]	Area$_{norm}$ [%]		Amount$_{norm}$ [%]
270	647	19.5	Fe_{tet}	19.5	1.76
319	613	18.5	Fe_{oct}	18.5	1.67
380	1715	51.8	Fe_xO_y olig.	57.9	5.21
479	204	6.17			
530	134	4.04	Fe_xO_y particles	4.04	0.364

MI10

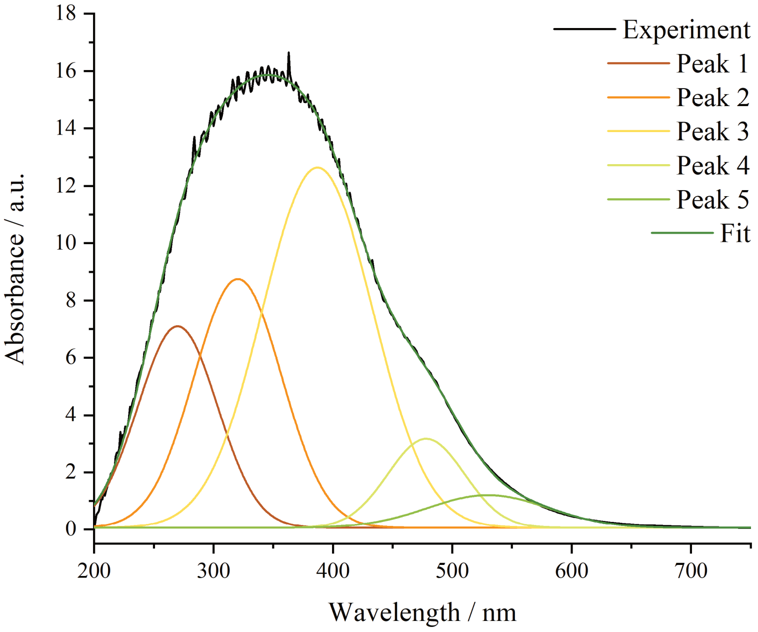

Figure SI 9.20: Experimental DRUV spectrum of MI10 and the peaks and fit obtained by peak deconvolution.

Table SI 9-33: Parameters of DRUVS peak deconvolution of MI10.

Model	Gauss				
Equation	y=y0 + (A/(w*sqrt(pi/2)))*exp(-2*((x-xc)/w)^2)				
Plot	Peak 1	Peak 2	Peak 3	Peak 4	Peak 5
y_0	0.0612 ± 0.0138	0.0612 ± 0.0138	0.0612 ± 0.0138	0.0612 ± 0.0138	0.0612 ± 0.0138
x_c	270 ± 19.9568	320.4125 ± 12.1153	387.0987 ± 47.2930	478.1473 ± 10.1158	530 ± 35.8438
Area	586.7682 ± 818.1107	802.5131 ± 2534.4263	1454.3937 ± 1957.2588	250.0871 ± 279.9128	145.5106 ± 107.7114
χ^2_{red}	0.02143				
r^2_{corr}	0.99937				

Table SI 9-34: Assignment of the peaks and their normalized areas to tetrahedral, octahedral and oligomerized iron oxide. Percentual amounts of the respective iron species of the overall amount of catalyst, calculated from the percentual areas multiplied by the iron.

X_C [nm]	Area [a.u.]	$Area_{norm}$ [%]	$Area_{norm}$ [%]		$Amount_{norm}$ [%]
270	587	18.1	Fe_{tet}	18.1	1.81
320	803	24.8	Fe_{oct}	24.8	2.48
387	1454	44.9	Fe_xO_y olig.	52.6	5.26
478	250	7.72			
530	146	4.49	Fe_xO_y particles	4.49	0.449

SI10

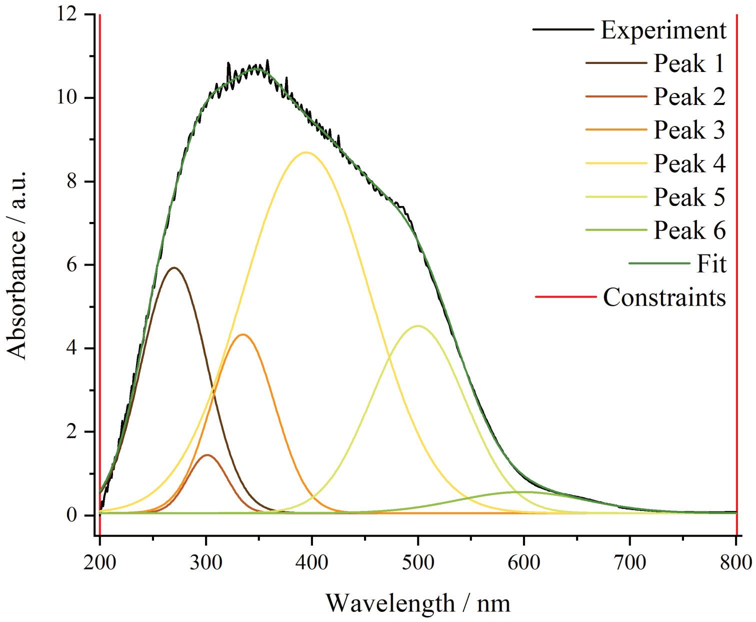

Figure SI 9.21: Experimental DRUV spectrum of SI10 and the peaks and fit obtained by peak deconvolution.

Table SI 9-35: Parameters of DRUVS peak deconvolution of SI10.

Model	Gauss					
Equation	y=y0 + (A/(w*sqrt(pi/2)))*exp(-2*((x-xc)/w)^2)					
Plot	Peak 1	Peak 2	Peak 3	Peak 4	Peak 5	Peak 6
y_0	0.06 ± 0.0187	0.06 ± 0.0187	0.06 ± 0.0187	0.06 ± 0.0187	0.06 ± 0.0187	0.06 ± 0.0187
x_c	270 ± 7.08479	301.3849 ± 2.20721	334.83215 ± 7.06392	394.62209 ± 15.70688	500 ± 13.92637	598.0647 ± 34.06944
Area	459.63412 ± 284.63794	64.43605 ± 100.46947	324.12057 ± 487.49222	1307.74984 ± 1098.38842	500.25388 ± 455.6295	77.01028 ± 45.76026
χ^2_{red}	0.00918					
r^2_{corr}	0.99943					

Table SI 9-36: Assignment of the peaks and their normalized areas to tetrahedral, octahedral and oligomerized iron oxide. Percentual amounts of the respective iron species of the overall amount of catalyst, calculated from the percentual areas multiplied by the iron.

X_C [nm]	Area [a.u.]	$Area_{norm}$ [%]	$Area_{norm}$ [%]		$Amount_{norm}$ [%]
270	460	16.8	Fe_{tet}	16.8	1.68
301	64.4	2.36	Fe_{oct}	2.36	0.236
335	324	11.9	Fe_xO_y olig.	59.7	5.97
395	1308	47.8			
500	500	18.3	Fe_xO_y particles	21.1	2.11
598	77.0	2.82			

9.4 X-Ray Absorption Spectroscopy

9.4.1 Pre-Peak Analysis: Fe01 - Fe20

For pre-peak Analysis the main edge was subtracted as a Boltzmann-type function. To obtain the precise pre-peak position an inverse polynomial function was applied for catalysts Fe01, Fe025, Fe05, Fe10 and Fe20 while for the references α-Fe_2O_3 and γ-Fe_2O_3 two Lorentzian functions were applied.

Fe01

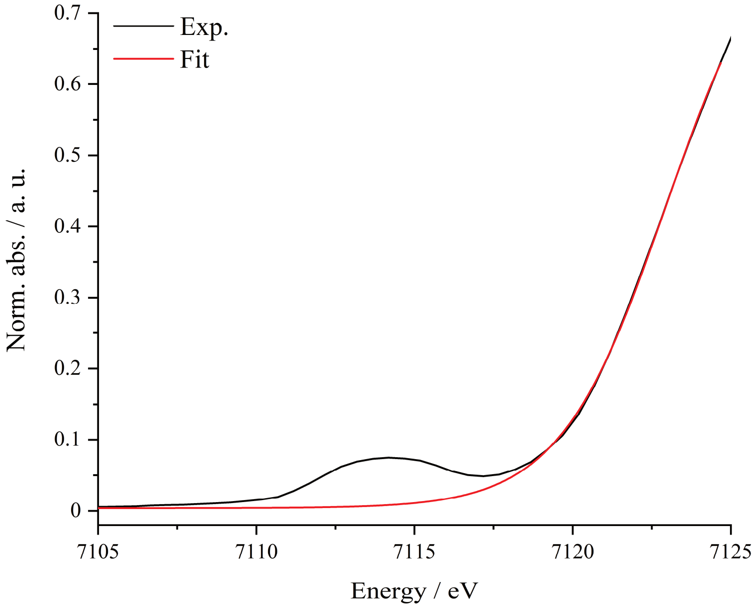

Figure SI 9.22: Pre-peak area of Fe01 and the background to remove the main edge, obtained by a Boltzmann function.

Table SI 9-37: Fit parameters of the background fit for Fe01.

Model	Boltzmann
Equation	y = A2 + (A1-A2)/(1 + exp((x-x0)/dx))
Plot	Fe01
A1	0.00386 ± 5.57691E-4
A2	0.84933 ± 0.01596
x0	7122.92897 ± 0.07218
dx	1.671 ± 0.02862
χ^2_{red}	1.2797E-5
r^2_{COD}	0.99952
r^2_{corr}	0.99949

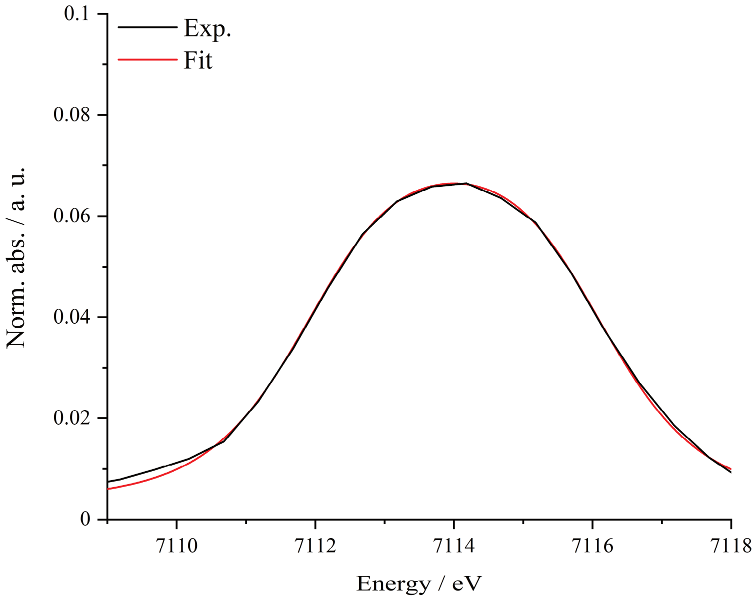

Figure SI 9.2: Pre-peak area of Fe01 with inverse polynomial fit after removal of the main edge.

Table SI 9-38: Fit parameters of the pre-peak fit for Fe01.

Model	InvsPoly
Equation	y=y0+A/(1 + A1*(2*(x-xc)/w)^2 + A2*(2*(x-xc)/w)^4 + A3*(2*(x-xc)/w)^6)
Plot	Fe01
y0	0.00328 ± 0.00117
xc	7113.997 ± 0.02694
w	4.91615 ± 3842539.08757
A	0.06328 ± 0.00147
A1	0.50915 ± 795920.44293
A2	0.56888 ± 1778571.15333
A3	0.19565 ± 917539.61378
χ_{rd}^2	2.96405E-6
r_{COD}^2	0.99601
r_{corr}^2	0.99469

Fe025

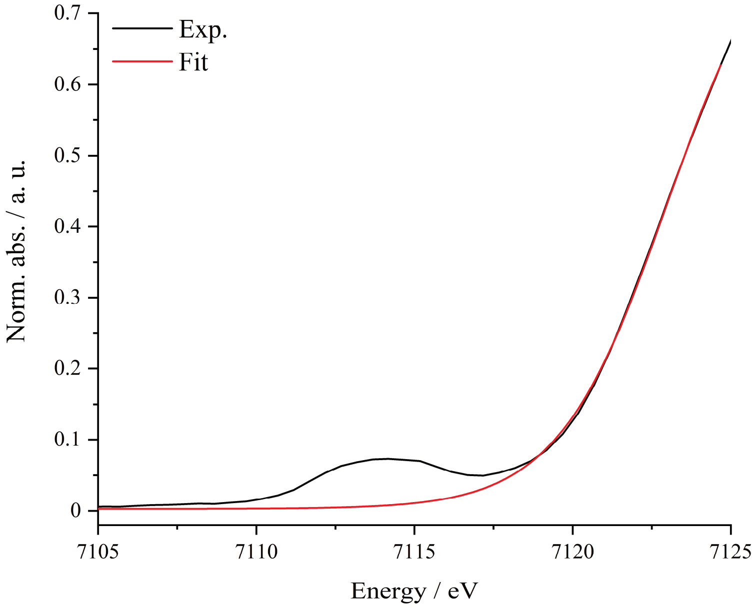

Figure SI 9.3: Pre-peak area of Fe025 and the background to remove the main edge, obtained by a Boltzmann function.

Table SI 9-39: Fit parameters of the background fit for Fe025.

Model	Boltzmann
Equation	y = A2 + (A1-A2)/(1 + exp((x-x0)/dx))
Plot	Fe025
A1	0.00273 ± 7.69022E-4
A2	0.86027 ± 0.02297
x0	7122.97922 ± 0.10451
dx	1.72551 ± 0.03988
χ_{re}^2	2.43738E-5
r_{COD}^2	0.99907
r_{corr}^2	0.99902

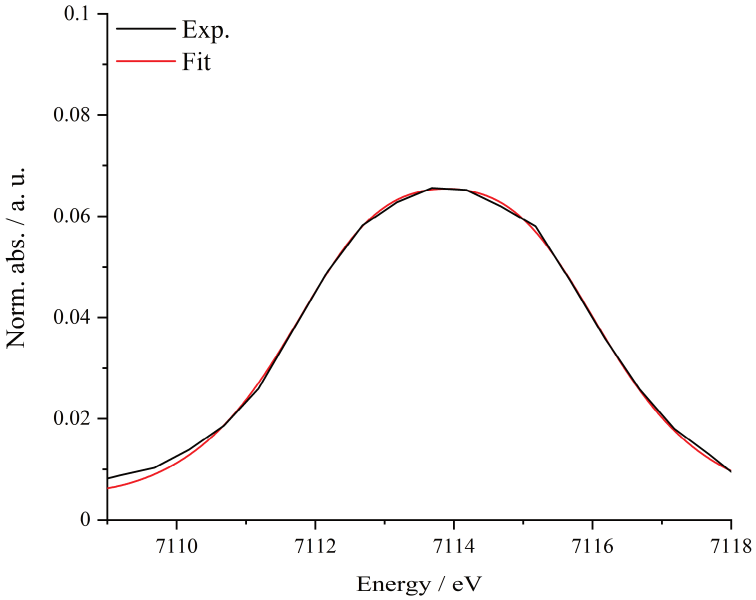

Figure SI 9.4: Pre-peak area of Fe025 with inverse polynomial fit after removal of the main edge.

Table SI 9-40: Fit parameters of the pre-peak fit for Fe025.

Model	InvsPoly
Equation	y=y0+A/(1 + A1*(2*(x-xc)/w)^2 + A2*(2*(x-xc)/w)^4 + A3*(2*(x-xc)/w)^6)
Plot	Fe025
y0	-0.00433 ± 0.00603
xc	7113.8922 ± 0.02596
w	4.75552 ± 2515279.36997
A	0.06976 ± 0.00643
A1	0.30799 ± 325803.2086
A2	0.59565 ± 1260203.86425
A3	-0.0843 ± 267540.07923
χ_{ed}^2	2.60441E-6
r_{COD}^2	0.99645
r_{corr}^2	0.99493

Fe05

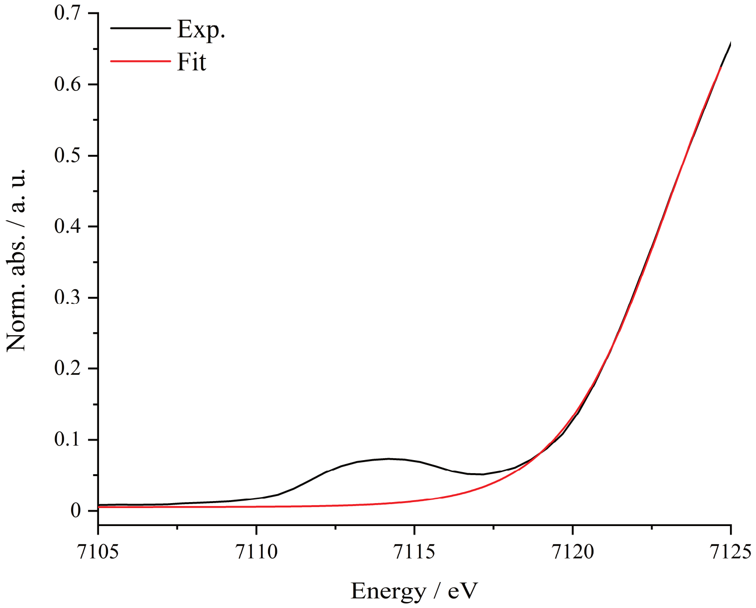

Figure SI 9.5: Pre-peak area of Fe05 and the background to remove the main edge, obtained by a Boltzmann function.

Table SI 9-41: Fit parameters of the background fit for Fe05.

Model	Boltzmann
Equation	y = A2 + (A1-A2)/(1 + exp((x-x0)/dx))
Plot	Fe05
A1	0.00529 ± 6.10835E-4
A2	0.86658 ± 0.01905
x0	7123.05039 ± 0.08636
dx	1.74262 ± 0.03219
χ_{re}^2	1.5013E-5
r_{COD}^2	0.99942
r_{corr}^2	0.99939

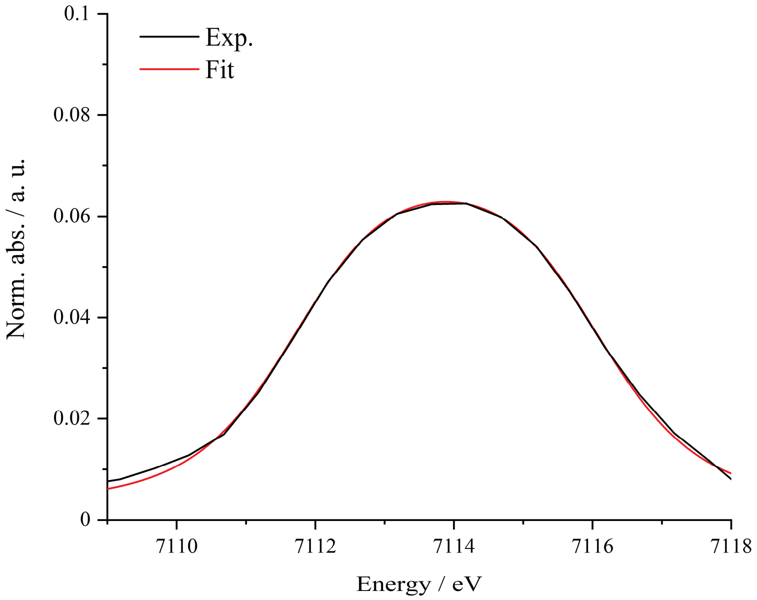

Figure SI 9.6: Pre-peak area of Fe05 with inverse polynomial fit after removal of the main edge.

Table SI 9-42 Fit parameters of the pre-peak fit for Fe05.

Model	InvsPoly
Equation	y=y0+A/(1 + A1*(2*(x-xc)/w)^2 + A2*(2*(x-xc)/w)^4 + A3*(2*(x-xc)/w)^6)
Plot	Fe05
y0	0.00346 ± 0.00173
xc	7113.88537 ± 0.02625
w	4.59746 ± 3171995.4929
A	0.05939 ± 0.00178
A1	0.40488 ± 558690.86759
A2	0.41616 ± 1148502.29772
A3	0.11773 ± 487381.4119
χ^2_{red}	2.45021E-6
r^2_{COD}	0.99636
r^2_{corr}	0.99491

Fe10

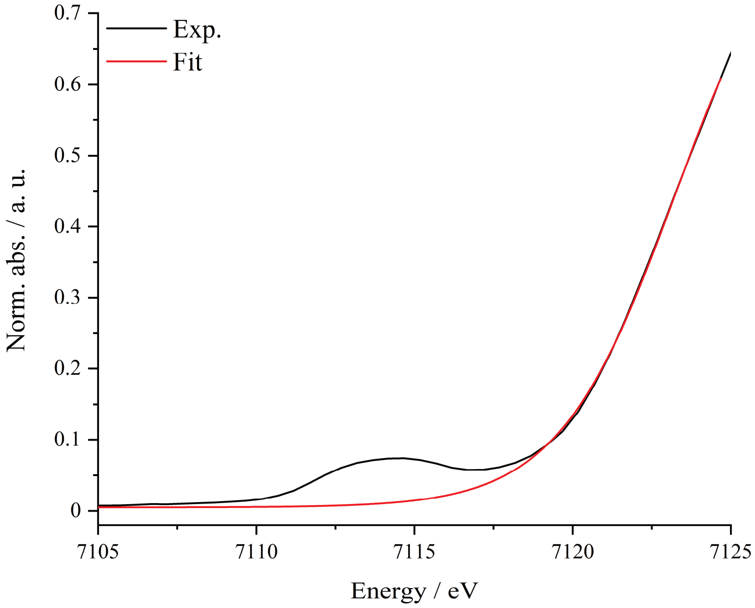

Figure SI 9.7: Pre-peak area of Fe10 and the background to remove the main edge, obtained by a Boltzmann function.

Table SI 9-43: Fit parameters of the background fit for Fe10.

Model	Boltzmann
Equation	y = A2 + (A1-A2)/(1 + exp((x-x0)/dx))
Plot	Fe10
A1	0.00496 ± 6.03096E-4
A2	0.88208 ± 0.02301
x0	7123.22575 ± 0.10531
dx	1.83865 ± 0.03722
χ^2_{re}	1.49001E-5
r^2_{COD}	0.9994
r^2_{corr}	0.99936

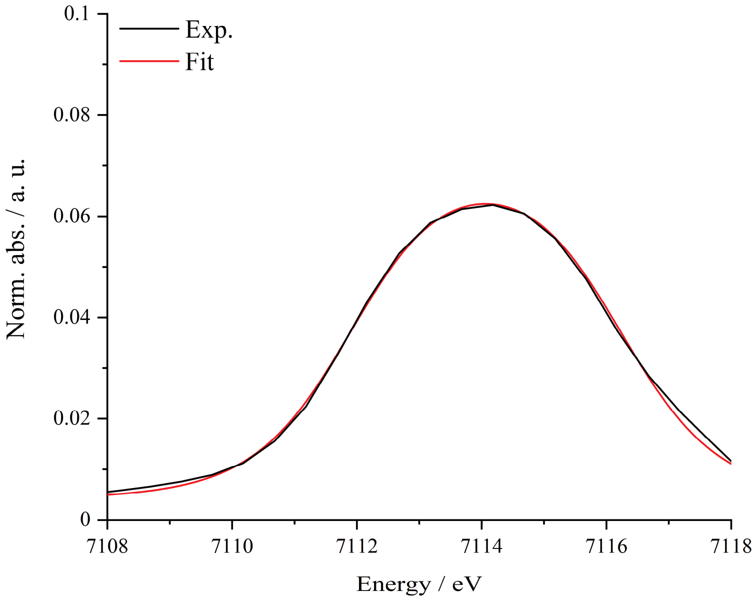

Figure SI 9.8: Pre-peak area of Fe010 with inverse polynomial fit after removal of the main edge.

Table SI 9-44: Fit parameters of the pre-peak fit for Fe10.

Model	InvsPoly
Equation	y=y0+A/(1 + A1*(2*(x-xc)/w)^2 + A2*(2*(x-xc)/w)^4 + A3*(2*(x-xc)/w)^6)
Plot	Fe10
y0	Fe10
xc	0.00648 ± 0.00725
w	7114.06544 ± 0.017
A	4.05682 ± 5774125.59664
A1	0.05577 ± 0.00704
A2	0.32289 ± 919147.83869
A3	0.30113 ± 1714388.62247
χ^2_{red}	0.05151 ± 439853.97278
r^2_{COD}	8.89577E-7
r^2_{corr}	0.99832

Fe20

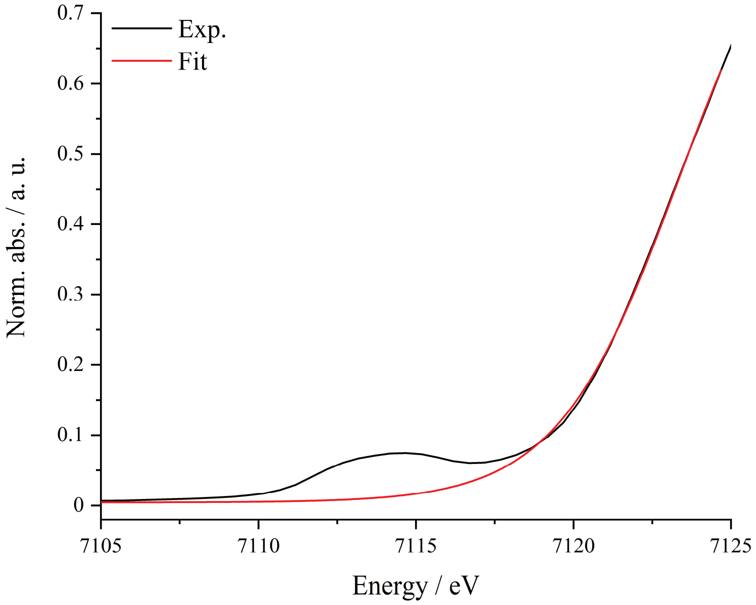

Figure SI 9.9: Pre-peak area of Fe20 and the background to remove the main edge, obtained by a Boltzmann function.

Table SI 9-45: Fit parameters of the background fit for Fe20.

Model	Boltzmann
Equation	y = A2 + (A1-A2)/(1 + exp((x-x0)/dx))
Plot	Fe20
A1	0.00435 ± 6.52698E-4
A2	0.93461 ± 0.02803
x0	7123.38387 ± 0.12485
dx	1.94507 ± 0.04109
χ^2_{red}	1.7425E-5
r^2_{COD}	0.99931
r^2_{corr}	0.99927

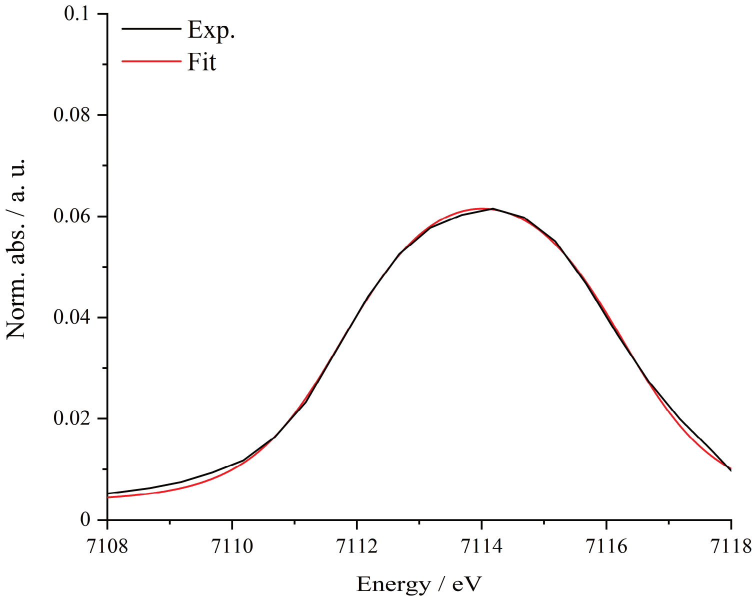

Figure SI 9.10: Pre-peak area of Fe20 with inverse polynomial fit after removal of the main edge.

Table SI 9-46: Fit parameters of the pre-peak fit for Fe20.

Model	InvsPoly
Equation	y=y0+A/(1 + A1*(2*(x-xc)/w)^2 + A2*(2*(x-xc)/w)^4 + A3*(2*(x-xc)/w)^6)
Plot	Fe20
y0	0.0035 ± 8.78886E-4
xc	7114.01046 ± 0.02646
w	5.12845 ± 3.9464E7
A	0.05802 ± 0.00121
A1	0.5623 ± 8653906.19097
A2	0.42336 ± 1.30313E7
A3	0.28062 ± 1.29566E7
χ^2_{rd}	2.30855E-6
r^2_{COD}	0.99634
r^2_{corr}	0.99512

9.4.2 Pre-Peak Analysis: MI01 - MI10, SI10

For pre-peak analysis the main edge was subtracted as a Lorentzian-type function. To obtain the precise pre-peak position a Gaussian-type function was applied for catalysts MM01 to MM10 and two Gaussian-type functions for SI10 while for the references α-Fe_2O_3 and γ-Fe_2O_3 two Lorentzian functions were applied.

MI01

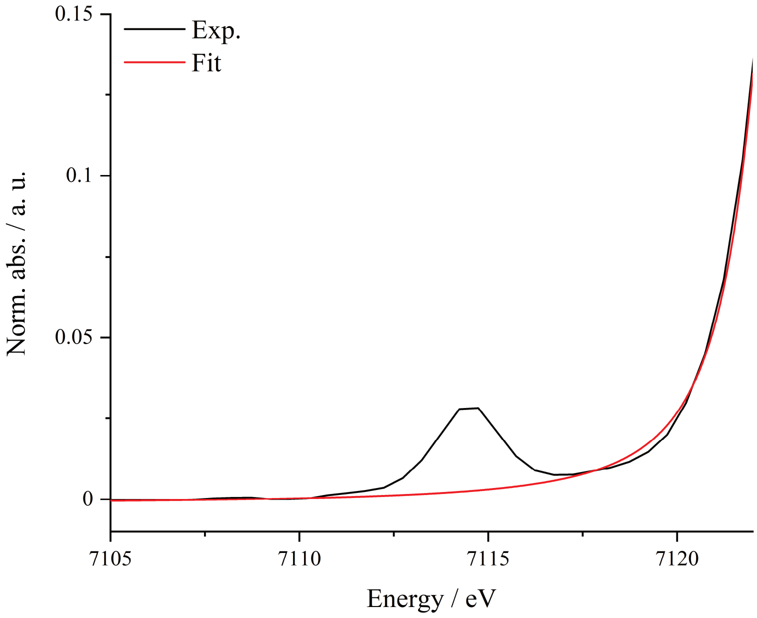

Figure SI 9.23: Pre-peak area of MI01 and the background to remove the main edge, obtained by fit of a Lorentzian-type function.

Table SI 9-47: Fit parameters of the background fit for MI01.

Model	Lorentz
Equation	y = y0 + (2*A/pi)*(w/(4*(x-xc)^2 + w^2))
y0	-0.00134 ± 2.53206E-4
xc	7122.99894 ± 0.02745
w	2.16249 ± 0.02851
A	0.83085 ± 0.01965
χ_{red}^2	1.50014E-6
r_{corr}^2	0.99938

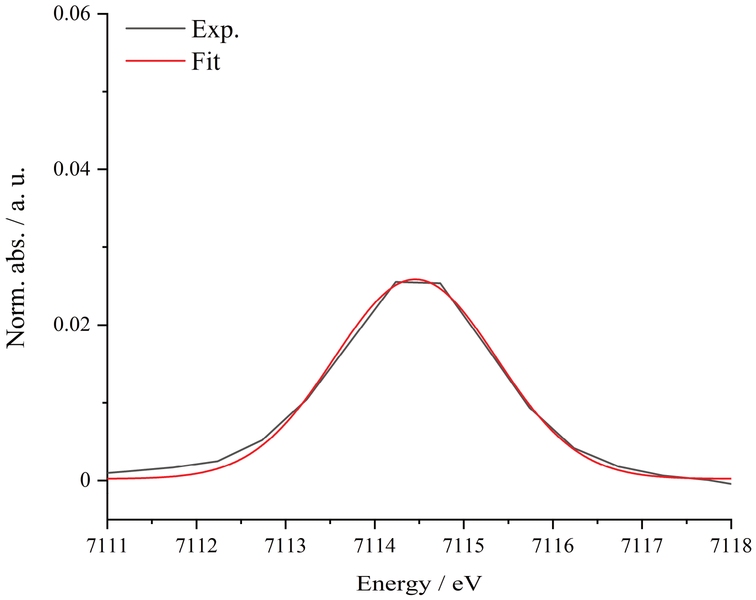

Figure SI 9.24:Background-corrected pre-peak of MI01 and Gaussian-type fit.

Table SI 9-48: Fit parameters of the Gaussian-type fit for MI01.

Model	Gauss
Equation	y=y0 + (A/(w*sqrt(pi/2)))*exp(-2*((x-xc)/w)^2)
y0	2.21708E-4 ± 1.68166E-4
xc	7114.45632 ± 0.02012
w	1.81936 ± 0.04363
A	0.05846 ± 0.00138
χ^2_{red}	5.18256E-7
r^2_{corr}	0.99149

MI02

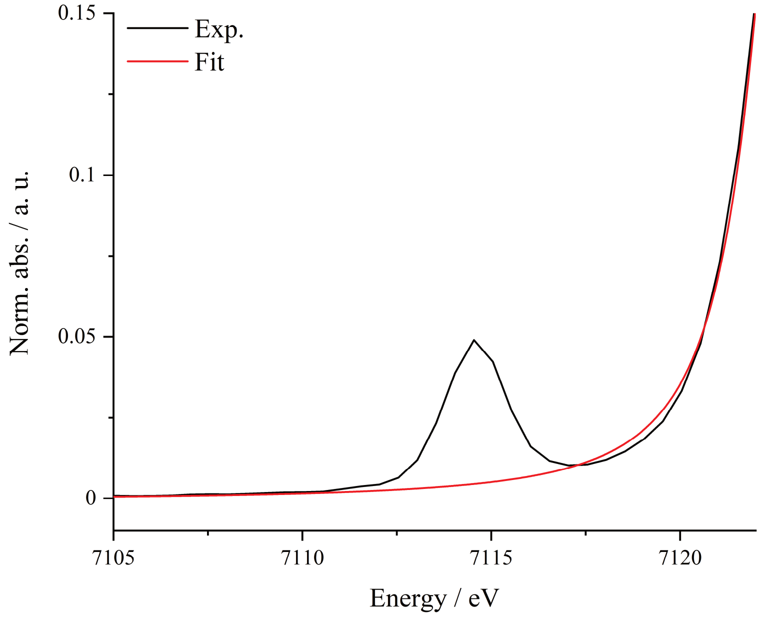

Figure SI 9.25: Pre-peak area of MI02 and the background to remove the main edge, obtained by fit of a Lorentzian-type function.

Table SI 9-49: Fit parameters of the background fit for MI02.

Model	Lorentz
Equation	y = y0 + (2*A/pi)*(w/(4*(x-xc)^2 + w^2))
y0	-6.27677E-4 ± 3.0974E-4
xc	7123 ± 0.04904
w	2.42445 ± 0.03433
A	0.97604 ± 0.03597
χ_{red}^2	2.20822E-6
r_{corr}^2	0.99902

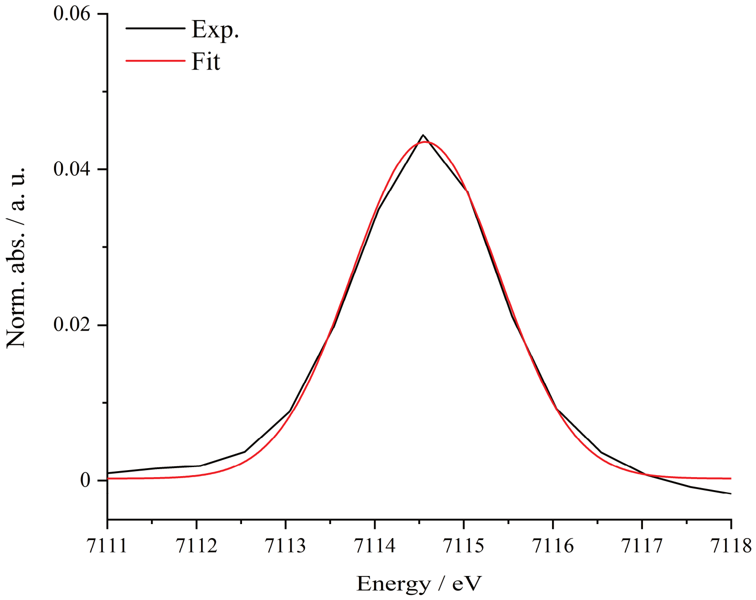

Figure SI 9.26:Background-corrected pre-peak of MI02 and Gaussian-type fit.

Table SI 9-50: Fit parameters of the Gaussian-type fit for MI02.

Model	Gauss
Equation	y=y0 + (A/(w*sqrt(pi/2)))*exp(-2*((x-xc)/w)^2)
y0	2.56433E-4 ± 2.14278E-4
xc	7114.56787 ± 0.01484
w	1.65791 ± 0.03187
A	0.08989 ± 0.00168
χ^2_{red}	8.80845E-7
r^2_{corr}	0.99455

MI03

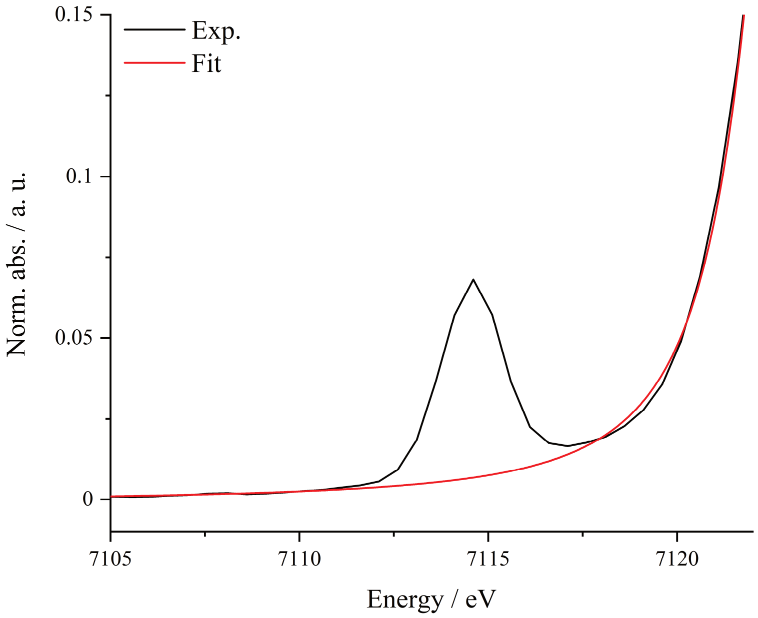

Figure SI 9.27: Pre-peak area of MI03 and the background to remove the main edge, obtained by fit of a Lorentzian-type function.

Table SI 9-51: Fit parameters of the background fit for MI03.

Model	Lorentz
Equation	y = y0 + (2*A/pi)*(w/(4*(x-xc)^2 + w^2))
y0	-6.94182E-4 ± 2.22514E-4
xc	7123.09779 ± 0.03697
w	2.79469 ± 0.02737
A	1.25556 ± 0.03032
χ^2_{red}	1.51575E-6
r^2_{corr}	0.99942

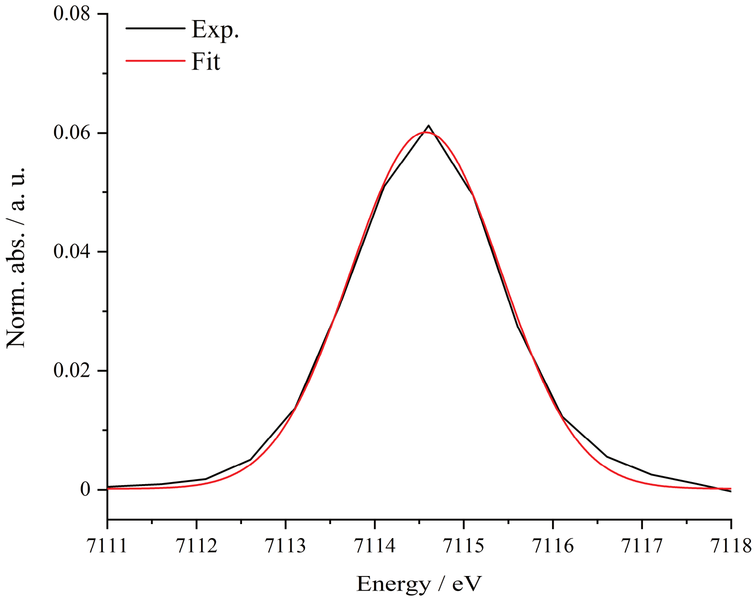

Figure SI 9.28: Background-corrected pre-peak of MI03 and Gaussian-type fit.

Table SI 9-52: Fit parameters of the Gaussian-type fit for MI03.

Model	Gauss
Equation	y=y0 + (A/(w*sqrt(pi/2)))*exp(-2*((x-xc)/w)^2)
y0	1.80232E-4 ± 2.0131E-4
xc	7114.57427 ± 0.01013
w	1.69761 ± 0.0218
A	0.12751 ± 0.0016
χ^2_{red}	7.68903E-7
r^2_{corr}	0.99756

MI04

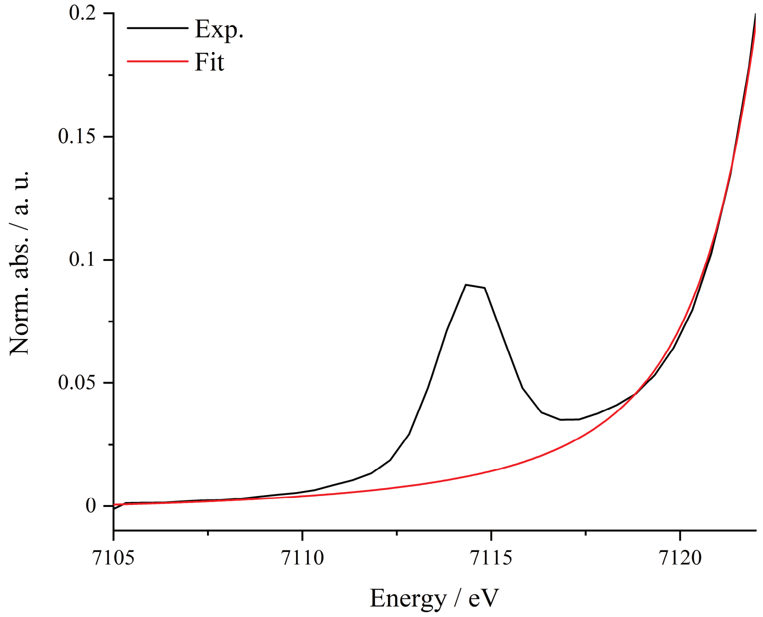

Figure SI 9.29: Pre-peak area of MI04 and the background to remove the main edge, obtained by fit of a Lorentzian-type function.

Table SI 9-53: Fit parameters of the background fit for MI04.

Model	Lorentz
Equation	y = y0 + (2*A/pi)*(w/(4*(x-xc)^2 + w^2))
y0	-0.00373 ± 3.88303E-4
xc	7124.19737 ± 0.11844
w	3.55839 ± 0.06338
A	2.80096 ± 0.18003
χ^2_{red}	3.89796E-6
r^2_{corr}	0.99907

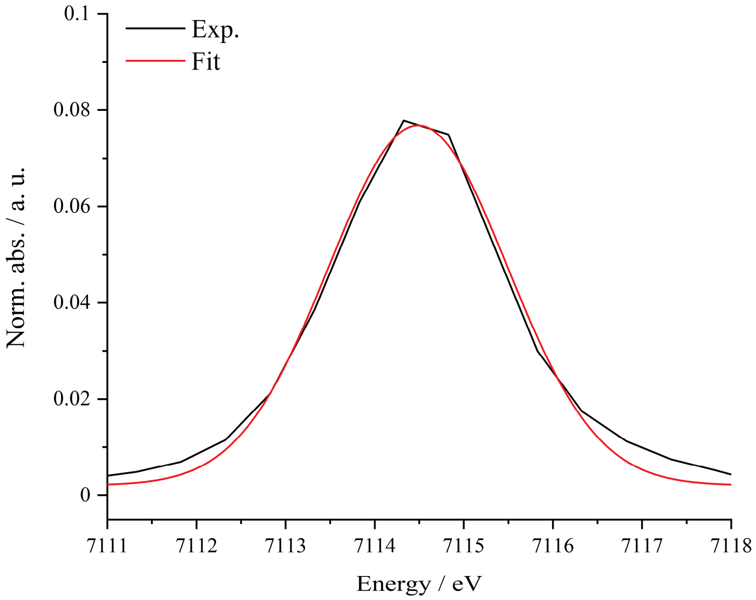

Figure SI 9.30:Background-corrected pre-peak of MI04 and Gaussian-type fit.

Table SI 9-54: Fit parameters of the Gaussian-type fit for MI04.

Model	Gauss
Equation	y=y0 + (A/(w*sqrt(pi/2)))*exp(-2*((x-xc)/w)^2)
y0	0.00208 ± 5.34704E-4
xc	7114.4867 ± 0.02241
w	2.00961 ± 0.04922
A	0.18825 ± 0.00462
χ^2_{red}	4.95046E-6
r^2_{corr}	0.99106

MI05

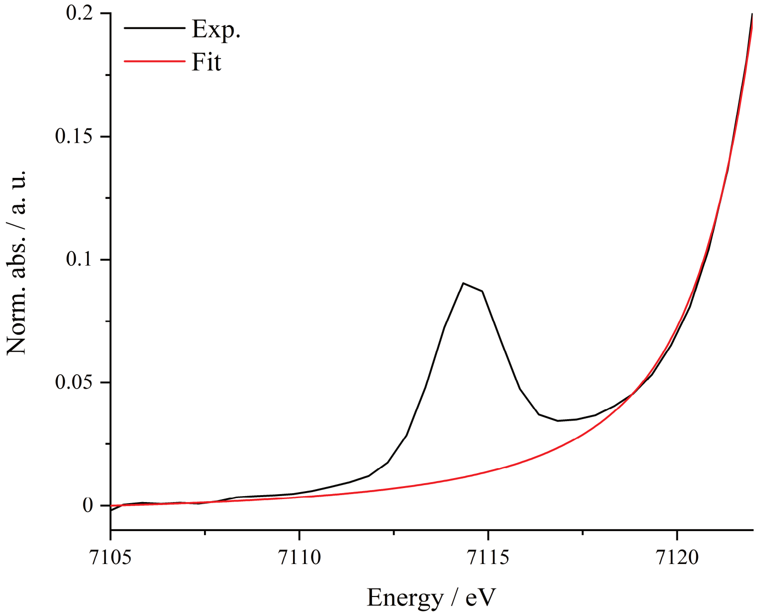

Figure SI 9.31: Pre-peak area of MI05 and the background to remove the main edge, obtained by fit of a Lorentzian-type function.

Table SI 9-55: Fit parameters of the background fit for MI05.

Model	Lorentz
Equation	y = y0 + (2*A/pi)*(w/(4*(x-xc)^2 + w^2))
y0	-0.00429 ± 5.02131E-4
xc	7124.1318 ± 0.1212
w	3.59614 ± 0.05732
A	2.72904 ± 0.17607
χ^2_{red}	4.56358E-6
r^2_{corr}	0.99914

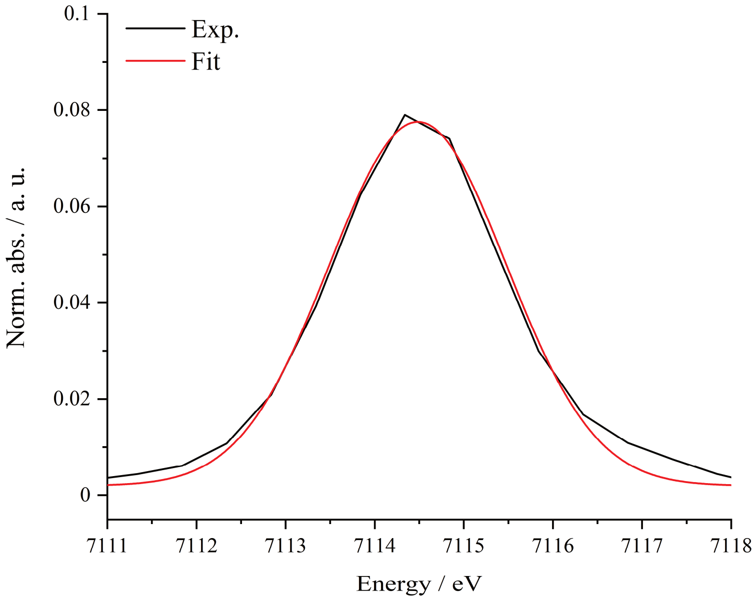

Figure SI 9.32: Background-corrected pre-peak of MI05 and Gaussian-type fit.

Table SI 9-56: Fit parameters of the Gaussian-type fit for MI05.

Model	Gauss
Equation	y=y0 + (A/(w*sqrt(pi/2)))*exp(-2*((x-xc)/w)^2)
y0	0.002 ± 4.9027E-4
xc	7114.48435 ± 0.02029
w	1.99062 ± 0.0445
A	0.18852 ± 0.00422
χ^2_{red}	4.18611E-6
r^2_{corr}	0.99255

MI06

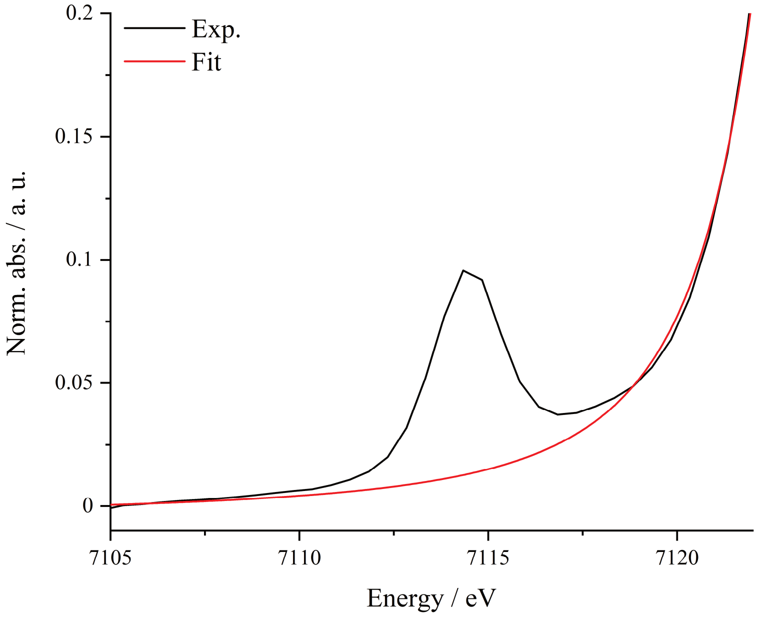

Figure SI 9.33: Pre-peak area of MI06 and the background to remove the main edge, obtained by fit of a Lorentzian-type function.

Table SI 9-57: Fit parameters of the background fit for MI06.

Model	Lorentz
Equation	y = y0 + (2*A/pi)*(w/(4*(x-xc)^2 + w^2))
y0	-0.00398 ± 4.51623E-4
xc	7124.14983 ± 0.12474
w	3.61093 ± 0.06099
A	2.88967 ± 0.19081
χ^2_{red}	5.32198E-6
r^2_{corr}	0.99888

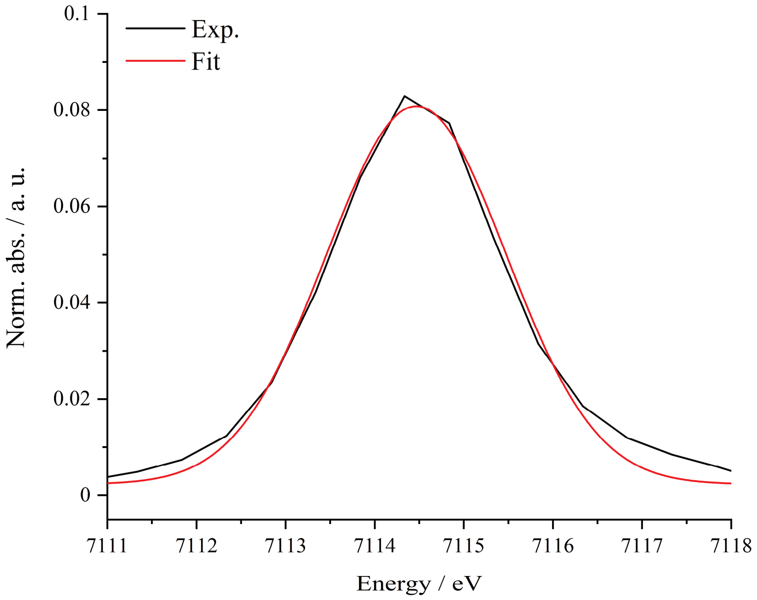

Figure SI 9.34: Background-corrected pre-peak of MI06 and Gaussian-type fit.

Table SI 9-58: Fit parameters of the Gaussian-type fit for MI06.

Model	Gauss
Equation	y=y0 + (A/(w*sqrt(pi/2)))*exp(-2*((x-xc)/w)^2)
y0	0.00232 ± 5.74127E-4
xc	7114.46738 ± 0.02294
w	2.0221 ± 0.05042
A	0.19896 ± 0.00498
χ^2_{red}	5.68547E-6
r^2_{corr}	0.99074

MI07

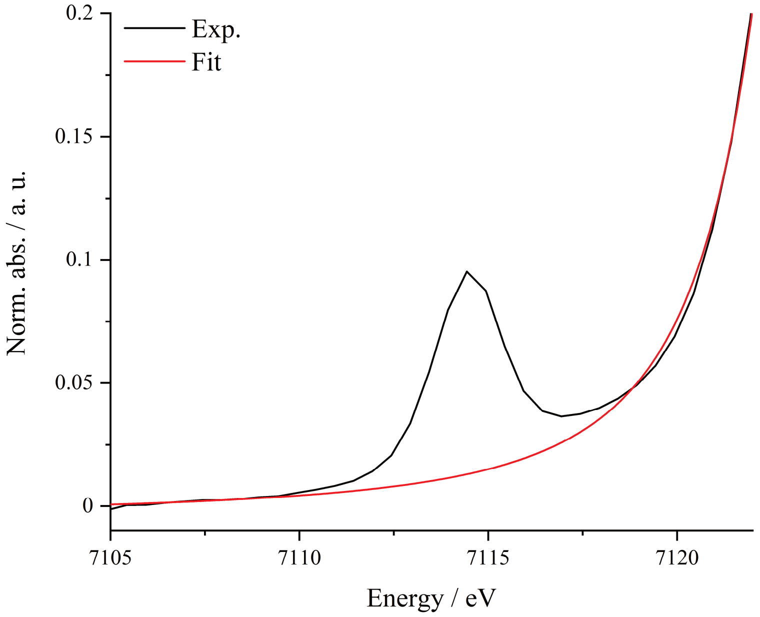

Figure SI 9.35: Pre-peak area of MI07 and the background to remove the main edge, obtained by fit of a Lorentzian-type function.

Table SI 9-59: Fit parameters of the background fit for MI07.

Model	Lorentz
Equation	y = y0 + (2*A/pi)*(w/(4*(x-xc)^2 + w^2))
y0	-0.00385 ± 5.11625E-4
xc	7124.20323 ± 0.12977
w	3.60798 ± 0.06208
A	2.90348 ± 0.19851
χ^2_{red}	6.82144E-6
r^2_{corr}	0.99864

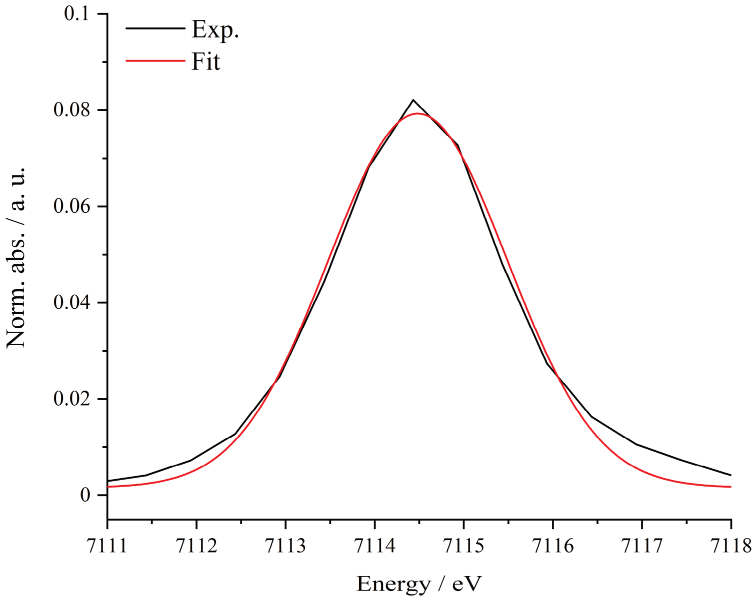

Figure SI 9.36: Background-corrected pre-peak of MI07 and Gaussian-type fit.

Table SI 9-60: Fit parameters of the Gaussian-type fit for MI07.

Model	Gauss
Equation	y=y0 + (A/(w*sqrt(pi/2)))*exp(-2*((x-xc)/w)^2)
Plot	MI07
y0	0.00161 ± 5.67413E-4
xc	7114.4837 ± 0.02291
w	2.0158 ± 0.05033
A	0.19616 ± 0.00491
χ^2_{red}	5.56397E-6
r^2_{corr}	0.99071

MI08

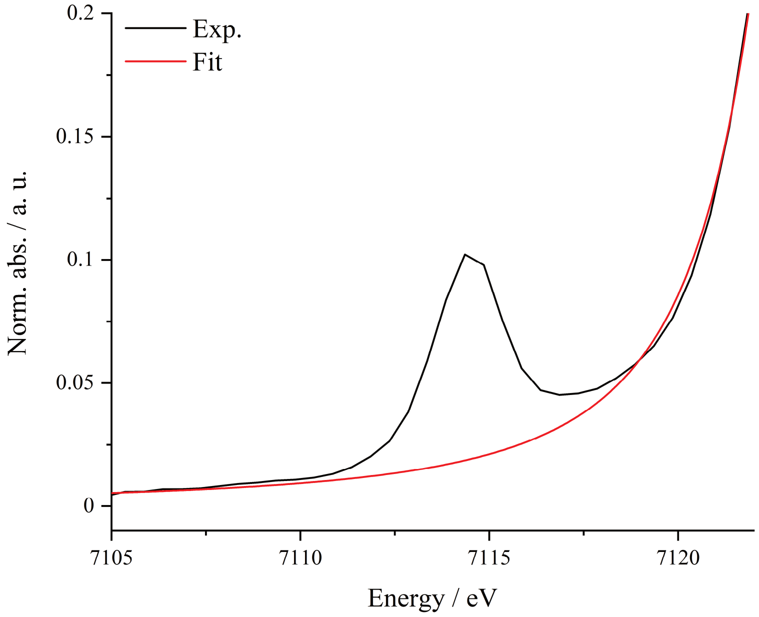

Figure SI 9.37: Pre-peak area of MI08 and the background to remove the main edge, obtained by fit of a Lorentzian-type function.

Table SI 9-61: Fit parameters of the background fit for MI08.

Model	Lorentz
Equation	y = y0 + (2*A/pi)*(w/(4*(x-xc)^2 + w^2))
y0	3.70286E-4 ± 4.97527E-4
xc	7124.30302 ± 0.14582
w	3.69952 ± 0.07951
A	3.18127 ± 0.24322
χ^2_{red}	6.14778E-6
r^2_{corr}	0.99879

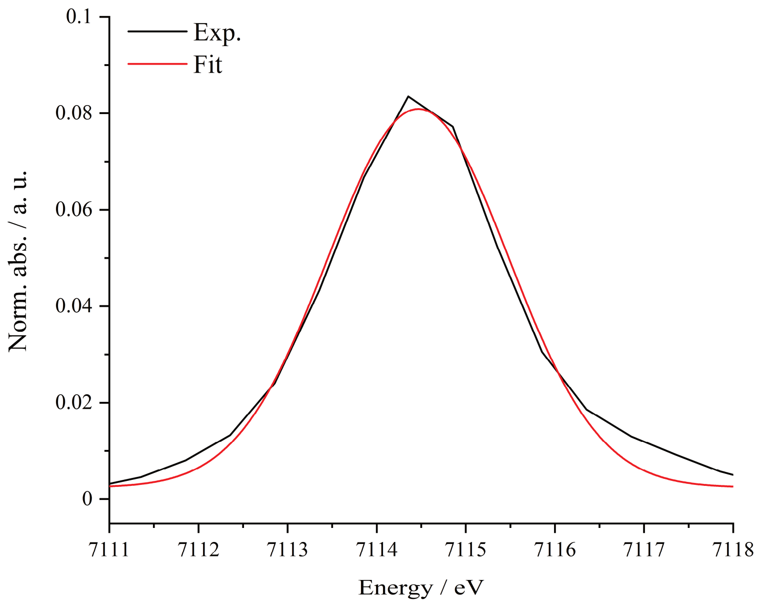

Figure SI 9.38: Background-corrected pre-peak of MI08 and Gaussian-type fit.

Table SI 9-62: Fit parameters of the Gaussian-type fit for MI08.

Model	Gauss
Equation	y=y0 + (A/(w*sqrt(pi/2)))*exp(-2*((x-xc)/w)^2)
y0	0.00245 ± 6.19254E-4
xc	7114.46707 ± 0.02477
w	2.02999 ± 0.05448
A	0.19964 ± 0.00538
χ^2_{red}	6.59826E-6
r^2_{corr}	0.98928

MI09

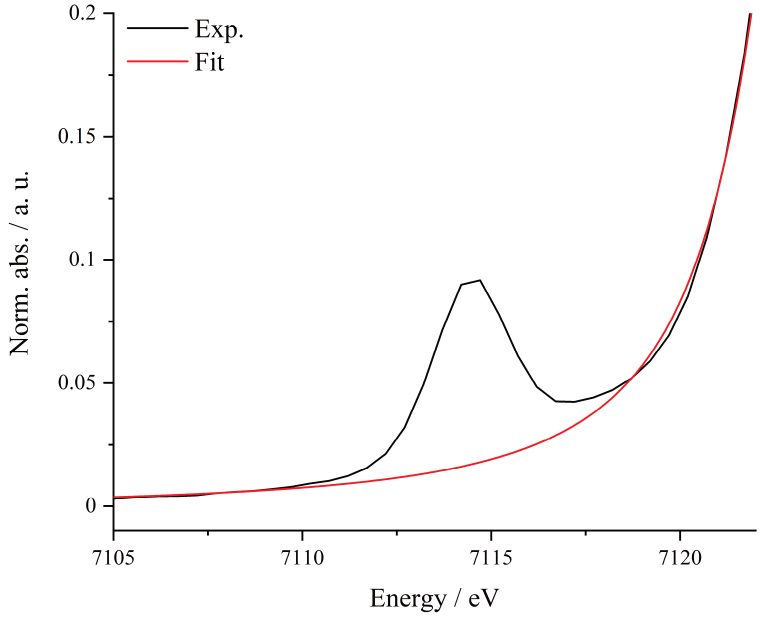

Figure SI 9.39: Pre-peak area of MI09 and the background to remove the main edge, obtained by fit of a Lorentzian-type function.

Table SI 9-63: Fit parameters of the background fit for MI09.

Model	Lorentz
Equation	y = y0 + (2*A/pi)*(w/(4*(x-xc)^2 + w^2))
Plot	MI09
y0	-0.00121 ± 6.8551E-4
xc	7124.24778 ± 0.19099
w	3.69777 ± 0.11336
A	3.07277 ± 0.31326
χ^2_{red}	7.39443E-6
r^2_{corr}	0.9986

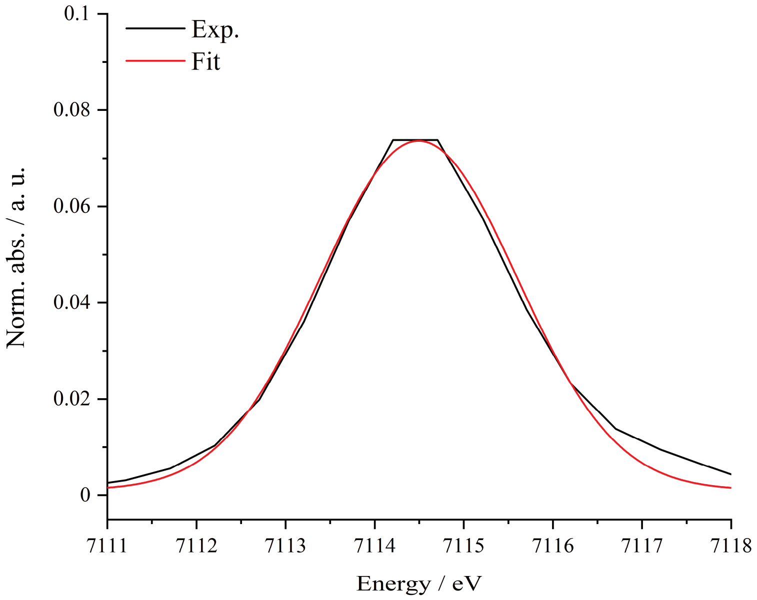

Figure SI 9.40: Background-corrected pre-peak of MI09 and Gaussian-type fit.

Table SI 9-64: Fit parameters of the Gaussian-type fit for MI09.

Model	Gauss
Equation	y=y0 + (A/(w*sqrt(pi/2)))*exp(-2*((x-xc)/w)^2)
y0	0.0011 ± 4.95314E-4
xc	7114.49345 ± 0.02176
w	2.21733 ± 0.0485
A	0.20146 ± 0.0045
χ^2_{red}	3.97863E-6
r^2_{corr}	0.99282

MI10

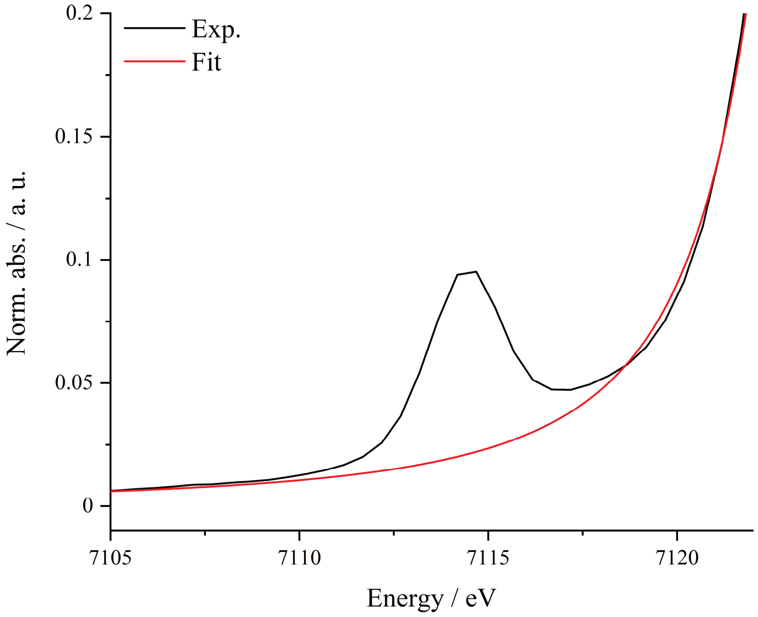

Figure SI 9.41: Pre-peak area of MI10 and the background to remove the main edge, obtained by fit of a Lorentzian-type function.

Table SI 9-65: Fit parameters of the background fit for MI10.

Model	Lorentz
Equation	y = y0 + (2*A/pi)*(w/(4*(x-xc)^2 + w^2))
y0	2.09368E-4 ± 5.49251E-4
xc	7124.70793 ± 0.23519
w	3.49844 ± 0.25309
A	4.0835 ± 0.60115
χ^2_{red}	6.5458E-6
r^2_{corr}	0.99851

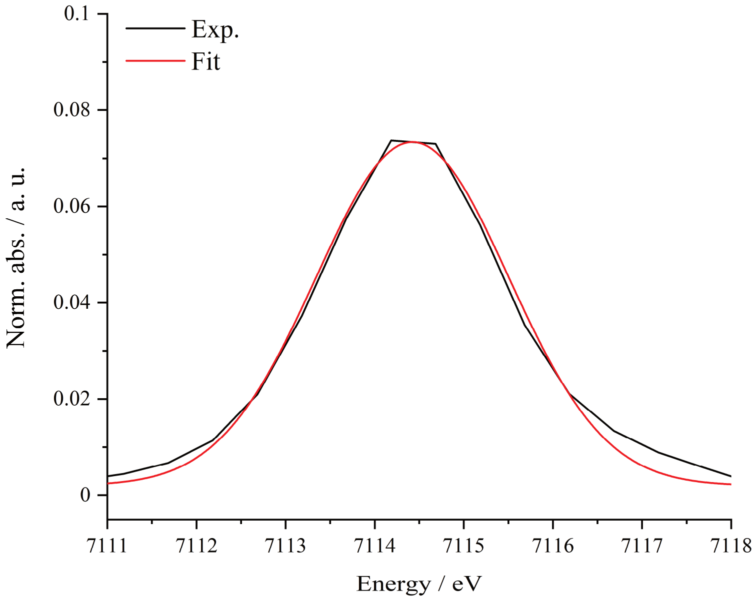

Figure SI 9.42: Background-corrected pre-peak of MI10 and Gaussian-type fit.

Table SI 9-66: Fit parameters of the Gaussian-type fit for MI10.

Model	Gauss
Equation	y=y0 + (A/(w*sqrt(pi/2)))*exp(-2*((x-xc)/w)^2)
y0	0.00201 ± 4.67511E-4
xc	7114.42308 ± 0.02079
w	2.16317 ± 0.04615
A	0.19347 ± 0.0042
χ^2_{red}	3.60672E-6
r^2_{corr}	0.99317

SI10

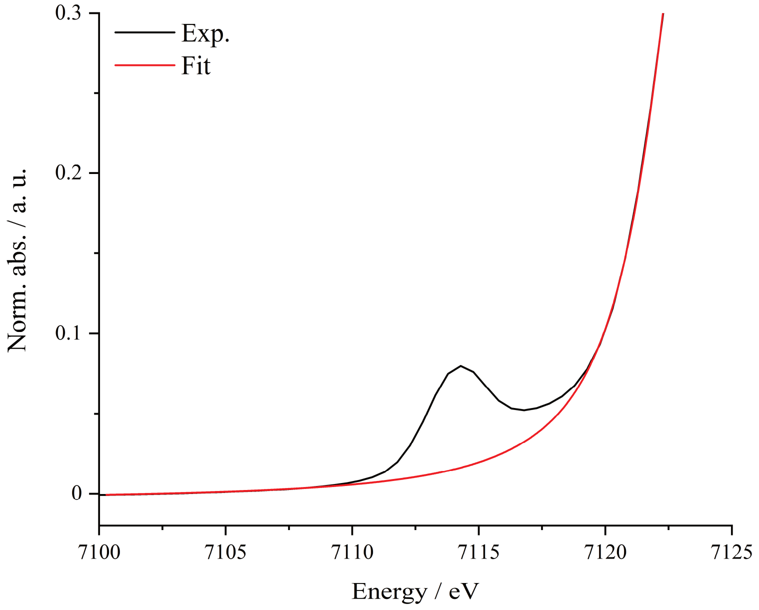

Figure SI 9.43: Pre-peak area of SI10 and the background to remove the main edge, obtained by fit of a Lorentzian-type function.

Table SI 9-67: Fit parameters of the background fit for SI10.

Model	Lorentz
Equation	y = y0 + (2*A/pi)*(w/(4*(x-xc)^2 + w^2))
y0	-0.0039 ± 1.61826E-4
xc	7123.54084 ± 0.02196
w	4.161 ± 0.01689
A	2.71869 ± 0.02793
χ^2_{red}	3.68074E-7
r^2_{corr}	0.99996

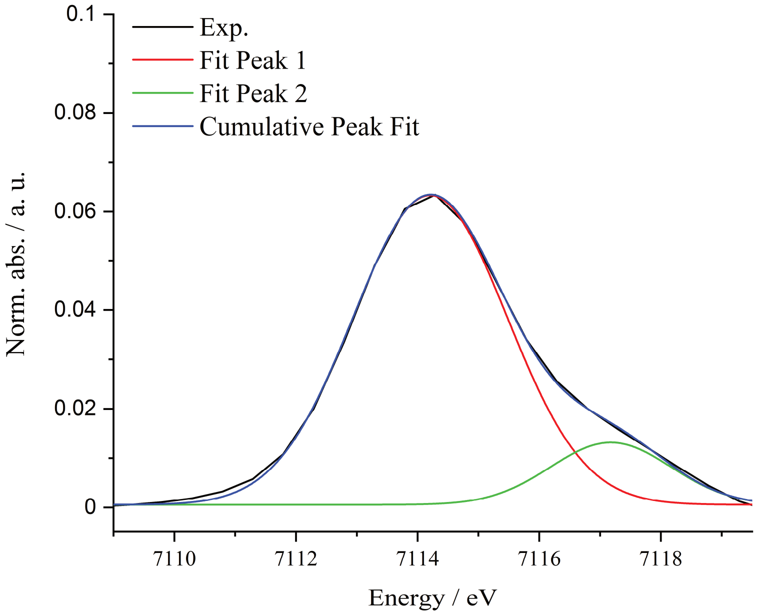

Figure SI 9.44: Background-corrected pre-peak of SI10 and two fitted Gaussian-type functions with the respective cumulative peak fit.

Table SI 9-68: Fit parameters of the Gaussian-type fit for SI10.

Model	Gauss	
Equation	y=y0 + (A/(w*sqrt(pi/2)))*exp(-2*((x-xc)/w)^2)	
Plot	Peak1	Peak2
y0	5.61417E-4 ± 2.55641E-4	5.61417E-4 ± 2.55641E-4
xc	7114.2061 ± 0.02122	7117.1761 ± 0.08881
w	2.53021 ± 0.03861	1.98046 ± 0.13914
A	0.199 ± 0.00337	0.0313 ± 0.00294
χ^2_{red}	4.41297E-7	
r^2_{corr}	0.99903	

9.4.3 Pre-peak Analysis: Mn K-edge, MM01 - MM04

For pre-peak analysis the main edge was subtracted as a Lorentzian-type function. To obtain the precise pre-peak position two Gaussian-type functions were applied for catalysts MM01 to MM04 and for the $LiMn_2O_4$ reference.

MM01

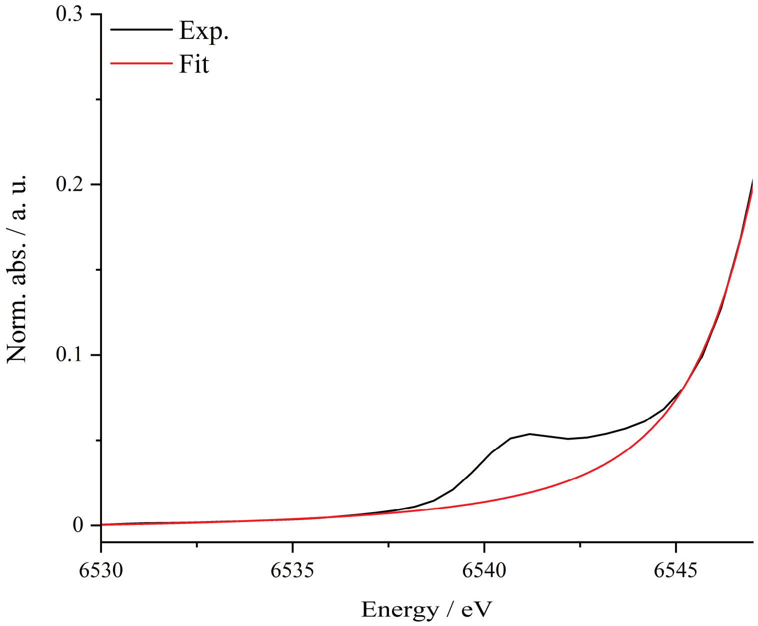

Figure SI 9.45: Pre-peak area of MM01 at the Mn K-edge and the background to remove the main edge, obtained by a Lorentz function.

Table SI 9-69: Fit parameters of the background fit for MM01.

Model	Lorentz
Equation	y = y0 + (2*A/pi)*(w/(4*(x-xc)^2 + w^2))
y0	-0.00362 ± 3.04277E-4
x_c	6548.7847 ± 0.07791
w	3.90446 ± 0.03095
A	2.27054 ± 0.08687
χ^2_{red}	1.14513E-6
r^2_{corr}	0.99979

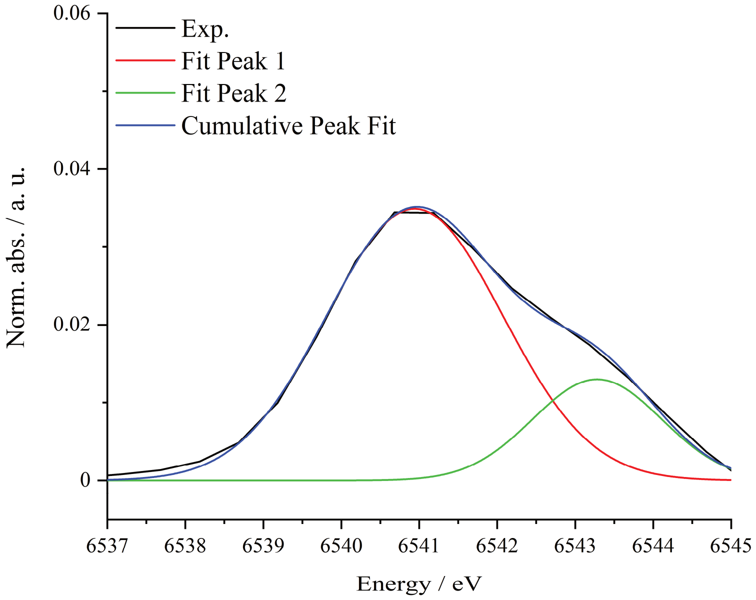

Figure SI 9.46: Background-corrected pre-peak of MM01, two Gaussian-type peak fits and cumulative peak fit.

Table SI 9-70: Fit parameters of the pre-peak fit of MM01.

Model	Gauss	
Equation	y=y0 + (A/(w*sqrt(pi/2)))*exp(-2*((x-xc)/w)^2)	
Plot	Peak1	Peak2
y0	0 ± 3.09765E-4	0 ± 3.09765E-4
xc	6540.9415 ± 0.0615	6543.28092 ± 0.11954
w	2.26204 ± 0.09828	1.65347 ± 0.16744
A	0.09896 ± 0.00513	0.0269 ± 0.00464
χ^2_{red}	7.00685E-7	
r^2_{corr}	0.99552	

MM02

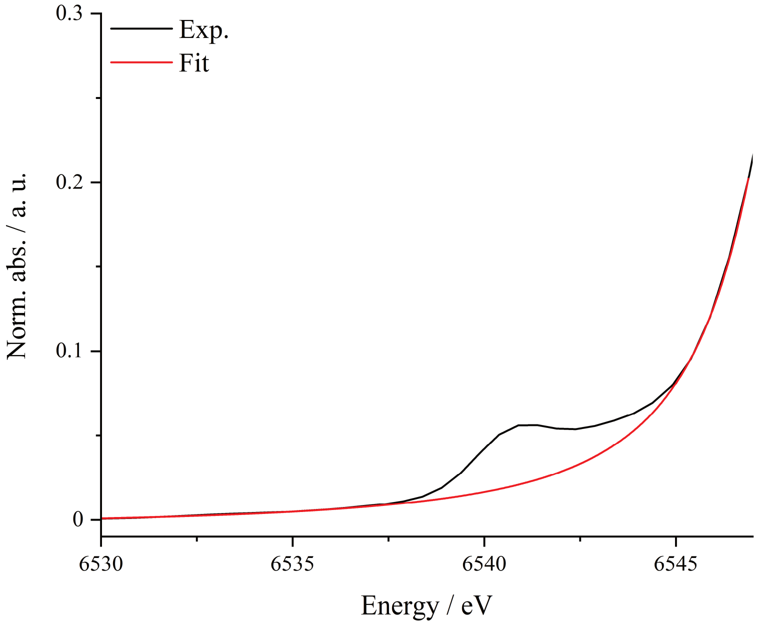

Figure SI 9.47: Pre-peak area of MM02 at the Mn K-edge and the background to remove the main edge, obtained by a Lorentz function.

Table SI 9-71: Fit parameters of the background fit for MM02.

Model	Lorentz
Equation	y = y0 + (2*A/pi)*(w/(4*(x-xc)^2 + w^2))
y0	-0.0041 ± 2.34388E-4
xc	6549.3513 ± 0.14317
w	3.43824 ± 0.16188
A	3.40026 ± 0.32516
χ^2_{red}	1.21784E-7
r^2_{corr}	0.99996

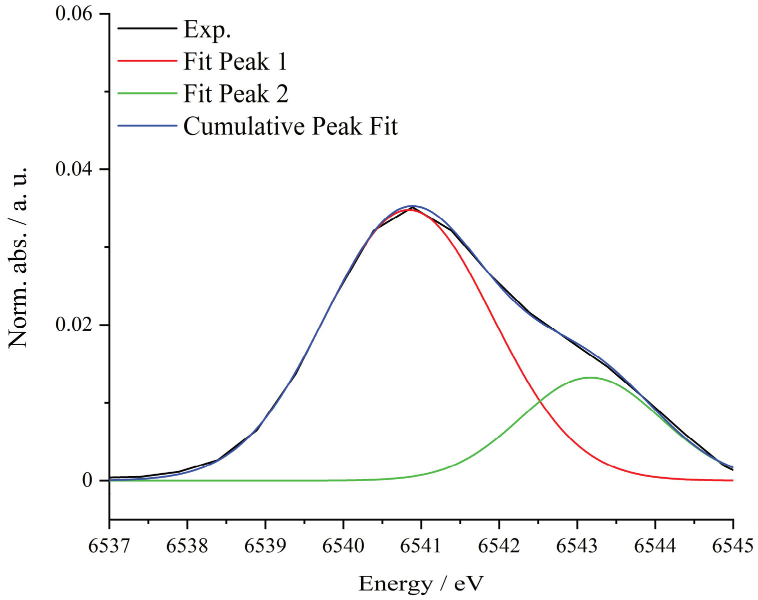

Figure SI 9.48: Background-corrected pre-peak of MM02, two Gaussian-type peak fits and cumulative peak fit.

Table SI 9-72: Fit parameters of the pre-peak fit of MM02.

Model	Gauss	
Equation	y=y0 + (A/(w*sqrt(pi/2)))*exp(-2*((x-xc)/w)^2)	
Plot	Peak1	Peak2
y0	0 ± 1.54719E-4	0 ± 1.54719E-4
xc	6540.84028 ± 0.03436	6543.17109 ± 0.07486
w	2.14782 ± 0.05001	1.79616 ± 0.09803
A	0.0937 ± 0.00287	0.02981 ± 0.00271
χ^2_{red}	1.72968E-7	
r^2_{corr}	0.99886	

MM03

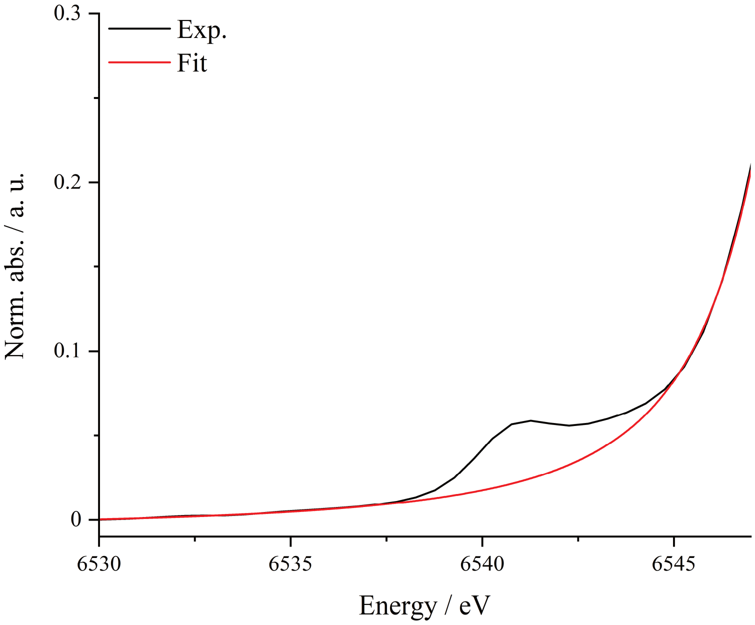

Figure SI 9.49: Pre-peak area of MM03 at the Mn K-edge and the background to remove the main edge, obtained by a Lorentz function.

Table SI 9-73: Fit parameters of the background fit for MM03.

Model	Lorentz
Equation	y = y0 + (2*A/pi)*(w/(4*(x-xc)^2 + w^2))
y0	-0.00543 ± 4.53545E-4
xc	6549.71204 ± 0.23309
w	3.58042 ± 0.2666
A	3.91759 ± 0.58432
χ^2_{red}	7.361E-7
r^2_{corr}	0.99983

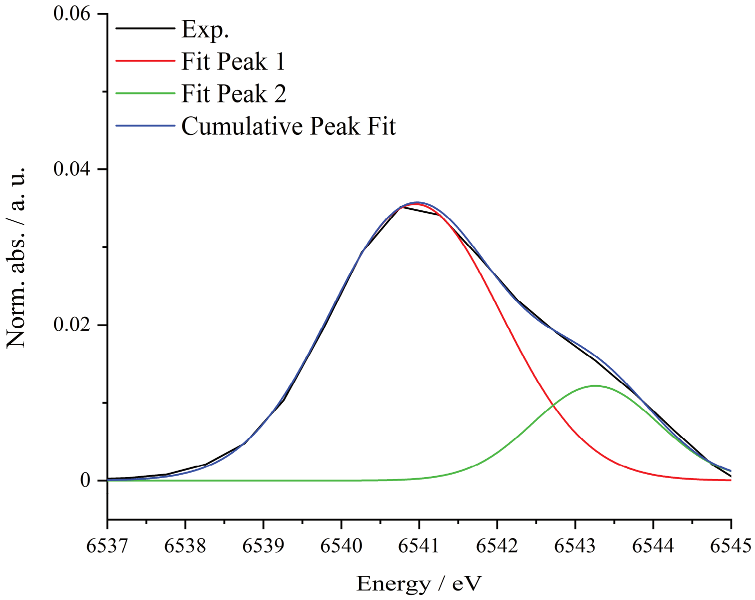

Figure SI 9.50: Background-corrected pre-peak of MM03, two Gaussian-type peak fits and cumulative peak fit.

Table SI 9-74: Fit parameters of the pre-peak fit of MM03.

Model	Gauss	
Equation	y=y0 + (A/(w*sqrt(pi/2)))*exp(-2*((x-xc)/w)^2)	
Plot	Peak1	Peak2
y0	0 ± 2.82835E-4	0 ± 2.82835E-4
xc	6540.94895 ± 0.05254	6543.26034 ± 0.11362
w	2.19263 ± 0.08553	1.61278 ± 0.16235
A	0.09768 ± 0.00446	0.02454 ± 0.00404
χ^2_{red}	6.105E-7	
r^2_{corr}	0.99611	

MM04

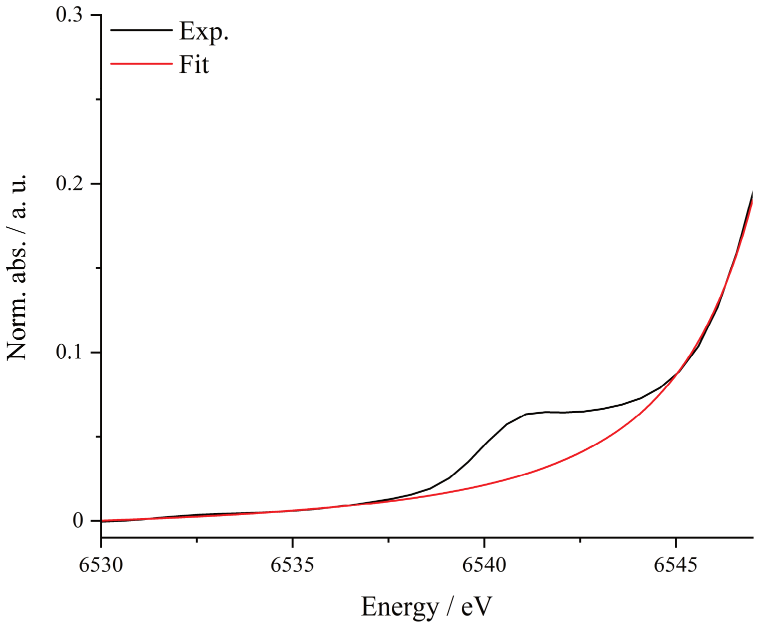

Figure SI 9.51: Pre-peak area of MM04 at the Mn K-edge and the background to remove the main edge, obtained by a Lorentz function.

Table SI 9-75: Fit parameters of the background fit for MM04.

Model	Lorentz
Equation	y = y0 + (2*A/pi)*(w/(4*(x-xc)^2 + w^2))
y0	-0.00796 ± 8.10045E-4
xc	6550.96858 ± 0.47016
w	3.05711 ± 1.08183
A	7.36903 ± 3.45244
χ^2_{red}	1.89524E-6
r^2_{corr}	0.99962

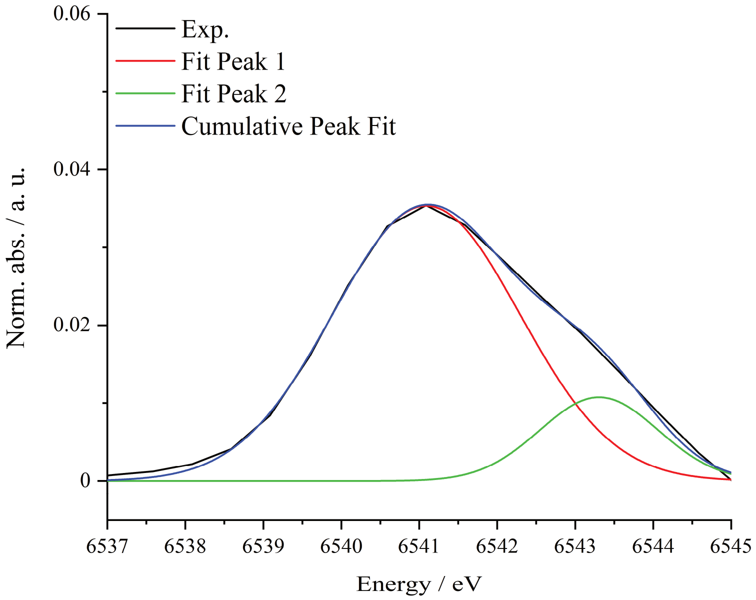

Figure SI 9.52: Background-corrected pre-peak of MM04, two Gaussian-type peak fits and cumulative peak fit.

Table SI 9-76: Fit parameters of the pre-peak fit of MM04.

Model	Gauss	
Equation	y=y0 + (A/(w*sqrt(pi/2)))*exp(-2*((x-xc)/w)^2)	
Plot	Peak1	Peak2
y0	0 ± 3.6518E-4	0 ± 3.6518E-4
xc	6541.08939 ± 0.07968	6543.30552 ± 0.14742
w	2.40219 ± 0.12714	1.51951 ± 0.22188
A	0.10642 ± 0.00671	0.02046 ± 0.0059
χ^2_{red}	9.8841E-7	
r^2_{corr}	0.99406	

9.4.4 Pre-peak Analysis: Fe K-edge, MM01 - MM05

For pre-peak analysis the main edge was subtracted as a Lorentzian-type function. To obtain the precise pre-peak position two Gaussian-type functions were applied for catalysts MM01 to MM05 and for the Fe_2O_3 references.

MM01

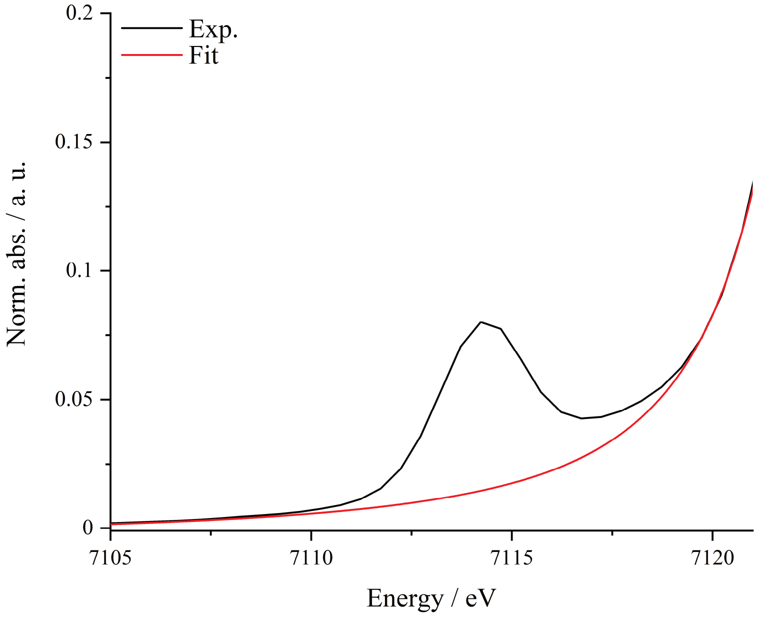

Figure SI 9.53: Pre-peak area of MM01 at the Fe K-edge and the background to remove the main edge, obtained by a Lorentzian-type function.

Table SI 9-77: Fit parameters of the background fit for MM01.

Model	Lorentz
Equation	y = y0 + (2*A/pi)*(w/(4*(x-xc)^2 + w^2))
y0	-0.0036 ± 2.66606E-4
xc	7124.65682 ± 0.26843
w	2.40237 ± 0.68373
A	5.22864 ± 1.88842
χ^2_{red}	2.6322E-7
r^2_{corr}	0.9999

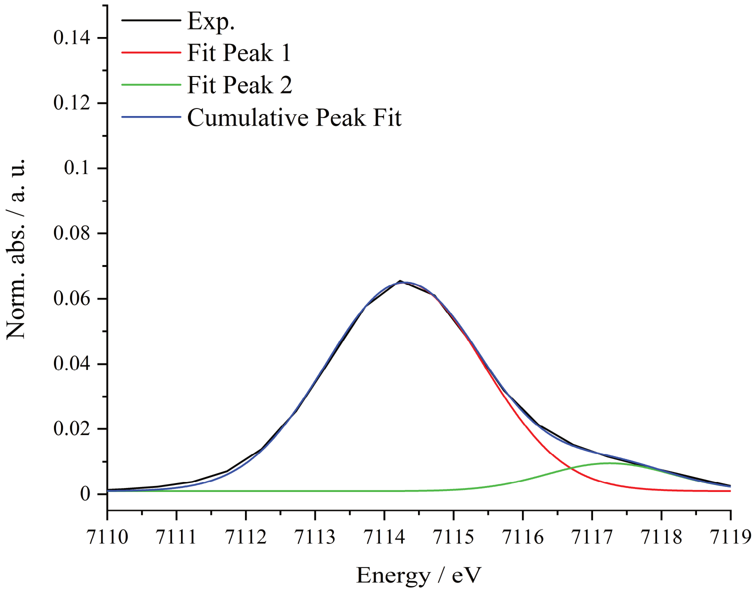

Figure SI 9.54: Background-corrected pre-peak of MM01 and corresponding Gaussian-type peak fits and cumulative peak fit.

Table SI 9-78: Fit parameters of the pre-peak fit of MM01.

Model	Gauss	
Equation	y=y0 + (A/(w*sqrt(pi/2)))*exp(-2*((x-xc)/w)^2)	
Plot	Peak1	Peak2
y0	9.43939E-4 ± 3.25475E-4	9.43939E-4 ± 3.25475E-4
xc	7114.29329 ± 0.01879	7117.25275 ± 0.12428
w	2.28715 ± 0.03825	1.81866 ± 0.22249
A	0.18368 ± 0.00318	0.0196 ± 0.00274
χ^2_{red}	7.12872E-7	
r^2_{corr}	0.99846	

MM02

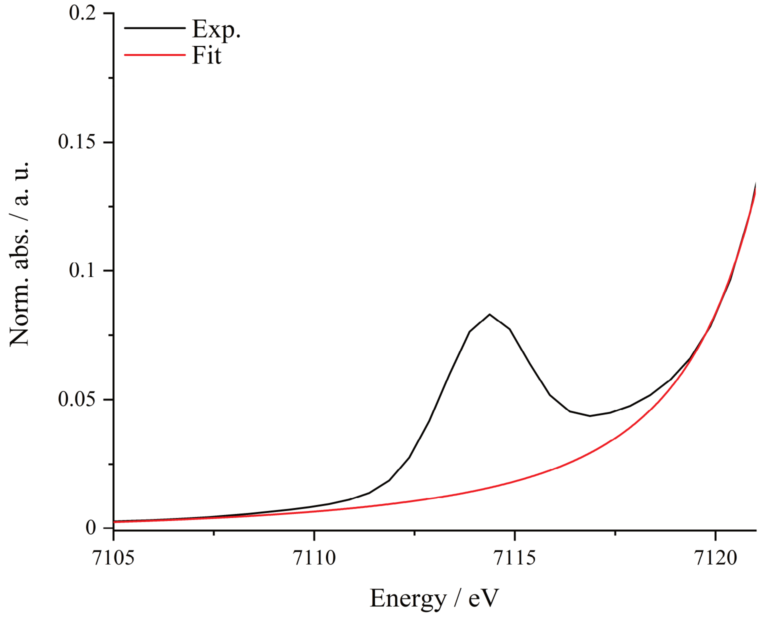

Figure SI 9.55: Pre-peak area of MM02 at the Fe K-edge and the background to remove the main edge, obtained by a Lorentzian-type function.

Table SI 9-79: Fit parameters of the background fit for MM02.

Model	Lorentz
Equation	y = y0 + (2*A/pi)*(w/(4*(x-xc)^2 + w^2))
y0	-0.00263 ± 2.01165E-4
xc	7124.49691 ± 0.18058
w	2.92837 ± 0.3211
A	4.13282 ± 0.67727
χ^2_{red}	2.82287E-7
r^2_{corr}	0.9999

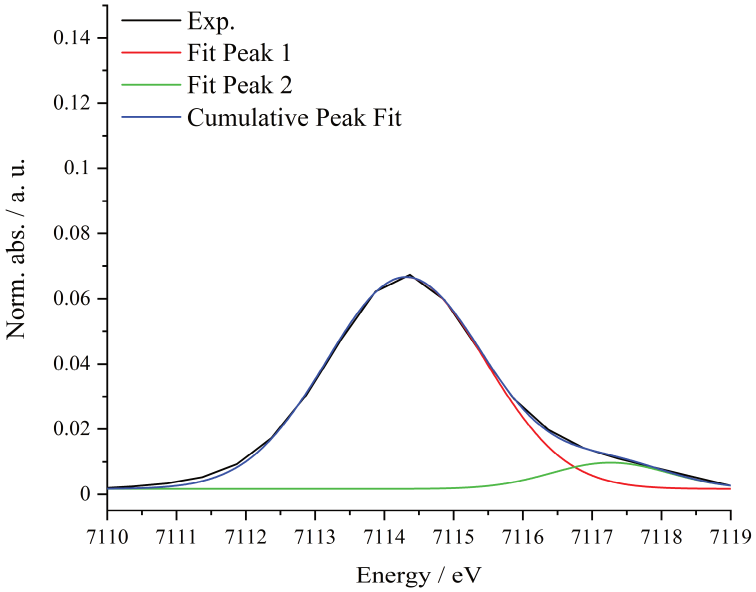

Figure SI 9.56: Background-corrected pre-peak of MM02 and corresponding Gaussian-type peak fits and cumulative peak fit.

Table SI 9-80: Fit parameters of the pre-peak fit of MM02.

Model	Gauss	
Equation	y=y0 + (A/(w*sqrt(pi/2)))*exp(-2*((x-xc)/w)^2)	
Plot	Peak1	Peak2
y0	0.00166 ± 3.9843E-4	0.00166 ± 3.9843E-4
xc	7114.31205 ± 0.01944	7117.26343 ± 0.13512
w	2.28832 ± 0.042	1.69621 ± 0.24876
A	0.18643 ± 0.00352	0.0172 ± 0.00284
χ^2_{red}	9.64173E-7	
r^2_{corr}	0.99802	

MM03

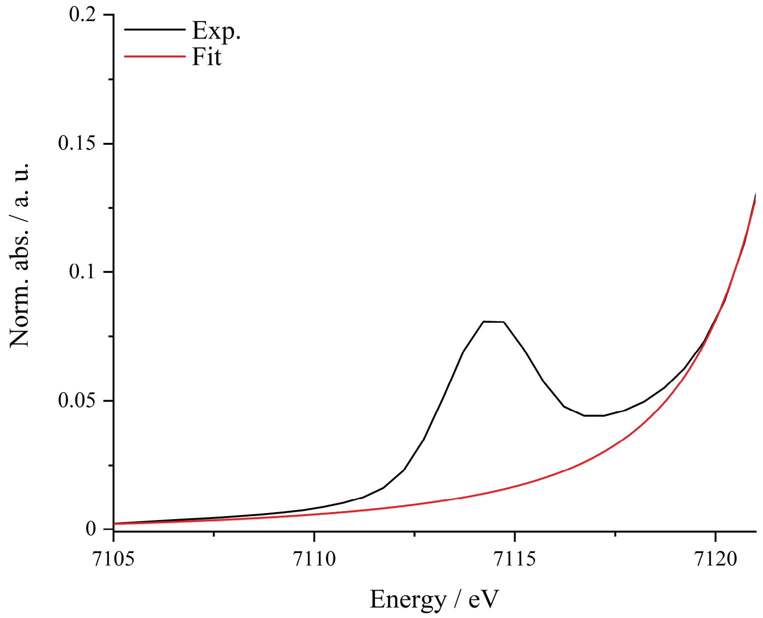

Figure SI 9.57: Pre-peak area of MM03 at the Fe K-edge and the background to remove the main edge, obtained by a Lorentzian-type function.

Table SI 9-81: Fit parameters of the background fit for MM03.

Model	Lorentz
Equation	y = y0 + (2*A/pi)*(w/(4*(x-xc)^2 + w^2))
y0	-0.00218 ± 1.58591E-4
xc	7123.87947 ± 0.08773
w	3.78408 ± 0.04036
A	2.5811 ± 0.11894
χ^2_{red}	3.17152E-7
r^2_{corr}	0.99992

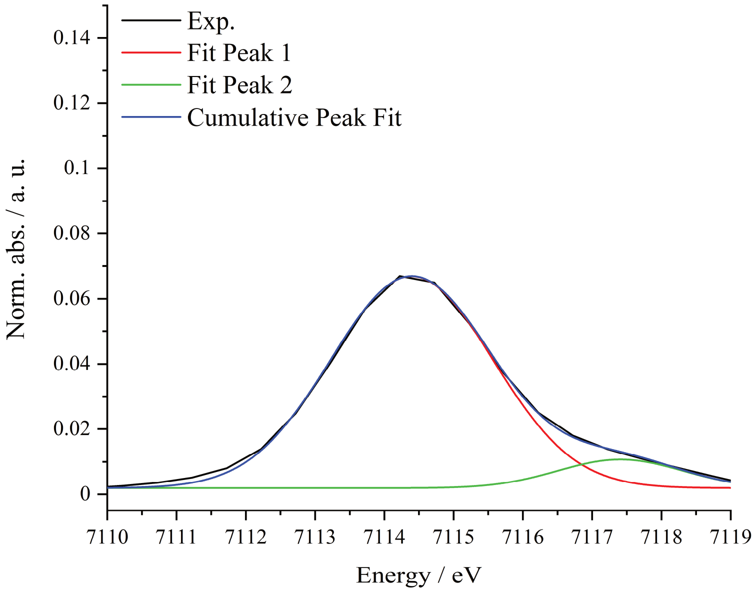

Figure SI 9.58: Background-corrected pre-peak of MM03 and corresponding Gaussian-type peak fits and cumulative peak fit.

Table SI 9-82: Fit parameters of the pre-peak fit of MM03.

Model	Gauss	
Equation	y=y0 + (A/(w*sqrt(pi/2)))*exp(-2*((x-xc)/w)^2)	
Plot	Peak1	Peak2
y0	0.00192 ± 4.2918E-4	0.00192 ± 4.2918E-4
xc	7114.39539 ± 0.02341	7117.40661 ± 0.15104
w	2.34096 ± 0.04891	1.79644 ± 0.27293
A	0.19072 ± 0.00411	0.01983 ± 0.00343
χ^2_{red}	1.20828E-6	
r^2_{corr}	0.99749	

MM04

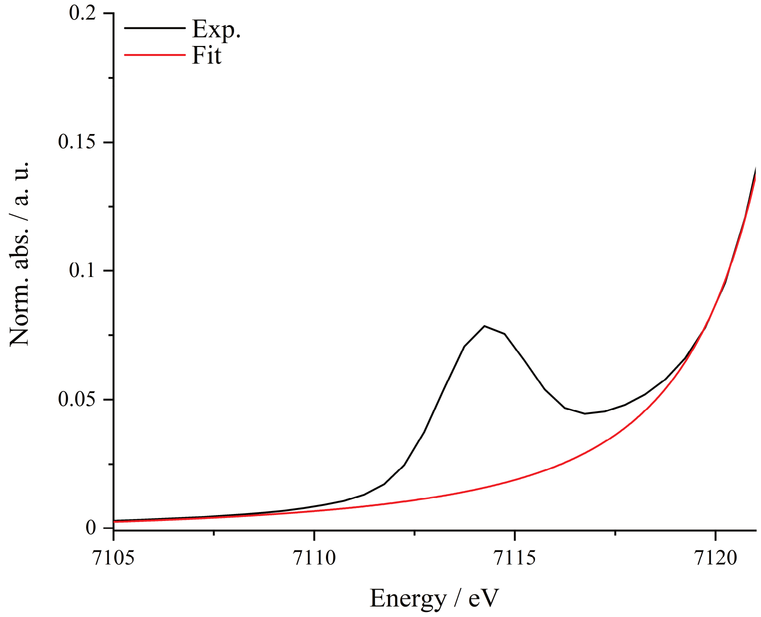

Figure SI 9.59: Pre-peak area of MM04 at the Fe K-edge and the background to remove the main edge, obtained by a Lorentzian-type function.

Table SI 9-83: Fit parameters of the background fit for MM04.

Model	Lorentz
Equation	y = y0 + (2*A/pi)*(w/(4*(x-xc)^2 + w^2))
y0	-0.00262 ± 2.28266E-4
xc	7124.32867 ± 0.21066
w	3.29089 ± 0.29528
A	3.66862 ± 0.5703
χ^2_{red}	2.62212E-7
r^2_{corr}	0.9999

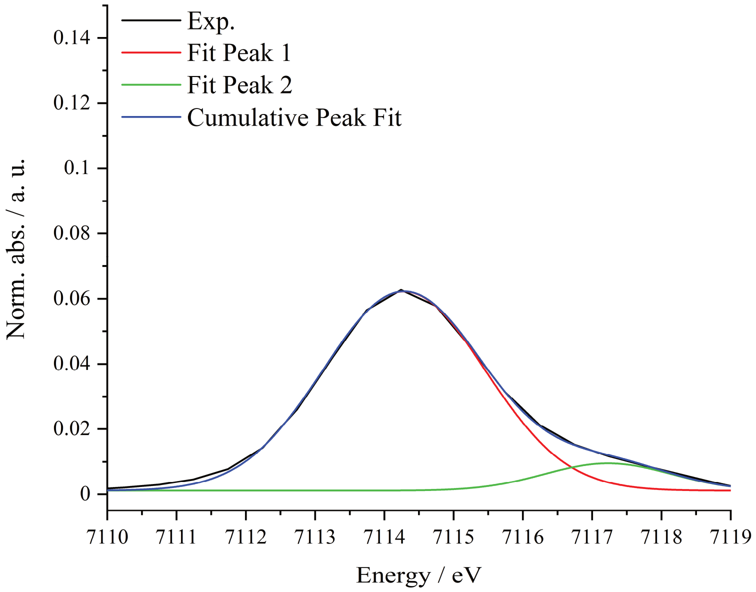

Figure SI 9.60: Background-corrected pre-peak of MM04 and corresponding Gaussian-type peak fits and cumulative peak fit.

Table SI 9-84: Fit parameters of the pre-peak fit of MM04.

Model	Gauss	
Equation	y=y0 + (A/(w*sqrt(pi/2)))*exp(-2*((x-xc)/w)^2)	
Plot	Peak1	Peak2
y0	0.00112 ± 3.69157E-4	0.00112 ± 3.69157E-4
xc	7114.28376 ± 0.02354	7117.22796 ± 0.14864
w	2.3385 ± 0.04716	1.82478 ± 0.2593
A	0.17915 ± 0.00378	0.01928 ± 0.00324
χ^2_{red}	8.9902E-7	
r^2_{corr}	0.9979	

MM05

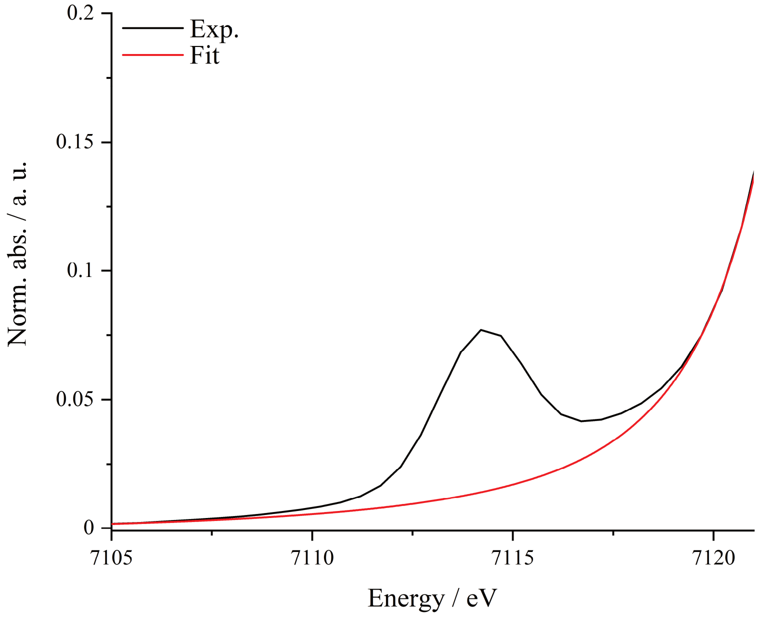

Figure SI 9.61: Pre-peak area of MM05 at the Fe K-edge and the background to remove the main edge, obtained by a Lorentzian-type function.

Table SI 9-85: Fit parameters of the background fit for MM05.

Model	Lorentz
Equation	y = y0 + (2*A/pi)*(w/(4*(x-xc)^2 + w^2))
y0	-0.00291 ± 1.56467E-4
xc	7123.94623 ± 0.12947
w	3.60206 ± 0.12065
A	2.88725 ± 0.22679
χ^2_{red}	1.3149E-7
r^2_{corr}	0.99995

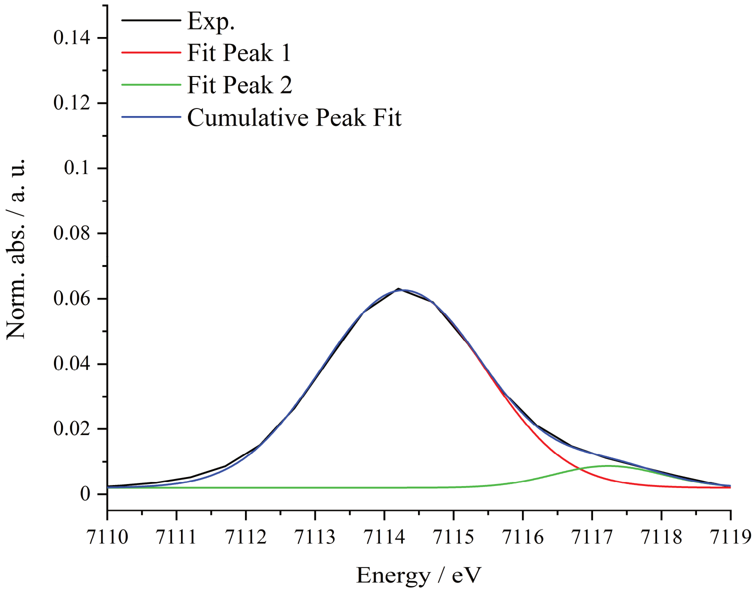

Figure SI 9.62: Background-corrected pre-peak of MM05 and corresponding Gaussian-type peak fits and cumulative peak fit.

Table SI 9-86: Fit parameters of the pre-peak fit of MM05.

Model	Gauss	
Equation	y=y0 + (A/(w*sqrt(pi/2)))*exp(-2*((x-xc)/w)^2)	
Plot	Peak1	Peak2
y0	0.00199 ± 3.46526E-4	0.00199 ± 3.46526E-4
xc	7114.27263 ± 0.01723	7117.23291 ± 0.12766
w	2.3575 ± 0.0388	1.58086 ± 0.23853
A	0.17908 ± 0.00302	0.01334 ± 0.00226
χ^2_{red}	7.38995E-7	
r^2_{corr}	0.99829	

9.4.5 Pre-peak Analysis: Co K-edge, MM02 - MM05

For pre-peak analysis at the Co K-edge the main edge was subtracted as a Lorentzian-type function. To obtain the precise pre-peak position a Gaussian-type function was applied for catalysts MM02 to MM05.

MM02

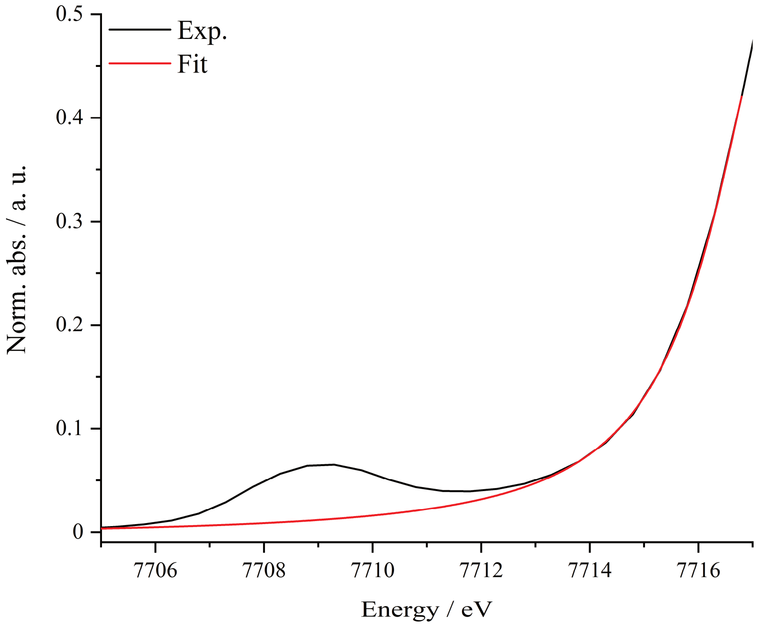

Figure SI 9.63: Pre-peak area of MM02 at the Co K-edge and the background to remove the main edge, obtained by a Lorentzian-type function.

Table SI 9-87: Fit parameters of the background fit for MM02.

Model	Lorentz
Equation	y = y0 + (2*A/pi)*(w/(4*(x-xc)^2 + w^2))
y0	-0.00404 ± 3.53109E-4
xc	7717.57722 ± 0.03212
w	2.96066 ± 0.01498
A	2.52413 ± 0.05136
χ^2_{red}	1.18002E-6
r^2_{corr}	0.99991

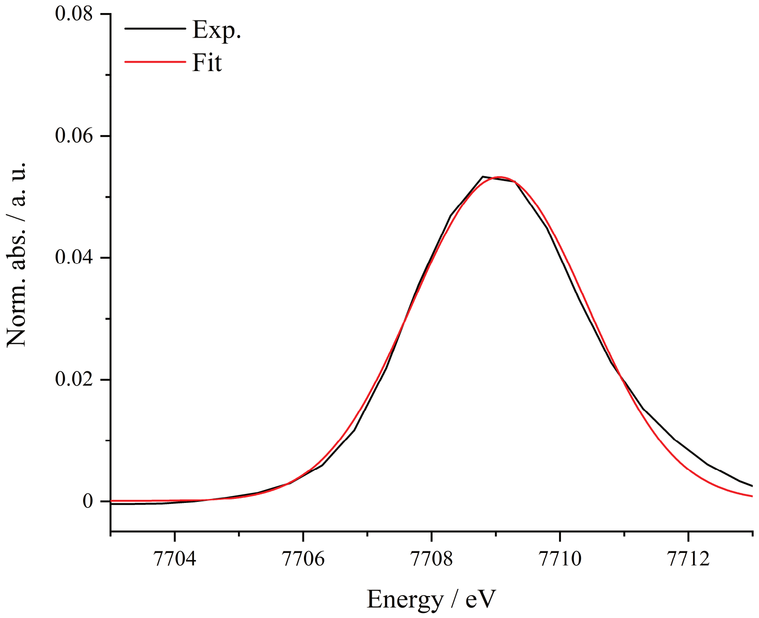

Figure SI 9.64: Background-corrected pre-peak of MM02 and corresponding Gaussian-type peak fit.

Table SI 9-88: Fit parameters of the pre-peak fit of MM02.

Model	Gauss
Equation	y=y0 + (A/(w*sqrt(pi/2)))*exp(-2*((x-xc)/w)^2)
y0	9.14777E-5 ± 4.20646E-4
xc	7709.05801 ± 0.02356
w	2.72628 ± 0.05614
A	0.18151 ± 0.00408
χ^2_{red}	2.03584E-6
r^2_{corr}	0.99409

MM03

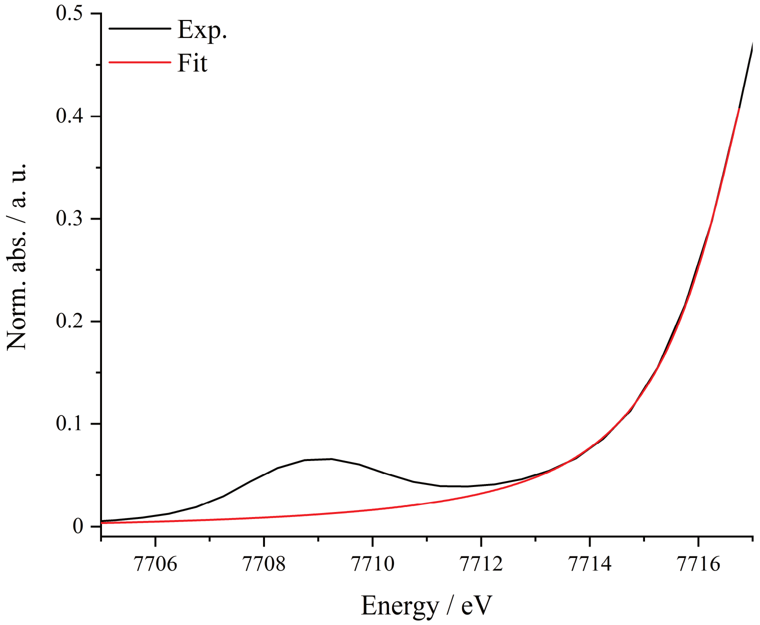

Figure SI 9.65: Pre-peak area of MM03 at the Co K-edge and the background to remove the main edge, obtained by a Lorentzian-type function.

Table SI 9-89: Fit parameters of the background fit for MM03.

Model	Lorentz
Equation	y = y0 + (2*A/pi)*(w/(4*(x-xc)^2 + w^2))
y0	-0.00411 ± 3.49569E-4
xc	7717.53702 ± 0.03287
w	3.01704 ± 0.0156
A	2.47836 ± 0.05071
χ^2_{red}	1.14917E-6
r^2_{corr}	0.99991

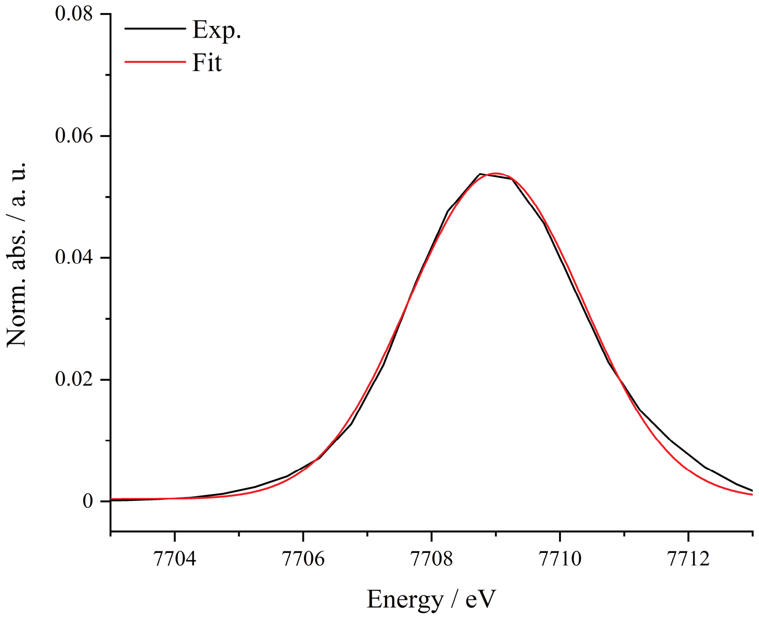

Figure SI 9.66: Background-corrected pre-peak of MM03 and corresponding Gaussian-type peak fit.

Table SI 9-90: Fit parameters of the pre-peak fit of MM03.

Model	Gauss
Equation	y=y0 + (A/(w*sqrt(pi/2)))*exp(-2*((x-xc)/w)^2)
y0	4.66408E-4 ± 3.69045E-4
xc	7709.00106 ± 0.01966
w	2.71859 ± 0.04743
A	0.18199 ± 0.00351
χ^2_{red}	1.43726E-6
r^2_{corr}	0.99593

MM04

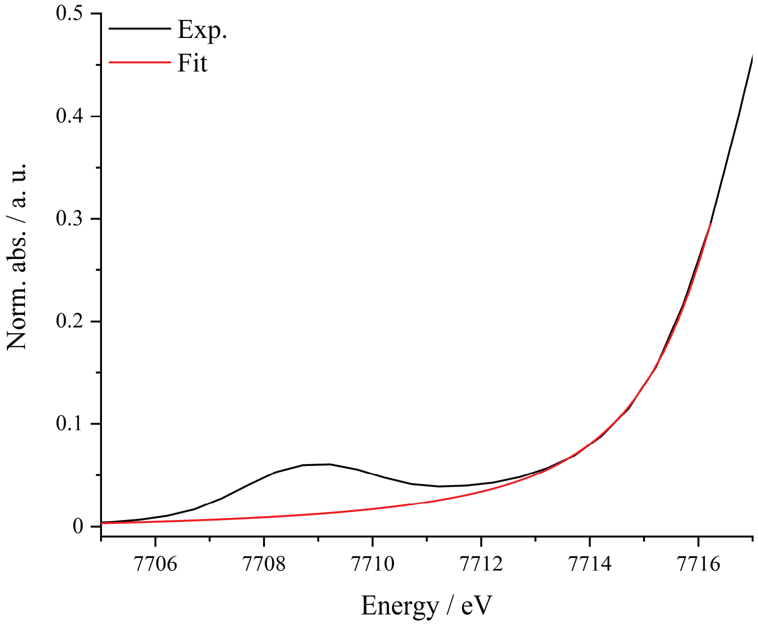

Figure SI 9.67: Pre-peak area of MM04 at the Co K-edge and the background to remove the main edge, obtained by a Lorentzian-type function.

Table SI 9-91: Fit parameters of the background fit for MM04.

Model	Lorentz
Equation	y = y0 + (2*A/pi)*(w/(4*(x-xc)^2 + w^2))
y0	-0.00495 ± 4.88376E-4
xc	7717.59054 ± 0.10873
w	3.14965 ± 0.06024
A	2.60744 ± 0.17912
χ^2_{red}	1.7379E-6
r^2_{corr}	0.99975

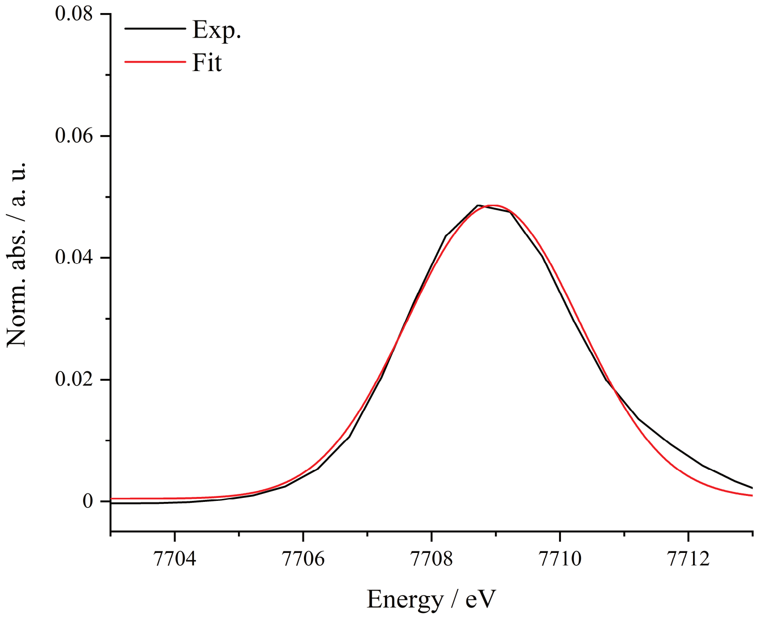

Figure SI 9.68: Background-corrected pre-peak of MM04 and corresponding Gaussian-type peak fit.

Table SI 9-92: Fit parameters of the pre-peak fit of MM04.

Model	Gauss
Equation	y=y0 + (A/(w*sqrt(pi/2)))*exp(-2*((x-xc)/w)^2)
y0	5.13461E-4 ± 5.08383E-4
xc	7708.95751 ± 0.02734
w	2.67667 ± 0.06756
A	0.16133 ± 0.0046
χ^2_{red}	2.28935E-6
r^2_{corr}	0.99224

MM05

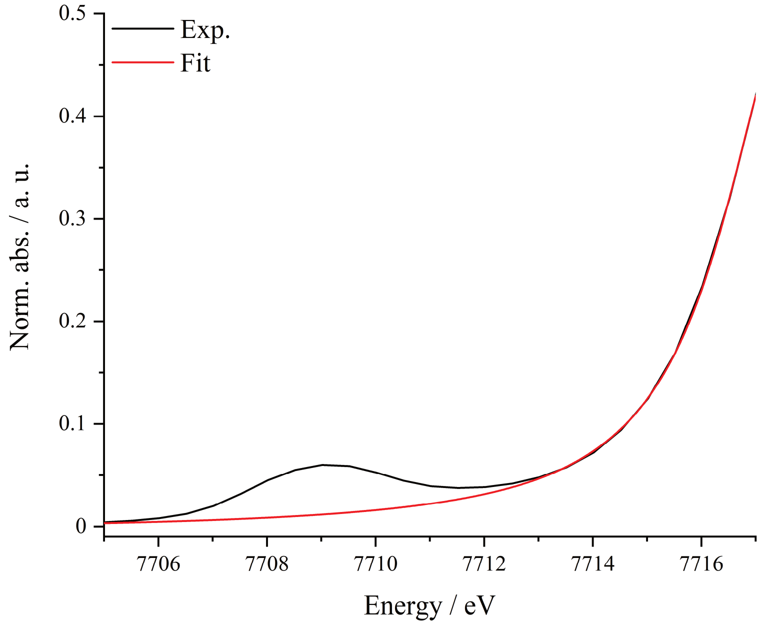

Figure SI 9.69: Pre-peak area of MM05 at the Co K-edge and the background to remove the main edge, obtained by a Lorentzian-type function.

Table SI 9-93: Fit parameters of the background fit for MM05.

Model	Lorentz
Equation	y = y0 + (2*A/pi)*(w/(4*(x-xc)^2 + w^2))
y0	-0.0044 ± 4.16942E-4
xc	7717.68494 ± 0.0306
w	3.13747 ± 0.01959
A	2.48717 ± 0.04606
χ^2_{red}	1.52442E-6
r^2_{corr}	0.99989

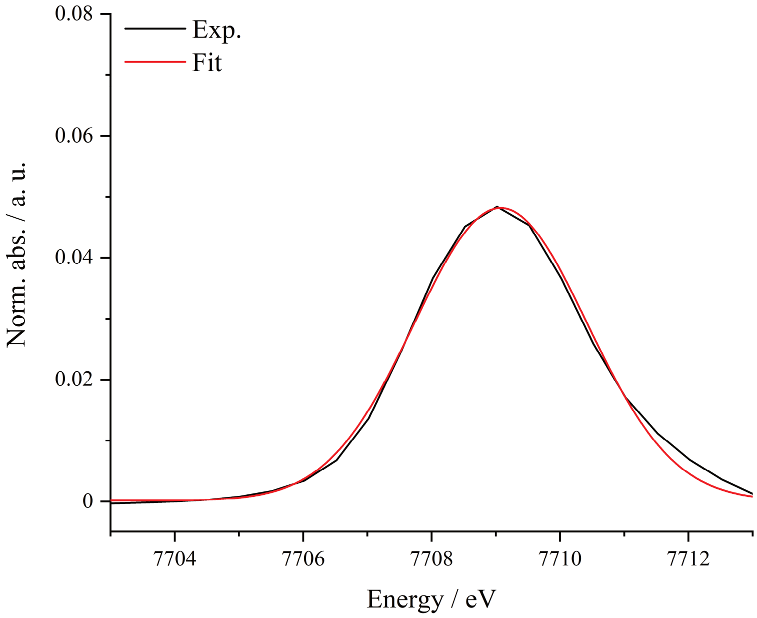

Figure SI 9.70: Background-corrected pre-peak of MM05 and corresponding Gaussian-type peak fit.

Table SI 9-94: Fit parameters of the pre-peak fit of MM05.

Model	Gauss
Equation	y=y0 + (A/(w*sqrt(pi/2)))*exp(-2*((x-xc)/w)^2)
y0	1.71596E-4 ± 3.41993E-4
xc	7709.07666 ± 0.0194
w	2.68627 ± 0.04722
A	0.16157 ± 0.00317
χ^2_{red}	1.14361E-6
r^2_{corr}	0.99604

9.4.6 Pre-peak Analysis: References

Lithium manganese(III, IV) oxide ($LiMn_2O_4$)

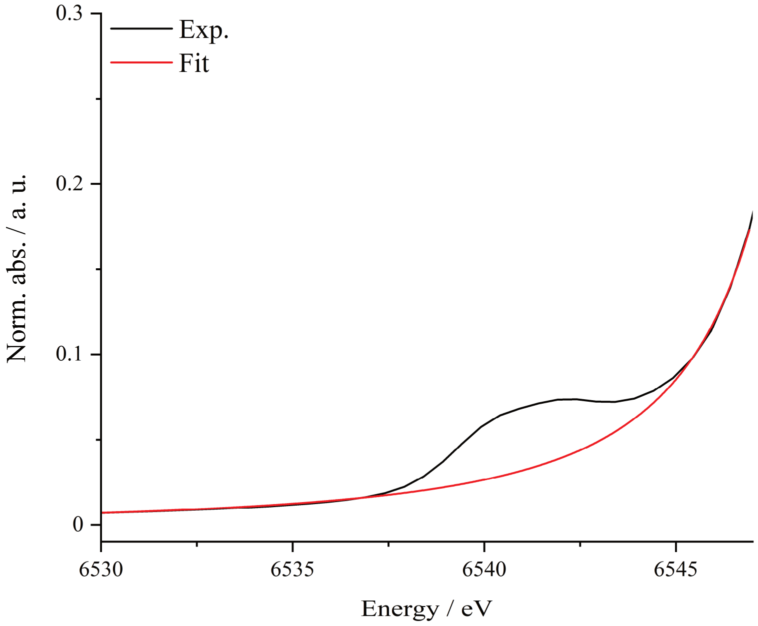

Figure SI 9.71: Pre-peak area of $LiMn_2O_4$ at the Mn K-edge and the background to remove the main edge, obtained by a Lorentz function.

Table SI 9-95: Fit parameters of the background fit for $LiMn_2O_4$.

Model	Lorentz
Equation	y = y0 + (2*A/pi)*(w/(4*(x-xc)^2 + w^2))
y0	-7.44769E-4 ± 5.26328E-4
xc	6551.45274 ± 0.59326
w	0.09914 ± 61.77847
A	226.84275 ± 141379.98022
χ^2_{red}	5.74178E-7
r^2_{corr}	0.9997

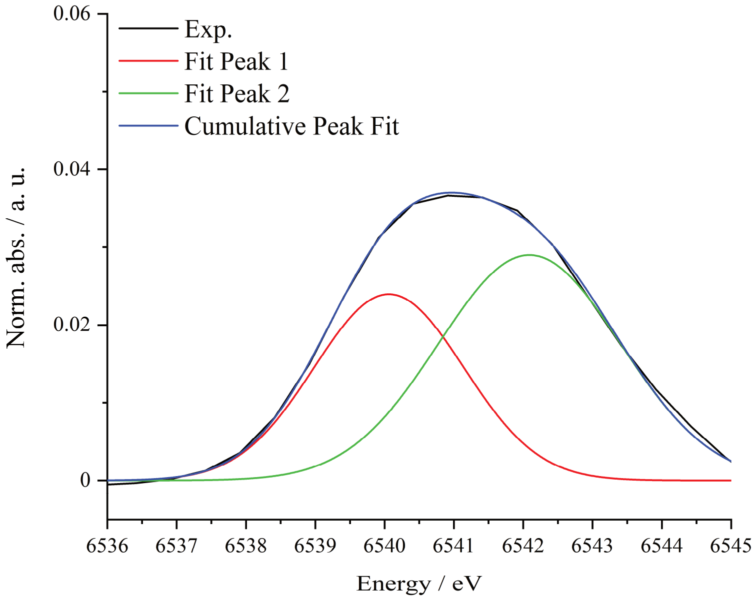

Figure SI 9.72: Background-corrected pre-peak of $LiMn_2O_4$, two Gaussian-type peak fits and cumulative peak fit.

Table SI 9-96: Fit parameters of the pre-peak fit of $LiMn_2O_4$.

Model	Gauss	
Equation	y=y0 + (A/(w*sqrt(pi/2)))*exp(-2*((x-xc)/w)^2)	
Plot	Peak1	Peak2
y0	0 ± 3.38908E-4	0 ± 3.38908E-4
xc	6540.0621 ± 0.25008	6542.09008 ± 0.34039
w	2.1599 ± 0.20581	2.62764 ± 0.30302
A	0.06489 ± 0.02517	0.09548 ± 0.02549
χ^2_{red}	7.2193E-7	
r^2_{corr}	0.99659	

Hematite (α-Fe_2O_3)

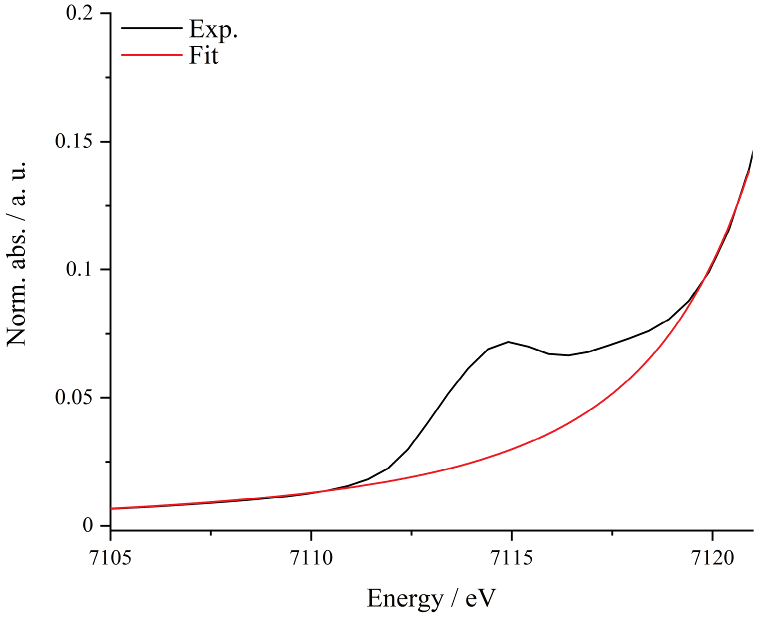

Figure SI 9.73: Pre-peak area of α-Fe_2O_3 at the Fe K-edge and the background to remove the main edge, obtained by a Lorentzian-type function.

Table SI 9-97: Fit parameters of the background fit for α-Fe_2O_3.

Model	Lorentz
Equation	y = y0 + (2*A/pi)*(w/(4*(x-xc)^2 + w^2))
y0	-0.00178 ± 6.17985E-4
xc	7125.08027 ± 0.59067
w	5.35235 ± 0.72219
A	4.0458 ± 1.05539
χ^2_{red}	3.41027E-7
r^2_{corr}	0.99979

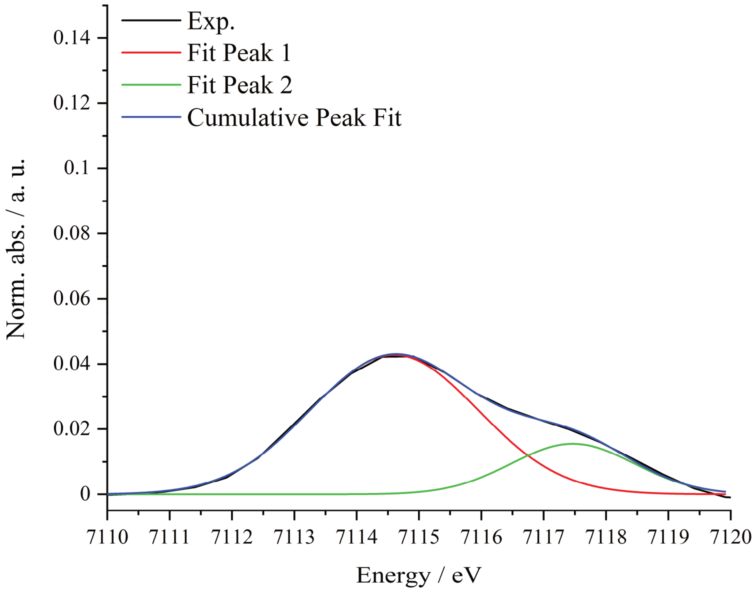

Figure SI 9.74: Background-corrected pre-peak of α-Fe_2O_3 and corresponding Gaussian-type peak fits and cumulative peak fit.

Table SI 9-98: Fit parameters of the pre-peak fit of α-Fe_2O_3.

Model	Gauss	
Equation	y=y0 + (A/(w*sqrt(pi/2)))*exp(-2*((x-xc)/w)^2)	
Plot	Peak1	Peak2
y0	0 ± 2.84616E-4	0 ± 2.84616E-4
xc	7114.60158 ± 0.03656	7117.46756 ± 0.0772
w	2.68567 ± 0.06306	1.98719 ± 0.10987
A	0.14395 ± 0.00405	0.03863 ± 0.00339
χ^2_{red}	3.6954E-7	
r^2_{corr}	0.99839	

Maghemite (γ-Fe_2O_3)

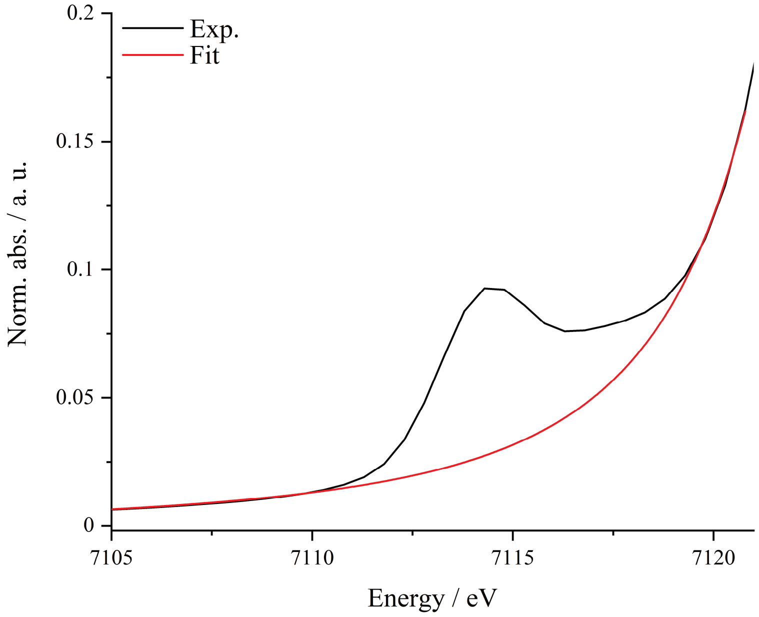

Figure SI 9.75: Pre-peak area of γ-Fe_2O_3 *at the Fe K-edge and the background to remove the main edge, obtained by a Lorentzian-type function.*

Table SI 9-99: Fit parameters of the background fit for γ-Fe_2O_3*.*

Model	Lorentz
Equation	y = y0 + (2*A/pi)*(w/(4*(x-xc)^2 + w^2))
y0	-0.00211 ± 6.79682E-4
xc	7124.56476 ± 0.56585
w	4.81389 ± 0.69828
A	4.28828 ± 1.19353
χ^2_{red}	4.27368E-7
r^2_{corr}	0.99981

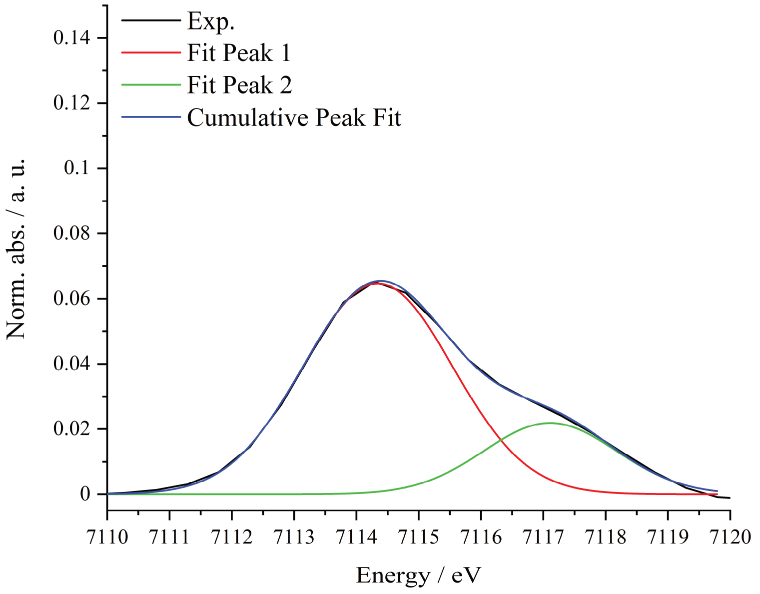

Figure SI 9.76: Background-corrected pre-peak of γ-Fe_2O_3 and corresponding Gaussian-type peak fits and cumulative peak fit.

Table SI 9-100: Fit parameters of the pre-peak fit of γ-Fe_2O_3.

Model	Gauss	
Equation	y=y0 + (A/(w*sqrt(pi/2)))*exp(-2*((x-xc)/w)^2)	
Plot	Peak1	Peak2
y0	0 ± 3.00394E-4	0 ± 3.00394E-4
xc	7114.34287 ± 0.02922	7117.10866 ± 0.07861
w	2.39884 ± 0.04445	2.14073 ± 0.10752
A	0.19461 ± 0.00474	0.0586 ± 0.00441
χ^2_{red}	4.62017E-7	
r^2_{corr}	0.99908	

Cobalt(II) bromide ($CoBr_2$)

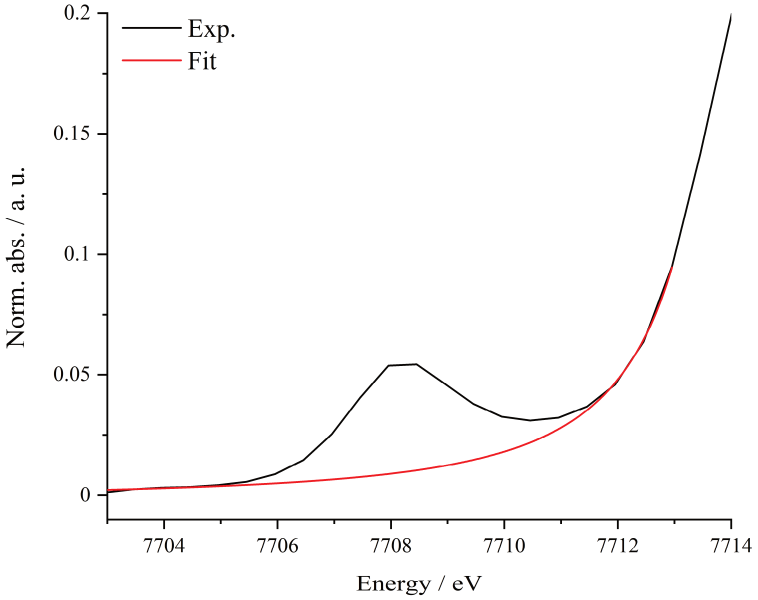

Figure SI 9.77: Pre-peak area of the $CoBr_2$ reference at the Co K-edge and the background to remove the main edge, obtained by a Lorentzian-type function.

Table SI 9-101: Fit parameters of the background fit for $CoBr_2$.

Model	Lorentz
Equation	y = y0 + (2*A/pi)*(w/(4*(x-xc)^2 + w^2))
y0	-0.0014 ± 0.00151
xc	7715.3792 ± 1.44752
w	0.04863 ± 163.27909
A	72.89278 ± 244790.29135
χ^2_{red}	1.0979E-6
r^2_{corr}	0.99906

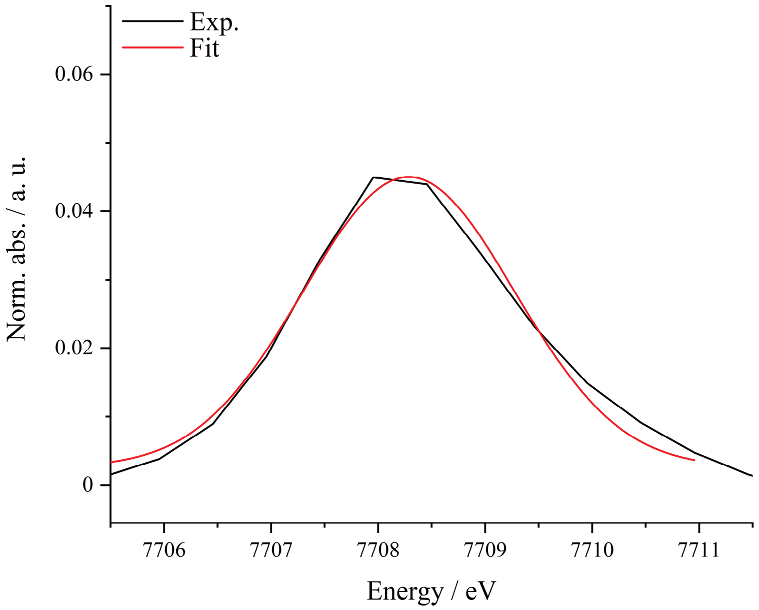

Figure SI 9.78: Background-corrected pre-peak of $CoBr_2$ and corresponding Gaussian-type peak fit.

Table SI 9-102: Fit parameters of the pre-peak fit of $CoBr_2$.

Model	Gauss
Equation	y=y0 + (A/(w*sqrt(pi/2)))*exp(-2*((x-xc)/w)^2)
y0	0.00254 ± 0.0015
xc	7708.28695 ± 0.03575
w	1.97586 ± 0.1182
A	0.10519 ± 0.00841
χ^2_{red}	4.13526E-6
r^2_{corr}	0.98303

9.4.7 EXAFS Analysis

9.4.7.1 Fe01 - Fe20

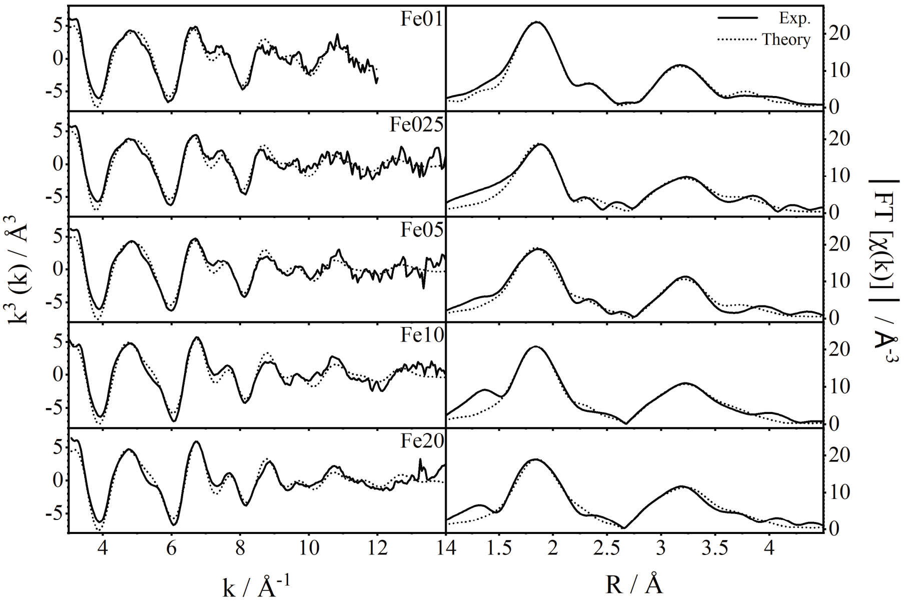

Figure SI 9.15: $k^3\chi(k)$ of the EXAFS spectra (left) and the corresponding Fourier transformed functions (right) of catalyst Fe01 to Fe20 and the fitted spectra.

9.4.7.2 MI01 - MI10 & SI10

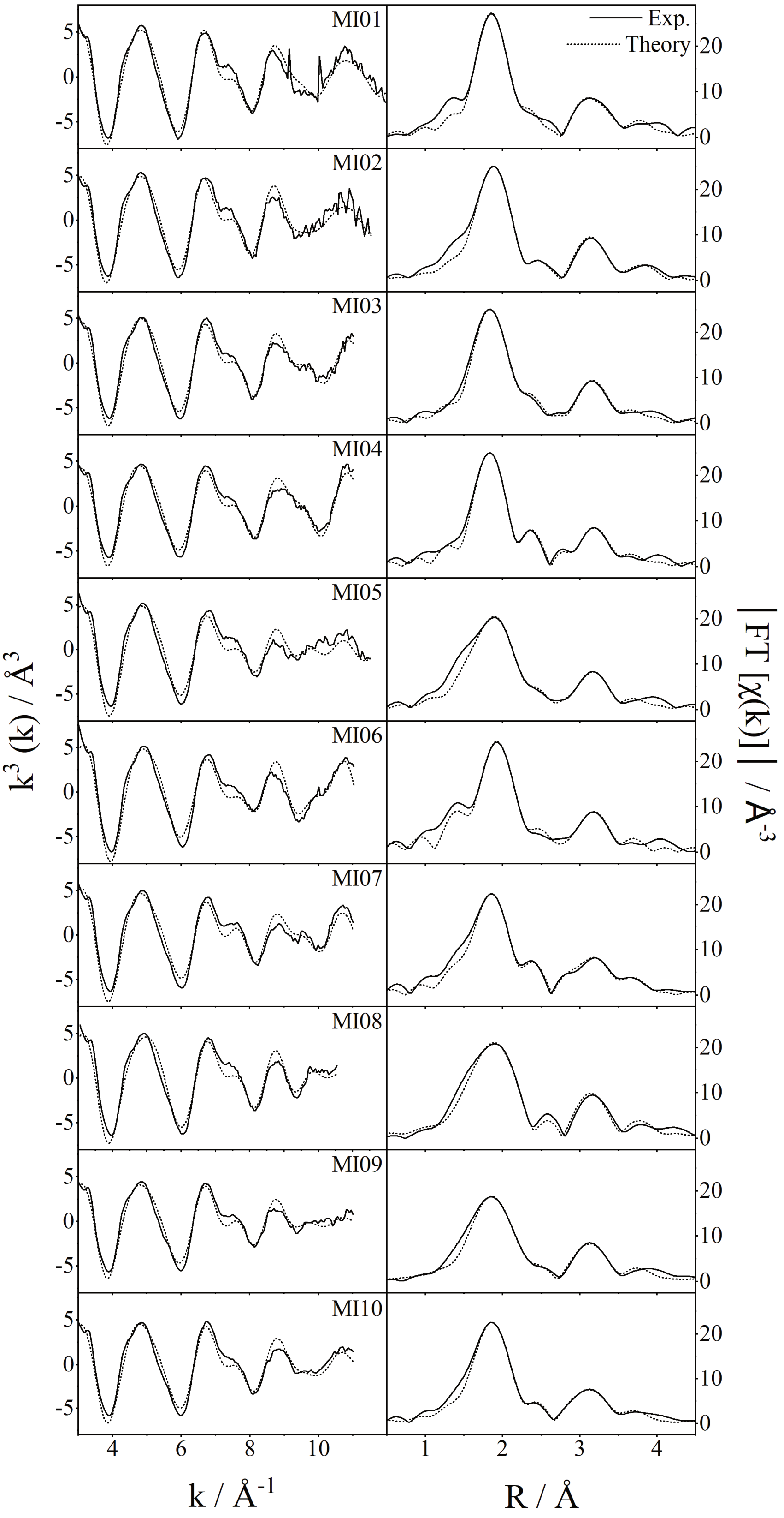

Figure SI 9.79: $k^3\chi(k)$ of the EXAFS spectra (left) and the corresponding Fourier transformed functions (right) of catalyst MI01 - MI10 and the fitted spectra.

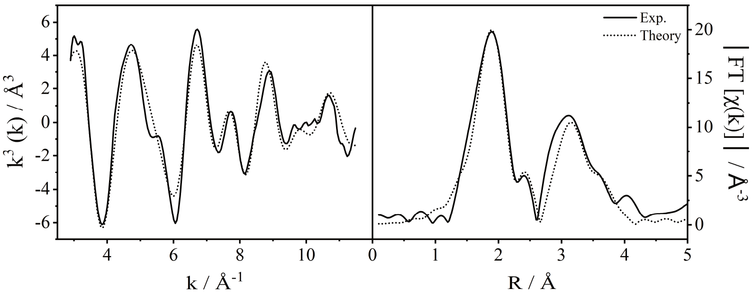

Figure SI 9.80: k³χ(k) of the EXAFS spectra (left) and the corresponding Fourier transformed functions (right) of SI10 and the fitted spectra.

9.4.7.3 MM01 - MM04: Mn K-edge

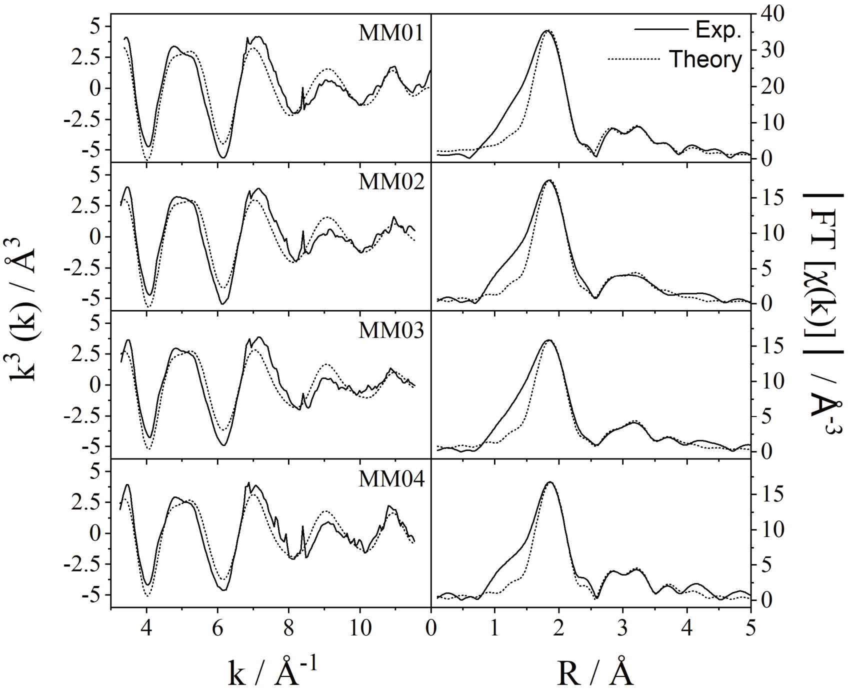

Figure SI 9.81: $k^3\chi(k)$ of the EXAFS spectra (left) and the corresponding Fourier transformed functions (right) of catalyst MM01 to MM04 at the manganese K-edge and the fitted spectra.

9.4.7.4 MM01 - MM05: Fe K-edge

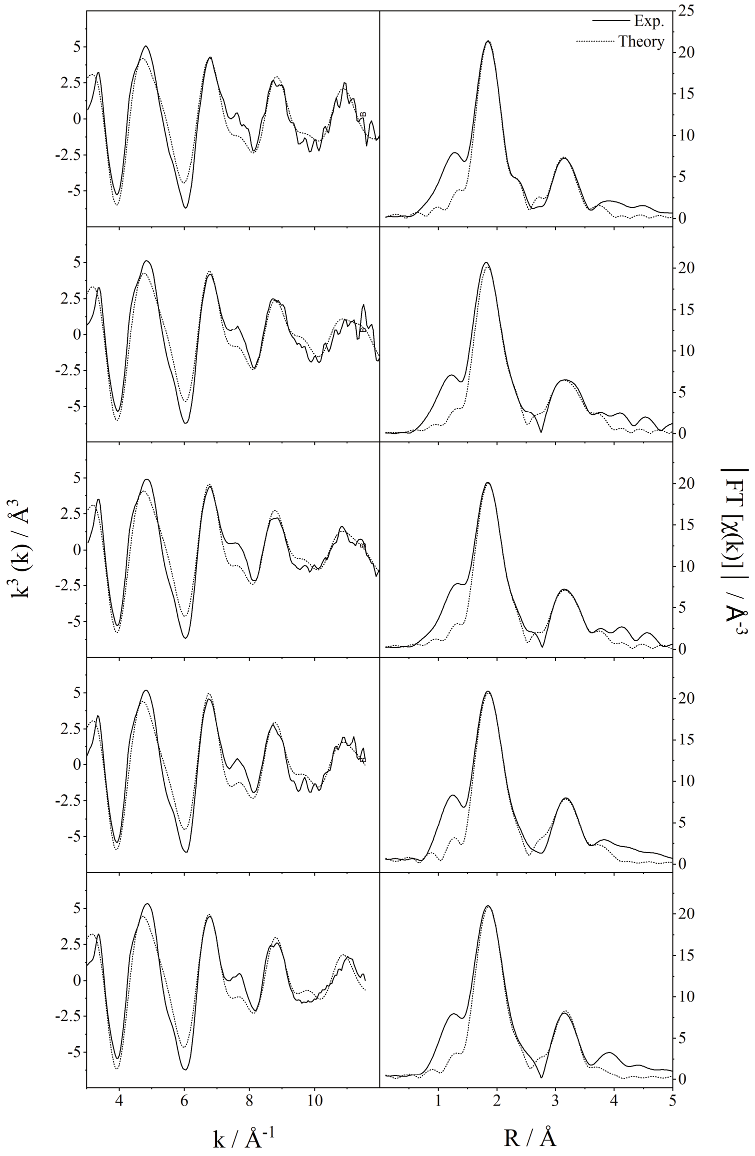

Table SI 9-103: k³χ(k) of the EXAFS spectra (left) and the corresponding Fourier transformed functions (right) of catalyst MM01 to MM05 at the iron K-edge and the fitted spectra.

9.4.7.5 MM02 - MM05: Co K-edge

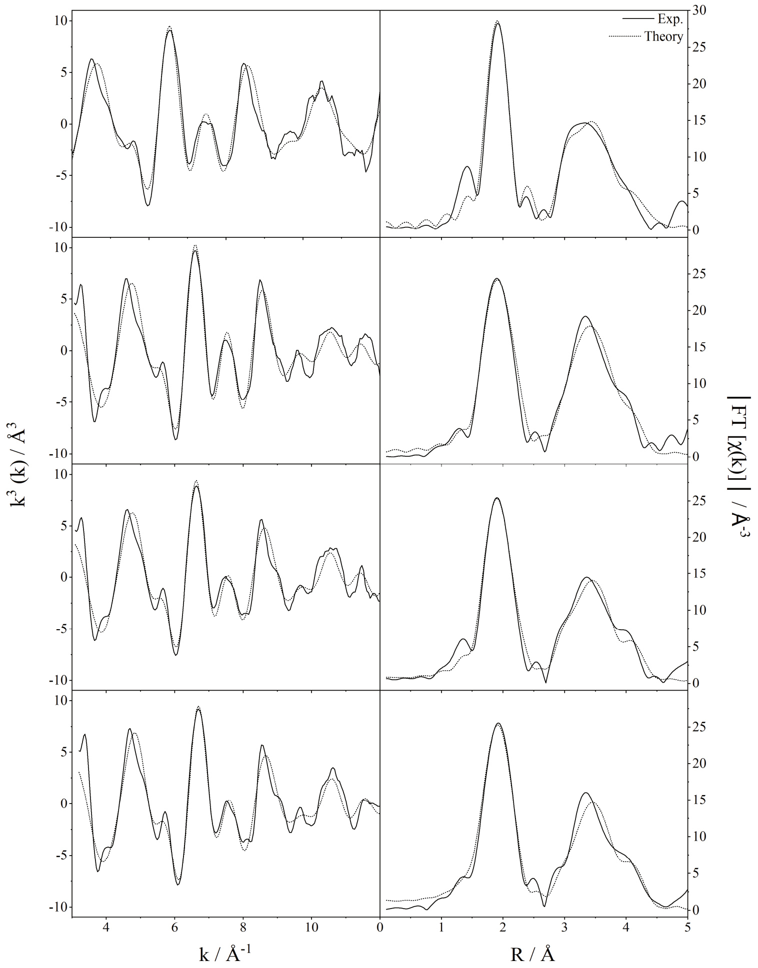

Table SI 9-104: $k^3\chi(k)$ of the EXAFS spectra (left) and the corresponding Fourier transformed functions (right) of catalyst MM02 to MM05 at the cobalt K-edge and the fitted spectra.

9.5 Optimization MM06

Table SI 9-105: Fit parameters of the fit shown in Figure 5.9.

Model	Cubic
Equation	y = A + B*x + C*x^2 + D*x^3
Plot	C
A	0.62291 ± 0.03149
B	-0.30869 ± 0.05938
C	0.04336 ± 0.02666
D	-2.45467E-4 ± 0.00294
χ^2_{red}	9.94072E-4
r^2_{COD}	0.99524
r^2_{corr}	0.98094

Alternative Zitate,
welche es nicht geschafft haben:

i bin halt a dummerle.
M. Bauer

*You did it. You crazy son of a b****, you did it.*
Ian Malcolm